Nuclear Resonance Fluorescence for Nuclear Materials Assay

by

Brian Joseph Quiter

A dissertation submitted in partial satisfaction of the
requirements for the degree of
Doctor of Philosophy

in

Engineering - Nuclear Engineering

in the

GRADUATE DIVISION
of the
UNIVERSITY OF CALIFORNIA, BERKELEY

Committee in charge:
Stanley Prussin, Chair
Eric Norman
James Siegrist
Jasimina Vujic

Fall 2010

Nuclear Resonance Fluorescence for Nuclear Materials Assay

Abstract

Nuclear Resonance Fluorescence for Nuclear Materials Assay

by

Brian Joseph Quiter

Doctor of Philosophy in Engineering - Nuclear Engineering

University of California, Berkeley

Stanley Prussin, Chair

This dissertation examines the measurement of nuclear resonance fluorescence γ-rays as a technique to non-destructively determine isotopic compositions of target materials that are of interest for nuclear security applications. The physical processes that can result in non-resonant background to nuclear resonance fluorescence measurements are described and investigated using a radiation transport computer code that relies on the Monte Carlo technique, MCNPX. The phenomenon of nuclear resonance fluorescence is discussed with consideration of the angular distributions of resonance emissions, the effects of nuclear recoil, and the influence of thermal motion.

Models describing two ways of measuring nuclear resonance fluorescence rates in materials are considered. First the measurement of back-scattered photons is considered. In this type of measurement, the portion of the interrogating photon beam that is scattered into large relative angles is measured. When the radioactivity of the target can be overcome by shielding or by use of intense photon sources, direct measurement of γ-rays, emitted during nuclear resonance fluorescence can provide quantitative signatures that appear to be useful for applications such as forensic age-dating of large radiological sources. However, if the target radioactivity is too intense, as in the case for most spent nuclear fuel, a second measurement type, where indirect measurement of transmitted resonant-energy photons can also provide quantitative information. This method allows radiation detectors to be better-shielded from

target radioactivity, but suffers from a slower accrual rate of statistical confidence. The models described herein indicate that very intense photon sources and large high-resolution detector arrays would be needed to measure ^{239}Pu content in spent fuel to precisions desired by nuclear safeguards organizations. However, the rates at which statistics accrue are strongly proportional to the strengths of the resonances, and measurement of a plutonium isotope with stronger resonances may provide more practical measurement rates.

The model for predicting relative detection rates of nuclear resonance fluorescence γ-rays in the transmission measurement was experimentally tested using the ^{238}U in a mixture of depleted uranium and lead as a surrogate for ^{239}Pu in spent fuel. The experiment indicated that the model was approximately correct, but that the process of notch refilling, which was excluded from the initial model, appears to be visible. Data files of the computer code, MCNPX, were modified to allow for nuclear resonance fluorescence to be simulated and a bug in the code was repaired to allow the code to more accurately simulate non-resonant elastic photon scattering. Simulations using this modified version of MCNPX have indicated that the magnitude of the notch refill process is comparable to that of the difference between the analytical model and the experimental data.

This dissertation is dedicated to my advisor, Stan, who has taught me much more than can ever be put into words.

Contents

List of Figures

List of Tables

Acknowledgments

I would like to thank Vladimir M. for the numerous discussions we had on nuclear resonance fluorescence and the countless computer-hours he spent trying to accurately simulate back-scattered photon spectra, Bethany G., Dan C., and Amanda J. for proving to me that Stan will someday free me, Jim S., Ed M. and Bernhard L. for the financial and academic support, Steve T., Laurie W., and John H. at LANL for providing me with the environment and opportunity to learn MCNPX and nuclear safeguards, Bill B., Steve K., Cody W. and Chat C. for all your efforts performing experiments at the HVRL, and most importantly, my mother and father Elaine and John, and my wife Melissa, who have loved supported me as I work to make something of myself.

List of Acronyms

ADC	Analogue-to-Digital Converter
CDF	Cumulative probability Distribution Function
DBLP	Doppler-broadened Lorentzian cross section Profile
ENDF	Evaluated Nuclear Data File
EPDL	Evaluated Photon Data Library
ETRAN	computer program Electron TRANsport
FWHM	Full-Width at Half-Maximum
GDR	Giant Dipole Resonance
HIγS	High Intensity γ-ray Source
HPGe	High-Purity Germanium detector
IAEA	International Atomic Energy Agency
IOI	Isotope of Interest for transmission assay measurements
KN	Klein-Nishina differential scattering cross section
MCNP	computer program Monte Carlo N-Particle
MCNPX	computer program Monte Carlo N-Particle eXtended
MUF	Material Unaccounted For
NIST	National Institute of Standards and Technology
NJOY	daughter nuclear data processing code of program MINX: Multi-group Interpolation of Nuclear X-Sections
NRF	Nuclear Resonance Fluorescence
PDF	Probability Distribution Function
RIPL	Reaction/Interaction Parameter Library
TD	Transmission detector (comprised of IOI)
TTB	Thick-Target Bremsstrahlung model
wt.%	weight percent
XCOM	NIST X-ray attenuation coefficient database

Chapter 1

Introduction

After the end of the Cold War, the United States perceived a dramatic downturn in the severity of national security threats. More recently, increased concern for international terrorism has changed this perception. President Obama recently stated that terrorists acquiring a nuclear weapon is "the most immediate and extreme threat to global security." (1)

Nuclear terrorism can take many forms. Fission devices may be stolen by terrorist groups or provided to terrorist groups by rogue nations, or they may be produced by terrorist groups that have obtained fissile material. Large quantities of radioactive material may also be mixed into conventional explosives to create a radiological dispersal device, which, when detonated, could spread radioactive material over a large area.

Efforts toward preventing nuclear terrorism take three primary approaches. One approach is to ensure that terrorist organizations do not obtain the necessary nuclear materials. If such materials are obtained, border and port security is intended to make it difficult to deliver the material into the United States or allied countries. And if material is recovered by law enforcement agencies, the capability to identify the source of the material through forensics measurements may help law-enforcement activities to disrupt channels by which terrorists may obtain other nuclear material. Reliable forensics may also provide an incentive for nations and industrial concerns to secure their nuclear material. This dissertation examines the potential use of the phenomenon of nuclear resonance fluorescence (NRF) to perform measurements on nuclear materials that may contribute to preventing nuclear terrorism.

1.1 Nuclear Safeguards

1.1.1 Worldwide Weapons Material Production Capacity

Operation of nuclear reactors for power generation has supplied the world with about 2×10^6 GW·d of electricity since 1980(2). Official projections indicate that

both domestic and world-wide nuclear power generation will increase in the future(3). Operation of nuclear power plants results in the production of plutonium through the absorption of neutrons by ^{238}U atoms, followed by two radioactive decays occurring by β^--particle emission[1]. Although the exact quantity depends upon reactor type and operation conditions, approximately 300 g of Pu are produced per GW·d of electrical energy produced by the operation of nuclear reactors. Therefore, approximately 6×10^5 kg of Pu have been produced world-wide since 1980 as a result of nuclear power generation(4)(5).

As little as 4.4 kg of ^{239}Pu can be used to make a nuclear weapon, although with plutonium isotopic compositions of typical spent fuel, this mass increases to approximately 10 kg(5). Thus, the amount of plutonium generated by civilian power production in the past 30 years is sufficient to make approximately 6×10^4 nuclear weapons and the current plutonium production rate is sufficient to produce approximately 3×10^3 plutonium weapons annually.

Enrichment of uranium is necessary to make fuel for light water reactors (LWRs). Typical nuclear reactor fuel is currently enriched from natural composition (0.72% ^{235}U) to around 5% ^{235}U. Further enrichment to around 80% ^{235}U results in weapons-grade uranium. The world has enough enrichment capacity to produce 3×10^6 kg of weapons-grade uranium, or enough for approximately 10^4 uranium bombs annually(6).

The capacity of the civilian nuclear power infrastructure to produce nuclear weapons is what motivates the implementation of measures to safeguard nuclear material. The primary safeguards activities include security and accountancy of plutonium and enriched uranium at nuclear facilities that are declared civilian in nature, as well as ensuring that clandestine nuclear materials activities do not occur at un-declared facilities.

1.1.2   Safeguarding Enrichment Facilities

The primary safeguards concern for an enrichment facility that is that it is able to enrich uranium to levels needed for use in nuclear weapons construction. The ability to measure relative concentrations of uranium isotopes in materials at enrichment facilities is therefore of prime interest for safeguards purposes. Presently, uranium enrichments are measured by one of two methods. Either gaseous samples (i.e., UF$_6$) are collected and later analyzed via mass spectrometry, or passive counting of the 185.7-keV γ-ray, emitted in the decay of ^{235}U is conducted.

Facility operators strongly oppose sampling because the fear that sampling itself may introduce impurities into sensitive enrichment equipment. Mass spectrometry is also costly and therefore is performed irregularly. Passive counting measurements

---

[1]The described sequence generates ^{239}Pu, which may undergo additional neutron reactions to produce other plutonium isotopes. More circuitous pathways can also result in plutonium production.

rely on calibrations to relate count rates to ^{235}U content and therefore enrichment. These measurements are prone to inaccuracy because the calibration is sensitive to container thicknesses, which may vary because of erosion or deposition of solid UF_6 on the container surface. In principle, a measurement of fluorescent γ-rays could be conducted continuously on UF_6 at selected locations at an enrichment facility and thus, non-intrusively measure relative concentrations of ^{235}U and ^{238}U. Furthermore, if the pressure and volume of the UF_6 is known, then enrichment measurements allow for independent checks on the mass balance of uranium material entering, leaving, and present at the enrichment facility.

1.1.3   Safeguarding Spent Fuel Reprocessing Facilities

Spent nuclear fuel is another example where measurement of fissile material content is of interest for safeguards purposes. Reprocessing involves chemical separation of actinides from fission products, as well as possible separation of different elemental actinides from each other. A reprocessing system such as UP3 operating at the La Hague site in France is capable of reprocessing about 8×10^5 kg of spent fuel annually(8). This corresponds to approximately three 3.5 m tall, 15x15 fuel assemblies per day, indicating an approximate scale to the time permitted for safeguards measurements that will not disrupt the reprocessing rate.

Presently, the quantities of plutonium and ^{235}U are not directly measured in spent fuel before reprocessing. Rather, surrogate signatures such as the γ-rays emitted in the decay of ^{134}Cs, ^{137}Cs, and ^{154}Eu may be measured as an indicator of burn-up, which can be correlated to the plutonium and ^{235}U content through reactor model calculations. These measurements, however, do not provide independent information regarding fissile material content and are prone to systematic inaccuracies due to dependence on reactor operating conditions(4).

To overcome the shortcomings of indirect plutonium and ^{235}U measurement, these constituents are directly measured during the aqueous reprocessing process. After fuel dissolution, the solution is transferred to a tank of well-known volume, called the *input accountability tank*, and a sample is taken for analysis. Concentrations of plutonium and ^{235}U in the sample are determined to nominally 0.3% uncertainties through analytical radiochemistry methods. Because the volume of the input accountability tank is well-known, measured concentrations in the sample can be related to quantities of uranium and plutonium in the entire reprocessed assembly. However, because the sampling process occurs after dissolution, there is the potential for material to be diverted before it reaches the input accountability tank. Furthermore, many non-aqueous reprocessing techniques are under consideration for new fuel cycle systems. Some of these techniques do not allow for the method of aqueous dissolution and sampling to quantify fissile material content.

The precision to which fissile actinide content in spent fuel must be measured varies by application. Currently, the International Atomic Energy Agency (IAEA),

which is the primary international safeguarding agency, has a goal of "no material unaccounted for" (MUF). The MUF is defined as the difference between the amount of material that has entered a facility and the sum of the material leaving and present at the facility. For example, if more ^{239}Pu has entered a facility than is found to be present and has left, the MUF would be positive, indicating there is material unaccounted for. Because every measurement is associated with a degree uncertainty MUF must also have an associated uncertainty. A goal of improving safeguards technology is to reduce the uncertainty in MUF to as low as possible.

In principle, and in the absence of systematic uncertainty, measurements of fissile material in spent fuel should vary from the true value by a Gaussian distribution whose width is described by the standard deviation of the measurement uncertainty. Current spent fuel reprocessing systems process about three PWR assemblies per day, each containing about 3 kg of ^{239}Pu. If, before dissolution of each assembly, measurements of ^{239}Pu content were conducted at 10% precision, the system would yield an expected monthly ^{239}Pu MUF uncertainty of about 2.5 kg due to statistical errors alone, and excluding any systematic errors. Over the course of a year, the mass uncertainty would be about 8.7 kg. This implies that continuous deviations of small amounts of ^{239}Pu could go un-noticed by materials accountancy methods based on 10% measurements, and that over the course of one or two years, the quantity of Pu necessary to create a weapon could be stolen while the facility satisfies safeguards regulations.

Reprocessing facilities presently use destructive analysis of an aqueous sample taken from the input accountability tank to provide the fissile material measurement at a nominal accuracy of $\pm 1\%$. This implies that uncertainties in input ^{239}Pu quantities are one-tenth as large as those assumed above, and that continuous deviations would need to occur over the course of approximately 100 years, (or at multiple reprocessing facilities) to go un-detected.

However, diversion of dissolved spent fuel that circumvents the input accountability tank could dramatically increase the rate of un-detected ^{239}Pu diversion. This has motivated research into measuring the content of intact spent fuel assemblies.

Indirect measurements of plutonium content in spent fuel assemblies can result in impressive precision when well-known reactor conditions are compared to reactor models. However, without knowledge of reactor operating conditions (such as power level variations with time), these models tend to be accurate to only $\pm$ 10-20%. Because operators may intentionally or unintentionally supply inaccurate information regarding the irradiation history of a fuel, the most robust safeguards measurement would be direct measurement of fissile material content We therefore conclude that any technique capable of directly measuring, with moderate precision and high accuracy, plutonium or ^{235}U content in intact spent nuclear fuel would be a technological improvement. Studies into several methods to conduct such measurements are underway(9), and it is from this perspective that nuclear resonance fluorescence is considered as a technology to assay isotopic content of spent nuclear

fuel.

1.2   Nuclear Forensics

Nuclear forensics is an endeavor devoted to identifying the origin of nuclear materials by measuring the composition and structure of a material, which may help to indicate its source. Typical forensics analyses usually involve sample separation through physical structure studies, wet chemical processes, and a combination of mass spectrometry and γ-ray counting to identify isotopic compositions. Such methods normally represent the most effective way to perform nuclear forensics measurements. However, for certain types of samples, these methods have shortcomings.

Forensics analyses require that the analytical chemical processes be conducted on a representative sample or its entirety and thus the sample must be opened, processed, and in the sense of changing its form, destroyed. If a significant fraction of the initial radioactive material has undergone decay, chemical fractionation may also have occurred due to stoichiometric changes resulting from radioactive decay. Likewise, highly radioactive sources may produce sufficient heat to accelerate chemical diffusion that can cause spatial segregation of elements and thus make it difficult to select a "representative" sample of the whole.

For relatively weak sources, dissolution and analysis is fairly straightforward. However, sampling or sources of more than 10^2 Ci in such a manner is a daunting task. Examples that consider the use of NRF to perform non-destructive forensics assays for very large radiological sources are considered in Section 3.1.3.

1.3   Potential of Nuclear Resonance Fluorescence

While a detailed description of the physics of nuclear resonance fluorescence is provided in Section 2.11, it is worthwhile here to provide a qualitative description of the main features of NRF that make its measurement very attractive as a non-destructive assay signature. NRF is the process by which a nucleus is excited by the absorption of a specific quantum of energy, followed by de-excitation of the excited nucleus via the emission of one or more γ-rays. The energies of the excited state, as well as the emitted γ-rays, are specific to a given nucleus. By measuring the resonant absorption and/or the emitted γ-rays, the quantity of an isotope undergoing NRF may be ascertained. Correlating the rates at which NRF processes are measured to the quantity of the isotope within a target is the subject of Chapter 3. Unfortunately, the isotope-specific signatures of NRF can be difficult to measure because the intensities of these signals are often small compared to background signals induced either by interactions of the interrogating photon beam or by radioactivity in the assay geometry. Photon scattering processes that can result in significant background limitations is the primary subject of Chapter 2.

The potential of using nuclear resonance fluorescence to non-destructively measure the isotopic composition of a target has been previously applied to measurements of ^{13}C content in synthetic diamonds as part of studies on the mechanism of diamond formation(10). With the exception of H (whose isotopes have no nuclear structure), all measured isotopes have demonstrated a NRF signature(67). In recent years, the NRF responses of ^{235}U and ^{239}Pu were measured for the purpose of using NRF signatures to identify nuclear weapons material in cargo(123). These measurements also enable studies of the use of nuclear resonance fluorescence signatures to measure ^{235}U and ^{239}Pu in other applications.

1.4   Dissertation Outline

This dissertation discusses the measurement NRF signatures by inducing resonance excitation in an assay target. It subsequently relates the strengths of these signatures to the quantity of the resonant material within the assay target. The intensity of these NRF signatures is generally very small compared to the intensities of photons that leave the assay target due to all other processes. Through consideration of the cross sections for NRF and other processes that induce photon emission from an assay target, the relative intensity of NRF signals and background signals are compared. This comparison of signal and background intensities is then used to relate the uncertainty in counting of NRF γ-rays to the statistical uncertainty of the measured concentration of the resonating isotope.

Chapter 2 begins by describing the processes that contribute to the photon background. These processes include elastic and inelastic photon scattering, as well as more complicated processes such as those that yield bremsstrahlung emitted from photo-electrons. Because of the complexities of these processes the Monte Carlo radiation transport code, MCNPX was used to simulate processes that contribute to the background.[2] Photon scattering physics dictate that for 1.5 to 4 MeV incident-energy photons, the scattered photons will be mostly forwards-directed and, at large relative angles, will be reduced in intensity and energy. This trend indicates that the detection of 1.5 to 4 MeV NRF γ-rays may be achieved by measuring the photon spectrum from a target at back angles with respect to the direction on the interro-

---

[2]Surprisingly, it was found in this work that MCNPX had been inadvertently coded to neglect a significant portion of the elastic photon scattering process. Repair of this problem is described in Appendix A, and all MCNPX calculations described herein either use this modified version of MCNPX, or explicitly do not include elastic scattering in the calculation, the latter being implemented when the contribution to the scattered spectrum is desired to be known more accurately. In this case, the spectrum due to elastic scattering cross sections is calculated from angle-differentiated elastic scattering cross sections that include contributions due to photo-nuclear and S-Matrix atomic Rayleigh scattering amplitudes. This spectrum is subsequently added to the MCNPX results that exclude elastic photon scattering. See Reference(45) for a description of the changes to MCNPX that will be implemented in the next release of the code and Section 2.10 for a description of formulating elastic scattering cross sections.

gating photon beam.

After descriptions of non-resonant photon scattering, the physics of nuclear resonance fluorescence, descriptions of models describing NRF states, angular dependences of emitted NRF γ-rays, and the effect of the medium on the energy of the emitted γ-rays are presented. Chapter 2 concludes with a brief discussion of radiation detector responses, focusing on energy resolution and how relative rates of signal and background events relate to the statistical uncertainty in the measured signal. This relationship proves to be important because it is infrequent that NRF signal detection can be considered separately from the background.

Chapter 3 describes model approaches to predicting the effectiveness of NRF assay measurements. These predictions are made by comparing expected rates at which high-purity germanium detectors would measure NRF γ-rays and background photons. For most predictions, it is assumed that bremsstrahlung-spectrum photons are used to induce NRF. However, estimates are also made for a hypothetical quasi-monoenergetic photon source. Two assay methods are outlined and are followed by more detailed descriptions of models examining how each method would perform in an assay measurement of nuclear material.

The first assay method considered is one where NRF γ-rays are observed by measuring the intensity of photons leaving the assay target at large angles, relative to the incident interrogating radiation. Assaying spent fuel for nuclear safeguards purposes and radiological sources for nuclear forensics purposes are specifically considered in Section 3.1. Section 3.2 presents model predictions for a more complicated assay method in which the transmitted photon spectrum is measured, and the relative reduction in resonant-energy photon intensities indicates the concentration of an isotope in the assay target. Chapter 4 describes a series of measurements designed to test the model predictions of the transmission assay method.

Appendices A and B are also included to document modifications to the Monte Carlo radiation transport code, MCNPX, and the nuclear data files used by the code to enable it to more-accurately simulate physical processes relevant to nuclear resonance fluorescence. Appendix C documents MCNPX simulations conducted in support of this work.

Chapter 2

Photon Scattering Physics

The physics that defines photon scattering is central to applying nuclear resonance fluorescence for materials assay. The physics processes can be divided as either photon scattering due to interactions with atomic electrons or with nuclear material. In this chapter, this physics is discussed in the context of non-destructive assay measurements using NRF. The chapter begins by describing photo-atomic scattering and pair production before discussing Monte Carlo simulation results to describe more complex photon scattering processes. Thereafter, photonuclear scattering processes and NRF are discussed.

Although a detailed description of the physics and phenomena of NRF is included later in the chapter, it is instructive to give an overview of NRF to provide context for the discussions of other scattering processes.

Nuclear resonance fluorescence is the process by which a nucleus absorbs energy in the form of electromagnetic radiation, is excited to a nuclear state, and then subsequently de-excites to the ground state by the emission of one or more γ-rays. As will be discussed later, the angular distribution of re-emitted photons is governed by the angular momenta of the states involved in the process, however, to zeroth-order, the emitted photons can be considered isotropic, and of energy equal to the NRF-inducing photon.

The energies of the photon that induced the initial excitation, and the energy of the re-emitted photon(s) are characteristic of the specific state that underwent NRF and therefore, are also characteristic of the isotope. Photons produced during de-excitation of a NRF state are referred to herein as NRF γ-rays. Because the NRF states are simply excited nuclear states, the energies possible for NRF γ-rays range from 10's of keV up to many MeV. However, for the purpose of using NRF to assay materials, photons of energy between 1.5 and 4 MeV are most useful.

Both the elastic and inelastic scattering of photons may provide background for the detection of characteristic NRF γ-rays. However, physical properties of these scattering mechanisms cause the background intensity for the detection of NRF γ-rays to be a function of both the interrogating beam's energy spectrum and the geometry of the detection setup. In this chapter, it will be demonstrated that mea-

surement of NRF γ-rays at backwards angles – relative to the interrogating beam direction – yields backgrounds that are significantly reduced relative to a comparable setup with measurement of forward-directed photons.

2.1 Thomson Scattering

2.1.1 Polarized Incident Beam

Thomson scattering is the classically-predicted way in which a charged particle interacts with an electromagnetic plane wave. Thompson scattering can also be predicted quantum mechanically and forms the basis for Rayleigh and incoherent scattering, as well as nuclear Thomson scattering. Thomson scattering of a photon incident upon an electron defines the unit r_e, the classical electron radius, which is often seen in photo-atomic scattering formulas.

An ensemble of photons traveling through space can be described by a plane wave whose electric field is:

$$\mathbf{E} = \hat{\epsilon} E_0 e^{i(\mathbf{k} \cdot \mathbf{r} - \omega t)} \tag{2.1}$$

Where E_0 is the amplitude of the incident plane wave, $\hat{\epsilon}$ is the polarization of the plane wave, $\mathbf{k}$ is the wave vector (which is normal to $\hat{\epsilon}$), and ω is the angular frequency of the plane wave.

The Poynting vector defines the power per unit area carried by an electromagnetic wave.

$$\mathbf{S} = \epsilon_0 c^2 (\mathbf{E} \times \mathbf{B}) \tag{2.2}$$

where ϵ_0 is the permeability of free space, c is the speed of light, and $\mathbf{B}$ is the magnetic field vector. Because for a plane wave the magnetic field is normal to the electric field (and also normal to $\hat{\epsilon}$) and $|\mathbf{B}| = |\mathbf{E}|/c$, we can express the time-averaged Poynting vector as

$$< \mathbf{S} > = \epsilon_0 c < |\mathbf{E}|^2 > \tag{2.3}$$

$$= \epsilon_0 c \frac{E_0^2}{2}$$

A free electron subjected to the oscillating electromagnetic field will likewise oscillate. The equation of motion for this oscillation is given by

$$\mathbf{F} = q\mathbf{E} = m \frac{d^2 x}{dt^2} \hat{\epsilon} \tag{2.4}$$

where q and m are the charge and mass of the stationary charged particle, respectively, and x is the distance from the equilibrium position of the particle. An oscillating electric charge produces an oscillating electromagnetic field, which emits

power in a distribution that is approximated as a dipole distribution. This approximation is valid when the position at which $\mathbf{F}$ and $mathbf{E}$ are evaluated, r, is large and the magnitude of the oscillations is smaller than the wavelength of the radiation.

$$\frac{dP}{d\mathbf{\Omega}} = \left(\frac{q^2}{4\pi\epsilon_0 mc^2}\right)^2 \frac{\epsilon_0 c E_0^2}{2} sin^2\phi. \tag{2.5}$$

Here, ϕ is the angle of emitted radiation relative to the polarization vector and also defines the direction of oscillation of the charged particle.

The differential scattering cross section is given by

$$\frac{d\sigma}{d\mathbf{\Omega}} = \frac{dP/d\mathbf{\Omega}}{<\mathbf{S}>} \tag{2.6}$$

which by substitution, yields

$$\frac{d\sigma_{Th}}{d\mathbf{\Omega}}_{polarized}(\phi) = \frac{q^4}{16\pi^2\epsilon_0^2 m^2 c^4}\sin^2\phi \tag{2.7}$$

2.1.2   Unpolarized Incident Radiation

To this point only polarized incident radiation has been considered. To extend the derivation to unpolarized incident radiation, we must average the result from equation 2.7 over all polarizations. We define an orthogonal coordinate system, shown in Figure 2.1, spanned by $\hat{\epsilon}$, $\hat{\mathbf{k}}$, and $\hat{\epsilon}'$. (Note, $\hat{\epsilon}$ has been previously defined, $\hat{\mathbf{k}} = \mathbf{k}/|\mathbf{k}|$ and $\hat{\epsilon}' = \hat{\epsilon}\times\hat{\mathbf{k}}$.) An arbitrary polarization vector, $\hat{\mathbf{n}}$, is located in this space, and can be described in terms of the orthonormal basis vectors as

$$\hat{\mathbf{n}} = \sin\theta\sin\psi\,\hat{\epsilon} + \sin\theta\cos\psi\,\hat{\epsilon}' + \cos\theta\,\hat{\mathbf{k}} \tag{2.8}$$

We now must determine the quantity $\sin^2\phi$ averaged over all polarizations. This is equivalent to averaging over all values of ψ, since $\hat{\epsilon}$ must always be normal to $\hat{\mathbf{k}}$. This is done by noting

$$\hat{\epsilon}\cdot\hat{\mathbf{n}} = \cos\phi = \sin\theta\sin\psi \tag{2.9}$$

and using $\sin^2\phi + \cos^2\phi = 1$, to obtain

$$\sin^2\phi = 1 - \sin^2\theta\sin^2\psi \tag{2.10}$$

Averaging equation 2.10 over all possible values of ψ yields

$$\overline{\sin^2\theta} = 1 - \sin^2\theta\,\overline{\sin^2\psi} = 1 - \frac{\sin^2\theta}{2} = \frac{1+\cos^2\theta}{2} \tag{2.11}$$

Replacing $\sin^2\theta$ in equation 2.7 with $\overline{\sin^2\theta}$, we have the classical Thomson differential scattering cross section for unpolarized radiation.

$$\frac{d\sigma_{Th}}{d\mathbf{\Omega}}(\theta) = \frac{q^4}{16\pi^2\epsilon_0^2 m^2 c^4}\left(\frac{1+\cos^2\theta}{2}\right) \tag{2.12}$$
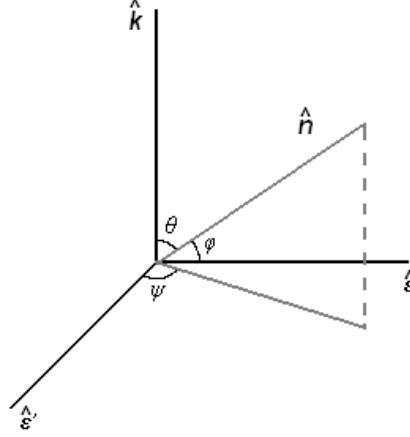
Figure 2.1 Geometric orientation of axes and vectors for calculation of differential Thomson scattering cross section for unpolarized radiation.

If the charged particle is an electron of mass $m = m_e$ and charge $q = q_e$, this is further simplified by the relation

$$r_e = q_e^2/4\pi\epsilon_0 m_e c^2 \tag{2.13}$$

to yield

$$\sigma_{Th}(\theta) = \frac{d\sigma_{Th}}{d\mathbf{\Omega}}\bigg|_{e^-}(\theta) = \frac{r_e^2}{2}(1 + \cos^2\theta) \tag{2.14}$$

The differential Thomson scattering cross section is independent of the energy of the incident radiation, and contributes significant intensity to all directions. We will later note that these observations hold true for Thomson scattering of photons incident upon nuclei, but that the influence of the binding of atomic electrons significantly alters these findings for Rayleigh scattering.

2.2   Compton Scattering

Compton scattering involves the inelastic scatter of a photon due to interaction with an electron. The kinematics of the collision can be derived using conservation of kinetic energy and momentum. The differential cross section for Compton scattering was derived by Klein and Nishina(11) in 1929 using second-order perturbation theory in quantum electrodynamics.

2.2.1   Compton Scattering Kinematics

The derivation of the kinematics of Compton scattering requires that the photon's momentum must be explicitly considered. This implies that the derivation

must be done with considerations of special relativity.

We start by stating kinetic energy and momentum conservation, for a photon of initial energy and momentum E and $\mathbf{p}$, that interacts with an electron at rest, giving the electron energy, E_e, and momentum, $\mathbf{p_e}$, and leaving with energy and momentum E' and $\mathbf{p}'$.

$$E = E' + T_e \tag{2.15}$$

$$\mathbf{p} = \mathbf{p}' + \mathbf{p}_e \tag{2.16}$$

The total electron energyl, E_e is related to momentum and its rest-mass by,

$$E_e^2 = p_e^2 c^2 + m_e^2 c^4 \tag{2.17}$$

By substituting $T_e = E_e - m_e c^2$ (where E_e is the total energy of the e⁻) into equation 2.15 and squaring, we find

$$E_e^2 = (E - E')^2 + m_e^2 c^4 + 2 m_e c^2 (E - E') \tag{2.18}$$

Squaring the vector difference, $\mathbf{p}_e = \mathbf{p} - \mathbf{p}'$, we obtain

$$p_e^2 = p^2 + p'^2 - 2 p p' \cos \theta \tag{2.19}$$

where θ is the angle between the incident and scattered photons, and p indicates the magnitude of the momentum vector, $\mathbf{p}$.

We multiply equation 2.19 by c^2, and note that for photons, $E = pc$, to yield

$$p_e^2 c^2 = E^2 + E'^2 - 2 E E' \cos \theta \tag{2.20}$$

Using equation 2.17, and rearranging, we have

$$E_e^2 = E^2 + E'^2 - 2 E E' \cos \theta + m_e^2 c^4 \tag{2.21}$$

We can equate this to equation 2.18 and cancel like terms to find

$$-2 E E' + 2 m_e c^2 (E - E') = 2 E E' \cos \theta \tag{2.22}$$

Collecting all E' terms, we find

$$E' = \frac{2 m_e c^2 E}{2 m_e c^2 + 2 E (1 - \cos \theta)} \tag{2.23}$$

which is further simplified to

$$E' = \frac{E}{1 + \alpha (1 - \cos \theta)} \tag{2.24}$$

by use of the common definition, $\alpha = E_0/m_e c^2$. α is often referred to as the *reduced photon energy*. Re-expressing equation 2.24 for the kinetic energy of the electron, we have

$$T_e = E - E' = E\frac{\alpha(1 - \cos\theta)}{1 + \alpha(1 - \cos\theta)} \tag{2.25}$$

By conserving the parallel and perpendicular components of momentum, one can also derive an expression for the angle at which the electron is ejected, ϕ.

$$\cot\phi = (1 + \alpha)\tan\frac{\theta}{2} \tag{2.26}$$

The relations derived above assume that the electron is free. The real description of the kinematics of inelastic scattering of a photon due to interaction with an atomic electron would necessarily include the binding energy of the electron. However, given that we are most interested in MeV-energy photons, the binding of outer-shell electrons to atoms is typically several eV, and even the K-shell electrons of uranium have a binding energy of only 116 keV(12), we conclude that the real kinematics experienced by MeV photons when undergoing inelastic scattering due to atomic electrons can be considered very similar to those described by equations 2.24 through 2.26.

The energy of emitted photons is plotted as a function of angle and various reduced energies as the black curves in Figure 2.2. For a photon of $\alpha = 10$, or $E = 5.1$ MeV, the energy of a scattered photon drops below 1 MeV at an angle $\phi \geq 53.9$ degrees. Even for Compton-scattering of a 50-MeV photon, the energy of the scattered photon drops below 1 MeV at 60 degrees. This indicates that Compton scattering cannot produce high-energy photons in large angles relative to the initial photon trajectory.

The gray curves in Figure 2.2 correspond to energies of electrons emitted during the Compton scattering of a photon of initial reduced energy α scattered into the angle θ. These curves indicate that while Compton scattering cannot produce high-energy secondary photons in large scattering angles, the energies of Compton electrons can remain quite high. However, equation 2.26 indicates that the Compton electron is always emitted in relatively forward directions and that the emission is symmetric about $\phi = 0$. Figure 2.3 presents the same Compton electron energies as those shown in Figure 2.2, but as a function of the Compton electron angle, ϕ. From this we can see that energetic Compton electrons are only emitted in small angles relative to the direction of the incident photon.

2.2.2 Klein-Nishina Formula

The derivation of the Compton differential scattering cross section is based on a second-order perturbation of the relativistic Dirac equation. This formulation is capable of reproducing the Thomson scattering cross sections, however there is no classical analogue for the Klein-Nishina formula (KN).
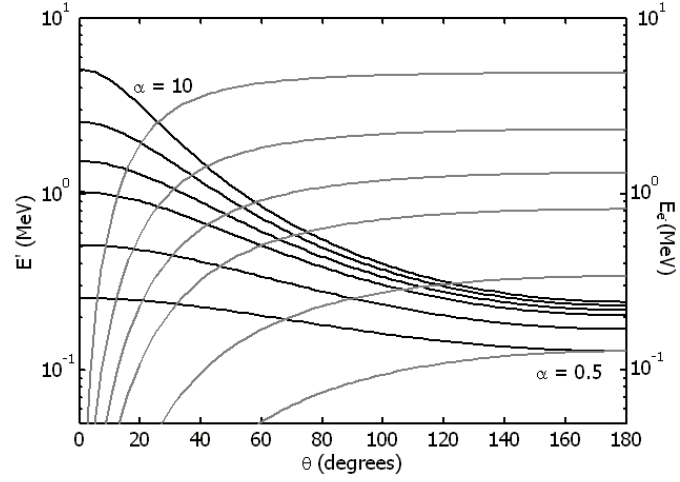
Figure 2.2 Energies of Compton-scattered photons (black) and Compton electrons (gray) as a function of photon scattering angle, θ for various initial reduced photon energies, $\alpha = 0.5, 1, 2, 3, 5,$ and 10.
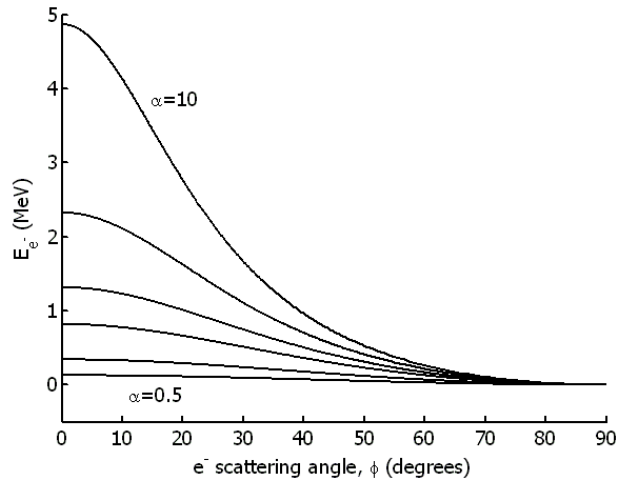
Figure 2.3 Energies of Compton electrons as a function of angle relative to the incident photon trajectory for various incident reduced photon energies, $\alpha = 0.5, 1, 2, 3, 5,$ and 10.

In perturbation theory, differential scattering cross sections for photon interactions can be calculated as

$$\frac{d\sigma}{d\Omega} = \frac{V^2}{(2\pi)^3 ct} \int_0^\infty k'^2 |\mathcal{M}_{fi}|^2 dk' \tag{2.27}$$

where V is an arbitrary volume over which the calculation is normalized, k' is the wave vector of the scattered photon, the integral over all k' corresponds to the density of final states, and $\mathcal{M}_{fi}$ is the interaction matrix element linking the initial and final states.

For Compton scattering, the matrix element, or transition amplitude is obtained by evaluation the second-order perturbation expansion of the electromagnetic field operator linking the initial and final states[1]

$$\mathcal{M}_{fi} = \sum_n \frac{<\mathtt{f}|\mathcal{H}_1|\mathtt{n}><\mathtt{n}|\mathcal{H}_1|\mathtt{i}>}{E_\mathtt{n} - E_\mathtt{i}} \tag{2.28}$$

Derivation involves assuming that a virtual positron is created and propagates between two interaction points. The Compton interaction may be defined in two topologies, one where the virtual positron propagates between the point in space-time where the initial electron and photon interact and the point where the scattered photon and Compton electron are produced. The alternative topology assumes that the incident electron and scattered photon are located at one point and connected by the virtual positron to the point in space-time where the incident photon and Compton electron converge.

By analyzing the matrix elements described by these two topologies, averaging over all polarization in a fashion similar to that described in Section 2.1.2, and taking the phase-space of the products into account, one may arrive at the KN

---

[1] The Hamiltonian of matter with charge, q, and magnetic moment, μ, in an electromagnetic field containing photons is often written as $\mathcal{H} = \sum_\lambda \hbar\omega_k a_\lambda^+ a_\lambda + \frac{1}{2m}\left(\mathbf{p} - \frac{q}{c}\mathbf{A}\right)^2 + \boldsymbol{\mu} \cdot B$, where the vector potential is given by $\mathbf{A} = \sqrt{\frac{2\pi^2}{V}} \sum_\lambda \frac{1}{\sqrt{\omega_k}} \left[\epsilon_\lambda a_\lambda \exp(i\mathbf{k}\cdot\mathbf{r}) + \epsilon_\lambda^* a_\lambda^+ \exp(-i\mathbf{k}\cdot\mathbf{r})\right]$, and the magnetic field is given by $\mathbf{B} = \sqrt{\frac{2\pi^2}{V}} \sum_\lambda \frac{1}{\sqrt{\omega_k}} \left[i(\mathbf{k}\times\epsilon_\lambda)a_\lambda \exp(i\mathbf{k}\cdot\mathbf{r}) - i(\mathbf{k}\times\epsilon_\lambda^*)a_\lambda^+ \exp(-i\mathbf{k}\cdot\mathbf{r})\right]$. In these expressions, the sum over λ implies all possible polarizations, denoted by ϵ_λ, and all possible photon wave vectors, $\mathbf{k}$. a_λ and a_λ^+ are the photon annihilation and creation operators respectively, and V is an arbitrary volume over which the spatial wave functions that the Hamiltonian acts upon must be normalized. Re-writing $\mathcal{H}$ to apply perturbation theory; $\mathcal{H}_0 = \frac{\mathbf{p}^2}{2m} + \sum_\lambda \hbar\omega_k a_\lambda^+ a_\lambda$ is the un-perturbed Hamiltonian, which corresponds to a state containing an arbitrary number of photons and a particle, with kinetic energy, $\frac{p^2}{2m}$. To first-order, the perturbing Hamiltonian is $\mathcal{H}_1 = \frac{q}{mc}\mathbf{p}\cdot A + \boldsymbol{\mu}\cdot\mathbf{B}$. At second-order the Hamiltonian, $\mathcal{H}_2 = \frac{q^2}{2mc^2}\mathbf{A}^2$ must be considered as well as second-order perturbation element of $\mathcal{H}_1$.
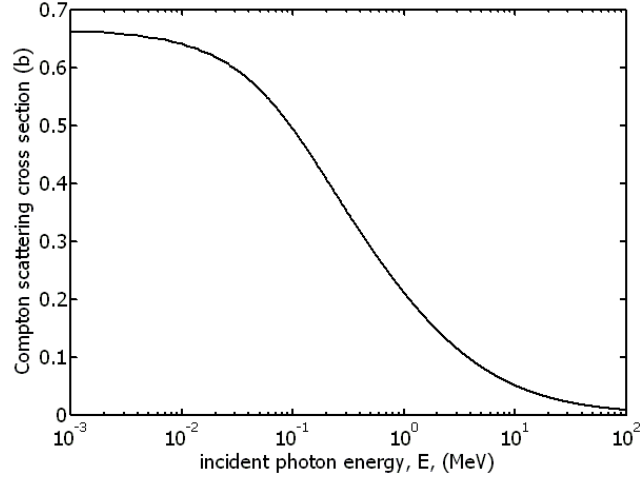
Figure 2.4 Compton scattering cross section vs. incident photon energy for photons incident upon a single free electron.

formula describing the angle-differentiated Compton scattering cross section.

$$\sigma_{KN}(\mathbf{\Omega}) = \frac{r_e^2}{2}[1+\alpha(1-\cos\theta)]^{-3}[-\alpha\cos^3\theta + (\alpha^2+\alpha+1)(1+\cos^2\theta) - \alpha(2\alpha+1)\cos\theta] \tag{2.29}$$

Integrating equation 2.29 over all angles yields the total Compton scattering cross section, which is a function only of the incident photon's energy.

$$\sigma_{Compton}(E) = 2\pi r_e^2 \left(\frac{1+\alpha}{\alpha^2} \left[\frac{2+2\alpha}{1+2\alpha} - \frac{1}{\alpha}\ln(1+2\alpha) \right] \right.$$
$$\left. + \frac{1}{2\alpha}\ln(1+2\alpha) - \frac{1+3\alpha}{(1+2\alpha)^2} \right) \tag{2.30}$$

This is plotted for a wide range of E in Figure 2.4. We will note in the following sections how the processes of Compton scattering differs when the scattering material is comprised of atoms containing bound electrons.

Equation 2.29 can be integrated over the azimuthal angle to yield a cross section proportional to the probability of scattering a photon into the angle $\theta + d\theta$.

$$\sigma_{KN}(\theta) = \int_0^{2\pi} \sigma_{KN}(\mathbf{\Omega})\sin\theta d\phi \tag{2.31}$$
$$= 2\pi\sin\theta\sigma_{KN}(\mathbf{\Omega}) \tag{2.32}$$

because $\sigma_{KN}(\mathbf{\Omega})$ is independent of ϕ. This angle-differentiated cross section is plotted versus θ for a range of incident photon energies, E, in Figure 2.5. Clearly, for $E \gtrsim 1$ MeV incident photons, Compton scattering predominantly produces scattered photons in forward directions.
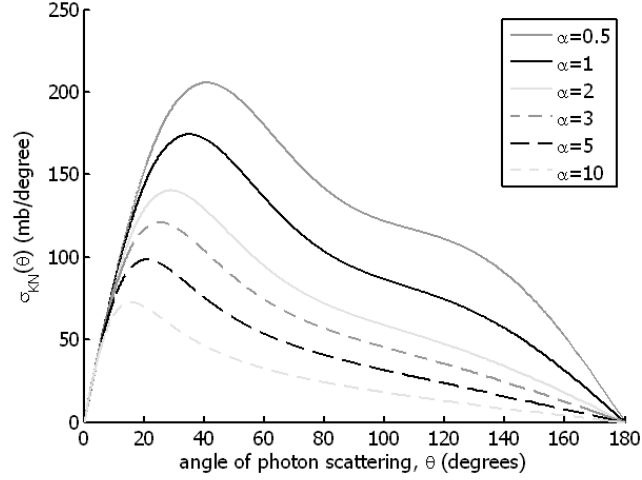
Figure 2.5 The KN differential scattering cross section for photon scattering of angle θ for incident photons of energy α=0.5, 1, 2, 3, 5, and 10.

To further examine the forward-directed nature of Compton scattering, we evaluate the fraction

$$\frac{\int_{\theta_{min}}^{\pi} \sigma_{KN}(\theta)}{\int_{0}^{\pi} \sigma_{KN}(\theta)} \qquad (2.33)$$

This expression is calculated for the case of backwards-scattering, i.e. $\theta_{min} = 90^o$, and plotted as a function of incident photon energy, E, in Figure 2.6. For $E \to 0$, this fraction is $1/2$, which corresponds to the fact that as $E \to 0$, Compton scattering approaches the symmetrical distribution predicted in the Thomson scattering limit. However, at $E = 1$ MeV, the fraction of Compton-scattered photons emitted into the backwards hemisphere is only 0.268, and drops to 0.165 at $E = 10$ MeV. Thus, while Compton scattering is predominantly forward-directed there is a non-negligible probability of scattering photons into the backwards direction. It should be remembered, however, that in Figure 2.2 indicates the energy of Compton backscattered photons is below 500 keV for incident photon energies of interest.

2.3 Rayleigh Scattering

Rayleigh scattering is the process where the electronic cloud of an atomic elastically scatters an incident photon. It is the dominant elastic photon scattering mechanism for the majority of incident photon energies considered here. Because of this dominance, the term *coherent scattering* – which refers to the coherent sum of all elastic scattering processes – is often used in place of Rayleigh scattering to describe this process. However, in the case of **backscattering** of 1.5 - 4 MeV photons, Rayleigh scattering is not particularly dominant, and the distinction between different scattering mechanisms must be made.
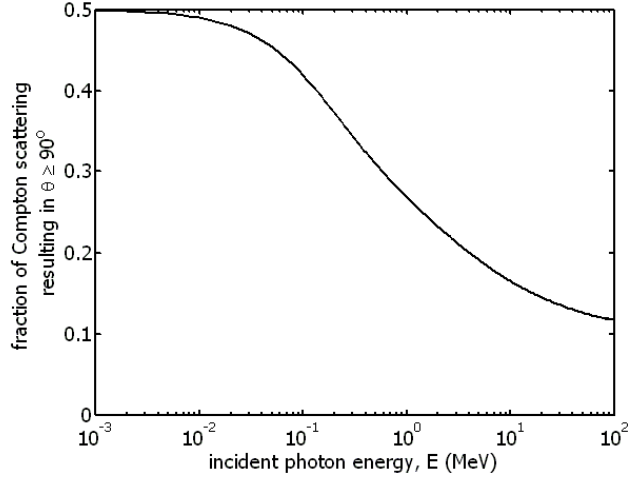
Figure 2.6 The fraction of Compton-scattered photons that scatter into the direction $\theta \geq 90^o$.

When expanding the concept of Thomson scattering from an isolated electron to an atomic electron, the primary effect is that the electron is no longer a point particle at rest. Instead, the electron is bound, and therefore is described by a distributed atomic orbital wave function. Because of this, we must now take a quantum electrodynamics approach to the interaction of the incident photon with the atom in its ground state. Symbolically, the initial state is written as, $|\Psi_0, k >$ and the final state, $|\Psi_0, k' >$, where k and k' are the wave vectors of the incident and scattered photon, respectively and Ψ_0 is the ground state wave function of the atom.

The operator connecting these two states is that of the electromagnetic field, described in Section 2.2.2, but equation 2.27 must also contain the wave functions of the atomic electron that causes the scatter. We will first discuss the simplest approach to describe cross sections for Rayleigh scattering in Section 2.3.1. This will be followed by a brief outline of a more thorough description of the scattering process, a comparison of results from the two approaches, and the effects of the approximation for background calculations for NRF measurements in Section 2.3.2

2.3.1   Form Factor Approximation

The form factor approximation is the simplest method to theoretically include considerations of the wave function of the atomic electron. The form factor results from modifying the matrix element (equation 2.28) to take electron-atom binding into account. This is done by assuming that electrons in the scattering atom can each be described by a single-particle wave function, $|\Psi_0 >$ and that the electron wave functions are estimated in a self-consistent manner. By assuming that the electromagnetic field of the incident photon may be considered as a small perturbation

to the atomic electron wave functions, one may obtain from equation 2.28 a factor by which free electron Thomson scattering cross sections are multiplied to obtain Rayleigh scattering cross sections:

$$F(q, Z) = \sum_{n=1}^{Z} <\Psi_0| \exp(i\mathbf{q} \cdot \mathbf{r}_n)|\Psi_0> \tag{2.34}$$

$F(q, Z)$ is known as the coherent scattering form factor. Here, $\mathbf{r}_n$ is the radial coordinate of the nth electron, relative to the nucleus, Z is the total number of electrons in the neutral atom, $\mathbf{q}$ is the vector momentum transferred to the electron during the interaction whose amplitude is given by

$$q = 2\hbar\mathbf{k}\sin(\theta/2) \tag{2.35}$$

and the term $\exp(i\mathbf{q}\cdot\mathbf{r}_n)$ represents the momentum transfer between the photon and electron. It should be noted that q is frequently tabulated in units of $\mathring{A}^{-1}$, which is the wave number corresponding to the electron's momentum. (Conversion between photon energy and momentum units is discussed in Appendix A.)

By making the first-order approximation that the momentum transfer action commutes with $|\Psi>$, [2] one can simplify equation 2.34 to

$$F(q, Z) = \int \rho(\mathbf{r}) \exp(i\mathbf{q} \cdot \mathbf{r}_n)d^3\mathbf{r} \tag{2.38}$$

where it is assumed that $<\Psi_0^*|\Psi_0>= \rho(\mathbf{r})$ and $\int \rho(\mathbf{r})d^3\mathbf{r} = Z$.

With the assumption that $\rho(\mathbf{r})$ is spherically symmetric, we can express equation 2.38 as

$$F(q, Z) = 4\pi \int_0^\infty \rho(r)\frac{\sin(qr)}{qr}r^2 dr \tag{2.39}$$

which is the expression evaluated using theoretically predicted electron density distributions to tabulate $F(q, Z)$.

The result of this formulation,

$$\sigma_{Ray}(\theta) = \sigma_{Th}(\theta)\left[F(q, Z)\right]^2 \tag{2.40}$$

---

[2]It can be seen that this is not strictly correct, since

$$\exp(i\mathbf{q} \cdot \mathbf{r}_n) = 1 + i\mathbf{q} \cdot \mathbf{r}_n + \frac{(i\mathbf{q} \cdot \mathbf{r}_n)^2}{2!} + \frac{(i\mathbf{q} \cdot \mathbf{r}_n)^3}{3!} + \cdots \tag{2.36}$$

and by representing $\mathbf{q} = \mathbf{p}/\hbar = -i\nabla$, generally

$$\int d^3\mathbf{r}\Psi^*\nabla \cdot (\mathbf{r}_n\Psi) \neq \int d^3\mathbf{r}\nabla \cdot (\mathbf{r}_n\Psi^*\Psi) \tag{2.37}$$

Therefore the linear approximation of $\exp(i\mathbf{q} \cdot \mathbf{r}_n)$ does commute with $|\Psi>$, and this remains true for further expansions.
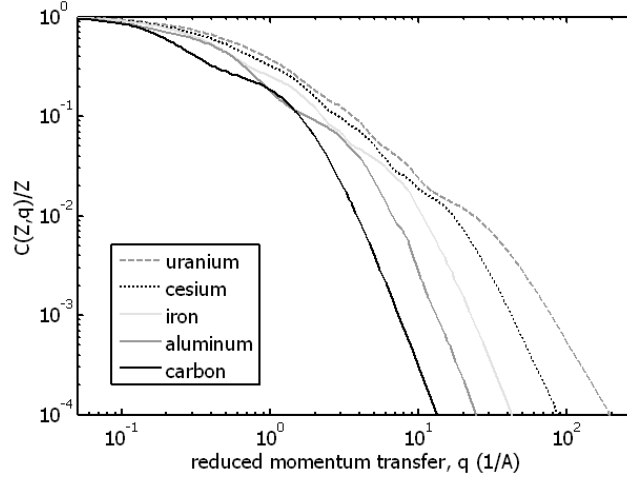
Figure 2.7 Coherent scattering form factors from EPDL97 for uranium, cesium, iron, aluminum and carbon, divided by respective atomic numbers.

is the form factor approximation of the angle-differentiated Rayleigh scattering cross section for an atom of atomic number Z.

As $q \to 0$, the term $\frac{\sin(qr)}{qr} \to 1$, therefore for very low momentum transfer interactions, $F(q, Z) = Z$. Conversely, as $q \to \infty$, the term $\frac{\sin(qr)}{qr} \to 0$, and $F(q, Z) \to 0$, and we expect $\sigma_{Ray} \to 0$ as well. This, however, is where the distinction between coherent and Rayleigh scattering becomes important, and where the approximation that resulted in equation 2.38 becomes problematic. Coherent scattering form factors taken from the evaluated photon data library EPDL97(19) are shown in Figure 2.7, where they are divided by Z and plotted versus q. The curves indicate that higher atomic numbers result in slower decreases of form factor values with increasing q. In the following section, we will see that angle-differentiated cross sections of Rayleigh scattering cannot simply be defined by the form factor approximation. In Section 2.10 it will be observed that at MeV-range energies, other elastic scattering processes render the form factor approximation completely invalid for description of coherent scattering.

2.3.2   S-Matrix Rayleigh Scattering Formulation and Comparison with the Form Factor Approximation

If, instead of neglecting the non-commutation of $|\Psi_0 >$ and $\exp(i\mathbf{k}r)$ in equation 2.34, the full relativistic quantum-electrodynamic calculation is performed starting with equation 2.28, the result is the so-called S-Matrix evaluation of the Rayleigh scattering cross section.

For the case of S-Matrix calculations of Rayleigh scattering, formulations of each electron's wave function, computed via self-consistent field method where each

electron is assumed to interact with the mean field, are explicitly used for the state, $|\Psi_0>$. Using these wave functions and the momentum transfer action, matrix elements are calculated numerically for the inner-shell electrons, and in a few test cases all atomic electrons. The inner shell S-Matrix calculations were combined with form factor approximations of outer shell electrons for all atoms, but only for a limited number of energies. The results are tabulated in the Rayleigh scattering database known as RTAB(15).

The S-Matrix calculations generally agree with experiment where photonuclear interactions are insignificant. Reference (16) demonstrates this agreement to within experimental uncertainties, for theoretical uncertainties (due to atomic structure calculations) of 2% for a wide variety of experiments with the following paramters: 59 keV $\leq E \leq 1332$ keV, for Al, Zn, Mo, Sn, Nd, Ta, Pb, and U, and $10^o \leq \theta \leq 150^o$.

Figure 2.8 presents the Rayleigh scattering differential cross sections for photons incident upon uranium, as retrieved form the S-Matrix tabulation of reference(17) as well as cross sections based on the form factor approximation, calculated using equation 2.40 and form factors tabulated in the evaluated nuclear data files ENDF/B-VII(18). The form factor data contained in the ENDF/B-VII files are from the evaluations of the evaluated photon data library EPDL97(19). These tabulations also include terms called anomalous scattering factors. These are theoretical corrections to the form factor approximation in which the impulsive nature of the momentum transfer between the photon and an atomic electron is defined by a relativistic dispersion relation rather than assuming a δ-function in the reaction coordinate. The comparison made here excludes anomalous scattering factors because derivations of the latter were obtained with the assumption of low-energy photons (< 100 keV), and the resulting angular dependence in the differential scattering cross sections become very inaccurate above these energies(20).

In Figure 2.8, we can see that the results from the two calculational methods agree up to approximately 30° for $E = 0.344$ MeV, 14° for $E = 1.173$ MeV, and 7° for $E = 2.754$ MeV. The disagreement between the two calculational methods increases with increasing angles. Since the majority of the total Rayleigh scattering cross section is due to small-angle scattering, this fact also indicates a degree of agreement in the total Rayleigh cross section between the methods. However, at higher energies, the angle at which deviation becomes significant becomes progressively smaller. Further, the relative disagreement between the two formulations becomes larger at higher energies. The S-Matrix value for the 2.754-MeV cross sections at $\theta = 135^o$ is 3.3 times that of the form factor result, whereas for 0.344-MeV photons the S-Matrix calculation gives a differential cross section that is 1.3 times that of the form factor result.

Another important quality of the S-Matrix approach to Rayleigh scattering is that the matrix elements in the transition amplitude expression, equation 2.28, are complex quantities. This is important because the coherent photon scattering cross
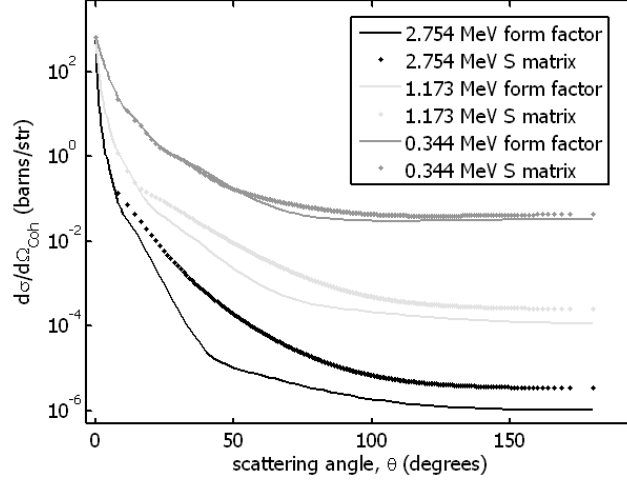
Figure 2.8 S-Matrix and form factor-calculated Rayleigh scattering differential cross sections for photons of $E = 2.754$, 1.173, and 0.344 MeV incident upon uranium.

section is defined as

$$\sigma_{Coh} = \left| \sum a_i \right|^2 \tag{2.41}$$

Therefore scattering amplitudes can destructively interfere. This will be discussed in further detail in Section 2.9.

Because of the differences between the form factor and S-Matrix cross sections, calculated intensities of scattered photons will depend upon the method used to predict them. The most commonly used Monte Carlo radiation transport codes, Geant4(21), Cog(22), MCNP5(25), and MCNPX(23) all use the form factor approximation with the EPDL97 as the data source. However, by explicitly excluding elastic scattering processes from simulations and subsequently adding the expected spectrum from elastic scattering, many results shown in Chapter 3 contain S-Matrix Rayleigh scattering cross sections.

2.4   Incoherent Scattering

Incoherent scattering is the process of Compton scattering by electrons bound to an atom. The theoretical treatment of incoherent scattering is very similar to that of Rayleigh scattering with the exception that the cross section is given by

$$\sigma_{Inc}(\theta) = \sigma_{KN}(\theta) \, S(q, Z) \tag{2.42}$$

where $S(q, Z)$ is called the incoherent scattering function.

The incoherent scattering function can be derived on a similar basis to that used to define the coherent scattering form factor, with the exception that the final atomic

state includes all excited atomic states, explicitly including all unbound states. With this, equation 2.34 for a single excited state becomes

$$F_\epsilon(q, Z) = \sum_{n=1}^{Z} <\Psi_\epsilon| \exp(i\mathbf{q} \cdot \mathbf{r}_n)|\Psi_0> \tag{2.43}$$

where $|\Psi_\epsilon>$ corresponds to an excited single electron state.

The incoherent scattering function is then related to equation 2.43 by

$$S(q, Z) = \sum_{\epsilon>0} |F_\epsilon(q, Z)|^2 \tag{2.44}$$

Using the completeness identity:

$$\sum_\epsilon |\Psi_\epsilon><\Psi_\epsilon| = 1 \tag{2.45}$$

we have,

$$S(q, Z) = \sum_{m=1}^{Z}\sum_{n=1}^{Z} <\Psi_0| \exp[i\mathbf{q} \cdot (\mathbf{r}_m - \mathbf{r}_n)]|\Psi_0> -|F(q, Z)|^2 \tag{2.46}$$

Which implies that the computation if uncoherent scattering functions only requires analytical descriptions of ground state wave functions(27).

The momentum transfer quantity, q in incoherent scattering functions is, like q for Rayleigh scattering, the momentum transferred to the electron during the scattering interaction. However, because the scattered photon loses energy, it is given by

$$q = \frac{\upsilon E}{\sqrt{2}}\sqrt{1 + \left(\frac{E'}{E}\right)^2 - 2\frac{E'}{E}\cos(\theta)} \tag{2.47}$$

where $\upsilon = \frac{1}{hc}$[3].

Figure 2.9 presents q as a function of scattering angle for inelastic scattering of photons with incident energies 0.5, 1, and 2 MeV. Figure 2.10 presents $S(q, Z)$ for aluminum ($Z = 13$) and uranium ($Z = 92$). The functions approach their maxima, Z, above $q \approx 3$ and 20 $\mathring{A}^{-1}$, respectively. In general, incoherent scattering functions will behave similarly to the two examples shown, with normalized scattering functions for intermediate Z falling between the two examples shown in Figure 2.10. Since the momentum transfer for inelastic scattering of photons above 0.5 MeV and $\theta \geq 90$, is always greater than 30 $\mathring{A}^{-1}$, the differential cross section for incoherent photon scattering, for the purpose of considering photon backscattering in the 1.5 - 4 MeV energy range can be taken as $Z \cdot \sigma_{KN}(\theta)$.

---

[3]When υ is expressed as $\upsilon = \frac{m_e c}{h} = 41.21655\,(\text{MeV}\mathring{A})^{-1}$, q is then in reduced wave vector form and in the units for which $S(q, Z)$ is most commonly tabulated(26).
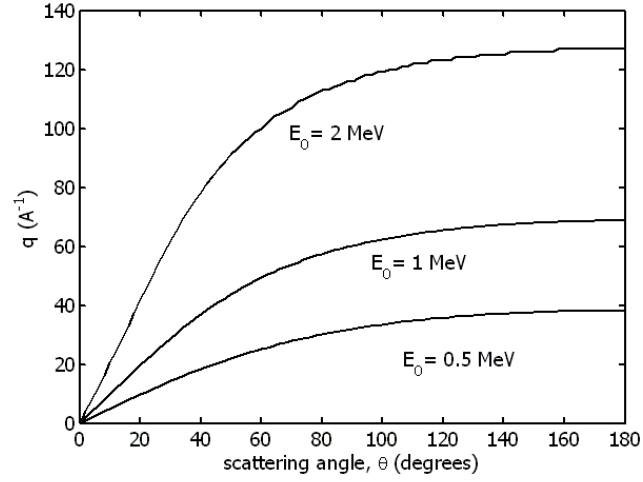
Figure 2.9 Momentum transfer, q, versus angle of scattering, θ, for various incident photon energies, E. Momentum transfer values are in units of reduced reduced wave vector ($\mathring{A}^{-1}$).
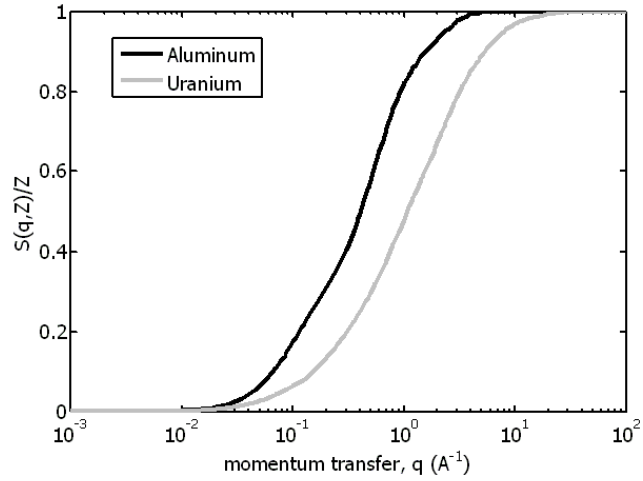
Figure 2.10 Incoherent scattering functions $S(q, Z)$ normalized to their maxima, Z, for uranium and aluminum. Note the logarithmic scale of the abscissa.
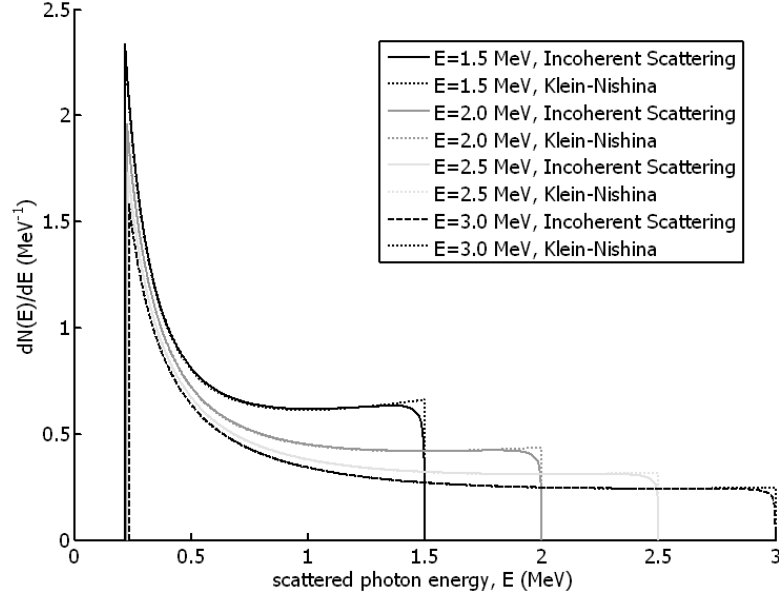
Figure 2.11 Spectrum of photons scattered that have been scattered by uranium based on the Klein-Nishina cross section (dotted) and using incoherent scattering function modifications (solid) for incident photon energies of 1.5, 2, 2.5, and 3 MeV.

Figure 2.11 displays scattered photon spectra as predicted by the Klein-Nishina differential scattering cross section, and spectra calculated using the incoherent scattering function of uranium is applied to the KN result. The Klein-Nishina spectra use the relation

$$N_{KN}(E') = \frac{d\theta}{dE'}\sigma_{KN}(\theta) \tag{2.48}$$

whereas the incoherent spectra use the relation

$$N_{Inc}(E') = \frac{d\theta}{dE'}\sigma_{Inc}(\theta) \tag{2.49}$$

For most scattered photon energies, E', the Klein-Nishina and incoherent scattering function spectra are nearly identical. However, for scattered photons that remain near the incident energy, E, the scattering functions significantly suppress such events. From equation 2.25, we know that this also corresponds to photons scattered into the smallest scattering angles, θ.

Figure 2.12 shows the ratio of the differential cross section predicted by KN to that of incoherent scattering as a function of angle, for photons incident upon uranium. The ratio approaches ∞ as $\theta \to 0$, but at $\theta = 2$ degrees, KN only over predicts the scattering of photons into that angle by a factor of $\lesssim 3$, and above $\theta = 10$ degrees, KN is quite accurate.

We conclude the discussion of incoherent scattering by presenting the angular distribution of the electrons emitted during the scattering process. The angular
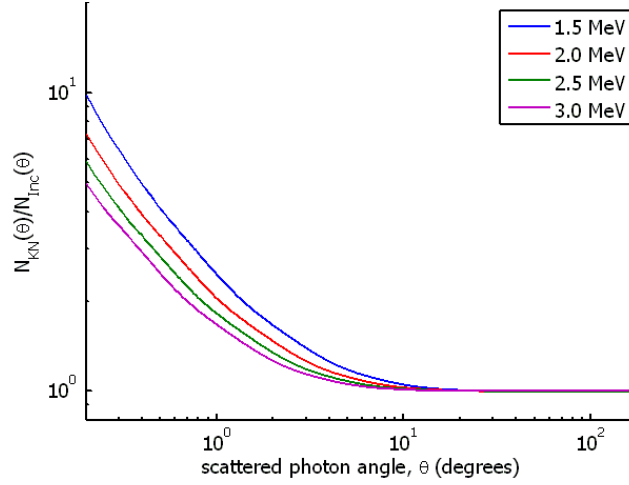
Figure 2.12 Factor by which the Klein-Nishina distribution over predicts scattered photon intensity versus scattering angle for photons of energy 1.5, 2, 2.5, and 3 MeV incident upon uranium.

distribution can be derived from the incoherent scattering cross section and the relationship between the emitted photon angle, θ and the electron angle, ϕ, given by equation 2.26.

$$N_{e^-}(\phi) = \left| \frac{d\theta}{d\phi} \right| N_{Inc}(\theta) = \frac{2 + 2(1-\alpha)^2 \tan^2 \theta/2}{(1+\alpha)(1+\tan^2 \theta/2)} N_{Inc}(\theta) \tag{2.50}$$

We divide by $2\pi \sin \phi$ to yield the differential cross section for electron emission. Both this quantity, and 92 times the corresponding Klein-Nishina cross section are plotted in Figure 2.13 for electrons emitted during incoherent and Compton scattering of photons in uranium. The electron is always emitted into the forward 2π, and becomes increasingly more forward-biased with increasing photon energy. The effects of the incoherent scattering function are relatively small, decrease with higher photon energy, and only manifest themselves to reduce the probability of electron emission at angles near $\phi = 90°$.

As discussed later, Compton electrons can become a photon source due to bremsstrahlung emission. Recalling Figure 2.3, we note that electron emission at small ϕ results in the highest electron energies. Thus forward-directed, high-energy electron emission is a significant part of the incoherent scattering process.

2.5   Photoelectric Absorption

Photoelectric absorption is the process by which a photon incident upon an atom is absorbed, resulting in the ejection of an atomic electron.
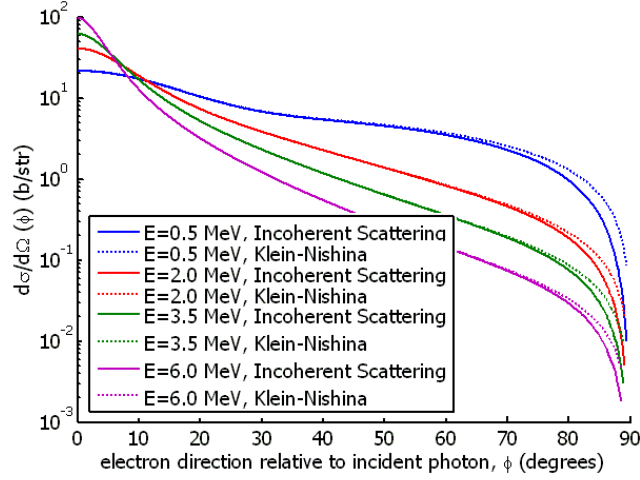
Figure 2.13 Angular distribution of electrons emitted during incoherent (solid) and Compton (dotted) scattering of photons off of uranium for incident photon energies of 1.5, 2, 2.5, and 3 MeV.

Energy conservation requires that the atomic electron receive an amount of kinetic energy equal to

$$E_e = E - \Phi \tag{2.51}$$

where Φ is known as the work function, equal to the binding energy of the ejected electron to the atom.

Perturbation theory predicts that the cross section for photoelectric absorption can be written as

$$\frac{d\sigma}{d\boldsymbol{\Omega}}_{PA} = \frac{V^2}{(2\pi)^3 ct} \int_0^\infty k_e^2 |\mathcal{M}_{fi}|^2 dk_e \tag{2.52}$$

which is completely analogous to equation 2.27, except that now the phase space is determined by integrating over all electron momenta. Photoelectric absorption is also a first-order process, so the equation analogous to equation 2.28 is

$$\mathcal{M}_{fi} = <\Psi^* \mathbf{k}_e | \mathcal{H}_1 | \Psi_0 > \tag{2.53}$$

Where $\mathcal{H}_1$ is again the first-order electromagnetic field operator (and only the term that annihilates a photon contributes), $\frac{e}{mc} \mathbf{p} \cdot \mathbf{A}$, $|\Psi_0 >$ is the ground state wave function of energy E_0, and $|\Psi^* \mathbf{k}_e >$ is the wave function of both the excited ion after emission of the electron and the now free electron with momentum $\mathbf{p}_e = \hbar \mathbf{k}_e$.

These wave functions are generally only calculated for the case where the incident photon energy, $E \gg E_0$. Also by considering photoelectric absorption by hydrogen or hydrogen-like atoms, the wave function of the ion can be neglected because there are no remaining atomic electrons. With these approximations, the differential cross section for photoelectric absorption by K-shell electrons, accompanied by electron emission into the angle, θ, relative to the incident photon is found
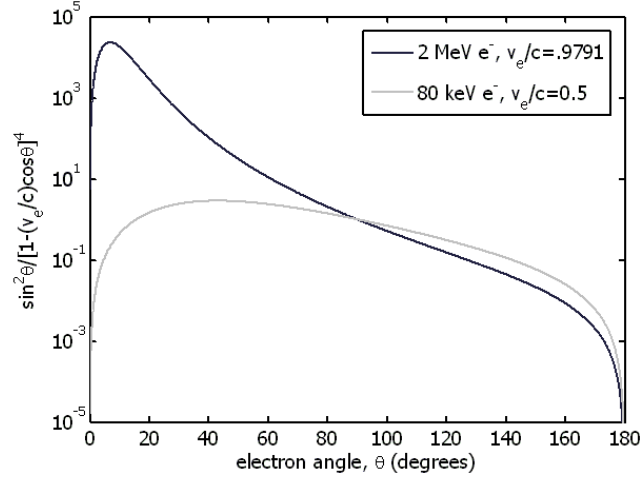
Figure 2.14 The angular portion of equation 2.54 plotted for photoelectrons emitted with kinetic energies of 80 keV and 2 MeV.

to be(28)

$$\frac{d\sigma}{d\Omega}_{PA} = \frac{16Z^5}{k(k_e a_0)^5}\frac{q_e^2}{mc^2}\frac{\sin^2\theta}{[1-(v_e/c)\cos(\theta)]^4} \tag{2.54}$$

The angular dependence of equation 2.54 is plotted in Figure 2.14 for emitted electron velocities, $v_e/c = 0.5$ and 0.9791, corresponding to electron energies of $E_e = 80$ keV, and 2 MeV, respectively. For relativistic photoelectrons, the tendency is to be emitted in a direction close to the initial photon trajectory, whereas non-relativistic photoelectrons approaching the limit $v_e/c \to 0$, tend toward a symmetric emission distribution peaked at $\theta = 90°$. However, at lower photoelectron energies, the assumption $E_e \gg E_0$ is no longer valid.

By integrating equation 2.54 over all solid angles, and assuming that $E = E_e$, one arrives at the total photoelectric absorption cross section for K-shell electrons.

$$\sigma_{PA}(E) \approx \frac{16\pi\sqrt{(2)}}{3}\alpha_f^8 Z^5 a_0^2\left(\frac{mc^2}{E}\right)^{7/2} \tag{2.55}$$

Where α_f is the fine structure constant, $\alpha_f = \frac{q_e^2}{4\pi\epsilon_0\hbar c} \approx 1/137$, and a_0 is the Bohr radius, $a_0 = \frac{4\pi\epsilon_0\hbar^2}{m_e q_e^2} = 0.53\mathring{A}$.

$\sigma_{PA}(E)$ are taken from the database XCOM(29) and plotted as a function of incident photon energy, E, for four different elements in Figure 2.15. The cross sections vary between 10^6 and 5×10^4 b at $E = 1$ keV, and between 2×10^{-3} b and 2×10^{-7} b, at $E = 10$ GeV for uranium, and aluminum, respectively. In the range of 1-4 MeV, photoelectric absorption cross sections for lower-Z materials such as iron and aluminum have already dropped below a tenth of a barn, whereas for uranium the cross section remains above one barn. This implies that photoelectric absorption
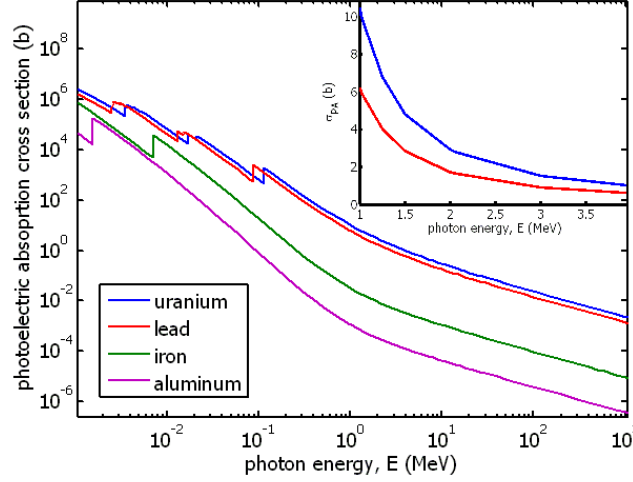
Figure 2.15 Photoelectric absorption cross sections as reported in XCOM,(29) versus incident photon energy, E for photons incident upon uranium, lead, iron, and aluminum. The inset shows the uranium and lead cross sections in energy range of 1 - 4 MeV on linear scales.

remains a significant photon interaction process, and that energetic photoelectrons (i.e. electrons ejected due to photoelectric absorption) are also created with non-negligible probability.

2.6   Bremsstrahlung from Photon Scattering

Although bremsstrahlung is not directly produced by photon scattering, it is often produced as secondary radiation by the electrons emitted during photoelectric absorption or incoherent scattering. The process of bremsstrahlung production has been theoretically examined,(30),(32),(33) yielding closed expressions for the differential bremsstrahlung cross section, but with approximations that either assume the electron is non-relativistic, or highly-relativistic. In the intermediate electron energy range (including 1.5 - 4 MeV), interpolation between the two limits has yielded the most widely accepted bremsstrahlung cross sections(32). These cross sections are included in Monte Carlo codes such as Penelope(31) and the MCNP codes(23),(25).

2.6.1   Bremsstrahlung Cross Sections

In the limit that the electron is considered to be non-relativistic, the Bethe-Heitler bremsstrahlung cross section, differentiated with respect to the bremsstrahlung photon energy and direction, k and $\mathbf{\Omega}_k$, respectively, and electron deflection,

$\mathbf{\Omega}_{p_2}$, is given by

$$\frac{d^3\sigma_B}{dkd\mathbf{\Omega}_kd\mathbf{\Omega}_{p_2}} = \frac{\alpha Z^2 r_e^2}{4\pi^2}\frac{p_2}{kp_1q^4}\left[(4\epsilon_2^2 - q^2)\frac{p_1^2\sin^2\theta_1}{(\epsilon_1 - p_1\cos\theta_1)^2} + (4\epsilon_1^2 - q^2)\frac{p_2^2\sin^2\theta_2}{(\epsilon_2 - p_2\cos\theta_2)^2}\right.$$
$$- (4\epsilon_1\epsilon_2 - q^2 + 2k^2)\frac{2p_1p_2\sin\theta_1\sin\theta_2\cos\phi}{(\epsilon_1 - p_1\cos\theta_1)(\epsilon_2 - p_2\cos\theta_2)}$$
$$\left. + 2k^2\frac{p_1^2\sin^2\theta_1 + p_2^2\sin^2\theta_2}{(\epsilon_1 - p_1\cos\theta_1)(\epsilon_2 - p_2\cos\theta_2)}\right] \quad (2.56)$$

where

$$q^2 = 2k[(\epsilon_1 - p_1\cos\theta_1) - (\epsilon_2 - p_2\cos\theta_2)]$$
$$+ 2[\epsilon_1\epsilon_2 - p_1p_2(\cos\theta_1\cos\theta_2 + \sin\theta_1\sin\theta_2\cos\phi) - 1] \quad (2.57)$$

ϵ_1 and p_1 are the energy and momentum of the electron before bremsstrahlung emission, and ϵ_2 and p_2 after emission. θ_1 and θ_2 are the angles between the emitted photon and the electron before and after emission, respectively, and ϕ defines the angle between the initial and final electron trajectories, θ_{12} through the following relation:

$$\cos\theta_{12} = \sin\theta_1\sin\theta_2\cos\phi + \cos\theta_1\cos\theta_2 \quad (2.58)$$

Also, Z is the atomic number of the stopping material, and can be set to unity for consideration of bremsstrahlung emitted during the slowing of a single electron due to the electric field of a single atomic electron. The cross sections for bremsstrahlung emission from the energetic electron's interaction with each atomic electron and each nucleus can be summed to give a total bremsstrahlung emission cross section, however screening and nuclear recoil corrections are also commonly implemented.

The form of equation 2.56 is valid for a pure $\frac{Z}{r}$ electromagnetic potential when $\epsilon_1 \ll m_ec^2$, which is not valid for most NRF problems. Equation 2.56 was derived using the first-order Born approximation. Bremsstrahlung cross sections extending up to 2 MeV electron energies were accomplished by Pratt and Tseng by numerically solving higher-order terms of the Born series(34).

2.6.2   Bremsstrahlung Spectrum from Monoenergetic Electrons

Figure 2.16 shows bremsstrahlung cross sections differentiated with respect to emitted photon energy, $\frac{d\sigma_B}{dk}(k)$ for electrons in uranium. The values shown are taken from the MCNP el03 library(38),(40), which follows the Seltzer and Berger method of interpolating between the Pratt and Tseng low-energy cross sections and the Sommerfeld cross sections at highly relativistic energies. Clearly, the cross section for bremsstrahlung emission is large compared to photon cross sections, however, the range of an electron is much shorter than that of a photon, and in the energy
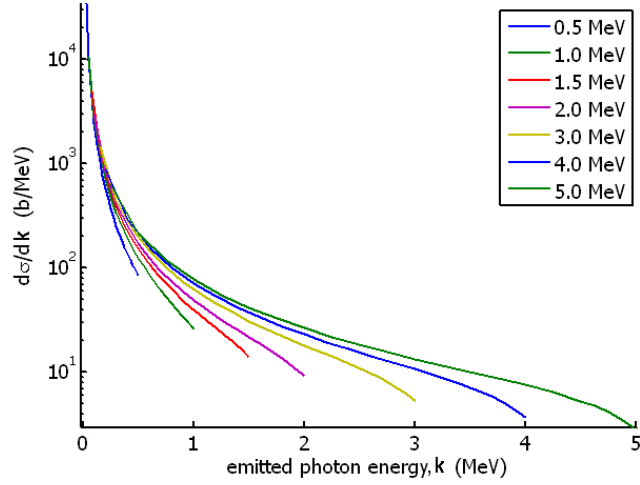
Figure 2.16 Differentiated bremsstrahlung emission cross section, $\frac{d\sigma_B}{dk}(k)$, for electrons of energies 0.5, 1.0, 1.5, 2.0, 3.0, 4.0, and 5.0 MeV in uranium. Values are taken from MCNP el03 datafile.

ranges of interest the cross section for emission of bremsstrahlung near the electron's energy is much lower than the cross section for photon emission to energies of $\lesssim 200$ keV.

To provide an example of bremsstrahlung emission from energetic electrons interacting in a very thin target, Figures 2.17 and 2.18 demonstrate the angular dependence of bremsstrahlung emitted from 2.5-MeV electrons. The values shown in the plots were obtained from simulations with MCNPX by impinging 2.5-MeV electrons normally upon a uranium foil of thickness 1 μm. For a single electron, the average number of bremsstrahlung photons emitted was estimated to be 2.6×10^{-3}. Figure 2.17 presents the spectra of the bremsstrahlung photons as a function of energy, for selected angular ranges. Estimated $\pm 1\sigma$ statistical errors from the Monte Carlo calculation are shown for each bin. They are generally small, with the exception of the highest emission angles, in which case the uncertainties reach 22% in the highest-energy bins. Seltzer and Berger also reported that uncertainties in their evaluation should be considered to be approximately 10%.

The shape of the histograms in Figure 2.17 is, as expected, quite similar to the cross section curves in Figure 2.16, with about a factor of 10^{-2} decrease in intensity between the $0.1 \leq k \leq 0.2$ MeV bin and the highest bin.

The results of the same calculation are also plotted as a function of the angle between the bremsstrahlung-inducing electron and the photon, θ_1, in Figure 2.18. This demonstrates that at all energies bremsstrahlung photons are predominantly forward-directed, but the angular distribution becomes progressively more strongly forward-directed as they approach the electron's energy.
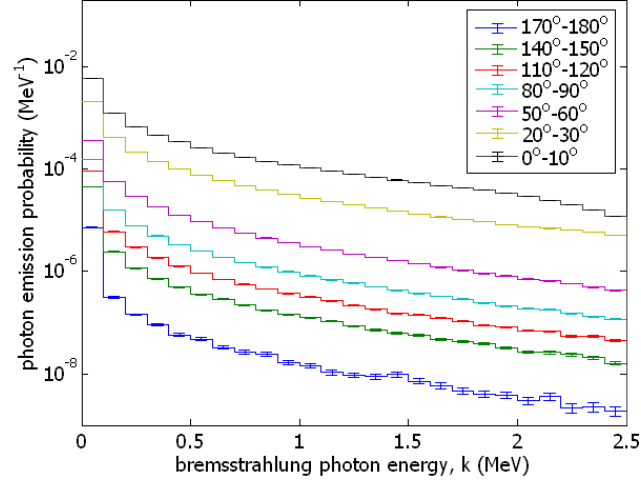
Figure 2.17 MCNPX-computed bremsstrahlung spectra from 2.5-MeV electrons incident upon 1 μm uranium for various angular ranges of bremsstrahlung photon production. $\pm 1\sigma$ errors are shown when they are wider than the width of the line. An average 0.0026 bremsstrahlung photons were computed to be emitted per electron.
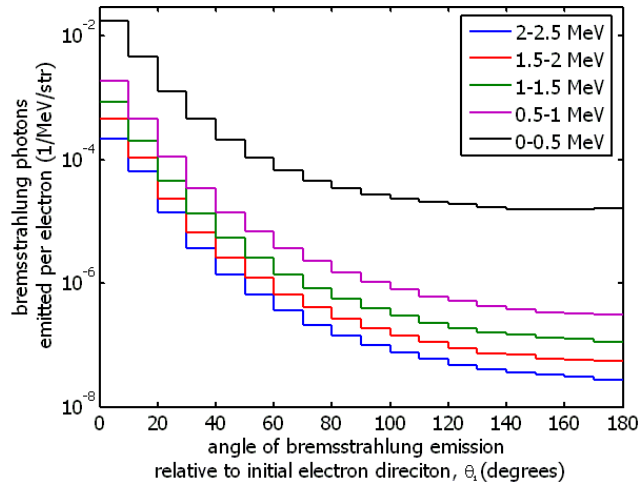
Figure 2.18 Angular dependence of the bremsstrahlung spectrum shown in Figure 2.17 for various photon energy ranges, k. The abscissa is the angle between the bremsstrahlung photon and the electron before emission, θ_1. Statistical errors from the Monte Carlo computation are negligible.
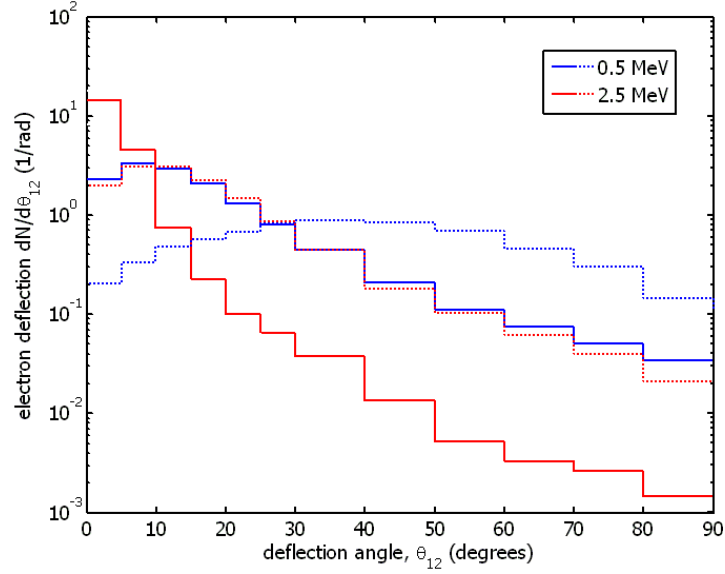
Figure 2.19 Angular deflection of 0.5 and 2.5 MeV-electrons after they traverse 1 μm (solid lines), or 10 μm (dotted lines) of uranium. Statistical errors from the Monte Carlo computation are negligible.

2.6.3   Bremsstrahlung Spectra from Thick Targets

The previous discussion involved only the first 1 μm of a 2.5-MeV electron's track. However, bremsstrahlung is emitted through an electron's entire trajectory, which is very non-linear due to of the high probability of electron scattering through large angles. This in turn, results in a much larger angular distribution of emitted bremsstrahlung from the initial trajectory vector. Figure 2.19 demonstrates the deflection of energetic electrons as they pass through both 1 μm (solid lines) and 10 μm (dotted lines) of uranium. After 1 μm, higher-energy electrons remain predominantly forward-directed, but after only 10 μm, 500-keV electrons have already experienced significant deflection.

To demonstrate bremsstrahlung spectra emitted from energetic electrons, spectra from MCNPX simulations, binned as a function of angle are presented in Figures 2.20 and 2.21. In Figure 2.20, the bremsstrahlung spectrum is for 4-MeV electrons incident upon a 0.75 cm-thick slab of tungsten. For Figure 2.21, the spectrum was simulated 2.5-MeV electrons incident upon a uranium cube with sides of length 10 μm. Both spectra indicate that even with thicker targets, bremsstrahlung is forward-directed. However, Figure 2.22 is a plot of the angular dependence of the 1.9 - 2 MeV energy bin shown in Figure 2.21. Comparing this with Figure 2.18, we can see that between the forward and 40 degree angular bins, the spectrum from 2.5-MeV electrons incident upon 10 μm of uranium shows a decrease in intensity by a factor of four compared to a factor of over 100 for the 1 μm uranium target. Thus in general, we can observe that thicker targets increase the intensity of bremsstrahlung
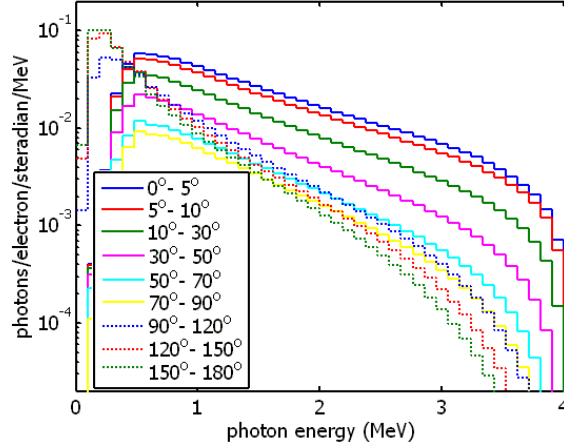
Figure 2.20 MCNPX-computed bremsstrahlung spectra from 4-MeV electrons incident upon 7.5 mm-thick tungsten for various angular ranges of bremsstrahlung photon production. An average of 0.373 bremsstrahlung photons were computed to be emitted per electron.

emission into larger angles, relative to the initial electron direction.

For thick targets and energetic electrons, a significant fraction of the electron energy is converted into photons, with photons being emitted in directions that are significantly different from the electron's initial trajectory. The average fraction of an electron's energy emitted as electromagnetic radiation during the complete stopping of an electron is called the *radiation yield*. Radiation yields are plotted for uranium, gold and iron as a function of electron energy in Figure 2.23. The radiation yield increases with energy and Z.

From the phenomena of electron stopping and bremsstrahlung emission, we conclude this section by observing that upon creation of energetic electrons in materials, radiation in the form of bremsstrahlung is often emitted. Further, although the process is less probable, the emission of energetic photons in directions significantly different from the initial trajectory of the electron can occur. This process can contribute significantly to the effective flux of scattered radiation in NRF-related measurements. When appropriately used, it has been documented that MCNP can simulate this to an accuracy of approximately 10%(41).

2.7   Pair Production and Positron Annihilation

At this point we have discussed all relevant photo-atomic scattering mechanisms, electron transport, and bremsstrahlung which includes photon production due to electron interaction with both atomic electrons and nuclei. The process of pair production produces an energetic electron and positron pair. These subsequently
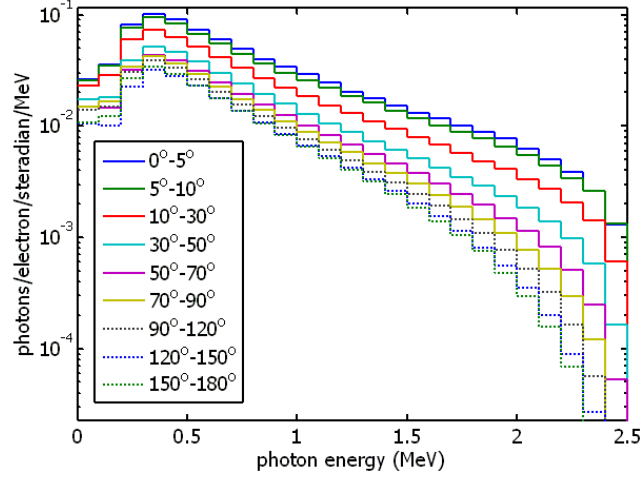
Figure 2.21 MCNPX-computed bremsstrahlung spectra from 2.5-MeV electrons incident upon a cube of uranium with 10 μm sides, for various angular ranges of bremsstrahlung photon production. A total of 0.112 bremsstrahlung photons were computed to be emitted per electron.
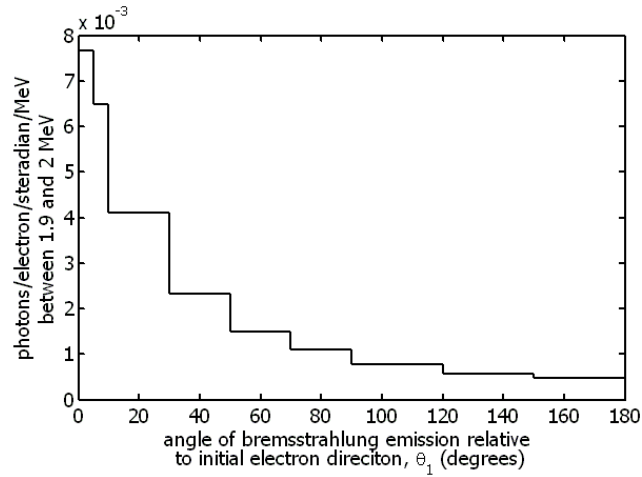
Figure 2.22 Angular dependence of the 1.9 - 2 MeV bin from the bremsstrahlung spectrum shown in Figure 2.21. The abscissa is the angle between the bremsstrahlung photon and the initial electron before direction.
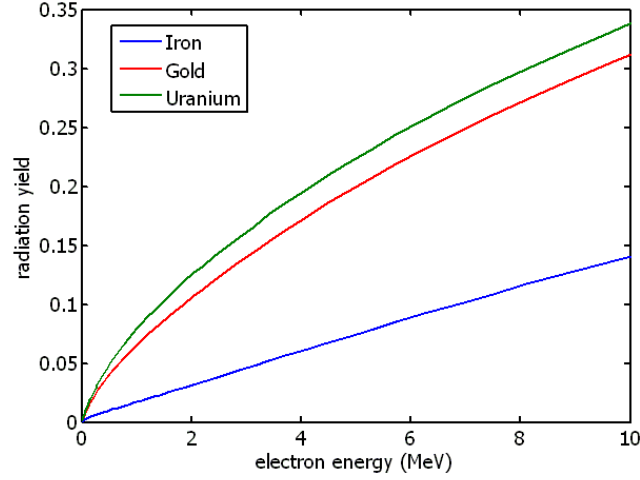
Figure 2.23 Radiation yield versus energy for electrons stopping in uranium, gold, and iron.

produce additional photons, effectively resulting scattered photons. Like bremsstrahlung, the process of pair production results from photon interaction with an electromagnetic field, and therefore can result from photon interactions of both the atomic and nuclear Coulomb fields. Likewise, the theoretical framework predicting the cross section for pair production follows a similar form as that for bremsstrahlung, except that it is the final state is represented as a series of Born waves in a Coulomb field(42).

Pair production is the process by which a photon interacts with an electromagnetic field and produces an electron-positron pair. The energetics of the process are defined by conservation of energy.

$$E_{e^-} + E_{e^+} = E_\gamma - 2m_e c^2 \tag{2.59}$$

The energetic electron and positron subsequently slow down and can emit bremsstrahlung as described in Section 2.6 (despite their charge, positrons slowing is nearly identical to that of electrons). As a positron slows, it becomes more likely to form a state known as *positronium*, an electron and positron orbiting each other, which quickly ($\sim 10^{-10}$s) annihilates resulting in the emission of two anti-parallel photons with total energy equal to the sum of the rest masses of the electron and positron (plus any kinetic energy possessed by the positronium). The axis of these γ-rays is isotropic and uncorrelated to the direction of the photon that underwent pair production. These γ-rays almost always have an energy $E_{An} \approx m_e c^2$, and are the highest intensity photons (per unit energy) created and measured in NRF experiments.

2.8   MCNPX Simulations of Photon Scattering

With the physical processes described, we now turn to a discussion of MCNPX computations of the combination of these processes and the effective scattered spectrum that results, acknowledging that most photonuclear processes are not included in the simulations. Documentation of a bug relating to Rayleigh scattering treatment in MCNP is presented in Appendix A as well as modifications to MCNPX and NJOY which fix the error. The bug is only important when coherently-scattered photons can be distinguished from incoherently-scattered and annihilation photons.

2.8.1   Scattering of Monoenergetic Photons as Simulated by MCNPX

The photon scattering physics described in the proceeding sections is implemented for photon transport in MCNP. In this section, scattered photon spectra, as calculated by MCNPX, are presented and their features are analyzed. In many regards this section is a continuation and elaboration on work previously done by Hagmann and Pruet(46), with additional accuracy due to the inclusion of Rayleigh scattering, which had previously been omitted due to legacy MCNP coding. Figures 2.24 and C.3 show spectra computed by MCNPX, where monoenergetic photons interact in various targets and are scattered into solid angles defined by an angle relative to the incident photon trajectory. The spectra have 5 general features;

- A peak in the highest energy bin, corresponding to elastic scattering. As discussed in Appendix A, the intensity of this peak is due primarily to Rayleigh scattering – as is described in EPDL97 – and is missing nuclear elastic scattering contributions. The integrated area of the elastic scattering peak is very small compared to the remainder of the photon spectrum, which illustrates the relative unimportance of the elastic backscattering of photons for applications less sensitive to backscattered photon spectra than NRF.

- A peak at 511 keV due to annihilation of positrons produced during pair production. The 511-keV photons are emitted isototropically.

- An incoherent photon peak. The energy of this peak is defined by equation 2.24. It ranges from near the incident photon energy for small-angle scattering to $\left(\frac{E}{1 + 2E/m_e c^2} \right)$ in backwards directions.

- x-rays. Photoabsorption results in the isotropic emission of x-rays. For uranium, these extend up to 109 keV. The x-ray emission is essentially isotropic.

- The continuum. The spectral continuum is primarily due to bremsstrahlung produced by electron and positron slowing in the targets. Energetic electrons

bremsstrahlung source	e^- energy (MeV)	e^- direction	normalization
primary photoelectrons	1.7	forward	$R\frac{\mu_{PE}}{\mu_{tot}}$
Compton electrons	1.48	forward	$0.4R\frac{\mu_{Inc}}{\mu_{tot}}$
pair production leptons	0.339	isotropic	$2R\frac{\mu_{PP}}{\mu_{tot}}$

Table 2.1 Treatment of electrons for bremsstrahlung spectra normalization for Figure 2.24.

and positrons are produced by pair production, incoherent scattering, and photoelectric absorption.

While the bremsstrahlung process producing the continuum is fairly complex, a simple model that sums constituent parts of the continuum can provide significant insight. The angular distribution of electrons emitted from photoelectric absorption is very forward-directed as given by equation 2.54. As discussed in Section 2.4, Compton electrons with energies close to incident γ-ray energy are also forward-directed. Thus we consider bremsstrahlung from incoherent scattering and photoelectric absorption to be represented approximately by simulation of monoenergetic forward-directed electrons emitted uniformly along the incident photon's trajectory.

In a simple approximation, we consider bremsstrahlung from three contributions: photoelectric absorption of 1.7-MeV electrons, forward-emitted Compton electrons, and pair production leptons. To determine the proper normalization for each contribution, we must determine the number of electrons (or positrons) produced per 1.7 MeV-photon incident upon the target. These values are shown in Table 2.1, along with the directionality and energies of the electrons. The value, R, corresponds to the total number of photon interactions within the target based on simple attenuation.

$$R = 1 - \exp(-\mu_{Tot}x) \qquad (2.60)$$

where μ_{Tot} is the total photon attenuation coefficient at 1.7 MeV and x the thickness of the target. The rate of electron creation is determined by multiplying R by the fraction of the photon cross section that corresponds to the given reaction type, times the number of electrons (or leptons) produced for a reaction; thus pair production produces two leptons per interaction, photoelectric absorption one, and for the case of Compton electrons we make an additional simplification. By integrating the spectrum of Compton electrons derived in equation 2.50, we find that 40% of electrons are emitted into the forward 20°. Roughly applying this result, we reduce the Compton electron-induced bremsstrahlung spectrum by an additional factor of 0.4.

The bremsstrahlung spectra due to these three electron sources have been included in Figure 2.24. The similarity of the distributions indicates that the simple model describes the continuum fairly well. With the exception of the energy range 1.4 - 1.55 MeV, the model provides good agreement with the overall spectrum at higher energies. Between 1.4 and 1.55 MeV, the assumption that all electrons are forward-directed, along with the neglect of electrons from multiple-scattered photons is rather inaccurate. At lower energies, many more processes appear to contribute to the photon spectrum, including multiple scattering of photons and bremsstrahlung from lower-energy Compton electrons.

From these scattered photon spectra, we can conclude that the most probable processes resulting in backscattered photons are incoherent scattering, pair production, and x-ray emission. However, the energies of these photons are quite low. MCNPX predicts that backscattered, energetic photons are primarily due to bremsstrahlung from energetic photo-excited electrons, but the contribution due to Rayleigh scattering is not negligible, and dominates near the initial photon energy. This implies that the accuracy with which MCNPX calculates bremsstrahlung spectra is important for predicting backscattered photon spectra and that the omission of other elastic scattering physics processes may be very problematic for making conclusions based on MCNPX-predicted spectra.
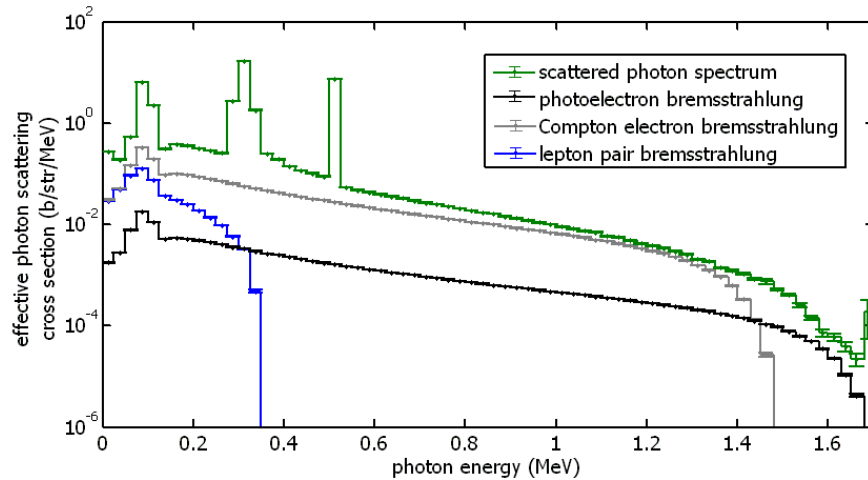
Figure 2.24 MCNPX-simulated differential cross section for scattering of 1.7-MeV photons from 100 μm-thick uranium to the $100^\circ - 110^\circ$ angular range with electron induced bremsstrahlung spectra overlain.

2.9   Photonuclear Interactions

The physics of photon interactions with the nucleus is generally quite similar to that of photo-atomic interactions, with the exceptions that the nuclear force is more

complex, stronger, and shorter-range than the electromagnetic force, which is solely responsible for the potential field experienced by atomic electrons. These facts cause the nuclear potential to be much deeper, the nucleus to be much smaller, and the energy separation between nuclear states to be much larger. For the photon energies considered here, the nuclear potential well is sufficiently deep that photon-induced particle emission cannot occur for most isotopes. Because of this, no processes analogous to incoherent scattering will be considered. The excitation energies of nuclear states are such that both photon scattering via intermediate nuclear states and elastic scattering due to the electromagnetic field are of interest.

It is instructive to consider a photon as a particle whose energy is stored in oscillating electric and magnetic fields and that the transverse nature of the oscillations require the photon to have at least one unit of angular momentum. When light interacts with nuclear states, the oscillating fields are capable of inducing excitation, as well as transferring angular momentum. Even when photon energies are far different from nuclear transition energies, photons can still scatter in the nuclear electromagnetic field. Nuclear Thomson and Delbrück scattering are two examples of elastic scattering in the structureless field of the nucleus. Pair production, discussed in Section 2.7, also involves photons interacting with the nuclear field, except the resulting particles are leptons instead of photons.

An additional complication that must be discussed before we delve into nuclear elastic scattering cross sections is the effects of wave function phase shifts on total elastic scattering cross sections. To this point, we have determined cross sections as quantities proportional to the square of the amplitude of a transition's matrix element. However for elastic photon scattering, the scattering amplitudes of each mechanism must be summed before the total scattering cross section is obtained by squaring the summed amplitude. This can cause interference due to differences in the complex phases of amplitudes resulting from different scattering mechanisms.

2.9.1 Nuclear Thomson Scattering

Nuclear Thomson scattering involves identical physics as that of Thomson scattering described in Section 2.1 with the mass and charge of the charged particle in equation 2.12 being replaced by $m = AM_N$ and $q = Zq_e$, where A, Z, and M_N are the atomic number, mass number, and average nucleon mass, respectively. Since the nucleus is much smaller than the wavelength of photons of interest ($\lambda_{1\text{MeV}} = 1.24$ pm, whereas $r_n \lesssim 80$ fm), the individual nucleons do not influence nuclear Thomson scattering in a similar way as electronic structure does Rayleigh scattering. Therefore, the typical nuclear Thomson scattering cross section is independent of photon energy and is given by

$$\sigma_{NT}(\theta) = \frac{r_e^2}{2} \left(\frac{Z^2 m_e}{AM_n} \right)^2 (1 + \cos^2 \theta) \tag{2.61}$$
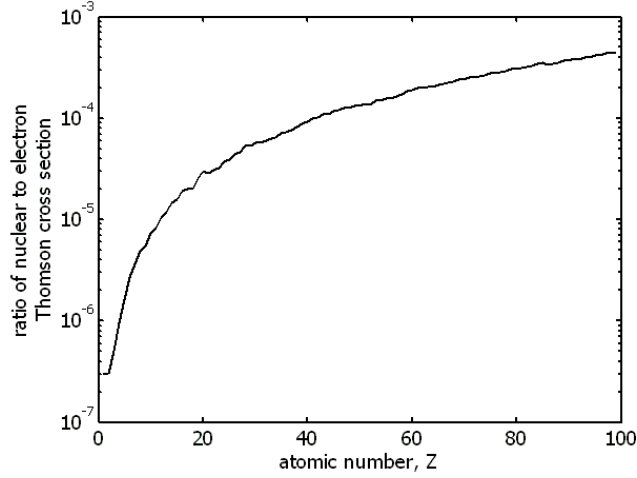
Figure 2.25 Ratio of Thomson scattering cross sections for a photon incident upon a nucleus of charge Zq_e and mass AM_n to that for a photon incident upon a free electron. The ordinate is the square of the constants in the parentheses in equation 2.61.

Figure 2.25 shows the ratio of the constants in the parentheses in equation 2.61 plotted for every element. Although the cross section is isotope-specific, in this case each element's mass was taken to be the weighted mean mass for a natural isotopic concentration. For man-made elements, the mass was assumed to be the average of the known isotopes' masses. Thomson scattering cross sections for nuclei vary from 3×10^{-7} to almost 4×10^{-4} those of a single electron as Z increases from 1 to 92. While this seems to indicate that nuclear Thomson scattering would never be of any significance, it is important to note that for large-angle scattering, the momentum transfer, q increases with scattering angle and energy as given by equation 2.35. The form factor decreases dramatically with increasing q, and the Rayleigh scattering cross section is proportional to the square of the form factor.

In Table 2.2, values of q and the corresponding Rayleigh scattering form factors, $F(Z, q)$, for which the Rayleigh scattering cross section is equal to the nuclear Thomson scattering cross section, i.e

$$\frac{Z^2 m_e}{AM_n} = F(Z, q) \tag{2.62}$$

are tabulated. Also tabulated are photon energies through which scattering at indicated angles yield indicated momentum transfer values.

As indicated in Table 2.2, the energy at which a nuclear Thomson cross section is equal to a Rayleigh scattering cross section increases with increasing Z. However, with larger scattering angles, the form-factor predictions of $\sigma_{Ray}(\theta)$ become increasingly inaccurate(20). Thus, the energies given in Table 2.2 may be inaccurate, but the general trends remain correct. Furthermore, when photons of energy 1.5 - 4

MeV are backscattered, nuclear Thomson scattering is always of some practical importance.

element	q $(\mathring{A}^{-1})$	$F(Z,q)$	$E(45°)$ (MeV)	$E(90°)$ (MeV)	$E(135°)$ (MeV)	$E(180°)$ (MeV)
Carbon	10.4	1.64×10^{-3}	0.337	0.182	0.140	0.129
Aluminum	19.2	3.34×10^{-3}	0.622	0.337	0.258	0.238
Iron	33.1	6.64×10^{-3}	1.07	0.580	0.444	0.410
Cesium	68.1	1.25×10^{-2}	2.21	1.19	0.914	0.844
Uranium	152.9	1.95×10^{-2}	4.95	2.68	2.05	1.90

Table 2.2 Elastic scattering momentum transfer, q, and form factors, $F(Z,q)$, (from EPDL97(19)) where $\sigma_{NT}(\theta) = \sigma_{Ray}(\theta)$ for different elements. Also tabulated are photon energies, given by equation 2.35 that result in the given momentum transfers when scattering occurs at the indicated angles.

2.9.2   Delbrück Scattering

Delbrück scattering is the process by which a photon undergoes pair production within the Coulomb field of a nucleus, and the electron-positron pair promptly annihilates to create another photon whose energy is equal to the initial energy. Whereas Thomson scattering and pair production are considered to be second-order effects, Delbrück scattering is a fourth-order effect.

The matrix element for Delbrück scattering is given by(47)

$$A_{fi} = 2i\alpha \int d\mathbf{r_1} \int d\mathbf{r_2} \exp[i(\mathbf{k_1} \cdot \mathbf{r_1} - \mathbf{k_2} \cdot \mathbf{r_2})] \tag{2.63}$$

$$\times \int dE_1 \int dE_2 \delta(\omega - E_1 + E_2) \mathrm{Tr}[\hat{e}_1 G(\mathbf{r_1}, \mathbf{r_2}|E_2) \hat{e}_2^* G(\mathbf{r_2}, \mathbf{r_1}|E_1)]$$

where Tr signifies the trace of the indicated matrix, $\hat{e}_\mu = \epsilon_\mu \gamma^\mu$, γ^μ are Dirac matrices, and $G(\mathbf{r_a}, \mathbf{r_b}|E)$ are Green's functions in the Coulomb field. Calculations have exactly evaluated matrix elements in the limits $E \ll m_e c^2$ and $E \gg m_e c^2$ and by using the Born approximation at intermediate energies.

Matrix elements have been numerically integrated in the limit that $\hbar\omega \ll m_e c^2$(48). Resulting scattering amplitudes are proportional to $(Z\alpha)^2$, and therefore cross sections are generally proportional to $(Z\alpha)^4$. Empirical evaluations indicate that the Born-series calculations remain quite accurate up to a few MeV if $Z \lesssim 50$. At higher Z, stronger fields make the lowest-order Born approximation inaccurate. Numerical calculations of higher-order terms in the Born series have only partially been accomplished for very few angles and energies(49),(51), but semi-empirical
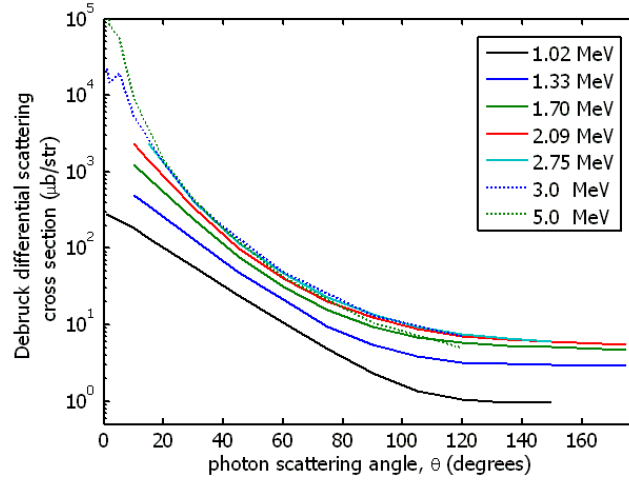
Figure 2.26 Calculated differential Delbrück scattering cross sections for various photon energies. The values ignore destructive interferences that reduce the summed cross section. Values are from references(53) except for the two highest energy curves, which are from(54).

Coulomb correction factors have been published(50),(47),(52). For uranium, these corrections can be a large fraction of the Delbrück differential scattering cross section, which, in turn can result in significant changes to the total theoretical elastic scattering cross section.

Figure 2.26 shows the sum of Delbrück scattering amplitudes squared for various photon energies. These would correspond to the Delbrück cross sections were they directly measurable. However, the addition of elastic scattering amplitudes from other processes can induce interferences that cause total scattering cross sections to differ from those predicted by summing cross sections of individual processes. The cross sections shown were calculated by high-precision numerical integration of the first-order Born series results(53),(54).

2.9.3   Giant Dipole Resonance Scattering

Although the process of photon absorption and re-emission by nuclear states is nuclear resonance fluorescence, for assay purposes, we are concerned with specific excited states of relatively low energy, whereas the primary strength of resonance photon scattering involves the Giant Dipole Resonance (GDR). Here, scattering due to the GDR is discussed, and a more detailed description of the NRF process is saved for Section 2.11.

The GDR is described as a collection of excited nuclear states that all express a collective nuclear motion where all nuclear protons oscillate relative to the neutrons. The large number of such states effectively yields a broad resonance whose cross section is well-described as a Lorentzian distribution. For spheroidal nuclei, the
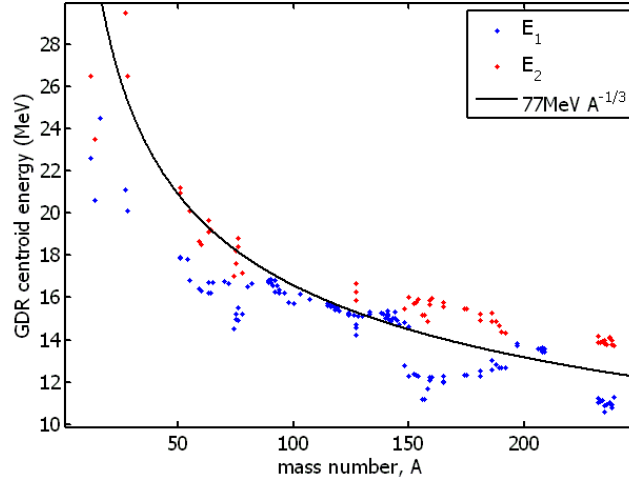
Figure 2.27 Giant Dipole Resonance Lorentzian distribution centroid energies, E_i, as taken from the RIPL-2 database (blue)(58). For deformed nuclei, the GDR is described by two Lorentzian functions and the centroid energy of the upper Lorentzian is shown in red. The curve corresponds to a fluid-dynamics theoretical prediction of the centroid energies for spherical nuclei, and is given by equation 2.64.

energy associated with GDR oscillations depends on the mode of oscillation, resulting in two broad Lorentzian functions. The centroid energies of these resonances are approximately given by the following relation, which assumes the nuclear excitation energy of the GDR is due to increased surface area in a liquid-drop model of the nucleus(55),(56),(57).

$$E_{\mathrm{GDR}} \approx 77[\mathrm{MeV}]A^{-1/3} \tag{2.64}$$

GDR centroid energies are plotted as a function of mass number, A in Figure 2.27 along with the trend-line from equation 2.64. The trend-line holds well for spherical higher-A nuclei, whereas GDR centroid energies for spheroidal nuclei bifurcate into two bands. These bands can be explained as the symmetry breaking of the spheroidal nucleus, where vibrations along the axis of symmetry of prolate (oblate) spheroids are decreased (increased) in excitation energy relative to a sphere.

The total cross section for photo-excitation of the GDR collection of states, and subsequent de-excitation is most commonly given by the single- or double-Lorentzian form

$$\sigma_{\mathrm{GDR}} = \sum_{i=1}^{n} \sigma_i \frac{E_i^2 \Gamma_i^2}{E_i^2 \Gamma_i^2 + (E^2 - E_I^2)^2} \tag{2.65}$$

where n is the number of Lorentzian modes, 1 for spherical nuclei and 2 for spheroidal nuclei, Γ_i is the effective width of the mode, σ_i is the maximum cross section of the mode, and E_i is the centroid energy of the mode.

The total cross section for photo-excitation of the GDR is then probabilistically subdivided into partial cross sections for each de-excitation mode that is energetically
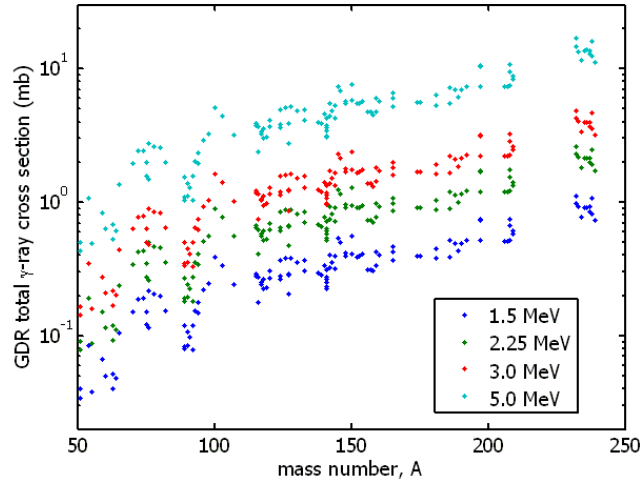
Figure 2.28 Photon cross sections due to lower-energy tails of GDRs as taken from the RIPL-2 database(58).

allowed. Charged particle emission, although often energetically allowed, does not significantly contribute to cross sections due to the Coulomb barrier for emission. The GDR centroid energies of all nuclei are greater than neutron separation energies, and the majority of the GDR cross section is due to neutron emission and fission, where possible. Neutron emission and fission can be accompanied by γ-ray emission to return the daughter nucleus or nuclei to their ground states. At lower energies, γ-ray emission is the most probable de-excitation mode. The large energy range over which the GDR extends causes the photon interaction cross section to remain non-negligible at these energies.

Figure 2.28 presents cross sections for elastic scattering of 1.5, 2.25, 3, and 5-MeV photons from GDR Lorentzians described in the RIPL-2 database(58). GDR resonance profiles are also shown in Figure 2.29. The neutron-emission thresholds are indicated as the vertical lines.

Two important points arise from Figure 2.29. The first is that by increasing photon energy in the 1.5 to 4 MeV energy range and above, GDR cross sections increase. Thus, with increasing NRF lines energies, the photon background due to GDR scattering increases. Secondly, increasing photon energies yields more (γ,n) reactions as more neutron emission thresholds are exceeded. Thermal neutron-capture γ-rays can be a major source of discrete background for NRF assay of materials.

2.10   Scattering Amplitudes and Cross Sections

To this point, all elastic photon scattering processes have been presented with the assumption that each may be considered independently of the others. This however, is not the case. The amplitudes of all scattering processes that leave the
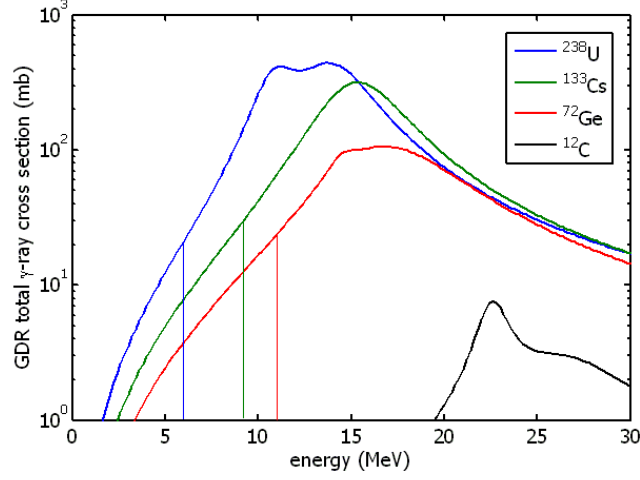
Figure 2.29 Giant Dipole Resonance Lorentzian Distributions for various isotopes(58). The vertical lines indicate (γ,n) threshold energies, which correspond to dramatically decreased elastic scattering cross sections as the majority of GDR de-excitations begin to occur via neutron emission .

state of the scattering atom unaltered and do not change the energy of the scattered photon must be summed to yield a total elastic scattering amplitude. Thus we write

$$A_{\text{Coh}} = A_{\text{Ray}} + A_{\text{Del}} + A_{\text{NT}} + A_{\text{GDR}} \tag{2.66}$$

Likewise, scattering amplitudes are often derived assuming a given photon polarization. Thus, for linearly polarized photons with polarization perpendicular or parallel to the plane of scattering, $A_\perp$ and $A_\parallel$, respectively, the total scattering cross section is given by

$$\frac{d\sigma}{d\Omega} = \frac{1}{2} \left[|A_\perp|^2 + |A_\parallel|^2 \right] \tag{2.67}$$

Amplitudes are often tabulated in units of the *reduced electron radius*, in which case the cross section would be given by

$$\frac{d\sigma}{d\Omega} = \frac{r_e^2}{2} \left[|A_\perp|^2 + |A_\parallel|^2 \right] \tag{2.68}$$

When amplitudes are derived for circularly polarized light, they can be related to linearly polarized amplitudes by the following expressions

$$A_\parallel = A_{++} + A_{+-} \tag{2.69}$$

$$A_\perp = A_{++} - A_{+-} \tag{2.70}$$

where A_{+-} and A_{++} indicate the photon polarization does, or does not change sign, respectively.

Data	Reference	Quoted Accuracy
Rayleigh	Kissel(15)	$< 5\%$
Delbrück	Falkenberg(53)	$\approx 20\%$
Nuclear Thomson	Ericson, Hufner(59)	$\approx 1\%$
GDR	RIPL2(58), Berman(61)	$< 30\%$

Table 2.3 Sources and accuracy of elastic scattering amplitude data and calculations.

Thus for a given set of calculated amplitudes, the total elastic scattering cross section for unpolarized incident radiation is calculated by summing each complex amplitude for a given polarization; squaring the magnitude of the summed amplitudes to yield a cross section for incident polarized photons; and averaging the cross sections resulting from both polarizations.

Figures 2.30 through 2.33 present real and imaginary parts of calculated complex scattering amplitudes for elastic scattering of photons incident upon uranium at a scattering angle of 120º due to the mechanisms discussed previously in this chapter. Dotted lines indicate that the amplitude is negative at the corresponding energy. In the phase convention used in the derivations, Nuclear Thomson scattering amplitudes are always purely real, and GDR amplitudes are real below the (n,γ) threshold energy. The data from these figures come from the references indicated in Table 2.3 and approximate accuracies are also included.

The quoted accuracies come with many caveats. The Rayleigh scattering calculations are thought to be very accurate, but were only performed for K-shell electrons. Corrections due to L-shell electrons have indicated that the errors are less than 5%(50), however the errors were initially estimated for high-Z atoms to be up to 20%(60). Delbrück scattering amplitudes are likewise calculated to high precision ($< 3\%$), but only for first-order terms in the Born series. Higher-order corrections have been estimated to be of the same magnitude as the first-order term for high Z and small scattering angles. At higher angles, the higher-order terms, or Coulomb corrections, appear to be approximately 20%. The nuclear Thomson cross section appears to be well-understood for spherical nuclei. Second-order corrections due to the polarizability of the nucleus and its finite size increase quadratically with energy and are approximately 1% at 4.5 MeV. Additional corrections for nuclei of non-zero spin increase linearly with energy but these corrections are generally small(62). GDR amplitudes are derived from reported cross sections(61). For spin-0 ground states, the GDR amplitudes are related by

$$A_{\parallel}^{\mathrm{GDR}} = A_{\perp}^{\mathrm{GDR}} \cos\theta \qquad (2.71)$$

With this, we can relate the amplitude to the total cross section by using equation 2.68.

$$\sigma_{\mathrm{GDR}} = \int d\Omega \frac{d\sigma_{\mathrm{GDR}}}{d\Omega} = 2\pi \frac{r_e^2}{2} |A_{\perp}|^2 \int_0^{\pi} (1 + \cos\theta) \sin\theta d\theta = \frac{8\pi r_e^2}{3} |A_{\perp}|^2 \qquad (2.72)$$
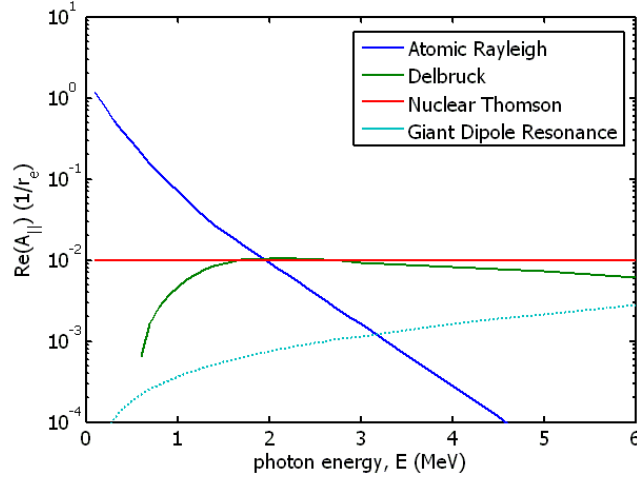
Figure 2.30 The real portion of elastic scattering amplitudes due to mechanisms of Rayleigh, Delbrück, nuclear Thomson, and GDR scattering at 120° for photons polarized parallel to the plane of scattering incident upon ^{238}U, $A_{\parallel}$. Dotted lines indicate a negative amplitude.

Solving for $|A_{\perp}|$, we find

$$|A_{\perp}| = \sqrt{\frac{3\sigma_{\mathrm{GDR}}}{8\pi r_e^2}} \tag{2.73}$$

Finally, errors reported for GDR scattering are due to differences between Lorentzian fits of experimental data for photon cross sections in the GDR energy range. These different shapes result in quite different GDR scattering cross sections at lower energies, however at the energies of interest, the GDR remains a minor contributor to the total elastic scattering cross section.

The amplitudes shown in Figures 2.30 - 2.33, are summed and squared to obtain contributions to the total photo-elastic scattering cross section due to each polarization. The real and imaginary parts of these amplitudes are shown in Figure 2.34 along with their sum, which is the total differential elastic scattering cross section for 120° scattering of photons incident upon ^{238}U. The same total differential scattering cross section is also plotted in Figure 2.35, however in this figure, the sum of the squared amplitudes for each individual elastic scattering process are also shown. The effect of coherence is prominent near $E_{\gamma} = 2$ MeV, where the sums of the individual scattering cross sections are significantly less than the total cross section. Likewise, Figure 2.36 shows the cross sections of the individual elastic scattering processes and the total differential cross section for 30° scattering of photons incident upon ^{238}U. In this case, destructive interference results in a smaller total cross section near 2.5 MeV than would be expected from the individual contributions of both Delbrück and Rayleigh scattering. Finally, Figure 2.37 shows the total differential elastic scattering cross section for 120° scattering of photons incident upon ^{138}Ba. At 120°, the
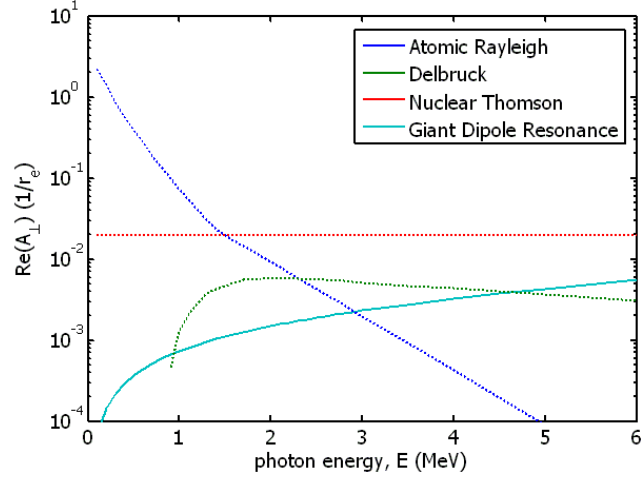
Figure 2.31 The real portion of elastic scattering amplitudes due to mechanisms of Rayleigh, Delbrück, nuclear Thomson, and GDR scattering at 120º for photons polarized perpendicular to the plane of scattering incident upon ^{238}U, $A_{\parallel}$. Dotted lines indicate a negative amplitude.
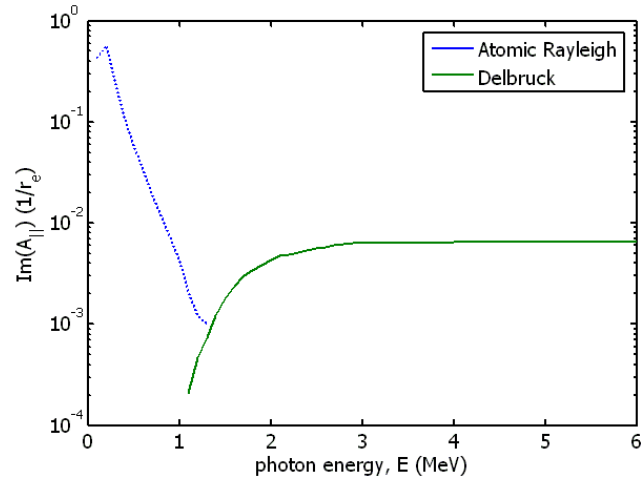
Figure 2.32 The imaginary portion of elastic scattering amplitudes due to mechanisms of Rayleigh, and Delbrück scattering at 120º for photons polarized parallel to the plane of scattering incident upon ^{238}U, $A_{\parallel}$. Dotted lines indicate a negative amplitude.
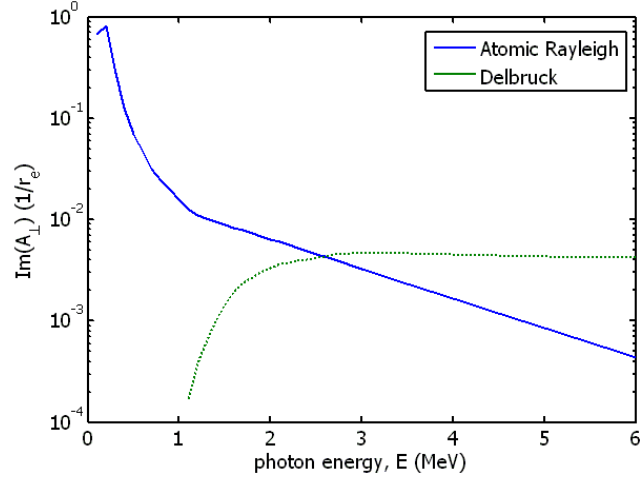
Figure 2.33 The imaginary portion of elastic scattering amplitudes due to mechanisms of Rayleigh, and Delbrück scattering at 120° for photons polarized perpendicular to the plane of scattering incident upon ^{238}U, $A_{\parallel}$. Dotted lines indicate a negative amplitude.

^{138}Ba cross section is approximately a factor of 5 smaller than the cross section for ^{238}U in the region of energy of interest for NRF, owing primarily to the decreased Rayleigh scattering cross section.

Data collected from the elastic scattering of 2.754-MeV photons on various isotopes are shown in Figures 2.38 and 2.39. These figures contain data and predictions from reference(50) and the experiments performed are described both there and in references (60),(63), and(64). The photon source is ^{24}Na which decays by β^{-} emission to excited states of ^{24}Mg, resulting in the emission of a 2.754-MeV γ-ray with an absolute intensity of 99.944%(65). A lithium-drifted germanium detector was used to detect elastically scattered photons. Targets consisted of ^{65}Zn, ^{92}Nb, Ce, ^{141}Pr, Nd, Ta, Pb and U. The figures include statistical counting errors. The angular acceptance of the detector was reported to be 0.7°. The dashed lines in the figures indicate the coherent sum of elastic scattering cross sections as described in this section. The difference between the data point and the dotted lines has been attributed to the Coulomb correction. Incomplete integration of the Coulomb correction has moved theoretical elastic scattering cross sections closer to the measured data. In 1995 it was noted that computational power was limiting more complete computations(49). This suggests that current computer technology may be able to satisfactorily tabulate Coulomb corrections to Delbrück scattering amplitudes for use in photon transport Monte Carlo codes and elsewhere.
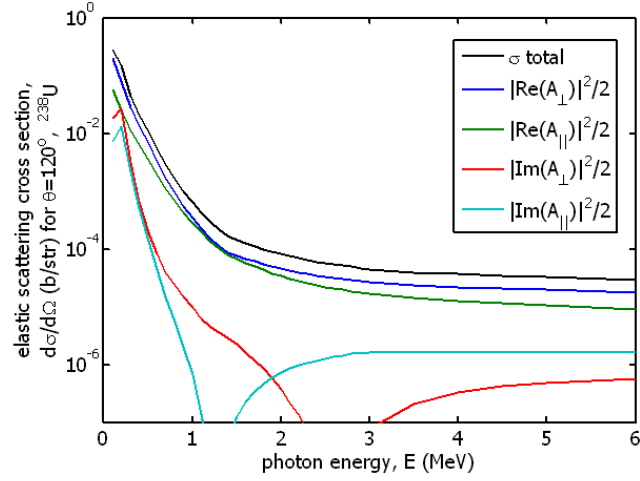
Figure 2.34 Calculated elastic scattering amplitudes and the total differential scattering cross section for 120° scattering of photons incident upon ^{238}U. The sources of the plotted values are discussed in the text
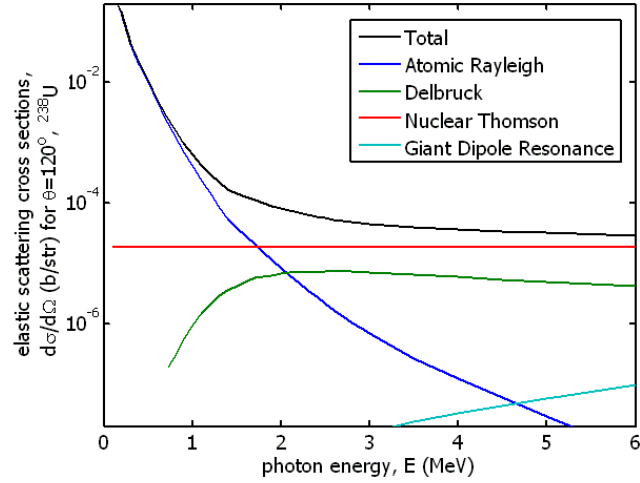
Figure 2.35 Calculated elastic scattering cross sections for individual scattering processes and the total differential scattering cross section for 120° scattering of photons incident upon ^{238}U. Individual cross sections are non-physical because they cannot be separately measured from the total cross section. The sources of the plotted values are discussed in the text.
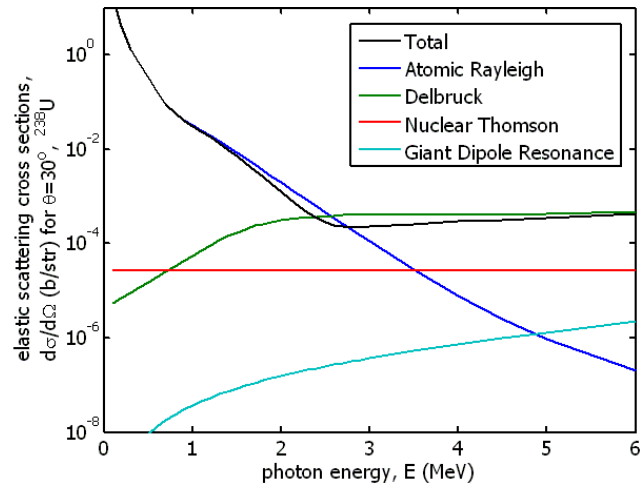
Figure 2.36 Same as Figure 2.35 but for 30° scattering.
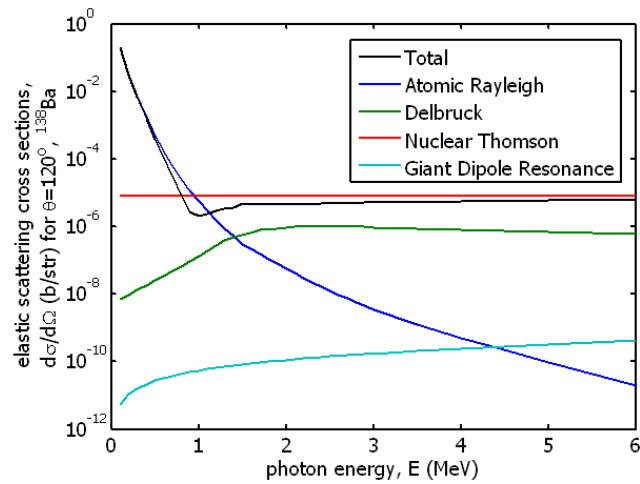
Figure 2.37 Same as Figure 2.35 but for ^{138}Ba.
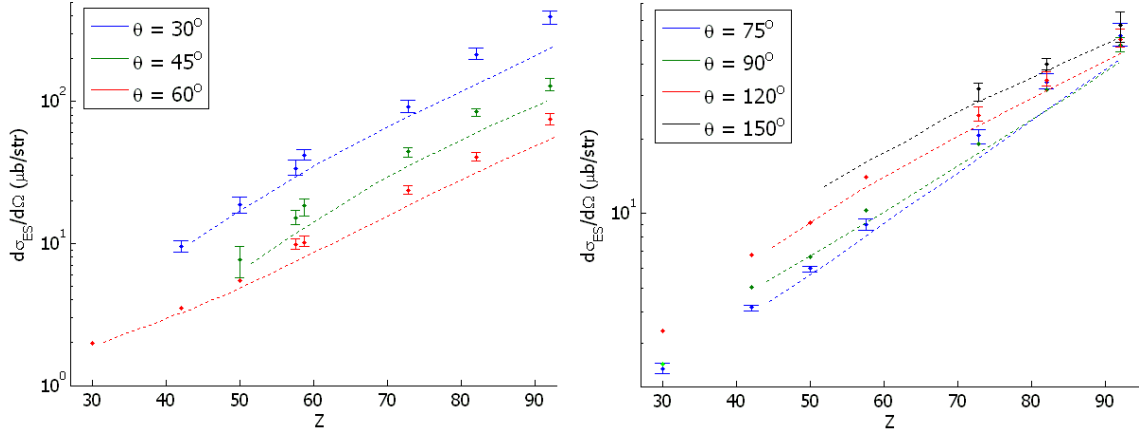
Figure 2.38 Measured and predicted elastic scattering cross sections for 2.754-MeV photons and scattering angles 30º - 60º incident upon ^{65}Zn, ^{92}Nb, Ce, ^{141}Pr, Nd, Ta, Pb and U. Dashed lines are theoretical predictions including summed amplitudes of Rayleigh, nuclear Thomson, GDR, and Delbrück scattering without Coulomb correction terms. The data for this figure are taken from reference(50).

Figure 2.39 Same as Figure 2.38 but for scattering angles of 75º - 150º. The data for this figure are taken from reference(50).

2.11   Nuclear Resonance Fluorescence

Nuclear resonance fluorescence (NRF) is the process by which an excited nuclear state emits γ-rays of specific energies to de-excite to its ground state. Herein these photons are referred to as *NRF γ-rays*. In the context of assaying materials, NRF is usually induced by exciting nuclear states with a beam of photons. The subsequent NRF γ-rays are measured using photon detectors such as high-purity germanium (HPGe) or scintillation detectors. Because NRF states correspond to excited nuclear levels, the photo-absorption and NRF γ-ray energies identify the nucleus that has undergone NRF. The identification is analogous to passive γ-ray spectroscopy used to identify decaying radioactive nuclides.

If the assay geometry and NRF cross section is known, measuring the rate at which NRF occurs allows the number of atoms of the corresponding isotope to be determined. The rate at which a nuclide undergoes NRF is given in thin targets by

$$R = \int N\Phi(E)\sigma(E)dE \tag{2.74}$$

Thicker targets require geometrical corrections due to the fact that the energy-dependent photon flux, $\Phi(E)$ may change as it traverses the target. This will be discussed in Section 3.1.1.

The cross section for photo-excitation of a nuclear state is given by the Breit-

Wigner distribution:

$$\sigma(E) = \pi g \frac{(\hbar c)^2}{E^2} \frac{\Gamma \Gamma_0}{(E - E_c)^2 + (\Gamma/2)^2} \tag{2.75}$$

where Γ is the full-width at half maximum (FWHM) of the state and is related to the state's mean lifetime, τ, by

$$\Gamma = \frac{\hbar}{\tau} \tag{2.76}$$

Γ_0 is the partial width of the state for decay by γ-ray emission to the ground state, E_c is the centroid energy of the resonance, and g is a statistical factor equal to the ratio of the number of spin states available for the excitation to the number of initial spin states. For NRF events where the initial nuclear state is the ground state,

$$g = \frac{2J + 1}{2(2J_0 + 1)} \tag{2.77}$$

where J and J_0 are the angular momentum quantum numbers of the excited and ground states, respectively. There are $2J+1$ magnetic substates for a state of angular momentum J, and the additional factor or 2 in the denominator is due to the fact that the photons inducing excitation can have two possible helicities. We will also refer herein to the ΔJ of a transition as the difference between the two angular momentum quantum numbers of transitioning states(67).

The probability for de-excitation of a state by a specific mode (i.e. neutron emission, γ-ray emission, etc.) yielding a lower-energy state can be defined by the state's partial width for that mode,

$$p_i = \frac{\Gamma_i}{\sum_j \Gamma_j} = \frac{\Gamma_i}{\Gamma} \tag{2.78}$$

where we have used

$$\Gamma = \sum_j \Gamma_j \tag{2.79}$$

implying that the summation over j includes all possible de-excitation modes. Combining equation 2.78 and 2.75, we note that the cross section for NRF to occur via emission of a single γ-ray, resulting in the ground state is given by

$$\sigma_{\text{GS}}(E) = \frac{\Gamma_0}{\Gamma} \sigma(E) = \pi g \frac{(\hbar c)^2}{E^2} \frac{\Gamma_0^2}{(E - E_c)^2 + (\Gamma/2)^2} \tag{2.80}$$

The partial width of a transition, Γ_j is related to the matrix element of the transition by

$$\frac{\Gamma_j}{2} = <\Psi_f|\mathcal{H}|\Psi_i> \tag{2.81}$$

Nuclear dimensions increase with mass number, A, by the following approximate relation; $r_n = r_0 A^{1/3}$, where $r_0 = 1.25$ fm is the *hard sphere radius* of a nucleon. Photon wavelengths are given by $\lambda_\gamma = hc/E_\gamma$. When $E_\gamma = 5$ MeV, $\lambda = 250$ fm and the corresponding wave number is $k = 1/2\pi\lambda = 6.4 \times 10^{-4}$ fm^{-1}. A photon plane wave can be described as a linear combination of products of spherical harmonics, $Y_{l,m}(\theta, \phi)$, and spherical Bessel functions, $j_L(kr)$ of angular momentum, $L \geq 1$. Spherical Bessel functions with $L \geq 1$ all have the limiting value of $j \to 0$ as $kr \to 0$, however the rate at which the functions approach zero differ with angular momentum. The asymptotic form of the spherical Bessel functions is given by:

$$j_L(kr)|_{kr \to 0} = \frac{(kr)^L}{(2L+1)!!} \tag{2.82}$$

In the rest-frame of the nucleus, photon wave functions within its vicinity become successively smaller with increasing angular momentum. Because of this, the probability for interaction with the nucleus similarly decreases with increasing angular momentum, and photonuclear interactions will preferentially occur via the lowest angular momentum transfer possible(66).

2.11.1   NRF γ-ray Angular Distributions

NRF is generally considered to only occur between states that differ by 2 or fewer units of angular momentum. The angular distribution of NRF γ-rays, relative to the NRF-inducing radiation can be described by the same spin algebra that is used to define angular correlations in γ-ray cascades(68).

The cross section for NRF γ-ray emission at a direction, θ, relative to the incident photon beam is given by

$$\sigma(\theta) = W(\theta)\sigma \tag{2.83}$$

where the function, $W(\theta)$, is called the angular correlation function. It is a normalized function, i.e.

$$\int_0^{2\pi} d\phi \int_0^\pi \sin(\theta)d\theta W(\theta) = 4\pi \tag{2.84}$$

and (un-normalized) values for $W(\theta)$ were derived for absorption of un-polarized dipole or quadrupole radiation followed by emission of dipole or quadrupole radiation in reference(68).

For transitions where only a single photon multipolarity is allowed, $W(\theta)$ has simple forms. For $0 \to 1 \to 0$ transitions, the normalized angular correlation function is

$$W(\theta) = \frac{3}{4}(1 + \cos^2\theta) \tag{2.85}$$

and for $0 \to 2 \to 0$ transitions, it is

$$W(\theta) = \frac{5}{4}(1 - 3\cos^2\theta + 4\cos^4\theta) \tag{2.86}$$
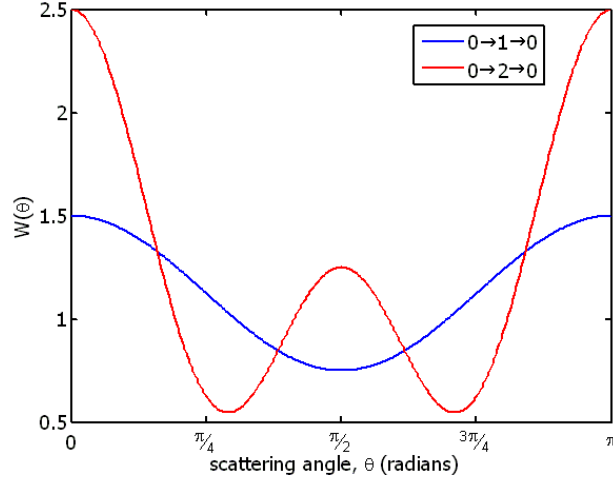
Figure 2.40 The angular correlation functions, $W(\theta)$ for photon transitions between states of spin 0, 1, and 0 (blue), and 0, 2, and 0 (red). This corresponds to the angular distribution of NRF γ-rays, relative to the un-polarized NRF-inducing photon's trajectory, if the NRF state has spin 1 (blue) or 2 (red), and the initial and final states are spin 0.

These functions are shown in Figure 2.40. The $0 \rightarrow 2 \rightarrow 0$ transition exhibits a very large angular dependence.

For transitions between states that exclude spin 0 states, the description of $W(\theta)$ becomes more complicated. This is because the transition may include more than one multipolarity. Take for example, a spin-1/2 state. Transitions of the form $1/2 \rightarrow 1/2 \rightarrow 1/2$, $1/2 \rightarrow 3/2 \rightarrow 1/2$, and $1/2 \rightarrow 5/2 \rightarrow 1/2$, are all expected to be possible in NRF ($\Delta J \leq 2$). Furthermore, the multipolarity of the $1/2 \rightarrow 3/2$ excitation may be either dipole or quadrupole (due to vector spin addition rules), and likewise for the $3/2 \rightarrow 1/2$ de-excitation. The angular distributions predicted for purely dipole-dipole and purely quadrupole-quadrupole transitions happen to be the same, but if one the excitation occurs via quadrupole and the de-excitation via dipole (or vice-versa) the expected $W(\theta)$ differs significantly. Because the actual intensities of quadrupole versus dipole transitions (commonly referred to as the *mixing ratio*, δ) can vary from state to state, any possible $W(\theta)$ distribution combination is allowed.

The cases of ground-state to ground-state NRF on spin 1/2 nuclei is presented in Figure 2.41. The red curve indicates a $1/2 \rightarrow 3/2 \rightarrow 1/2$ transition where both the photon multipolarities were both either dipole or quadrupole, whereas the green curve indicates a transition where one photon was dipole, and the other quadrupole. The area between the curves has been shaded gray to indicate that any possible angular correlation function between these two extremes is physically possible. Finally, the sequence $1/2 \rightarrow 5/2 \rightarrow 1/2$ (assuming octupole radiation is negligible) is only described by quadrupole transitions. The shape of this $W(\theta)$ curve is similar to that for the $0 \rightarrow 2 \rightarrow 0$ transition, however, the degree of variations with
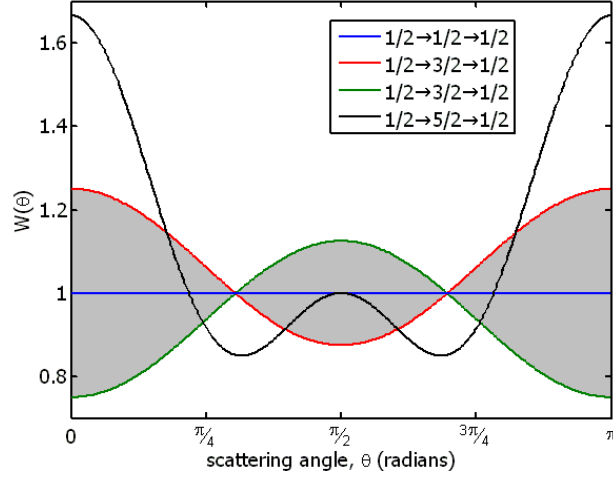
Figure 2.41 The angular correlation functions, $W(\theta)$ for NRF between states of initial and final spin $1/2$ allowed by dipole and quadrupole radiation. The red curve indicates a $1/2 \to 3/2 \to 1/2$ transition where both the photon multipolarities were both either dipole or quadrupole, whereas the green curve indicates a transition where one photon was dipole, and the other quadrupole. The area between the curves has been shaded gray to indicate that any possible angular correlation function between these two extremes is physically possible.

angle is about one-half as strong. The method of comparing angular distributions of NRF photons emitted from spin-$1/2$ ground-state nuclei has successfully identified spins of ^{113}Cd NRF states(69).

For completion, we consider two more examples. The first example demonstrates other probable spin-state combinations that may be seen during NRF induced on a spin-0 nucleus. If a spin-1 NRF state de-excites to a spin-2 level, the de-excitation process can occur via emission of either dipole or quadrupole radiation, resulting in different correlation functions. Thus, similar to the $1/2 \to 3/2 \to 1/2$ example, the $0 \to 1 \to 2$ sequence does not yield a theoretically well-defined angular distribution, but a range of distributions, that includes isotropy. The $0 \to 2 \to 1$ sequence has similar characteristics, although both idealized cases – where the de-excitation photon is either always dipole, or always quadrupole – yield suppressed emissions in the forwards and backwards directions relative to 45° emission.

The case of a $0 \to 2 \to 2$ sequence is also interesting because it may be observed in the case of quadrupole excitation of a ground state, followed by de-excitation to a the rotational or vibrational low-lying 2^+ state. These angular correlation functions are shown in Figure 2.43 for the cases where the de-excitation occurs by emission of a dipole or quadrupole photon. The actual angular distribution for this sequence may lie between the two extreme cases.

Finally, to introduce the possible emission spectra for ^{235}U (ground state spin-$7/2$), possible angular distributions for the processes $7/2 \to 7/2 \to 7/2$ and $7/2 \to$
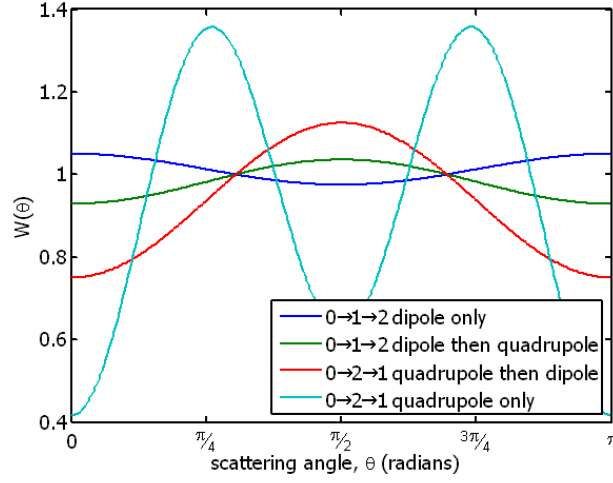
Figure 2.42 The angular correlation functions, $W(\theta)$ for NRF between states of initial spin-0 that do not return to a spin-0 state. Although not shown, the distributions for the sequence, $0 \rightarrow 1 \rightarrow 1$ are nearly identical to the shown distributions for $0 \rightarrow 1 \rightarrow 2$.
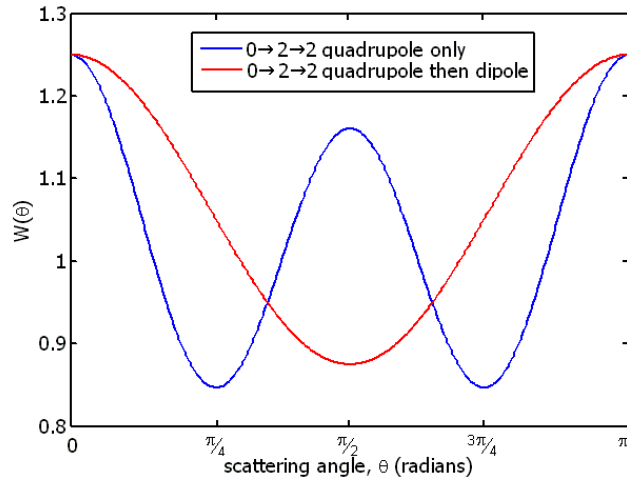
Figure 2.43 The angular correlation functions, $W(\theta)$ for NRF between states of initial spin-0 absorbing a quadrupole photon and subsequently de-exciting to a spin-2 state.
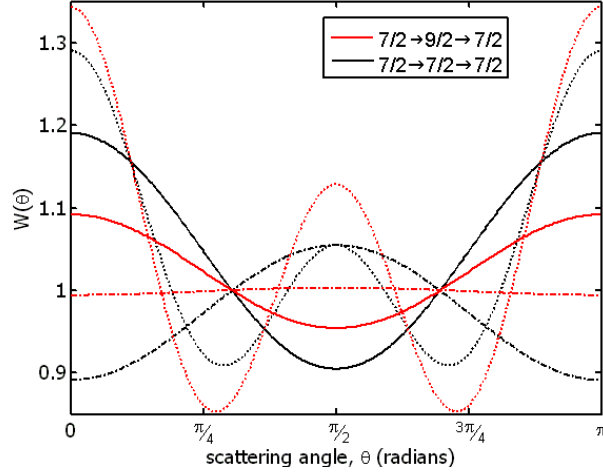
Figure 2.44 The angular correlation functions, $W(\theta)$ for NRF between states of initial spin-7/2 going through intermediate states of spin-7/2 (black) and 9/2 (red) for three hypothetical multipolarity combinations: only dipole (solid lines), only quadrupole (dashed lines), and one transition dipole, the other quadrupole, (dot-dashed lines).

$9/2 \rightarrow 7/2$ are shown in Figure 2.44. Here, the theoretical function, $W(\theta)$ is plotted as a solid line for the case of only dipole transitions, a dotted line for the case of only quadrupole transitions, and a dot-dash line for the case where one transition occurs via dipole and the other via quadrupole radiation. Again, the distribution functions show less directional dependence than the most severe case of $0 \rightarrow 2 \rightarrow 0$, but some non-isotropy may exist.

2.11.2   NRF States

States whose angular momentum differ from that of the ground state by one or two units of angular momentum can be physically described in several ways. The simplest such idealized description is that of a state where a single nucleon is excited into a higher level. States with approximately this character are easiest to identify near closed nuclear shells, and nuclear structure indicates that generally these states will have the same parity as the ground state. The majority of all nuclear states however, require considerably more complex descriptions. This section provides a simple framework for understanding NRF states and does not claim to contain an exhaustive list of all possible modes describing states that may undergo NRF(70).

The most common NRF states make up the GDR. As discussed in Section 2.9.3, the GDR is considered to be a collection of states in which the nuclear protons and neutrons collectively oscillate with respect to on another. Translation through the origin would swap the neutron-rich and proton-rich regions, which explains why the GDR is a parity-odd excitation mode. The angular momentum of GDR excitations is unity, which contributes to their large cross sections and effective widths. Large
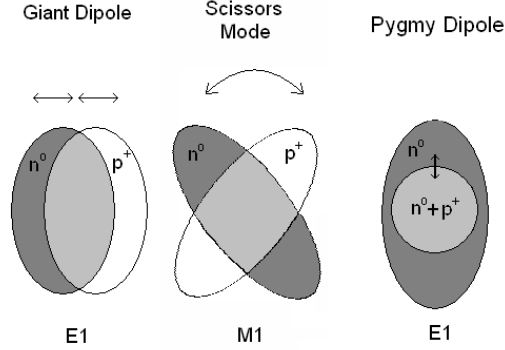
Figure 2.45 Schematic drawings of nuclei undergoing GDR, scissors-mode and PDR excitations. Where the ellipses are filled with white space indicates proton-rich space, dark-gray indicates neutron-rich space, and light-gray indicates comparable nucleon densities. The arrows indicate the direction of nucleon oscillation.

GDR widths limit the isotopic-specificity that could be derived from measurement of GDR-scattered photons because all nuclides have a GDR, and the resonances overlap in energy. Therefore measurement does not yield nucleus-specific information that can be used for identification. The trend for neutron emission following GDR excitations further limits the potential of measuring the GDR for NRF assay applications because of increased backgrounds induced by subsequent neutron capture.

Discrete resonances narrower than the GDR have been measured and have been attributed to more complex collective excitation models. The *scissors-mode excitation* model attributes nuclear states to the collective rotational oscillation of neutrons and protons with respect to one-another (as opposed to the GDR's translational oscillation). Simple consideration of the mean relative separation between neutrons and protons would imply that the scissors mode excitation would be lower in energy than the GDR and that such an excitation mode is only available to non-spherical nuclei. Translation through the origin for scissors mode oscillations is parity-symmetric, and thus scissors mode excitation is $\Delta J^{\pi} = 1^{+}$ and therefore M1(67).

Neutron-rich nuclei have been measured to undergo lower-energy E1 excitations that have been described as pygmy dipole resonances. The model for these excitations is that the excess *neutron skin* oscillates with respect to the proton and neutron core and have been studied in tin isotopes(71). Like the GDR, pygmy dipole resonances are excited from the ground state via E1 transitions.

Another model describing collective nuclear states is that where an entire non-spherical nucleus rotates around an axis normal to the symmetry axis of the nucleus. For even, even nuclei, the spins and parities of rotational states follow the following pattern: $2^{+}, 4^{+}, 6^{+}, 8^{+}, \cdots$, whereas for odd-A nuclei, odd-angular momentum excitations are also possible. Quantum mechanically, the rotational excitation energy of

a rigid body is given by

$$E_{rot} = \frac{\hbar^2}{2\mathfrak{J}} I(I+1) \tag{2.87}$$

where I is the rotational quantum number, and $\mathfrak{J}$ is the rotational inertia of the nucleus. The rotational inertia of an ellipsoid of mass, M, is classically given by $\mathfrak{J}_{class} = \frac{M}{5}(a^2 + b^2)$, where a and b are the lengths of the semi-major and semi-minor axes. With increasing atomic number, M, a, and b will generally increase, and therefore the rotational excitation energies dramatically decrease. For ^{12}C, the lowest excited state is a 2^+ state at 4.439 MeV(72). The pattern of this and the 4^+ state at 14.083 MeV indicate that they represent a rotational spectrum. The first four excited states in ^{238}U follow the spectrum predicted by the rigid rotor model quite closely; however, the excitation energies of these states are only 44.92, 148.38, 307.18, and 518.1 keV for the $2^+, 4^+, 6^+$, and 8^+ states, respectively. Thus, we can see that rotational excitation provides potential $\Delta J = 2$ NRF states for low-Z nuclei with even numbers of protons and neutrons, but the energies of rotational states become too low to be of use for applying an assay method that uses NRF to observe these types of states in higher-Z nuclides.

For nuclei with non-zero ground-state angular momentum, the rotational model becomes more complex. The angular momentum due to a purely rotational excitation may couple to the intrinsic angular momentum of the nuclear state, resulting in a series of excited states obeying rotational energy systematics for a single nucleus. Despite the more complicated spectra, the energy scales of the excitations are expected to remain the same(14). Therefore, pure rotationally excited states are only of interest for use of an NRF assay method of low-Z materials.

Nuclear vibration is an additional collective excitation model in which the shape of the nuclear matter oscillates around the ground-state shape. The restorative force that tends to return deformed nuclear shapes to the ground state is proportional to the magnitude of deformation. Therefore, simple nuclear vibrations may be described as a form of the harmonic oscillator problem. The nuclear shape may be described as a sum of spherical harmonic functions each with a given amplitude ($\alpha_{\lambda\mu}$). Each spherical harmonic ($Y_{\lambda\mu}$) corresponds to a state of specific angular momentum.

$$R(\theta, \phi) = R_0 \Big[1 + \sum_{\lambda\mu} \alpha_{\lambda\mu} Y_{\lambda\mu}(\theta, \phi) \Big] \tag{2.88}$$

All integer values of $\lambda > 1$ are possible. $\lambda = 1$ is prohibited because it would correspond to a translation of the entire nucleus, which is impossible without an external restorative force. The vibrational excitation model yields specific energy spectra, wherein the energy separation between successive states of a vibration mode is constant. The excitation between vibrational levels is generally considered to be due to a single *phonon* in analogue to vibrational modes in solid crystal lattices. The parity of the phonon mode follows the rule $\pi = (-1)^\lambda$(14). The excitation energy of quadrupole vibrational states tends to decrease with atomic number, however the decrease is less dramatic than for rotational excitations(73).

Another model describing collective $\Delta J = 1$ states is the coupling of nuclear octupole ($\Delta J^{\pi} = 3^{-}$) vibrations with vibrational or rotational excitations of $\Delta J^{\pi} = 2^{+}$. For even, even nuclei, this coupling results in states of spin and parity $1^{-}, 2^{-}, 3^{-}, 4^{-}$, and 5^{-} whose energies are near the sum of the octupole phonon and quadrupole state energies. The theoretical description of this coupling, the state ordering, and the influence of the GDR are discussed in reference(74). In short, the presence of the GDR can increase the transition strength for the 1^{-} state, resulting in strong E1 NRF resonances often with energies between ~ 2 and 4 MeV(67),(55).

The description of NRF levels becomes further complicated by the fact that the relatively simple forms described in this section can couple with one-another, yielding states that would be described by much more complex models. For example reference(75) discusses 2^{+} NRF states of even mass Sn isotopes. The lowest one-phonon quadrupole vibrational states in the Sn isotopes lie between 1.1 and 1.3 MeV. More 2^{+} NRF states were measured between 2 and 4 MeV that were identified as weakly collective states coupled to single particle states. The same experiment also identified strong E1 excitations for all isotopes between 3.2 and 3.5 MeV that were identified as two phonon octupole-quadrupole coupling(76). Another complicating factor is that interacting nucleons within a nucleus can yield an *exchange current* which results in more complex descriptions of nuclear states and transitions.

Despite the complexities in describing $\Delta J \leq 2$ excited nuclear states, the most important characteristics are their energies, and the strength by which they are coupled to the ground state. For a state to be considered important for an NRF assay techniques, its energy must be sufficiently high such that resonant γ-rays emitted by the state may be observed above inelastic and non-resonant elastic scattered background photons. The state's excitation energy must also be sufficiently low such that it is observable as a discrete state as opposed to higher-energy states that contain very large admixtures of the GDR and may overlap in energy.

2.11.3   NRF Transition Strengths

The strength of an NRF transition is most commonly referred to as its integrated cross section, with units of eV·barns. Integration of equation 2.75 over all energies $E \geq 0$ does not converge on account of the singularity at $E = 0$. However, $E = 0$ photons are non-physical, and for a small lower energy integration limit, ϵ, the integral converges.

$$\int_{\epsilon}^{\infty} \sigma(E)dE \approx \int_{0}^{\infty} \pi g \frac{(\hbar c)^2}{E_0^2} \frac{\Gamma \Gamma_0}{(E - E_c)^2 + (\Gamma/2)^2} dE$$

$$= 2\pi^2 g \Gamma_0 \frac{(\hbar c)^2}{E_0^2} \tag{2.89}$$

$$= 7684[\text{b} \cdot \text{MeV}^2] \frac{\Gamma_0}{E_0^2} g \tag{2.90}$$

For nuclear states, Γ can range from almost zero to several MeV. A state with $\Gamma \approx 0$ implies it has a very long lifetime, such as the 3167 keV excited state of ^{91}Zr, which has a lifetime of 5.28μs, corresponding to a width, $\Gamma = 1.5 \times 10^{-10}$ eV(77). Long-lived states typically have spins that differ significantly from the ground state, which makes them unlikely to be produced through photon excitation. The 3167 keV state in ^{91}Zr is suspected of having a spin of 21/2, compared with the ^{91}Zr ground state spin of 5/2.

Large values of Γ imply that the state is short-lived. The lowest exited state in ^{9}Be has a width, $\Gamma = 217$ keV and an energy of 1684 keV, relative to the ground state(78). The neutron separation energy of ^{9}Be is 1.67 MeV(79), which implies that the 1684 keV state can de-excite via neutron emission. When energetically allowed, de-excitation via neutron emission is very common and dramatically reduces level lifetimes, thereby increasing Γ.

For a state to be useful for NRF assay, it must be able to be excited via ground state photo-absorption and de-excite by γ-ray emission with significant probability. Neither level described in the preceding paragraph meets these requirements. Unhindered photon emission rates have been estimated by Weisskopf(13) based on single-particle models for various multipolarity transitions. Although the model tends to over-estimate the rates of E1 transitions, it provides an estimate as to the shortest lifetimes expected for levels that de-excite via γ-ray emission.

$$t_{1/2s.p.}(E1) = \frac{6.76 \times 10^{-6}}{E^3 A^{2/3}} \tag{2.91}$$

Where E is the excitation energy of the state in keV, and the half-life is in seconds. For the 4842 keV level in ^{208}Pb, the E1 transition to the ground state, the Weisskopf estimate results in a half-life of $t_{1/2s.p.} = 1.7 \times 10^{-18}$ s and a width, $\Gamma = 270$ eV. The actual width of this level has been measured to be 4.78 eV(80), which corresponds to a half-life of 9.5×10^{-17} s. This state is a relatively large NRF state. Most states that have been measured to undergo NRF have widths between of 5 meV and 10 eV, and although they are expected to exist, smaller resonances are difficult to measure via the detection of the NRF γ-rays above background levels.

Equation 2.91 indicates that for E1 transitions, Γ values tend to increase as E^3, whereas equation 2.75 showed that NRF cross sections are proportional to $\Gamma\Gamma_0/E^2$. This implies that neglecting hindrance, NRF resonances would increase in overall intensity linearly with energy. However, the formalism defining equation 2.91 assumes single particle levels undergoing transitions, whereas Section 2.11.2 reported that many states excited during NRF are distinctly collective and therefore their transition rates may exhibit hindrance due to structure effects.

Weisskopf state lifetime estimates are not only subject to overestimation. Electric quadrupole (E2) transitions for deformed nuclei are frequently observed at rates faster than anticipated by the Weisskopf E2 estimate,

$$t_{1/2s.p.}(\text{E2}) = \frac{9.52 \times 10^6}{E^5 A^{4/3}} \tag{2.92}$$

The explanation for this is that the ground state and essentially all excited states of the deformed nucleus have large intrinsic electric quadrupole moments and therefore the matrix element, $< \Psi^*|E2|\Psi_0 >$, can become large when the state, $|\Psi_0 >$, has a large collective component due to a quadrupole phonon. The 2^+ states of Sn are an example where the lowest states – thought to be predominantly vibrational – have transition rates approximately 10 times those predicted by equation 2.92. The higher-energy observed 2^+ NRF states were theoretically predicted to have a more complicated particle-phonon coupling and have transition rates that are slightly hindered relative to the Weisskopf single particle model.

NRF states may emit γ-rays that result in de-excitation to any state that is allowed by energetics and spin conservation. The Weisskopf estimates indicate that highest-energy γ-rays are most favored, however nuclear structure may play an important role for certain NRF states. The spins of highly deformed nuclei may be described by an additional quantum number, K which relates the total spin, J to its projection upon the nuclear symmetry axis. For even, even nuclei with low-lying rotational states, theory indicates that the de-excitation of a $J = 1$, $K = 1$ state is twice as probable to occur to the ground state as to the first rotational state, whereas for a $J = 1$, $K = 0$ state the de-excitation is twice as probable to occur to the first rotational state(81)(82).

2.11.4   Thermal Motion and Nuclear Recoil

To this point, we have only discussed the process of NRF in the context of nuclear states being excited and de-excited. The process, however, is connected to the environment of the nucleus before photon absorption as well as after re-emission. First we consider the fact that nuclei, as part of atoms, are not stationary, but are always in thermal motion. In the case where NRF is induced on a nucleus comprising a gaseous atom or part of a gaseous molecule, the velocity distribution of the nucleus is defined by a Maxwell-Boltzmann probability distribution.

$$P(v) = \sqrt{\frac{M}{2\pi k_B T}} \exp(-Mv^2/2k_B T) \tag{2.93}$$

where M is the mass of the atom or molecule, k_B is Boltzmann's constant, $(1.3806503 \times 10^{-23}\mathrm{m^2 kg\ s^{-2}K^{-1}})$, and T is the absolute temperature of the gas.

For a photon of energy E, a nucleus moving at velocity v will experience a photon of shifted energy, E' due to the Doppler effect.

$$E' = E \left(\frac{1 + v/c}{\sqrt{1 - (v/c)^2}} \right) \approx E \left(1 + \frac{v}{c} \right) \tag{2.94}$$

where we have assumed that the velocity of the gaseous nucleus is very small compared to the speed of light.

Substituting, we find that the effective energy distribution is given by

$$P(E')dE' = \frac{1}{\Delta\sqrt{2\pi}}\exp(-(E'-E)^2/2\Delta^2)dE' \qquad (2.95)$$

where we have used $dE' \approx \frac{E'}{c}dv$ and

$$\Delta = E\sqrt{\frac{k_B T}{Mc^2}} \qquad (2.96)$$

is the standard deviation of the distribution. We commonly refer to the *Doppler width* of an broadened resonance as

$$\Gamma_D \equiv 2\sqrt{2\ln 2}\Delta = 2.3548\Delta \qquad (2.97)$$

because it describes the FWHM of the distribution in equation 2.95[4].

The effective photo-absorption cross section that a photon incident upon a collection of nuclei that have a velocity distribution given by equation 2.93 is then found by averaging the Doppler-shifted energy probability distribution with the absorption cross section(83).

$$\sigma_D(E) = \int_0^\infty dE'\sigma(E')P(E') \qquad (2.98)$$

Substituting equations 2.75 and 2.95, we have the Doppler-broadened Lorentzian profile (DBLP):

$$\sigma_D(E) = \frac{\sqrt{\pi}g(\hbar c)^2\Gamma\Gamma_0}{\sqrt{2}\Delta}\int_0^\infty dE'\frac{1}{(E'-E_c)^2 + (\Gamma/2)^2}\frac{\exp(-(E'-E)^2/2\Delta^2)}{E'^{\,2}} \qquad (2.99)$$

As an illustrative example, Figure 2.46 demonstrates the effect that a Maxwell - Boltzmann energy distribution can have on the effective resonance shape that an incident photon experiences. This idealized case involves a 2 MeV-centroid energy (E_c) resonance with a width $\Gamma = 0.5$ eV and that always de-excites by photon emission to the ground state ($\Gamma_0 = \Gamma$). The states were assumed to have the same spin so that $g = 1/2$. This distribution is also broadened due to the motion of the atoms, which have been arbitrarily described by a Maxwell-Boltzmann velocity distribution with Doppler width, $\Gamma_D = 1$ eV. The corresponding energy probability distribution was multiplied by $\int \sigma(E)dE$, and is shown as the green line in the figure. Equation 2.99 was numerically integrated for these parameters for an array of incident photon energies and the resulting effective cross sections are shown as the dots on the red line in Figure 2.46. Although this example is not very realistic, it does demonstrate that the width of the effective cross section distribution will be broader than that of the energy distribution and that of the natural cross section. Before discussing more realistic examples we consider how binding in solid materials affects the energy distribution of nuclei.

---

[4]It should be noted that another common definition of the Doppler width is $\sqrt{2}\Delta$. This definition is not used in this document.
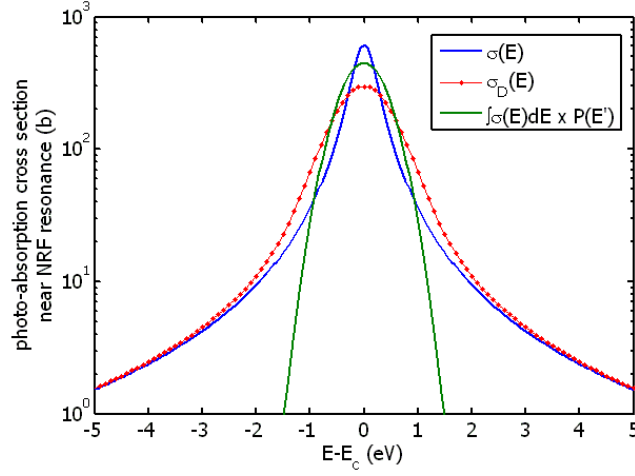
Figure 2.46 The natural cross section distribution for a hypothetical 2-MeV centroid energy resonance with $\Gamma = \Gamma_0 = 0.5$ eV (blue), the results of numerical integration of equation 2.99: the DBLP for $\Gamma_D = 1$ eV (red points), and the Maxwell-Boltzmann distribution that was used for broadening, multiplied by the integrated cross section for visualization purposes (green).

Non-amorphous solids are composed of crystalline arrangements of constituent atoms. These atoms vibrate with thermal energy about their equilibrium positions in the lattice. The momentum of an interacting may be converted into vibrational energy through the creation (or destruction) of one or more *phonons* – here the term phonon is used to describe vibrational excitations of crystalline atoms rather than nucleons. The effects of phonons are most evident when the nuclear recoil energy is not significantly greater than typical phonon energies. However, above ~ 1.5 MeV, the influence of crystalline phonons on the energy distribution of the nuclei continues to have measurable effects. In particular, the binding energy of the crystal and the phonon-induced motion causes crystalline atoms to vibrate faster than gaseous atoms at the same temperature. By ignoring the details of the phonon bands, Lamb was able to derive an expression for the effective temperature at which a crystal's atoms oscillate for the purpose of calculating Doppler broadening. In the limit that $\Delta/\sqrt{2} + \Gamma >> 2k_B\theta$, i.e. the effect of the width of the state is much larger than the thermal energy of the atom, crystalline binding does not significantly influence the atom's recoil and the effective temperature at which equation 2.99 should be evaluated(83),(86) is

$$\frac{T_{eff}}{T} = 3\left(\frac{T}{\theta}\right)^3 \int_0^{\theta/T} t^3 \left(\frac{1}{\exp(t)-1} + \frac{1}{2}\right) dt \qquad (2.100)$$

Here, θ is the Debye temperature of the crystal, which is a physical property of a material that is related to the theoretical maximum energy a single phonon can carry in the material. For elementals in their natural state, values of θ range from 38 K
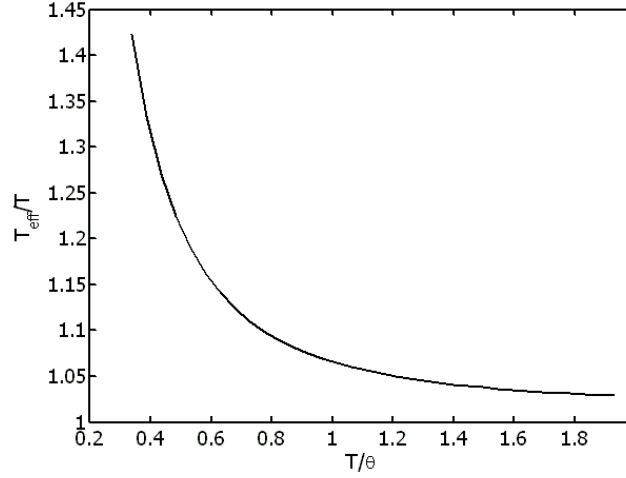
Figure 2.47 Predicted ratio of effective temperature to actual temperature for applying Maxwell-Boltzmann statistics to crystalline materials with a Debye temperature, θ versus temperature relative to θ.

for cesium to 2230 K for carbon (diamond), with most metals between 200 and 500 K(88).

We further investigate the *loose binding* limit, $\Delta + \Gamma >> 2k_B\theta$ by using equation 2.96 and assuming that Γ is smaller than Δ to re-write this limit. It becomes

$$\frac{E}{\theta}\sqrt{\frac{T}{A}} >> 285[\text{eV}/\sqrt{\text{K}}] \tag{2.101}$$

where A is the mass number of the atom in question. This indicates that for the losse binding approximation to be valid at $T = 300\text{K}$, E must be significantly greater than 52 keV for uranium, and 127 keV for diamond. All NRF resonances considered herein fall within this limit.

The results from equation 2.100 are shown in Figure 2.47. This helps explain the effects that phonons have on the effective temperature of a crystalline atom. At high temperatures, atoms oscillate with a similar energy spectrum as a gas of the same temperature. But at low temperatures, the binding energy of the crystal causes ion oscillations at higher velocities, corresponding to a Maxwell-Boltzmann distribution of a higher temperature.

Metallic uranium has a Debye temperature of 207 K(88). The resulting T_{eff} from equation 2.100 for a temperature of 300 K is 311.8 K. For the $E_c = 2175$ keV, $\Gamma = 54$ meV resonance of ^{238}U, this results in a Doppler width of 1.78 eV, or about 2% larger than for hypothetical gaseous uranium. Calculated natural and Doppler-broadened cross sections for this resonance, along with the energy distribution of the crystalline uranium atoms (as predicted by Lamb's application of the Debye model) are shown in Figure 2.48.
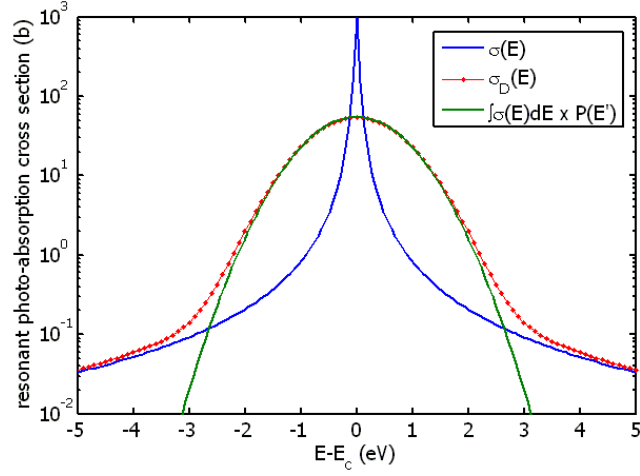
Figure 2.48 Same as Figure 2.46, except for the 2175-keV resonance of ^{238}U at 300 K. For this resonance, $\Gamma = 54$ meV, $\Gamma_0 = 37$ meV, and $g = 3/2$.

The same calculations were performed for the 4026-keV NRF line of ^{138}Ba. Barium has a Debye temperature of 110 K(88), which yields an effective temperature of 306.6K for an ambient temperature of 300 K. The Doppler width for metallic ^{138}Ba atoms is then 4.28 eV, and the 4026-keV state has a width, $\Gamma = \Gamma_0 = 297$meV(89). The same natural resonance shape, the DBLP and a renormalized Maxwell-Boltzmann distribution are shown in Figure 2.49. Compared with the ^{238}U resonance, this peak is much wider due to the higher resonance energy and lower mass, but otherwise the two are qualitatively very similar.

From the proceeding examples, we observe the following:

- Both natural and DBLP cross section profiles are nearly symmetric functions peaked at the centroid energy.

- Doppler-broadening does not alter the integrated cross section, i.e.
  $\int \sigma_D(E)dE = \int \sigma(E)dE$.

- Doppler-broadened widths will always be larger than natural widths, widening the effective cross section distribution near the resonance's centroid energy and correspondingly reducing its the maximum value.

- At photon energies far from the centroid energy, the cross section profile will closely follow the natural (Lorentzian) profile, even if $\Gamma << \Gamma_D$.

Finally, we consider the influence of momentum conservation on NRF physics, first for NRF of gaseous atoms, then in the context of crystalline solids. Conservation of momentum requires that when a nucleus of mass, M absorbs a γ-ray of energy E_γ and momentum E_γ/c, it will recoil with the γ-ray's momentum, which translates
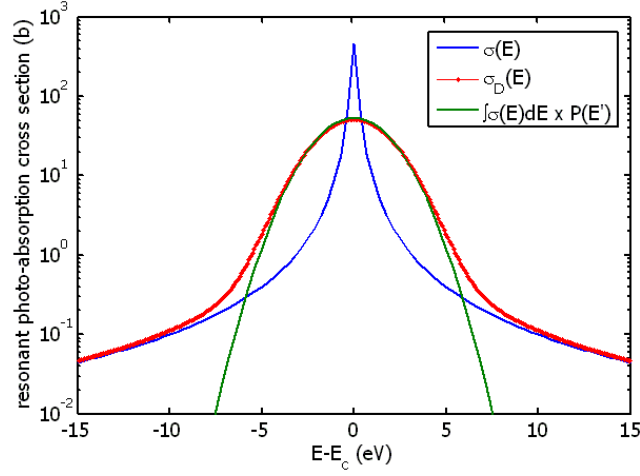
Figure 2.49 Same as Figure 2.48, except for the 4026-keV resonance of ^{138}Ba at 300 K. For this resonance, $\Gamma = \Gamma_0 = 297$ meV, and $g = 3/2$.

to an energy

$$E_{\text{recoil}} = \frac{E_\gamma^2}{2Mc^2} \qquad (2.102)$$

For the example resonances discussed above, this corresponds to a recoil energy of 10.6 eV and 64.5 eV for the ^{238}U and ^{138}Ba resonances, respectively. Of particular importance is the nuclear recoil energy for both resonances are significantly larger than the Doppler-broadened widths of the resonances.

We can equate the expressions for recoil energy and Doppler widths (assuming $\Gamma_D >> \Gamma$). With the simplifying assumption that $M \approx Am_n$, one finds the approximate result that recoil energies equal Doppler widths when

$$E = 11.4\,\text{keV} \times \sqrt{A} \qquad (2.103)$$

Assuming that the Doppler width of a resonance is larger than the natural line width, as long as the centroid energy is much greater than this limit, the NRF recoil energy is larger than the width of a resonance.

The conservation of momentum applies to the re-emission of NRF γ-rays as well. Upon resonance absorption, a nucleus will recoil with energy given by equation 2.102. NRF state lifetimes tend to be on the order of 10^{-17} to 10^{-12} s, implying that the nucleus will re-emit an NRF γ-ray before slowing down to thermal velocities. In the event that the γ-ray is emitted in precisely the same direction as the incident exciting photon, the nucleus would recoil back to its initial velocity. If the γ-ray is emitted in a different direction, the nucleus will again recoil from γ-ray emission and the resulting NRF γ-ray will be lower in energy than the initial photon. Most probably this energy difference will be larger than the Doppler-broadened width of the NRF resonance, and thus the emitted NRF γ-ray will no longer be resonant.

The presence of phonons in crystalline materials can alter these conclusions substantially. The most dramatic example is the phenomenon called the *Mössbauer effect*(84). In this case, rather than causing the absorbing nucleus to recoil, the absorbed photon's momentum annihilates a phonon in the crystal, resulting in recoil-less NRF. However, this process is more common for lower energy photo-absorption processes, with the highest energies for which it has ever been observed being about 150 keV(85). At higher energies, the recoiling atom will either remain bound in its lattice position or recoil and be displaced, most probably to an interstitial position. If the atom remains in its lattice position, it will, on average, undergo damped harmonic oscillation until it has re-equilibrated. The frequency of oscillation and rate of damping depend upon the crystal properties.

The velocity of a recoiling nucleus undergoing damped oscillation has been described as

$$v(t) = f(t)v_{max} \tag{2.104}$$

where the initial recoil velocity $v_{max} = E_\gamma/mc$ and $f(t)$ is given by the real part of the Fourier transform of the phonon frequency spectrum of the material. Where the phonon frequency spectrum has not been measured, the Debye approximation has proved qualitatively useful.

$$f(t) \sim \int_0^{\omega_D} \omega^2 \cos \omega t \tag{2.105}$$

The frequency, $\omega_D = k_B\theta/\hbar$ is called the Debye frequency. Additional complexity may be added to the model by including the Einstein-predicted acoustic modes and/or taking crystalline asymmetry into account. However, with this simple model, we can reach several conclusions that appear to be valid for our purposes.

The function $f(t)$ is shown for recoiling nuclei in the Debye approximation in Figure 2.50 for two materials, one with $\theta = 207$ K and the other with $\theta = 630$ K, corresponding to uranium metal (blue) and chromium metal (red), respectively. After resonant absorption, atoms oscillate with a frequency slightly larger than the Debye frequency that is damped with a characteristic time on the order of 100's of ps, until it equilibrates to low-magnitude Debye frequency oscillations. Given that most NRF states of interest have lifetimes shorter than 50 fs, we see that the recoiling atom will most probably be in the first period of oscillation when it re-emits an NRF γ-ray. So long as the natural width of the resonance is smaller than the energy loss indicated by the damping, re-emitted γ-rays will have less energy than required to be resonantly re-absorbed by another atom(90),(91),(92),(93).

The difference between $f(t)$, computed by the Debye approximation, and for actual phonon spectra has been considered for lanthanum(90). As is the case for U metal and UO_2,(94),(95) the maximum phonon frequency measured is near the Debye frequency, but phonon densities are higher at lower frequencies than predicted by the Debye model. In this case, $f(t)$ predicted from the phonon density of states differed from the Debye prediction at longer times, but for the first period of oscillation,
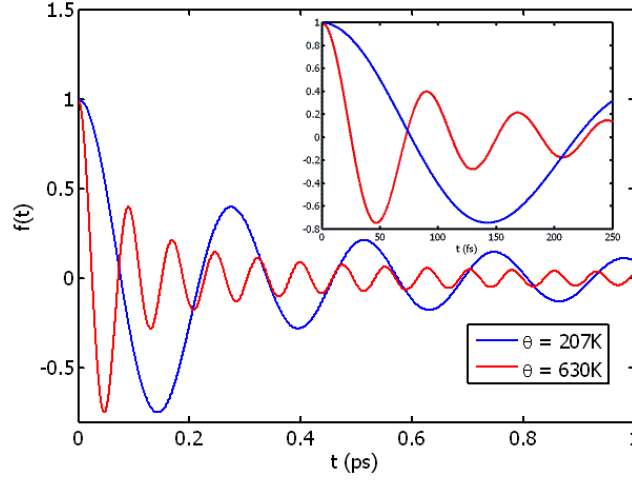
Figure 2.50 Recoiling atom relative velocities in the Debye approximation for two materials, $\theta = 207$ K and $\theta = 630$ K, corresponding to uranium metal (blue) and chromium metal (red), respectively. The box is a close-up of the curves for the first 250 fs after resonant excitation.

the difference was negligible. Thus, the assumption that re-emitted NRF γ-rays are below resonance energy should be satisfactory for examining NRF for materials assay purposes.

2.12   Detector Responses

In this chapter the physics governing photon scattering has been presented. However, in order to use NRF to assay a material, the resonantly scattered photons must be measured. The best energy resolution for detectors widely used today is found with high-purity germanium crystals (HPGe). Photons that interact within the crystals produce energetic electrons that thermalize by creation of secondary electron-ion pairs. These electron-ion pairs are collected by an applied voltage, resulting in an electric signal. The number of electron-ion pairs produced varies statistically, but the low average energy required to produce a particle-hole pair in Ge ($w = 2.96$ eV) along with good charge collection properties give HPGe excellent detector characteristics(96). Research on superconducting transition edge sensors has created devices with better energy resolution, but to date, they have only been successful in measuring low-energy photons ($\lesssim 200$ keV) and at very low count rates ($\lesssim 1$c s^{-1})(97)(98). Thus we consider use of HPGe detectors to be the state-of-the-art for measuring NRF. The energy resolution of an HPGe detector is approximately given by

$$\Delta E_{FWHM} = \sqrt{5.55FEw + \Gamma_e^2} \tag{2.106}$$

The first term in equation 2.106 is the square of the FWHM due to intrinsic charge production in the crystal, where F is a value between 0 and 1 known as the *Fano factor*. It accounts for the statistical correlation between ion-pair production events, resulting in a narrower ion-pair number distribution than would be anticipated by Poisson statistics. The second term, Γ_e is the FWHM due to all electronic noise. Typically, $\Gamma_e \approx 1$ keV. Fano factor values are usually near 0.16 for HPGe and thus, we find detector resolutions vary as $\Delta E_{FWHM} \approx \sqrt{0.0026E + 1}$ when E and ΔE_{FWHM} are in units of keV. At 2 MeV, we find detector resolutions near 2.5 keV. Actual resolutions depend on the exact geometry of the Ge crystal, the bias voltage and the electronics used to readout the signal, but this discussion presents the scale of HPGe detector resolution.

To relate the relative intensities of NRF signals and backgrounds to the precision with which a measurement may be made, we present a simple statistical model. Suppose the signal of interest is detected at a rate, S. The background rate, B, is estimated by examining the count rate in adjacent channels (where it is assumed that no full-energy peaks are located). The total signal rate is, $T = S + B$. We define the signal-to-background ratio as $S/B = \xi$. After a counting period of t, we expect $t(S + B)$ total counts within the area of interest (presumably where an NRF peak is expected). The total number of counts from the signal is $N_S = tS$, with fractional uncertainty of $\vartheta = \frac{\sigma_S}{N_S}$. Assuming Poisson statistics, the standard deviation of the expected number of total counts, N, is $\sqrt{N}$, and we have

$$\vartheta = \frac{\sqrt{t(T + B)}}{tS} = \frac{\sqrt{S + 2B}}{\sqrt{t}S} = \frac{\sqrt{1 + 2/\xi}}{\sqrt{N_S}} \equiv \frac{f(\xi)}{\sqrt{N_S}} \qquad (2.107)$$

The function, $f(\xi)$, that expresses the reduction in statistical quality of a measurement of N_S signal counts varies as $f \sim \sqrt{2/\xi}$ for small values of ξ, whereas for large ξ, $f \to 1$. $f(\xi)$ is shown in Figure 2.51 along with the limiting functions. This observation leads us to conclude that the NRF count rate must be almost as intense as the background signal rate within the detector's energy resolution to obtain counts with reasonable statistical quality.

Background signals due to processes such as elastic and inelastic scattering will vary slowly for photon sources that are broad in energy resolution compared to those of detectors. Therefore, using a HPGe detector, it is necessary that the NRF interaction rate to be approximately 1000 ($\approx \Delta_E/\Gamma_D$) times the scattering rate of non-resonant photons to accrue NRF count rate statistics in an efficient manner. This ratio will increase proportionally with detector resolution. As an example, a detector made of $LaCl_3$ scintillator has a resolution that is about 20 times worse than a HPGe detector(99). This implies that the background count rate within the detector's resolution will be about 20 times higher than it would be for an HPGe detector, and if $\xi_{HPGe} = 1$, the statistical value of a $LaCl_3$ count would be 3.75 times less than that of an HPGe count. However, $LaCl_3$ operates at much higher count rates than HPGe, which may result in its utility in high count-rate measurement
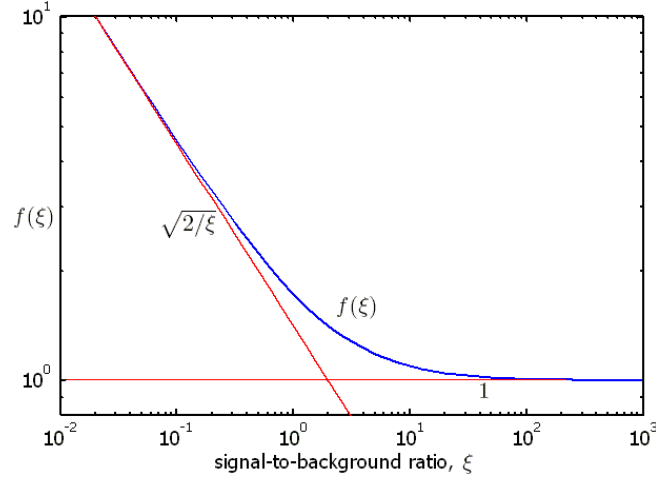
Figure 2.51 The relative increase in the fractional uncertainty of a measurement, $f(\xi)$ as a function of the signal-to-background ratio, ξ along with the functions (red) that describe $f(\xi)$ as $\xi \to 0$ and $\xi \to \inf$.

scenarios.

2.13   Photon Scattering Physics Implications

For very low energy photons, interaction with matter is dominated by the processes of Rayleigh scatter and photoelectric absorption, resulting in nearly isotropically scattered photons. As photon energies increase toward the pair production threshold, incoherent scatter becomes the most probable interaction mechanism, and Rayleigh scatter becomes more forwards-directed. Above the pair production threshold, pair production becomes increasingly important, as do photonuclear reactions. The processes that can produce large-angle scattered photons are coherent and incoherent scatter, pair production, bremsstrahlung emission by photoelectrons, and photonuclear reactions such as photon-induced neutron emission. Coherent scatter strongly favors forwards-directed scattering, but large angle events can occur. Incoherent scatter also favors forwards-directed scattering, photoelectrons emitted due to photoelectric absorption or incoherent scatter are predominantly forwards-directed, and the bremsstrahlung emitted during electron slowing also tends to be forwards-directed. γ-rays emitted by nuclear resonance fluorescence are either isotropic or nearly so, which implies that the measurement of NRF γ-rays is best accomplished by measuring the scattered photon intensity at large angles, relative to the interrogating beam.

Energetically, it is easiest to detect NRF γ-rays if the energy of the photon beam does not extend significantly beyond the energy of the resonances. Photons produced at large angles due to incoherent scatter are low energy, and the intensity of brems-

strahlung decreases approximately exponentially with energy. The pair production cross section increases with energy, resulting in more isotropically-emitted 511-keV photons as beam energy increases. These photons may not directly interfere with detection of high-energy NRF γ-rays, but they will produce a significant portion of the overall count rate registered by a radiation detector, which will in turn limit the intensity of the source photon beam that may be used.

While γ-rays emitted due to fluorescence of low-energy states may be difficult to identify because of the relatively large non-resonant photon back-scatter cross section, measurement of high-energy states also presents difficulties. Photoneutron emission threshold energies are as low as 1.67 and 2.22 MeV for ^{9}Be and ^{2}H, respectively, many isotopes have $\sim$8 MeV thresholds, and ^{73}Ge has a 6.78 MeV threshold. This threshold energy indicates that HPGe detectors become a neutron source when subjected to large intensities of photons above this energy. Neutrons thermalize and are subsequently captured, producing additional γ-rays that add to the background. Finally, with increasing energies, the giant dipole resonance increases elastic scatter cross sections and the density of nuclear states that can undergo resonance fluorescence increases. This begins to limit the isotopic-specificity that measurement of a γ-ray near a resonant energy can provide, since they may be attributed to more than one resonance. For these reasons, we consider the energy range between 1.5 and 5 MeV to be preferred for measurement of NRF as a non-destructive assay signature.

Chapter 3

Model Approaches to Nuclear Resonance Fluorescence Assay

In this chapter the development and use of models to predict expected nuclear resonance fluorescence detection rates for non-destructive materials assay studies are discussed. These models assume that NRF is detected by a single radiation detector, and that use of multiple detectors would proportionally increase the calculated count rates. The two assay methods considered here are termed *backscatter* and *transmission* assay. They differ in how photons undergoing NRF in the assay target are observed. Both assay methods use a photon source to induce NRF in the target material. In backscatter assay, a radiation detector is positioned at backwards angles relative to the incident photon beam trajectory. Transmission assay uses a detection system down-stream of the assay target to measure the excess attenuation of resonant-energy photons in the target. Both methods have advantages and disadvantages; they will be discussed in the following sections along with examples of measurements that have been modeled by a combination of computational and analytical methods.

3.1   Backscatter NRF Assay

A schematic drawing of a backscatter NRF assay geometry is shown in Figure 3.1. A source of energetic photons illuminates the target material and one or more radiation detectors measure the photon flux backscattered from the target. Section 2.12 indicates that improved detector energy resolution increases the statistical value of registered NRF counts. Because of this, high-purity germanium detectors (HPGe) are most commonly used for NRF experiments. The photon flux at the detector, $\Phi(\mathbf{r}), E)$ (which is proportional to the measured count rate) can be written as,

$$\Phi(\mathbf{r}, E) = \Phi_{\text{target}}(\mathbf{r}, E) + \Phi_{\text{radioactivity}}(\mathbf{r}, E) + \Phi_{\text{beam}}(\mathbf{r}, E) \tag{3.1}$$
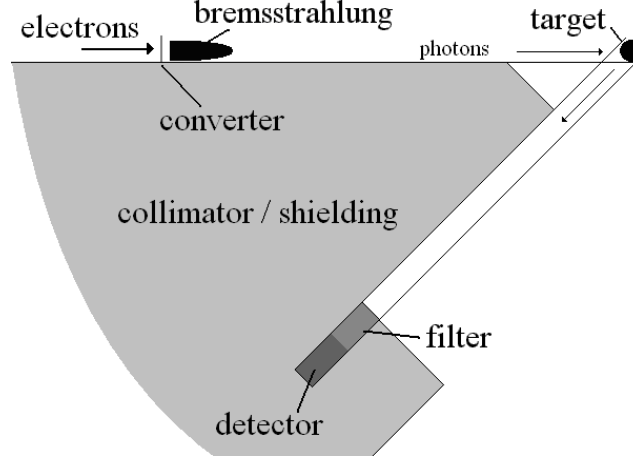
Figure 3.1 Schematic drawing of a bremsstrahlung-induced backscatter NRF assay setup. Lines indicating collimator acceptance have been extended to assay target region.

where $\Phi_{\text{target}}(\mathbf{r}, E)$ is the flux due to interrogating photons that were scattered toward the detector after interacting in the assay target, which includes the contribution due to NRF. $\Phi_{\text{radioactivity}}(\mathbf{r}, E)$ is due to photons that were emitted due to radioactive decay of materials within the interrogation geometry, and $\Phi_{\text{beam}}(\mathbf{r}, E)$ is due to interrogating beam photons that have reached the detector without interacting within the target material. The photons contributing to Phi_{beam} generally penetrate large quantities of shielding and will be discussed along with bremsstrahlung beam shielding requirements in Section 3.1.2.

Figure 3.1 illustrates several design features of a backscatter NRF assay system. First, the radiation detectors are generally positioned at a scattering angle of $\geq 90º$ to take advantage of the decreasing intensity of non-resonantly backscattered radiation discussed in Chapter 2. Second, the interrogating photon beam is shown to be bremsstrahlung. A nearly monoenergetic interrogating photon spectrum would have advantages, but such sources do not appear to be currently practical[1]. A third feature is the shielding directly between the detector and the target, labeled as 'filter'. The purpose of the filter is to shield the detector from the low-energy portions of $\Phi_{\text{target}}(\mathbf{r}, E)$ and $\Phi_{\text{radioactivity}}(\mathbf{r}, E)$. Filters may consist of up to ~ 200 g/cm^2 of high-Z material, depending on photon beam characteristics and detector count rate limitations. They are application-specific and will be discussed in specific assay examples in Sections 3.1.3 and 3.1.4.

---

[1]References(100),(101),(102),(103),(104), and(105) describe quasi-monoenergetic photon sources that are in use or under development. Cost and low photon intensities tend to be the short-comings of these technologies. The potential to develop compact high-gradient electron accelerators(106) provides further hope that such sources may become practical

3.1.1   NRF Count Rates in Backscatter Assay

For the contributions to $\Phi_{\text{target}}(\mathbf{r}, E)$, we consider the effects of resonant and non-resonant scattering separately. Resonant scattering produces NRF signals, whereas non-resonant scattering produces only background.

The rate at which NRF signals due to photons of energy, E, are detected by a radiation detector from a location, $\mathbf{r}$, within the target volume, V, is given by:

$$\frac{d^2 R_{\text{NRF}}}{dV\,dE} = N\Phi(E, \mathbf{r})\sigma_{\text{NRF}}(E)W_e(\theta)\exp[-\mu(E_\gamma)r_o]\left[\epsilon(E_\gamma)\frac{\Omega(\mathbf{r})}{4\pi}P_f(E_\gamma)\right] \qquad (3.2)$$

Where N is the number density of atoms in the target that undergo NRF with cross section $\sigma_{\text{NRF}}(E)$, $\Phi(E, \mathbf{r})$ is the energy-differentiated photon flux at the point $\mathbf{r}$, $W_e(\theta)$ is the effective angular correlation function taking into account the finite solid angle of the detector, E_γ is the energy of the emitted NRF γ-ray, which interacts within the target material with an attenuation coefficient, $\mu(E_\gamma)$ that results in a total attenuation of the NRF γ-ray of $\exp[-\mu(E_\gamma)r_o]$, $\epsilon(E_\gamma)$ is the probability that the radiation detector measures the full energy of the NRF γ-ray, $\frac{\Omega(\mathbf{r})}{4\pi}$ is the fraction of the solid angle subtended by the radiation detector from the point where the γ-ray is emitted, and $P_f(E_\gamma)$ is the probability that the NRF γ-ray penetrates through the radiation filter un-attenuated.

NRF γ-ray emission corresponding to de-excitation to the nuclear ground state occurs with a probability Γ_0/Γ. Likewise emission to a different excited state, labeled i would occur with a probability Γ_i/Γ. The resulting γ-ray energy is $E_\gamma = E - E_{\text{recoil}}$ where E_{recoil} is given by equation 2.102. Generally, the energy taken by the recoiling nucleus is sufficient to reduce the energy of the NRF γ-ray such that it is no longer resonant. Because of this energy shift, attenuation of NRF γ-rays is only due to nonresonant interactions.

Slab Geometry

The simplest geometry to consider is a slab target of thickness, t, irradiated with a uniform parallel beam of intensity, Φ_i, that is normally incident upon the slab. A radiation detector is assumed to be located sufficiently far from the target that the beam diameter and t are negligibly small compared to the detector distance, r_d. A schematic rendering of this geometry is shown in Figure 3.2. Although not indicated, the detector geometry may include a filter that NRF-energy photons have a probability, $P_f(E_\gamma)$, to penetrate without being attenuated.

For simplicity, we assume the photon flux is not a function of energy and that we may neglect photon down-scatter. Then $\Phi(E, \mathbf{r})$ only varies due to the attenuation of photons:

$$\Phi(E, x) = \Phi_i \exp[-\mu(E)x] \qquad (3.3)$$

and $\mu(E)$ now contains both resonant and non-resonant contributions:

$$\mu(E) = \mu_{nr} + N\sigma_{\text{NRF}}(E) \qquad (3.4)$$
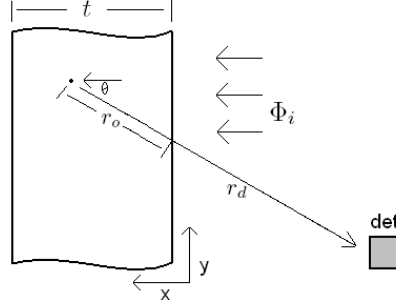
Figure 3.2 Schematic drawing of an NRF interrogation of a target slab.

Considering only photon energies near an NRF resonance, we may neglect the energy-dependence of the non-resonant attenuation coefficient, μ_{nr}. Likewise, the attenuation coefficient for NRF γ-rays, $\mu(E_\gamma) = \mu_{nr}$, because recoil has made them non-resonant.

   The length the photon must traverse to leave the target is given by $r_o = x/cos(\theta)$, where θ is the angle between the interrogating photon trajectory and the direction of the detector's location. The detector's surface area is assumed to be given by A.

   Substituting, the rate of detection of full-energy NRF γ-rays can be written as:

$$\frac{d^2 R_{\mathrm{NRF}}}{dx dE} \approx \exp\left[-\left(\mu_{nr}[1 + 1/cos(\theta)] + N\sigma_{\mathrm{NRF}}(E)\right)x\right] N\Phi_i \sigma_{\mathrm{NRF}}(E) W_e(\theta) \frac{A\epsilon P_f E_\gamma}{4\pi r_d^2}$$
$$(3.5)$$

   We define

$$\alpha = \mu_{nr}[1 + 1/\cos(\theta)] \qquad (3.6)$$

and $\mu_{\mathrm{NRF}}(E) = N\sigma_{\mathrm{NRF}}(E)$ and obtain:

$$\frac{dR_{\mathrm{NRF}}}{dE} = \int_0^t \frac{d^2 R_{\mathrm{NRF}}}{dx dE} dx \approx \frac{1 - \exp[-(\alpha + \mu_{\mathrm{NRF}}(E))t]}{\alpha + \mu_{\mathrm{NRF}}(E)} N\Phi_i \sigma_{\mathrm{NRF}}(E) W_e(\theta) \frac{A\epsilon P_f E_\gamma}{4\pi r_d^2}$$
$$(3.7)$$

   If we further approximate that

$$\sigma_{\mathrm{NRF}}(E) \approx \begin{cases} 0, & \text{if } E < E_C - \Gamma_D/2; \\ \sigma_{\mathrm{NRF}}^C, & \text{if } E_C - \Gamma_D/2 \le E \le E_C + \Gamma_D/2; \\ 0, & \text{if } E > E_C + \Gamma_D/2. \end{cases} \qquad (3.8)$$

where

$$\sigma_{\mathrm{NRF}}^C = \frac{\int \sigma_{\mathrm{NRF}}(E) dE}{\Gamma_D} \qquad (3.9)$$

E_C is the centroid energy of the resonance, and Γ_D is given by equation 2.97. We may integrate equation 3.7 to obtain:

$$R_{\mathrm{NRF}} \approx \frac{1 - \exp[-(\alpha + N\sigma_{\mathrm{NRF}}^C)t]}{\alpha + N\sigma_{\mathrm{NRF}}^C}[N\Phi_i\sigma_{\mathrm{NRF}}^C]\frac{W_e(\theta)A\epsilon P_f E_\gamma}{4\pi r_d^2} \qquad (3.10)$$

Equation 3.10 is arranged such that the expected rate at which NRF γ-rays are detected is divided into contributions due to three phenomena, the first term is due to the effective geometric attenuation of photons before and after NRF, the second term, $N\Phi_i\sigma_{\mathrm{NRF}}^C$ is the rate (per unit thickness) at which NRF would occur in the target without any attenuation, and the final term is due to the probability of detection of NRF γ-rays emitted from the target.

The assumption that the target is an infinite slab geometry, indicates that as $\theta \to 90^\circ$, $\alpha \to \infty$ due to the increasing amount of material NRF γ-rays would need to traverse to leave the target.

For thin targets, $\exp[-(\alpha + N\sigma_{\mathrm{NRF}}^C)t] \approx 1 - (\alpha + N\sigma_{\mathrm{NRF}}^C)t$ and equation 3.10 becomes

$$R_{\mathrm{NRF}} \approx tN\Phi_i\sigma_{\mathrm{NRF}}^C\frac{W_e(\theta)A\epsilon}{4\pi r_d^2} \qquad (3.11)$$

which is identical to the result for no photon attenuation within the target.

Although the constant cross section approximation of equation 3.8 will prove to be very flawed in analysis of transmission assay, the assumption that the solid angle subtended by the detector is independent of the interaction location within the target proves to be a largest approximation in many backscatter NRF assay geometries.

Finite Element Treatment of Target Geometry

The effective geometric attenuation can be easily computed for more complicated geometries using a finite element method. Returning to equation 3.2, and assuming that photon down-scatter can be neglected, we observe that $\Phi(E, \mathbf{r})$ is given by a combination of beam divergence and exponential attenuation of the incident flux over the length a photon must travel before interaction at the finite element point, r_i. Therefore, we find

$$\Phi(E, \mathbf{r}) \approx \Phi_i(E)\exp[-\mu(E)r_i]\left[\frac{d_s}{d_s + r_i}\right]^2 \qquad (3.12)$$

where d_s is the distance between the photon source and the front of the target. The quantity $[d_s/(d_s + r_i)]^2$ represents the divergence of the interrogating beam. The dimension r_o and r_d are easily determined for each finite element point. For an element grid point (i, j, k), values of r_i, r_o, θ, and r_d are calculated and substituted into the geometric attenuation expression to obtain an energy-differentiated NRF

γ-ray count rate:

$$\frac{dR}{dE} = \sum_i \sum_j \sum_k N\sigma_{\text{NRF}}(E)\Phi_i(E)P_f(E)A\epsilon(E)\exp[-\mu(E)r_i^{i,j,k}]\exp[-\mu_{nr}r_o^{i,j,k}]$$

$$\left(\frac{d_s}{d_s + r_i^{i,j,k}}\right)^2 W(\theta^{i,j,k})\frac{f^{i,j,k}}{4\pi(r_d^{i,j,k})^2}\Delta^i\Delta^j\Delta^k \quad (3.13)$$

where Δ^i, Δ^j and Δ^k refer to spatial dimensions of each finite element and $f^{i,j,k}$ indicates the volume fraction of the element that is contained within the target object. When a constant cross section approximation is assumed, and $P_f(E)$ and $\epsilon(E)$ are evaluated at the resonance energy, we obtain

$$R = \sum_i \sum_j \sum_k N\sigma_{\text{NRF}}^C\Gamma_D\Phi_iP_fA\epsilon\exp[-N\sigma_{\text{NRF}}^C r_i^{i,j,k}]\exp[-\mu_{nr}(r_i^{i,j,k} + r_o^{i,j,k})]$$

$$\left(\frac{d_s}{d_s + r_i^{i,j,k}}\right)^2 W(\theta^{i,j,k})\frac{f^{i,j,k}}{4\pi(r_d^{i,j,k})^2}\Delta^i\Delta^j\Delta^k$$

$$(3.14)$$

$$\equiv N\sigma_{\text{NRF}}^C\Gamma_D\Phi_iA\epsilon \times G \quad (3.15)$$

where G includes the sum of the products of all terms that contain a parameter that varies with between finite elements.

An example of the geometric correction, G as a function of spatial coordinate is shown in Figure 3.3. In this example, we assume that a 1 cm-radius sphere of UO$_2$ is irradiated by a uniform beam of photons incident along the x-axis. The ^{235}U abundance of the uranium is assumed to be 0.05 and the energy of the photon beam is assumed to be that of the centroid of the 1.733-MeV resonance in ^{235}U, which has an effective natural width, $g\Gamma_0 = 34$ meV. The detector is positioned in the x-y plane, 30 cm from the center of the sphere and at an angle of $\theta = 135°$, relative to the interrogating beam direction. The calculation was performed for one half of the z-dimension coordinates because of symmetry. The sphere was divided into a 30 x 30 x 15 grid, and the values plotted are the grid-point-dependent quantities of equation 3.14 for the plane $i = 15$, assuming $P_f = 1$, and $W(\theta) = 1$. The $f^{i,j,k}$ were assumed to be unity if the center of the corresponding finite element was within the sphere, and zero otherwise. The summed geometric factor is $G = 0.0579$ cm, yielding an expression for the expected NRF count rate of 0.0579 cm $\times N\sigma_{\text{NRF}}^C\Gamma_D\Phi_iA\epsilon$. This NRF γ-ray detection rate is the same as would be expected from irradiation of 1 cm^2 of a 0.0579 cm-thick pure ^{235}U slab, neglecting photon attenuation in the target. It is also 0.276 times the rate that would be estimated if attenuation due to non-resonant interactions in the target sphere were ignored.
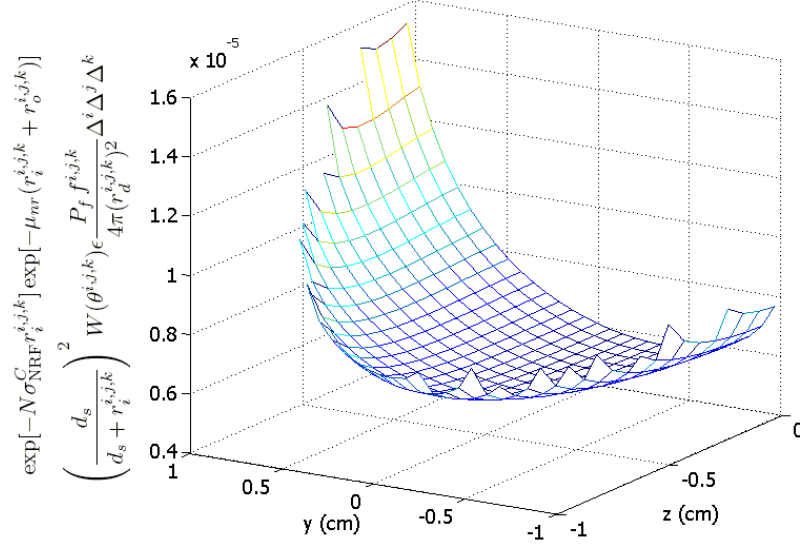
Figure 3.3 Grid-point dependent quantities, $G^{i,j,k}$ of equation 3.14 for $i = 15$. See text for details.

3.1.2   Background Contributions

γ-ray interactions counted by radiation detectors that are not due to NRF are considered background. These events may be due to scatter of the interrogating photon beam or radioactive decay of material in the assay geometry. It is also important to differentiate between background events at and near resonant energies and those at other energies.

Active Background Contributions – Interrogation Photons Scattered in Target

Detected background photons due to the interrogating beam may either directly reach the detector or do so via scattering in the assay geometry. The physical processes that result into photons being emitted in backwards angles relative to the incident photon direction have been discussed in Chapter 2. To summarize, incoherent scattering produces only low-energy backscattered photons and pair production results in 511 keV photons in all directions. Coherent scattering produces energetic photons, and while the coherent scattering processes are predominantly forward-directed, they do result in some energetic backscattered radiation. Similarly, multi-step processes such as multiple incoherent scattering events or bremsstrahlung emission from energetic photoelectrons can result in energetic backscattered radiation.

Spectra calculated with MCNPX provide significant information about the intensity and energy-dependence of the photon flux near radiation detectors that results from interrogating beam interactions in the assay target. Example spectra

(where photon intensities have been converted to effective differential cross sections) are presented for incident monoenergetic beams in Figures 2.24 and C.3. However, MCNPX does not include photonuclear elastic scattering processes and therefore, photon intensities due to these processes must also be added. In order to include these processes in a simple manner, the updated Rayleigh scattering form factor arrays discussed in Appendix A were not used in MCNPX calculations. Instead, intensities due to all elastic scattering processes were separately calculated and added to the simulation results.

As a first example, we consider the assay of a 1.75 cm-radius sphere of $CsCl_2/Ba$ mixture with an assumed stoichiometry of Cs:Ba:2Cl, and density of 2 g/cm^3, encased in a 3 mm-thick 316L stainless steel shell (107). This target geometry approximates a 1-kCi ^{137}Cs industrial irradiator source circa 1970[2](108),(109). A beam of 4-MeV electrons incident upon a 7.5 mm-thick slab of tungsten was used to model a bremsstrahlung source. The tungsten converter was located 60 cm from the target. The bremsstrahlung beam was heavily shielded except for a collimator opening with a radius of 1.75 cm. The fluence of photons scattering toward a detector located at an angle of 120° from the initial electron direction and a distance of 30 cm from the target center was simulated.

To estimate the coherent scattering contribution to the photon fluence, the finite element approach described by equation 3.13 was used with slight modifications. First, the value of $\sigma_{NRF}^C \Gamma_D$ preceding the exponents was replaced with the angle-differentiated coherent scattering cross section, $d\sigma_{Coh}/d\Omega$, shown for Ba in Figure 2.37. The value of σ_{NRF}^C in the exponent was taken as zero because there is no additional attenuation due to resonant-energy photons. The term, $W(\theta)$ was omitted because the angular dependence of the scattered photons has been accounted by including $\frac{d\sigma_{coh}}{d\Omega}$ instead of the total cross section for scattering. Finally, an additional attenuation factor due to penetration through the stainless steel shell was also included in the calculation. These changes lead to the following expression for the coherently scattered photon flux:

$$\frac{d\Phi}{dE} = N \frac{d\sigma_{coh}}{d\Omega}(E)\Phi_i(E)P_f(E) \sum_i \sum_j \sum_k \exp[-\mu_{steel}(E)r_{shell}^{i,j,k}]$$

$$\exp[-\mu_{nr}(r_i^{i,j,k} + r_o^{i,j,k})] \left(\frac{d_s}{d_s + r_i^{i,j,k}}\right)^2 \frac{f^{i,j,k}}{(r_d^{i,j,k})^2} \Delta^i \Delta^j \Delta^k \quad (3.16)$$

where $\mu_{steel}(E)$ is the energy-dependent attenuation coefficient of the stainless steel and $r_{shell}^{i,j,k}$ corresponds to the combined distances through the spherical steel shell a photon must pass to reach the finite element grid point, and after scattering to leave the target in the direction of the detector location (r_{shell} is analogous to $r_i + r_o$ in equation 3.14).

---

[2]Newer radiological sources tend to have the radio-isotope dissolved in boro-silicate glass(110)
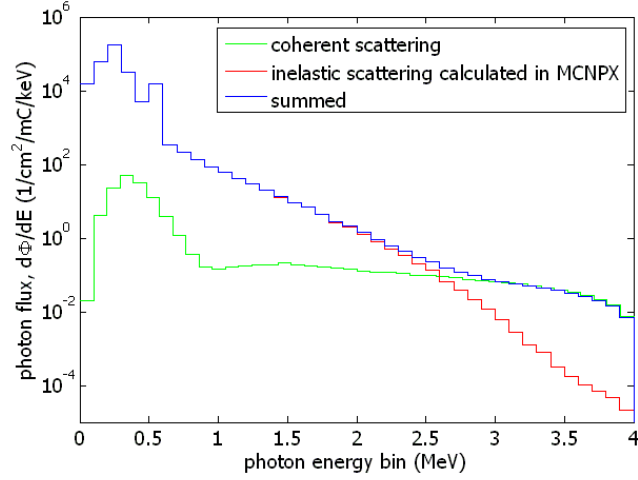
Figure 3.4 Calculated backscattered photon flux for assay of a 1-kCi Cs irradiator at a position un-shielded from the assay target, 30 cm from the target center, at 120º relative to initial electron beam direction. The flux is normalized per mC of 4-MeV electrons incident upon bremsstrahlung converter.

Equation 3.16 was evaluated for the 1-kCi ^{137}Cs target geometry at energies between 100 keV and 4 MeV in 100 keV intervals, using the MCNPX-calculated bremsstrahlung beam intensity and assuming that $P_f(E) = 1$. The intensity of this beam as well as the backscattered photon flux spectrum were both normalized per mC of electron beam current incident upon the bremsstrahlung converter and are shown along with their summed spectrum in Figure 3.4. For this geometry, the coherently scattered photons represent a significant contribution to the energy-differentiated flux for energies above 2.2 MeV and are the most important contributor of photons above 2.5 MeV.

A second example, the backscattered photon intensity was calculated for a 5 mm-diameter UO$_2$ cylinder. This geometry represents a simplified fuel pin. For this case the interrogating radiation was generated with 2-MeV electrons incident upon a 102-μm Au foil on a 1 cm-thick Cu backing. The resulting bremsstrahlung emanating from a 5 mm-diameter cylindrical hole in the shielding irradiated the UO$_2$ cylinder 60 cm downstream. The resulting backscattered fluence was calculated 60 cm from the target in a viewing window located at an angle of 120º relative to the direction of the electron beam and is shown in Figure 3.5. Compared to Figure 3.4, coherently scattered photons are an even more important contribution to the backscattered photon intensity.

The total fluences for the spectra shown in Figures 3.4 and 3.5 are approximately 3×10^7 and 1.6×10^5 photons/cm^2/s, respectively. Given that the front surface area of a large HPGe detector is ~ 60 cm^2, and that photons with energies below 4 MeV, when incident upon the front face of such a detector will have a large probability to interact with it, these fluences would result in exceedingly high detector signal rates.
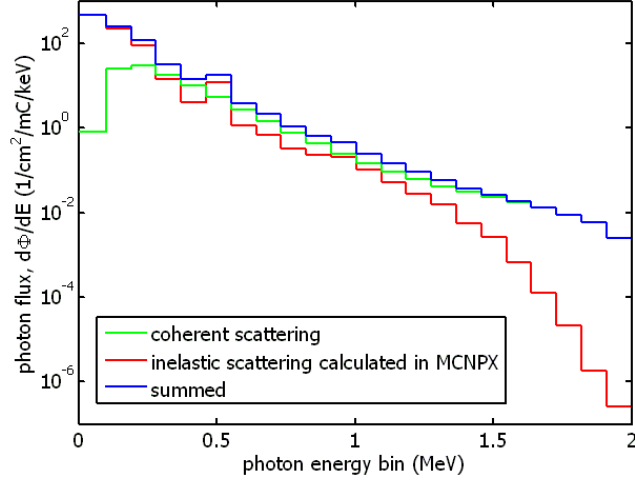
Figure 3.5 Calculated backscattered photon flux for assay of a UO$_2$ cylinder of 5 mm-diameter at a position un-shielded from the assay target, 60 cm from the target, at 120º relative to initial electron beam direction. The flux is normalized per mC of 2-MeV electrons incident upon bremsstrahlung converter.

This effect can be mitigated by the addition of a filter, as discussed in Section 3.1.3.

Active Background Contributions – Direct Detection of Interrogation Photons

To reduce direct detection of interrogation photons, large quantities of shielding are generally placed between the photon source and the radiation detectors. High-Z materials such as tungsten and lead have high densities and relative to lower-Z materials, have larger pair production and photoelectric absorption cross sections, compared to their incoherent scattering cross sections. However, incoherent scattering is still frequently the dominant process for multi-MeV photons. Incoherent scattering tends to produce forward-scattered photons with energies near the un-scattered photon energy, which implies that incoherent scatter is a relatively ineffective process for shielding, relative to other photon interactions. Therefore, simple exponential attenuation using the total interaction cross section, can significantly underestimate the transmitted photon flux.

Using the methods described in Section C.2, MCNPX simulations were performed to determine the transmission of bremsstrahlung-spectrum photons through large quantities of shielding. The simulated geometry was assumed to be a slab of tungsten whose thickness was varied between simulations. The photon spectrum incident upon the shielding slab was taken from a the results of a previous MCNPX simulation in which 2.5-MeV electrons irradiated a 1 mm-thick sheet of uranium. Photons emitted from the uranium converter within a bin of 40º − 50º from the initial electron trajectory were used as the photon source for the shielding penetration
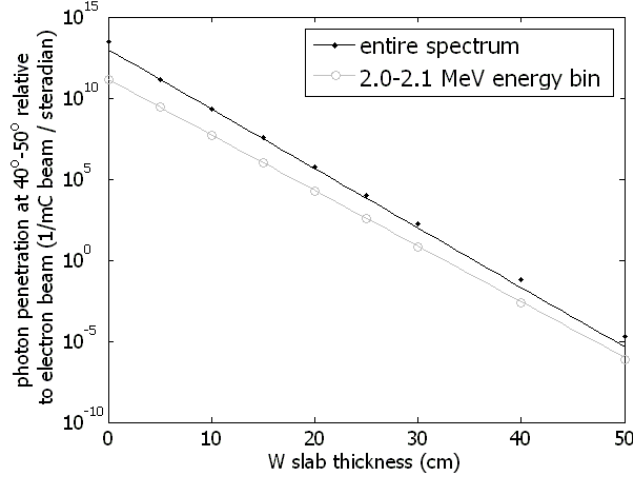
Figure 3.6 MCNPX-calculated photon intensities transmitted through a tungsten slab of varying thickness. The open and closed circles indicate calculation results and the solid line indicates exponential fits to the calculated results. The photon spectrum incident upon the shield is that of the $40°-50°$ angular bin bremsstrahlung beam created by impinging 2.5-MeV electrons upon a 1 mm-thick slab of uranium. Statistical errors are not shown, but the largest error fraction is 5.3% of the calculated value for the 2 - 2.1 MeV bin penetrating through 40 cm of tungsten.

simulation. Of interest are both total photon intensities and the intensity of photons with near-resonant energies that would provide background to observing NRF γ-rays. Figure 3.6 presents intensities of photons after the bremsstrahlung-spectrum photons penetrate through tungsten shielding. As an example of near-resonant photons, the photon intensity for energies between 2 and 2.1 MeV is shown along with the full energy-integrated spectrum. The spectra have been normalized to number of photons per steradian per mC of electron charge incident upon the bremsstrahlung converter.

The rates at which 2 - 2.1 MeV photons and the entire spectrum are attenuated both appear to follow exponential forms for thicker shields. Linear least-squares routines were applied to the logarithms of the attenuation values, yielding a function of the form $(I/I_0)_{\text{fit}} = a \exp(-bx)$. The results of these routines are shown in Table 3.1. When fitting the attenuation of the entire spectrum, the least-squares fitting routine was only applied to simulated values of photon transmission for W shielding thicknesses greater than 5 cm. The fits are compared to the calculated attenuations in Figure 3.7, where values of $\frac{(I/I_0)_{\text{MCNPX}} - (I/I_0)_{\text{fit}}}{(I/I_0)_{\text{MCNPX}}}$ are plotted versus tungsten slab thicknesses.

In an ideal NRF geometry, the bremsstrahlung flux intensity, $d\Phi/dE$, incident upon a detector that has penetrated the bremsstrahlung shielding is significantly lower than that due to NRF. Likewise, the energy-integrated flux must be sufficiently small to permit detector operation at low dead-time.

energy range	a	b (cm^{-1})
entire spectrum	$0.3275 \pm 6.4 \times 10^{-4}$	0.845 ± 0.0004
2 - 2.1 MeV	$4.737 \times 10^{-3} \pm 4 \times 10^{-8}$	0.7898 ± 0.0001

Table 3.1 Fit parameters for representing bremsstrahlung-spectrum photon intensities as $(I/I_0)_{\text{fit}} = a \exp(-bx)$ after attenuation through a thickness, x of shielding.
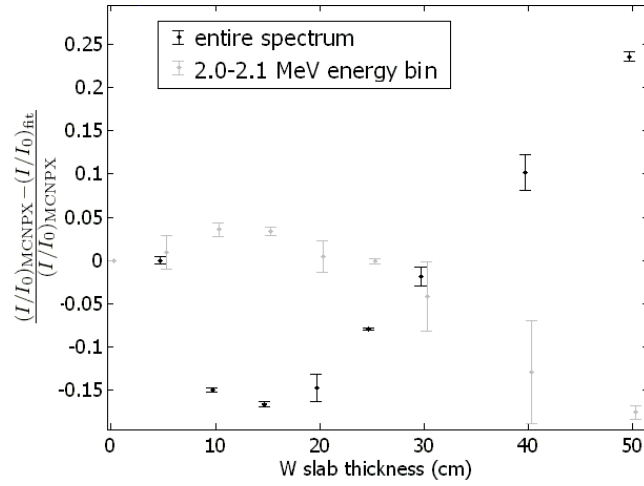
Figure 3.7 Fractional deviation between the calculated values of the transmitted photon intensity and those estimated by a linear least-squares fitting-routine. The error bars indicate $\pm 1\sigma$ errors from the MCNPX computation. The *entire spectrum* value is not shown for zero slab thickness, it is 0.72.

Radioactive Background Contributions

γ-rays due to radioactive decay of isotopes within the assay geometry are an additional source of background for NRF assay counting. Lead is contaminated with nuclides from primordial sources, including the ^{238}U and ^{232}Th decay chains. The radioactive decay of ^{208}Tl, present in the ^{232}Th decay chain, produces a 2.615-MeV γ-ray that is the highest-energy γ-ray from terrestrial sources, although cosmically-induced photons and charged particles will contribute higher energy radiations that must also be considered. The low-background facility at Lawrence Berkeley National Laboratory has lead-shielded germanium detectors that detect approximately 5×10^{-4} full-energy 2.615-MeV γ-rays per second, which corresponds to a 2.615-MeV γ-ray flux of $\sim 1 \times 10^{-4}$ cm^{-2}s^{-1}. This represents probably the lowest rate that can be expected from this source due to the fact that the lead and concrete shielding at the facility were selected for their low activity.

Additionally, targets for NRF-based assay measurements may contain significant quantities of radioactive materials. In the examples considered here, the targets are highly radioactive. When employing a transmission-based assay method, where radiation detectors are oriented to measure backscattered photons from a transmission detector (TD) foil, the TD itself may contain radioactive materials. In the experimental measurements summarized in Chapter 4, the 2.615-MeV γ-ray detection rate was 100 times that at the LBF. When a 1/2" lead filter was placed between the TD and the detectors, the 2.615 MeV count rate dropped proportionally to the expected attenuation of 2.615 MeV γ-rays through lead, indicating that the high count rate was due to radioactivity beyond the lead shielding (presumably the TD), rather than within the lead itself.

Filter thickness and target radioactivity are the design constraints that are first addressed in the following examples of the backscatter assay method.

3.1.3   NRF Assay of Radiological Sources

The motivation for assaying radioisotopes is simple. The possible use of large radioactive sources in radiation dispersal devices is of considerable national and international concern(109)(112). Of particular interest are the longer-lived fission product isotopes ^{90}Sr and ^{137}Cs that exist in sources whose activities can exceed 10^4 Ci. The age of such sources, i.e. the time since discharge of a sample from a reactor or the time since chemical isolation of a radioisotope from the fission products, have been identified as important parameters for forensic purposes, especially if other identifying characteristics are missing or uncertain(113). Sources used in the public and private domains may be as old as 60 y.

Although age-dating can, in principle, be accomplished with high precision and accuracy by careful use of radiochemical and mass spectrometric methodologies, there are significant shortcomings in practice. Of primary importance is that essentially all quantitative radiochemical methods require wet chemical manipulations on

Fission Product	Cumulative Fission Yield (%)						
	^{233}U Thermal	^{233}U Fast	^{235}U Thermal	^{235}U Fast	^{238}U Fast	^{239}Pu Thermal	^{239}Pu Fast
^{133}Cs	5.95	6.04	6.70	6.72	6.76	7.02	6.58
^{135}Cs	6.27	6.42	6.54	6.60	6.97	7.62	7.55
^{137}Cs	6.75	6.75	6.19	6.22	6.05	6.61	6.97
^{90}Sr	6.79	6.39	5.78	5.47	3.25	2.10	2.05
^{89}Sr	6.34	5.75	4.73	4.37	2.76	1.72	1.76
^{88}Sr	5.47	5.07	3.58	3.49	2.03	1.33	1.33

Table 3.2 Cumulative fission yield for common radiological sources as well as other isotopes produced in significant quantities via fission. Data are from reference (114), 'Thermal' indicates fission was induced by thermal spectrum neutrons and 'Fast' that fission was induced by a spectrum of neutrons from a fast pool reactor.

a representative sample of the entire source, and thus, the source must be opened and processed. For sources that have decayed for a time greater than one half-life, stoichiometric changes coupled with thermal effects can cause significant segregation of elements, making isolation of a representative sample difficult absent dissolution and homogenization of the entire source. For example, a ^{137}Cs source will undergo the following chemical process:

$$^{137}\text{CsCl} \rightarrow ^{137}\text{BaCl} \rightarrow \frac{1}{2} \, ^{137}\text{BaCl}_2 + \text{Ba} \tag{3.17}$$
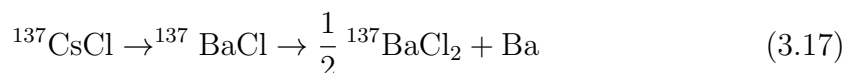
BaCl is chemically unstable, and CsCl and $BaCl_2$ are mutually insoluble. This provides the chemical potential for segregation.

While dissolution and homogenization of an entire radiological source is straightforward for small sources, sampling of more than 10^2 Ci in such a manner is a daunting task. Second, there are only few facilities that can handle such large sources and the disposal of the predominant bulk of the radioactivity from an opened source and decontamination of equipment are both difficult and expensive.

Radiological sources come in a variety of forms. ^{137}Cs and ^{90}Sr sources are produced by chemically separating Cs and Sr produced through fission from the other fission products and actinides. Chain yields of isotopes commonly found in radiological sources obtained from fission products are shown in Table 3.2.

Isotopic ratios are normally measured by chemically separating the elements of interest (such as Cs and Ba), and performing mass spectrometry to determine the relative concentrations of the Cs and Ba isotopes. When the initial isotopic content of the radiological source is known (or inferred), the ratio of the quantity of the radioactive isotope to its stable daughter is used to determine the time period over

which the stable daughter has been produced by radioactive decay[3].

In principle, relative concentration measurements can be accomplished by measuring the rate at which each isotope undergoes NRF. However, NRF has not yet been measured in isotopes of ^{137}Cs or ^{90}Sr. This is due to the fact that performing measurements on gram-quantities of these isotopes is a difficult undertaking because of the associated radioactivity. Regardless, by measuring the radioactivity of the parent isotope in a well-calibrated counting geometry, the activity (and therefore number) of parent isotopes in the sample should be measured with an uncertainty $\leq 3\%$. Therefore, it is the number of stable daughter atoms that must be measured in order to non-destructively and non-intrusively age-date a radiological sample.

Radiological Source Shielding

In the discussion that follows, we present the possible signal rates and expected measurement precision for the assay of a spherical ^{137}Cs radiological sources in CsCl chemical form that have initial source activities ranging from 10 Ci to 10 kCi. It is assumed that the ^{137}Cs was obtained from chemically-separated fission product cesium from thermal fission of ^{235}U. Assuming this, we estimate the rate at which ^{137}Ba NRF γ-rays are measured, along with background count rates.

The physics that allows a relatively weak NRF response to be measured from a highly radioactive material is the fact that nuclear resonances can occur at higher energies than the γ-rays emitted due to radioactive decay of the source. The NRF γ-rays are therefore more penetrating, and subsequently are more likely be detected atop a background that remains very intense at lower energies, but is quite weak near resonance energies.

To enable a detector to function without significant pile-up, we assume that the rate limit for operation of large HPGe detectors is approximately 2×10^4 c s^{-1}. The NRF γ-rays and non-resonantly scattered bremsstrahlung radiation contributes to the detection rate, therefore we estimate that the detector must be sufficiently shielded such that the rate at which the detector responds due radiological source activity is below $\sim 10^4$ c s^{-1}. Assuming a detector with a sensitive surface area of 60 cm^2, this implies a photon flux of less than ~ 170 cm^{-2}s^{-1}. For HPGe detectors located 60 cm from the target center, the shielding necessary to achieve this flux is shown for varying source intensities in Table 3.3. The table also includes the expected attenuation through the corresponding shielding thickness of 3.761 MeV photons, which are produced by de-excitation of the largest ^{137}Ba resonance. To operate an HPGe detector 60 cm from a 1-kCi ^{137}Cs source, approximately 13.2 cm of Pb must surround the source, resulting in a decrease in photon flux of $\sim 2 \times 10^{-7}$. This amount shielding however, will only decrease the intensity of NRF γ-rays by 2×10^{-3}, indicating that the shielding has attenuated 661 keV γ-rays by a factor of 10^4 relative to the NRF γ-rays. That the shielding can attenuate radiological source

---

[3]See for example equation 3.21.

Source Activity (Ci)	Shield Thickness (cm)	# of Photons Leaving Shielding per 661 keV γ-ray	Fraction of NRF γ-rays Penetrating Shielding
25	10.2	8.15×10^{-6}	7.89×10^{-3}
75	11.05	2.72×10^{-6}	5.27×10^{-3}
350	12.4	5.82×10^{-7}	2.78×10^{-3}
1000	13.2	2.04×10^{-7}	1.90×10^{-3}

Table 3.3 Lead shielding requirements to operate a 60 cm^2 detector at 60 cm from a ^{137}Cs source at a count rate of 10^4 c s^{-1}. Calculated fractions of un-attenuated 3.761-MeV NRF γ-rays penetrating corresponding amounts of Pb are also shown.

photons while still allowing some penetration of energetic NRF γ-rays is the physical reason why this assay method is feasible.

Backscattered NRF Intensities

The rate at which the NRF signal is detected was derived via a modification of equation 3.14. The assay target includes a steel spherical shell, and therefore the effect of attenuation within this shell, analogous to that resulting in equation 3.16, was also applied. This results in the following expressions for NRF count rates, R_{NRF}.

$$R_{\mathrm{NRF}} = \sum_i \sum_j \sum_k N \sigma^C_{\mathrm{NRF}} \Gamma_D \Phi_i P_f A \epsilon \exp[-N \sigma^C_{\mathrm{NRF}} r_i^{i,j,k}] \exp[-\mu_{\mathrm{steel}}(E) r_{\mathrm{shell}}^{i,j,k}]$$

$$\exp[-\mu_{nr}(r_i^{i,j,k} + r_o^{i,j,k})] \left(\frac{d_s}{d_s + r_i^{i,j,k}} \right)^2 W(\theta^{i,j,k}) \frac{f^{i,j,k}}{4\pi (r_d^{i,j,k})^2} \Delta^i \Delta^j \Delta^k \tag{3.18}$$

The expected NRF γ-ray fluence is

$$\Phi = \frac{R_{\mathrm{NRF}}}{A \epsilon} \tag{3.19}$$

NRF count rates were estimated for the 3.761-MeV resonance of ^{137}Ba. This resonance has a measured value of $g\Gamma_0 = 61.6$ meV, corresponding to an integrated cross section of 33.5 eV·b(115). Applying equation 3.18, we calculate an unattenuated NRF photon fluence emanating from the interrogated target at a distance of 60 cm to be $\Phi_{\mathrm{NRF}} = 0.98$ photons/cm^2 per mC of 4-MeV electrons incident upon the bremsstrahlung converter. The energy of these photons is assumed uniform across the Doppler width of the resonance, $\Gamma_D = 3.97$ eV. An HPGe detector has an energy resolution $\Gamma_{\mathrm{det}} \approx 4$ keV at 3.7 MeV, and therefore we may multiply the calculated

non-resonantly scattered fluence (shown in Figure 3.4) by Γ_{det} to compare the intensity of an NRF signal to that of the background spectrum. This indicates that for a ^{137}Cs radiological source that has entirely decayed to ^{137}Ba, we would expect the fluence due to NRF to be ∼40 times as intense as that due to non-resonant scattering of interrogating photons.

Large amounts of shielding are necessary to reduce the source intensity at the detector location. The down-scatter and attenuation of both NRF and non-resonantly scattered photons in the shielding, as well as HPGe detector responses were considered through further MCNPX simulations, which are described in Section C.4. The shield thicknesses in front of the simulated detector are those indicated in Table 3.3.

The detector response simulations provided the energy deposited within the germanium crystal for each photon incident upon the modeled shielded detector system, resulting in pulse-height spectra for monoenergetic photons incident upon the system. Simulated pulse-height spectra for 3.761 and-4 MeV photons incident upon the shielded detector are shown in Figure 3.8 for 13.2 cm-thick Pb shield. The simulation for 3.761-MeV photons indicates that the expected full-energy peak efficiency of the shielded detector is $\epsilon \approx 3.1 \times 10^{-5}$. The pulse-height spectrum for 4-MeV photons is similar to that for 3.761-MeV photons, except that the annihilation photon escape peaks and the Compton edge are at higher energies. The Compton edge for a 4-MeV photon is 3.760 MeV, and the probability that a 4-MeV photon deposits 3.760 MeV ± 2 keV is $\approx 5.5 \times 10^{-7}$.

The probability of ∼3.761 MeV energy deposition events was computed for all higher-energy photons that resulted from 4-MeV electrons incident upon the bremsstrahlung converter, resulting in the expected number of 3.761-MeV depositions per unit electron beam intensity. This value is the contribution to the expected background due to higher-energy backscattered interrogating beam photons depositing less than their full energy into the HPGe detector.

The detector response to 4-MeV photons shown in Figure 3.8 indicates the importance of using a bremsstrahlung spectrum with an endpoint energy near that of the resonance energy to measure NRF transitions. Increasing the endpoint energy increases the intensity of non-resonantly backscattered photons. These can subsequently interact within the shielding or detector producing an increased background over which the NRF signal must be measured. Spectral features such as Compton edges, and single and double escape peaks are all important features that result in significant increase of background at their respective energies. If the endpoint energy is very much greater than the energy of the NRF transition, increasing the amount of shielding between the assay target and the detector also increases the probability for down-scattering of photons and results in ever-increasing background at the NRF energy. We shall see shortly however, that even when ∼13 cm of lead shielding is used, the effect of down-scattering in the shielding appears to contribute less to the background at NRF energies than the non-resonant backscatter of interrogation photons.
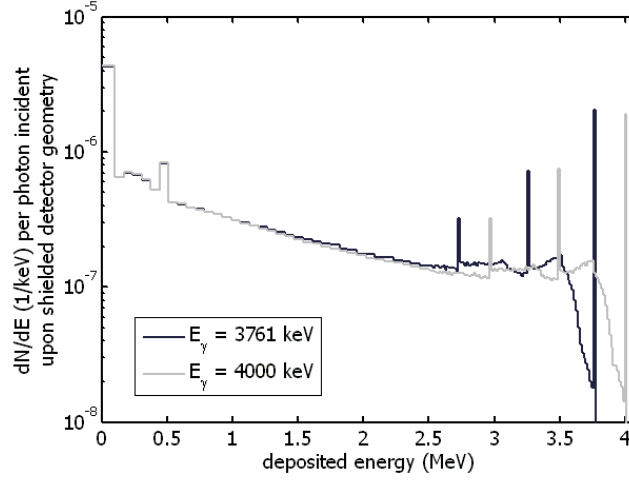
Figure 3.8 MCNPX-calculated pulse-height spectra for monoenergetic 3.761 and 4-MeV photons incident upon a HPGe detector with 13.2 cm-thick Pb shield. The simulations are discussed in Section C.4.1 and the geometry simulated is shown in Figure C.2. Bin-widths were 15 keV for energies above 2.5 MeV and 69 keV below. Statistical errors are up to 5% in narrow energy bins with low probabilities.

Assuming that the detector was located 60 cm from the assay target, the rate at which full-energy depositions from 3.761-MeV photons are detected when all ^{137}Cs has decayed is estimated as $R_{\mathrm{NRF}} = 0.013$ counts per mC of 4-MeV electrons incident upon the bremsstrahlung converter. If the HPGe detector resolution at 3.761 MeV is 4 keV, the NRF signal is then ∼40 times as intense as the signal due to full-energy deposition of non-resonantly backscattered photons, and ∼30 times the signal due higher energy backscattered photons depositing 3.761 ±0.002 MeV into the detector. Summing these background contributions, we find that the maximum NRF signal intensity is estimated as 17 times that of the expected background. The ratio of the NRF signal intensity to that of the detected background is shown in Figure 3.9 as a function of the time, t, since separation of cesium from the fission products.

Figure 3.9 indicates that the signal from the 3.761-MeV resonance of ^{137}Ba will be as intense as the background approximately 2.5 years after chemical separation. The NRF signal will be approximately 4 times as intense as the background after 10 years. From equation 2.107, we conclude that the statistical precision to which the NRF transition rate can be measured 10 years after separation is only 20% worse than if the background were negligible.

These calculations may be scaled to other ^{137}Cs sources. For sources of similar composition and shielding, the intensity of NRF signals will remain unchanged, relative to the non-resonantly backscattered photon intensity near NRF energies.

The quantity of lead necessary to shield the detector against the 661 keV photon from decay of ^{137}Cs will increase with source intensity. For initial source intensities large compared to 1 Ci, the thickness of lead required is given approximately by the
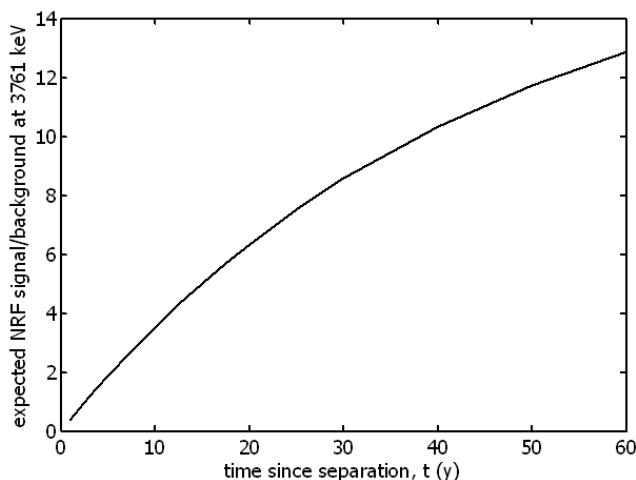
Figure 3.9 Calculated ratios of the expected NRF signal from ^{137}Ba to background as a function of time, t, since separation of cesium from the fission products. The assay target is assumed to be 1 kCi ^{137}Cs (initial activity), and the detector resolution is assumed to be 4 keV at the ^{137}Ba resonance energy of 3.761 MeV.

expression,

$$x = \frac{1}{1.28\text{cm}^{-1}} \ln \left[\frac{A[\text{Ci}]}{4.55 \times 10^{-5}\text{Ci}} \right] \tag{3.20}$$

The NRF γ-rays with energies of ~ 3.761 MeV are attenuated in lead with an attenuation coefficient of 0.47 cm^{-1} at 3.761 MeV(29). Thus, the rate at which the NRF signal is attenuated is always smaller than the increased NRF signal rate due to increased source strength. To a reasonable approximation, the method should then be applicable to the largest radiological sources. However, the backscatter NRF assay technique becomes subsequently less sensitive to the volume as a whole, and relatively more sensitive to that portion of the volume nearest the detector.

Using scaling and a re-calculated geometric factor, G from equation 3.14, we expect that the rate at which NRF γ-rays are counted for a target that was originally a 75-Ci source will be about 25% that of a 1-kCi source of the same age, and a 25-Ci initial activity source would accrue NRF counts at a rate 12% that of the 1-kCi source.

Newer, smaller radiological sources often contain their ^{137}Cs within boro-silicate glass(116)(109). These sources contain approximately 1% (atomic fraction) elemental cesium, compared to 50% for older sources. This decrease in cesium concentration, along with a tendency to produce lower-activity sources reduces the potential use of the backscatter NRF method for assay of newer radiological sources. Chemical segregation is also less likely to occur in borosilicate glasses, so obtaining a representative sample for destructive analysis techniques is less problematic.

Counting Statistics and Expected Measurement Timescales

To assess how accurately the NRF backscatter assay technique can measure the time since separation of a 1-kCi ^{137}Cs source, we assume an 8-hour (detector live time) measurement using a 20-mA 4-MeV source of electrons as can be generated by modern electron accelerators such as the Rhodotron(120). This results in a total beam charge of 570 C. For this beam current, the total count rate due to scattered interrogating photons in the shielded HPGe detector is estimated to be $\sim 10^4$ c s^{-1}.

The time since separation of cesium from the fission products is given by the expression,

$$t_{\text{sep}} = \frac{\ln\left(\frac{N_{\text{Ba}}}{N_{\text{Cs}}} + 1\right)}{\lambda} \tag{3.21}$$

where N_{Ba} and N_{Cs} are the number of ^{137}Ba and ^{137}Cs atoms present in the source at the time of the measurement, respectively, and λ is the decay constant for ^{137}Cs, given by $\lambda = \ln 2/t_{1/2}$. This assumes that initially there were no ^{137}Ba atoms present within the sample. This assumption may be confirmed by the absence of NRF response due to other barium fission product isotopes, or quantitatively corrected if these isotopes are observed.

The uncertainty in the measured value of t_{sep} is given by

$$\sigma_{t_{\text{sep}}} = \sqrt{\left(\frac{dt_{\text{sep}}}{dN_{\text{Ba}}}\right)^2 \sigma_{\text{Ba}}^2 + \left(\frac{dt_{\text{sep}}}{dN_{\text{Cs}}}\right)^2 \sigma_{\text{Cs}}^2} \equiv \sqrt{\Sigma_{\text{Ba}}^2 + \Sigma_{\text{Cs}}^2} \tag{3.22}$$

where σ_{Ba} and σ_{Cs} are the standard deviations of the measured values of N_{Ba} and N_{Cs}, respectively and Σ_{Ba} and Σ_{Cs} likewise refer to the contributions to the total uncertainty from the uncertainties in the measurements of ^{137}Ba and ^{137}Cs content. In equation 3.22, the contribution due to uncertainty in the ^{137}Cs decay constant has been neglected because it is very small (0.1%)(117), and has no effect on the conclusions drawn below.

The explicit forms of the differentials in equation 3.22 are

$$\frac{dt}{dN_{\text{Ba}}} = \frac{1}{N_{\text{Cs}}(1 + N_{\text{Ba}}/N_{\text{Cs}})\lambda} = \frac{f}{(1+f)\lambda}\frac{1}{N_{\text{Ba}}} \tag{3.23}$$

$$\frac{dt}{dN_{\text{Cs}}} = \frac{N_{\text{Ba}}/N_{\text{Cs}}}{N_{\text{Cs}}(1 + N_{\text{Ba}}/N_{\text{Cs}})\lambda} = \frac{f}{(1+f)\lambda}\frac{1}{N_{\text{Cs}}} \tag{3.24}$$

where

$$f \equiv \frac{N_{\text{Ba}}}{N_{\text{Cs}}} = \frac{1 - \exp[-\lambda t]}{\exp[-\lambda t]} \tag{3.25}$$

Thus,

$$\Sigma_{\text{Ba}} = \frac{f}{(1+f)\lambda}\frac{\sigma_{\text{Ba}}}{N_{\text{Ba}}} \tag{3.26}$$
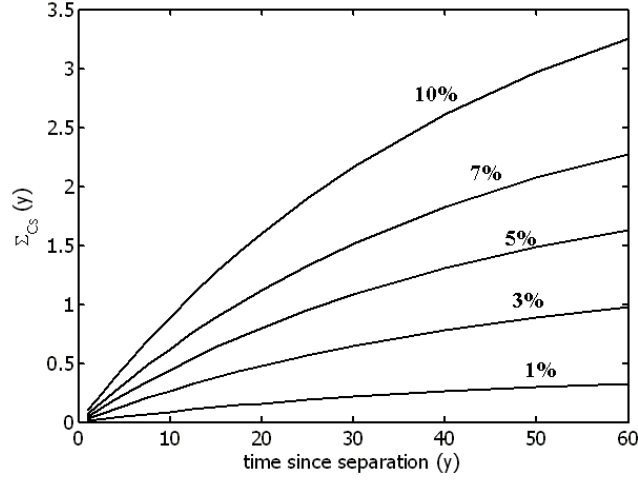
Figure 3.10 Calculated contributions to the uncertainty in the time since separation due to uncertainty in the measurement of the number of ^{137}Cs atoms, $\Sigma_{\text{Cs}}(t)$. The values adjacent to each curve indicates the assumed fractional uncertainty in N_{Cs}.

$$\Sigma_{\text{Cs}} = \frac{f}{(1+f)\lambda} \frac{\sigma_{\text{Cs}}}{N_{\text{Cs}}} \tag{3.27}$$

Due to lack of data, we are unable to make estimates for potential NRF γ-rays from ^{137}Cs. However, the rate at which the 661-keV γ-ray is emitted from the sample is proportional to the amount of ^{137}Cs present. Therefore, N_{Cs} can be determined by calibrated measurement of the 661-keV full-energy peak or by calorimetric methods. In a well-calibrated situation, these measurements can provide uncertainties as small as 1%, and should easily be able to provide uncertainties less than 10%. Figure 3.10 presents Σ_{CS} for a range of the uncertainty at which the ^{137}Cs content in the assay sample is measured.

Using the relationship between fractional uncertainty and signal-to-background ratios given in equation 2.107, we are able to evaluate $\Sigma_{\text{Ba}}(t)$. Using equation 3.22 and the values for $\Sigma_{\text{Cs}}(t)$ shown in Figure 3.10, we obtain estimates of $\sigma_t(t)$. These are plotted as a function of t for a ^{137}Cs source having an initial activity of 1 kCi (black) and 25 Ci (gray) in Figure 3.11.

These results indicate that non-destructive age-dating of radioisotope sources is possible using backscatter nuclear resonance fluoresce assay. The expected uncertainties for a 1 kCi initial activity source are such that measured values of the time since separation would be useful information for investigators and decision makers. Smaller radiological sources accrue statistics at slower rates, however measurement of a source of $A_0 = 25$ Ci still appears to provide very useful information within an 8-hour irradiation using an intense photon source.

The outlook for using a similar method to measure the time since chemical separation of ^{90}Sr radiological sources appears similar. ^{90}Sr has a 28.79-y half-life and undergoes β^- decay to ^{90}Y, which has a 64 h half-life before decaying to ^{90}Zr.
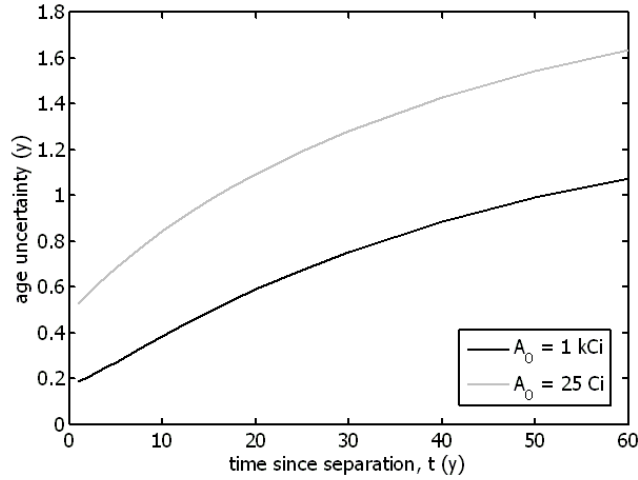
Figure 3.11 Calculated uncertainties (σ_t) in the time since separation, t, assuming the number of ^{137}Ba atoms was measured by nuclear resonance fluorescence via a bremsstrahlung beam generated by 570 C of 4-MeV electrons incident upon a bremsstrahlung converter. The number of ^{137}Cs atoms present in the assay material may be measured by NRF or by passive counting of the 661-keV γ-ray, and this uncertainty was assumed to be 3%. The black line indicates the age uncertainty for a target with an initial source activity, $A_0 = 1$ kCi, and the gray line indicates the age uncertainty for a target with initial activity, $A_0 = 25$ Ci.

The NRF response of ^{90}Zr has been measured, and it has a resonance of very similar intensity and energy to that of ^{137}Ba (30 eV·b at 3842 keV), therefore measurement of the number of ^{90}Zr atoms present in a sample should be a similar undertaking to that of measuring ^{137}Ba. However, there are two complicating factors pertinent to measuring the age of a ^{90}Sr source. First, the β^--decay of ^{90}Sr is not accompanied by any characteristic γ-rays. This indicates that the number of ^{90}Sr atoms cannot be directly measured from its activity. However, ^{90}Y will be in secular equilibrium with ^{90}Sr, and a 2186-keV γ-ray is emitted following ^{90}Y decay with a probability of $(1.4 \pm 0.3) \times 10^{-6}$. Although it is quite low in intensity, this γ-ray may be useful to measure the ^{90}Sr activity. β^--particles emitted from ^{90}Y can have energies up to 2186 keV. These will produce bremsstrahlung as they lose energy. The sources of higher-energy photons are much weaker than the 661-keV γ-ray that accompanies ^{137}Cs decay, but the resulting photons must be sufficiently shielded in order to perform a forensics measurement by counting induced NRF γ-rays.

Additional Forensics Information Available to NRF Assay Technique

The technique of measuring nuclear resonance fluorescence transitions to assay large radiological sources has the potential to provide additional auxiliary information that may be of use for nuclear forensics. The NRF responses of all stable barium

isotopes have been measured and resonances with stronger, or similar, intensities to that of the 3.761-MeV resonance were observed for ^{138}Ba (4026 keV, 211 eV·b)(89) and ^{136}Ba (3436 keV, 74.5 eV·b)(118) . This implies that significant quantities of these isotopes present in a ^{137}Cs source could be detected by measurement of their NRF signatures. If barium isotopes other than ^{137}Ba are detected, they would indicate poor chemical separation, which implies ^{137}Ba was also likely to be present after the separation. These measurements could provide the basis for a quantitative correction to the age of the radiological source estimated by equation 3.21.

Another interesting potential application of this assay technique is that it may provide information about the nuclear reactor that generated the constituents of the source. ^{135}Cs production is strongly suppressed by the large neutron absorption cross section of its decay parent, ^{135}Xe. Thus, measurements of the ^{135}Cs/^{137}Cs ratios that are lower than those indicated from Table 3.2 would indicate the source was generated in a high-flux reactor(119). Similarly, the rate of ^{133}Cs production compared to ^{137}Cs production can indicate which isotopes primarily underwent fission to produce the source. The accuracies with which these methods could be applied cannot be stated at this point, however, because the NRF responses of the cesium isotopes are unknown.

3.1.4   NRF Assay of Spent Fuel Pins

Measuring the content of actinides in intact spent fuel pins increases the difficulty of subverting nuclear safeguards and diverting special nuclear material. To ascertain the likelihood that NRF could be used to assay spent fuel, the backscatter measurement technique is examined. The modeled geometry for the assay is similar to that shown in Figure 3.1, except that the circular target indicated in the drawing is now the cross section of a cylindrical fuel pin. The pin was assumed to be 9.36 mm-diameter UO_2 pellets contained within 0.67 mm-thick Zr fuel cladding. For simulational purposes, photon fluences from fuel activity and from scattering of the interrogating beam were calculated at a point 60 cm from the pin inside a 1 cm-diameter cylindrical void within a large lead block. This is roughly equivalent to a detector viewing 1 cm of fuel while the remainder of the pin is heavily shielded by Pb.

Radioactivity of Spent Fuel

The first consideration for assay of spent fuel is the radioactivity of the fuel pin itself. Tanskanen et al. used the nuclide inventory code, ORIGEN-S(121) to calculate expected concentrations of actinides and fission products in boiling water reactor fuel that had undergone a burnup of 37.8 MWd/kgU. The actinide and fission product concentrations were tabulated at times of 0, 818.3, 1636.7, 2455.0, 3273.3, 4091.7, and 4910.0 days after discharge(122). Using these fission product concentrations, photon fluxes due to γ-ray emission and bremsstrahlung from slowing of β-particles
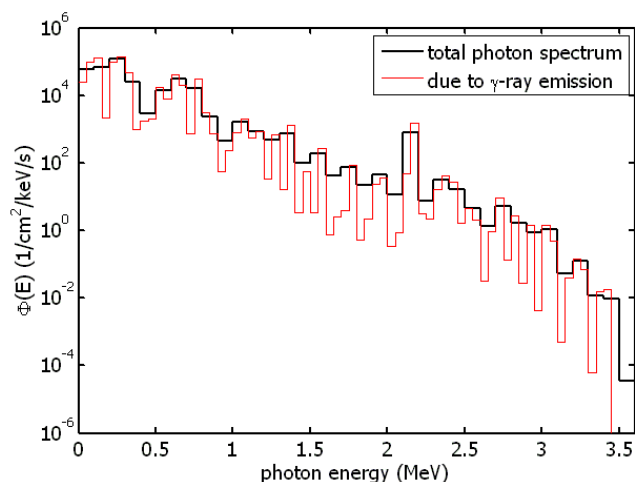
Figure 3.12 Calculated photon flux within a 1 cm-diameter collimator viewing a single spent fuel pin at a location 60 cm from the pin, immediately after fuel discharge from a reactor. The red lines indicate the flux contribution due to γ-ray emission in the spent fuel. Additional photons are due to bremsstrahlung emitted during slowing of emitted β-particles.

emitted from the spent fuel were calculated at the position 60 cm from the pin center, and are shown in Figures 3.12 and 3.13 directly after discharge, and $\sim$9 years after discharge, respectively. The spectra due to γ-ray emission are shown in red and the total spectra are shown in black. These spectra are dominated by relatively intense discrete γ-rays, whereas the difference between the total spectrum and that due to γ-ray emission is due to bremsstrahlung emitted from the slowing down of β-particles.

Comparing these figures, we note that the total intensity 9 years after discharge is smaller by a factor of $\sim$30 and the intensity above 1.6 MeV is smaller by a factor of $\sim$500 compared to the intensities immediately upon discharge of the fuel. The peak at 1596 keV is due to ^{154}Eu, which has an 8.5-y half-life. Higher-energy photons are primarily due to the decays of ^{144}Pr and ^{106}Rh, both of which are short-lived daughters of isotopes that decay with half-lives of about 1 y. These isotopes may also emit energetic β-particles during radioactive decay. These β-particles account for a large fraction of the bremsstrahlung emitted from the spent fuel.

The production of many important background-inducing fission products will vary with reactor operating conditions and types. For example, assuming a thermal neutron spectrum induces fission, the cumulative yield of ^{106}Rh from ^{239}Pu fission is approximately 10 times larger than from ^{235}U fission. Therefore longer irradiations or use of fuel that has high initial plutonium content will result in larger photon intensities between the energies of 1.6 and 3.6 MeV. Because of this variability, the fuel radioactivity values described in this section are for the purposes of describing an approximate scale to provide reference, rather than precise quantities.
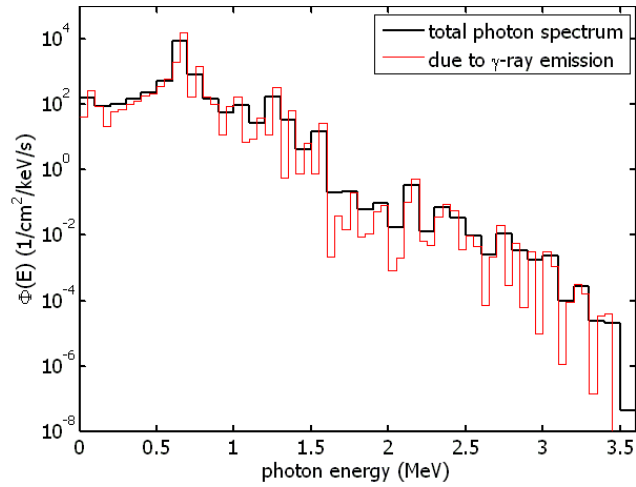
Figure 3.13 Calculated photon flux within a 1 cm-diameter collimator viewing a single spent fuel pin at a location 60 cm from the pin, 3273.3 days after fuel discharge from a reactor. The red lines indicate the flux contribution due to γ-ray emission in the spent fuel. Additional photons are due to bremsstrahlung emitted during slowing of emitted β-particles.

The calculated photon flux distributions in Figures 3.12 and 3.13 indicate one reason directly measuring the NRF response of ^{239}Pu or ^{235}U would be difficult. Even after 9 years of cooling, the radioactivity in the spent fuel results in a photon flux of approximately 10^6 cm^{-2}s^{-1} at the assumed detector location, 60 cm from the spent fuel center. Such a strong flux would result in almost complete pulse-summing in a HPGe detector, and therefore a filter between the fuel and detector will be necessary. Filters however, also down-scatter higher-energy photons. This can add to the energy continuum of background photons upon which NRF peaks must be measured.

A filter consisting of several inches of lead will increase the likelihood that γ-rays will not deposit their full energy into a detector, which increases the intensity of the spectral continuum relative to the intensity of full-energy peaks. For a single fuel pin, 9 y after removal from the reference reactor, approximately 8 cm of lead is needed directly between the detector and 1 cm of exposed fuel in order to operate a detector at a distance of 60 cm from the pin. This shielding dramatically alters the effective response of the radiation detector due to down-scattering of higher-energy photons within the filter. Folding shielded detector responses with the calculated fluence shown in Figures 3.12 and 3.13 results in the spectra shown in Figure 3.14.

Estimates of the background count rates in the vicinity of resonance energies are tabulated as R_{fuel} in Table 3.5. The values are from the spectrum shown in Figure 3.14 for spent fuel after a 9-year decay time that does no include γ-ray full-energy deposition. The decay time not only decreases the overall count rate to a reasonable level, but it also lowers the fraction of background that is due to higher-
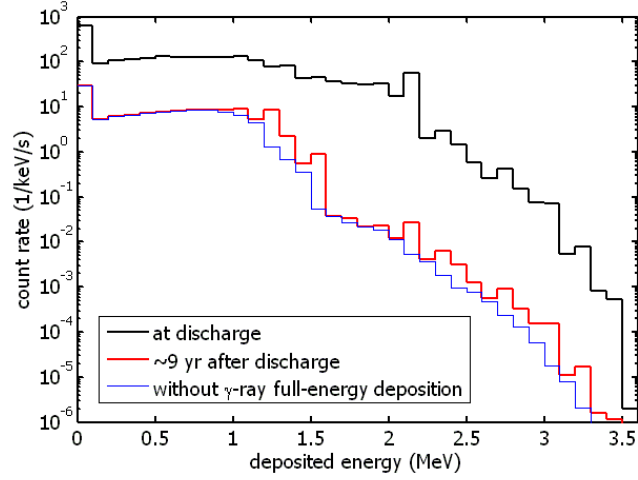
Figure 3.14 Calculated photon energy deposition spectra due to spent fuel radioac-
tivity at discharge (black) and ∼9 years after discharge (red). The spectra are
calculated for a 100% relative efficiency HPGe detector behind 8 cm of lead located
60 cm from the spent fuel pin. It is assumed that the space between the pin and
detector is filled with lead, with the exception of a hole that allows the shielded
detector to view 1 linear cm of the fuel. The contribution to the red spectrum that
is due to full-energy deposition of discrete γ-rays was also subtracted, resulting in
the blue spectrum. This spectrum is indicative of the expected counting continuum.

energy photons. In particular, a factor of 10 decrease in count rate is expected above
the 1596-keV ^{154}Eu peak.

   The R_{fuel} values indicated in Table 3.5 should quite accurately represent count
rates due to radioactive emissions from a reference fuel pin that had undergone
a continuous irradiation of 37.8 MWd/kgU and subsequently cooled for 9 years.
However, given the variety irradiation conditions that produce spent fuel, they should
only be taken as approximate values with the tacit acknowledgment that a wide
variety of spent fuel exists and that spent fuel radioactivity will vary.

NRF Count Rates from Backscatter Assay of Spent Fuel Pin

   The NRF responses of ^{235}U and ^{239}Pu were measured in 2006 and 2007(123), and
the results from these experiments are presented in Tables 3.4 and 3.7. Several pairs
of observed NRF γ-rays were found to have energy differences equal to the excitation
energy of low-lying excited states (7.9 ± 0.002 keV for ^{239}Pu and 46.21 ± 0.01 keV
for ^{235}U)(126). In these cases the sum of the measured cross sections is shown in the
table, and the tabulated value of Γ_0/Γ differs from unity. Subsequent experiments
attempting to measure higher-energy NRF resonances in these isotopes have not
yielded new transitions(124),(125).

   Equation 3.14 was evaluated for the assay geometry of a single UO$_2$ fuel pin

^{235}U			
Centroid Energy (keV)	$\int \sigma_{\mathrm{NRF}} dE$ (b·eV)	$g\Gamma_0$ (meV)	Γ_0/Γ
1656.23±.80	4.1±1.3	1.47±0.46	1
1733.60±.22	35.9±4.1	14.11±1.61	0.83
1815.31±.22	14.1±1.7	6.05±0.73	0.69
1827.54±.23	6.7±1.2	2.91±0.52	1
1862.31±.20	9.6±1.7	4.33±0.77	1
2003.32±.25	9.7±1.7	5.07±0.89	1
2006.19±.31	4.7±1.6	2.46±0.84	1

Table 3.4 Characteristics of measured NRF states in ^{235}U as reported in reference(123). Values of $g\Gamma_0$ were obtained by application of equation 2.89. States where $\Gamma_0/\Gamma \neq 1$ indicate that a γ-ray of energy, $E_\gamma = E_C - 46.2$ keV was observed. These lines are assumed to correspond to de-excitation of the NRF state via emission of a γ-ray populating the low-lying $9/2^-$ excited state of ^{235}U. Values of $\int \sigma_{\mathrm{NRF}} dE$ shown here are the sum of the reported values.

where ^{235}U comprises 1% of the actinide mass. The interrogating beam was a 2 MeV endpoint-energy bremsstrahlung beam. The detector response was modeled as described in Section C.4 and was assumed to be shielded in the configuration shown in Figure C.2, with a filter thickness, $x_f = 8$ cm.

Resulting expected count rates of NRF γ-rays from ^{235}U are tabulated in Table 3.5. The values are reported in units of counts/mC/keV, indicating that rates are proportional to the intensity of the electron beam that generates the bremsstrahlung beam, and that the intensity of the NRF γ-rays are spread out over the detector's energy resolution, which is assumed to be 3 keV. The expected uncertainties in the rate at which NRF γ-rays would be counted are primarily due to experimental uncertainties in the measured strengths of the NRF resonances. These values are up to 33% for the smaller resonances. Likewise, effects due to detector dead-time will proportionally decrease all rates listed in Table 3.5.

Referring to the results shown in Table 3.5, we observe that a beam current of approximately 400 mA would be necessary for the intensity of NRF γ-ray from the 1733-keV ^{235}U resonance to be equal that due to the radioactivity of spent fuel, 9 years after reactor discharge. With this beam intensity in mind, we now consider the intensity of non-resonantly backscattered photons, which also scales with the intensity of the interrogating beam.

Centroid Energy (keV)	$\int \sigma_{\mathrm{NRF}}\, dE$ (b·eV)	R_{NRF} (1/mC/keV)	R_{bkg} (1/mC/keV)	R_{fuel} (1/s/keV)
1656.23	4.1	9.2×10^{-6}	2.5×10^{-2}	3.6×10^{-2}
1733.60	35.9	6.6×10^{-5}	1.7×10^{-2}	2.8×10^{-2}
1815.31	14.1	2.0×10^{-5}	1.1×10^{-2}	2.4×10^{-2}
1827.54	6.7	9.6×10^{-6}	9.9×10^{-3}	2.3×10^{-2}
1862.31	9.6	1.2×10^{-5}	7.9×10^{-3}	2.1×10^{-2}
totals (energy-integrated)		3.8×10^{-4}	4.2×10^{2}	1.2×10^{4}

Table 3.5 Expected rates at which ^{235}U NRF γ-rays (R_{NRF}), non-resonantly backscattered interrogation photons (R_{fuel}), and photons emitted via radioactive decay spent fuel that has cooled for 9 years (R_{bkg}), are detected at energies corresponding to ^{235}U resonance γ-rays. The detector was assumed to be a 100% relative efficiency HPGe shielded behind 8 cm lead, with assumed energy resolution of 3 keV. The NRF γ-ray intensities have been uniformly spread over this resolution. Values in the last row represent total rates expected over the entire spectrum, and therefore, are not energy-differentiated.

Non-Resonantly Backscattered Photon Spectrum

The expected background photon spectrum due to detection of non-resonantly scattered interrogation photons is determined by summing the intensity of non-elastically scattered photons computed via MCNPX and the expected intensity due to elastic scattering processes that are not simulated in MCNPX. These spectra are shown in Figure 3.5 and values at resonant energies are tabulated as 'R'_{bkg} in Table 3.5. The total intensity is given by integrating the energy-differentiated spectrum over all energies. This results in 4.2×10^{2} counts/mC. Using a 25 mA electron beam to produce the bremsstrahlung beam would then result in approximately 10^{4} c s^{-1} in the counting geometry, which when summed with a background counting rate of 10^{4} c s^{-1}, yields a total count rate of $\sim 2 \times 10^{4}$ c s^{-1}.

Uncertainties in the energy-integrated value of R_{bkg} are primarily due to inaccuracies in the Monte Carlo calculation, which has been demonstrated to be quite small for total count rates. However, a large fraction of the counts above $\sim$1.5 MeV are due to elastic scattering, which had been neglected in benchmarking experiments. As discussed in Chapter 2, the elastic scattering cross sections now used in the Monte Carlo calculations are based on the form factor approximation, and may remain inaccurate by up to a factor of $\sim$10. Because of this, elastic scattered has been separately considered, but the cross sections used in this calculation may be inaccurate by a factor of $\sim$2 [4].

The significantly larger intensity of the non-resonantly scattered photons relative

---

[4]See Section 2.10 for a discussion of these cross sections and their associated uncertainties.

to the NRF photons indicates the difficulty in measuring backscattered NRF γ-rays to determine spent fuel content. Since longer cooling times can reduce the photon intensity due to radioactive decay in spent fuel, the fundamental limit is defined by the fact that the intensity of NRF γ-rays, relative to those non-resonantly scattered, is fixed and small. This indicates that very large numbers of photon counts would be required to precisely measure the quantity of ^{235}U or ^{239}Pu in spent fuel.

The rate at which statistics accrue is given in equation 2.107. For, the 1733-keV resonance of ^{235}U, using a 2 MeV endpoint-energy beam and neglecting the background due to radioactive decay within spent fuel, $\xi \approx 4 \times 10^{-3}$. Thus ~20 times more NRF counts are necessary than would be expected from standard $1/\sqrt{N}$ statistics. To make a measurement with 1% statistical uncertainty, 2×10^5 NRF counts would be needed. Such a measurement would take about 2 y using a 25 mA beam and a single 100% relative efficiency HPGe detector. Higher beam energies will increase the NRF rate, but will also decrease ξ.

Quasi-monoenergetic Photon Sources and Backscattered NRF

The prospect of using an intense quasi-monoenergetic photon beam to induce NRF changes the conclusions given above because the down-scattering of higher-energy photons is significantly reduced. The signal-to-background ratio limit is then defined by two factors: the elastic scattering cross section relative to the NRF cross section, and the energy resolution of the photon detector. Assuming a 3 keV detector resolution and considering the 1733-keV ^{235}U resonance, $\xi \approx 0.1$. With this, counting statistics would accrue at a rate 4.5 times slower than would be expected from the $1/\sqrt{N}$ limit. However, the total non-resonant backscattered photon detection rate would be reduced by an amount proportional to the energy width of the beam, relative to that of the bremsstrahlung spectrum. In principal, this enables a system to detect far more NRF events in a given time period. However, the largest operating quasi-monoenergetic photon source, the High Intensity γ-ray Source (HIγS) is capable of producing $\sim$ 250 γ/s/eV with a 20 mm-radius collimation (the beam is nearly mono-directional)(100), which is roughly equivalent to the number of resonant-energy photons from a bremsstrahlung beam produced by 2-μA 2-MeV electron beam in the interrogation geometry assumed here. Thus, the most intense quasi-monoenergetic photon source now available is much too weak for the present application. Significant technological advances need to be made if this method is to be considered further.

3.2   Transmission NRF Assay

The measurement of NRF γ-rays at backward angles suffers from the disadvantage that radioactivity emitted by the assay target can necessitate large amounts of shielding, which subsequently reduces the NRF γ-ray detection rate. The method
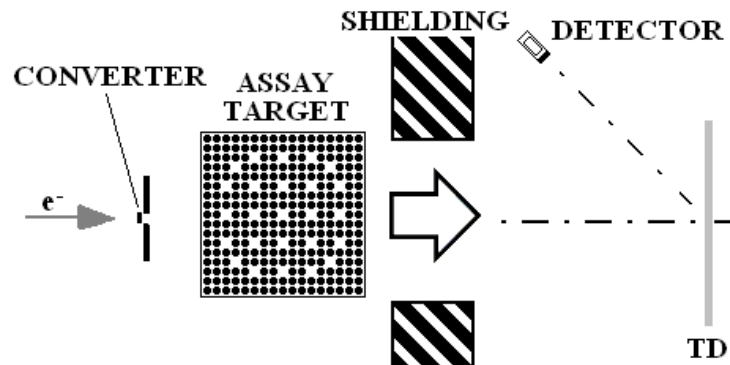
Figure 3.15 Schematic description of a geometry used for a transmission assay measurement.

is also more sensitive to radiation backscattered from the front of the target rather than from the target as a whole, resulting in potentially biased results for non-homogeneous targets. The following method mitigates these disadvantages at the expense of a more complicated assay system and the need for even stronger interrogating photon beams.

The concept of an NRF assay using the transmitted spectrum emanating from the assay target is as follows: an interrogating beam impinges upon the assay target and the spectrum transmitted through the target is then incident upon a thin sheet of material called the transmission detector (TD). The TD is (ideally) composed of the isotope that is to be assayed, which will be referred to as the *isotope of interest* (IOI). Resonant-energy photons that impinge upon the TD may induce NRF. The NRF γ-rays emanating from the TD are then detected by radiation detectors located at backward angles, relative to the incident bremsstrahlung beam. A schematic diagram of this assay type is shown in Figure 3.15.

The sensitive volume of the assay target is defined as the region though which interrogating photons can penetrate and subsequently reach the TD without scatter. The reduced rate at which the TD undergoes NRF is proportional to the intensity of preferential attenuation undergone by resonant-energy photons while traversing the sensitive volume of the target. This intensity is directly correlated to the areal density of the IOI within the sensitive volume of the target. Larger IOI areal densities decrease the relative rate at which NRF occurs in the TD, effectively producing a larger signal for the transmission measurement. Because the detectors are arranged to observe NRF in the TD, increasing the quantity of material in the assay target does not directly increase the rate at which the detectors measure radioactive decay in the target. Therefore, creating larger effective signals without increasing the background implies that thicker assay targets are advantageous for transmission measurements. For these reasons, measurements of plutonium content in spent fuel assemblies is

considered rather than in a single fuel pin.[5]

In Section 3.2.1, photon transport through a fuel assembly assay target is considered when no IOI atoms are present in the assay target. From this, the expected rates for detecting non-resonantly scattered photons and NRF γ-rays are estimated. The details of the process by which NRF γ-ray counts rates decrease from this maximum rate, called resonant attenuation are considered in Section 3.2.2. The use of approximating models for the form of NRF resonances is also considered in Section 3.2.3. Section 3.2.4 develops the means by which measured NRF γ-rays are related to the precision with which the IOI may be measured, and expected precisions for an assay of spent fuel assemblies is presented. Section 3.2.5 discusses the effects of down-scattering on the effective NRF signal.

3.2.1   Transmission Assay: NRF and Background Signal Rates

Photons penetrating the sensitive volume in the assay target undergo attenuation given by

$$\Phi(E) = \Phi_0(E) \exp[-\mu(E)x] \tag{3.30}$$

Where x is the thickness of the assay target, and $\mu(E)$ is the energy-dependent attenuation coefficient of the target, given by $\mu(E) = \sum_{ij} N_i \sigma_{ij}(E)$, where N_i is the number density of a given isotope, i, and $\sigma_{ij}(E)$ is the partial cross section for a photon interaction event of type j for that isotope (i.e., incoherent scattering, pair production, NRF, ...). There is also the potential for higher-energy photons to be down-scattered to the energy, E, resulting in higher photon fluences than indicated by equation 3.30. The phenomenon where a down-scattered photon becomes resonant in energy is discussed in more detail in Section 3.2.5, however for the case where the energy of an NRF resonance is near the maximum energy of the interrogating

---

[5]An estimate of the statistical uncertainty of the IOI areal density due to a transmission measurement of a resonance is given in equation 3.50. Likewise, the fractional uncertainty is given by

$$u \equiv \frac{\sigma_N x}{Nx} = \frac{\sqrt{1 + 2/\xi}}{Nx\alpha\sqrt{C}} \tag{3.28}$$

Assume the limiting factor in NRF measurements is the rate at which radiation detectors can operate, and that this value is held constant between measurements (presumably by adjusting the beam intensity). For measurements of actinide areal densities, Nx_{assembly} and Nx_{pin}, Nx in equation 3.28 significantly changes, whereas ξ and C only differ between measurements by an amount approximately proportional to $\mathbb{A}(Nx_{assembly})/\mathbb{A}(Nx_{pin})$. $Nx_{assembly} \approx 0.25$ g/cm^2 and $Nx_{pin} \approx 20$ mg/cm^2, therefore $\mathbb{A}(Nx_{assembly})/\mathbb{A}(Nx_{pin}) \approx 1$ (see Figure 3.28), and for a fixed total count rate,

$$\frac{u_{\text{assembly}}}{u_{\text{pin}}} \approx \frac{Nx_{\text{pin}}}{Nx_{\text{assembly}}} \tag{3.29}$$

Assuming sufficiently intense photon sources, the transmission assay of an entire fuel assembly yields equivalent statistical uncertainties, and therefore dramatically reduced fractional uncertainties, compared to assay of a single fuel pin.
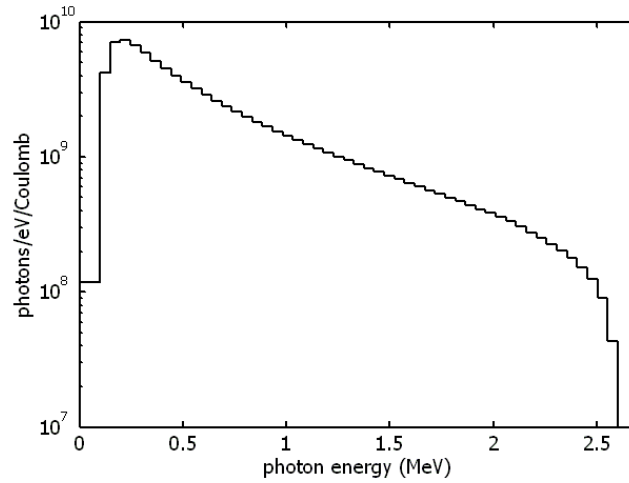
Figure 3.16 MCNPX-computed bremsstrahlung photons spectrum for photons leaving within 3.57º of the initial electron trajectory, for 2.6-MeV electrons normally incident upon 102 μm-thick Au foil backed by 1 cm-thick Cu.

photon spectrum, this occurrence is relatively rare. However, down-scattering significantly increases the photon flux for the low-energy portion of the transmitted spectrum, relative to that predicted by equation 3.30.

The processes by which non-resonant photons leaving the TD result in detected background events has essentially been discussed in Section 3.1.2, with the following differences: the assay target described in Section 3.1.2 is now the TD, the transmission target hardens the spectrum of the interrogating beam, and the shielding configuration for the radiation detectors are differently constrained.

We consider non-resonant photon transport through the a target composed of UO_2, Zr, and small quantities of other actinides and fission products. The target geometry is a homogenized mixture of these constituents at 4 g/cm^3 density and 21.8-cm square. This target is the homogenized equivalent of a 15 pin by 15 pin (15 x 15) spent fuel assembly. Expected photon intensities are estimated with MCNPX calculations, where the effects of resonant absorption are explicitly excluded these calculations. Resonant absorption will be calculated separately using the formalisms developed in Section 3.2.2.

First, the bremsstrahlung converter is assumed to be 102 μm-thick Au foil backed by 1 cm-thick Cu. These are the actual dimensions of the converter used in the experiment described in Chapter 4. The calculated photon spectrum emitted from the bremsstrahlung converter within 3.57º of the incident electron direction is shown in Figure 3.16. The electrons were assumed to have an energy of 2.6 MeV and to be normally incident upon the Au surface. For this calculation, source electrons were all assumed to strike the center of the Au surface.

In a second simulation, the bremsstrahlung spectrum shown in Figure 3.16 was assumed to be produced 150 cm from the side face of the 15 x 15 homogenized fuel
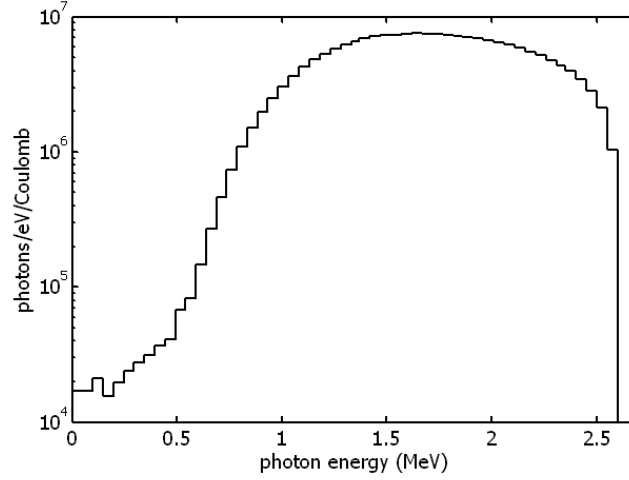
Figure 3.17 MCNPX-computed photon spectrum directed toward TD after penetration of bremsstrahlung spectrum through a homogenized fuel assembly.

assembly target and was used to irradiate the target. The geometry is such that the diameter of the un-scattered beam is 21.8 cm at the back plane of the target. The spectrum of photons leaving the target's back plane in the direction of the TD is shown in Figure 3.17. The entire spectrum is attenuated by a factor of $\sim$400, however, photons above 2 MeV are only attenuated by a factor of $40 - 50$.

A third computation simulated the transport of photons with the spectrum shown in Figure 3.17 as they impinge upon the TD. The energy-differentiated photon flux was calculated at a point 100 cm from the TD at an angle of 120°, relative to the initial beam direction. This photon energy distribution is then taken as the source spectrum for a final series of simulations in which the shielded detector response is examined. In these simulations, the thickness of the Pb filter was varied, and the backscattered photon spectrum was transported through a shielded HPGe detector geometry as described in Section C.4. For each incident photon, the energy deposited within the germanium was calculated, resulting in the expected photon spectrum as measured by a shielded HPGe detector.

The thicknesses of the Pb filters were 1.27, 2.54, 4, 6, and 8 cm for these simulations. With 8 cm of shielding, total count rate in the detector (100% relative efficiency HPGe) decreases from 4.4×10^7 to 1.2×10^5 counts per Coulomb of 2.6-MeV electrons incident upon the bremsstrahlung converter, compared to a shielding thickness of 1.27 cm. In general, an HPGe detector should operate at a maximum of between 2×10^4 and 8×10^4 Hz(139). Using 2×10^4 as a nominal maximum count rate, this defines the maximum allowable beam intensity for a given filter thickness. These values are summarized in Table 3.6.

Increasing the filter thickness results in more attenuation of the NRF γ-rays. This decreases the probability that a NRF γ-ray will deposit its full-energy in the HPGe detector. This attenuation is estimated with the expression $I = I_O \exp(-\mu x_f)$,

x_{f} (cm)	counts per 2.6-MeV e$^-$	I_{max} (mA)	$I_\gamma/I_{\gamma 0}$	R_{NRF} (1/C)
1.27	7.0×10^{-12}	0.46	0.53	49
2.54	1.8×10^{-12}	1.8	0.28	27
4.0	4.1×10^{-13}	7.8	0.14	13
6.0	7.6×10^{-14}	42	0.051	4.9
8.0	1.9×10^{-14}	170	0.019	1.8

Table 3.6 Effects of the photon filter on the photon spectrum that is calculated to be measured by a 100% relative efficiency HPGe detector. x_{f} indicates the thickness of the Pb filter. The values corresponding to 'counts per 2.6-MeV e$^-$' indicate the total number of expected counts per 2.6-MeV electron incident upon the bremsstrahlung converter, and from these values, the electron beam intensity resulting in 2×10^4 counts per second, I_{max}, is calculated. Values labeled as $I_\gamma/I_{\gamma 0}$ indicate the attenuation of a 2.25-MeV γ-ray as it penetrates through the corresponding filter thickness and R_{NRF} indicates the expected number of NRF γ-rays that would be counted by a detector per Coulomb of electrons impinging upon the bremsstrahlung converter.

where μ is the attenuation coefficient (without coherent scattering) taken from reference(29). The attenuation in the filter, $I_\gamma/I_{\gamma 0}$ is also shown in Table 3.6 for a 2.25-MeV γ-ray. Attenuation coefficients are not a strong function of energy in the range between 2 and 2.5 MeV, and therefore we can consider these values to be fairly representative of the behavior NRF γ-rays that would be induced by a 2.6 MeV endpoint-energy bremsstrahlung beam.

Neglecting the excess attenuation of resonant-energy photons (which will be explicitly examined in detail in Section 3.2.2), the rate at which NRF γ-rays are detected can be estimated using equation 3.10, where Φ_i now refers to the photon spectrum incident upon the TD (Figure 3.17), and ϵ must take into account the effect of the filter. With these modifications, we show in the last column of Table 3.6 expected count rates of a hypothetical 20 eV·b resonance at 2.25 MeV for a 100% relative efficiency HPGe detector located 100 cm from the TD per Coulomb of electrons incident upon the bremsstrahlung converter.

We now must examine how the expected rate at which NRF γ-rays are measured decreases due to resonant absorption of photons in the assay target. This creates the signal from which a measurement of the intensity of transmitted resonant-energy photons can be used to determine the areal density of the IOI in the target.

3.2.2   Analytical Considerations

In this section we consider the relative attenuation of photons at, and near, resonant-energies through materials containing varying amounts of an isotope of in-

terest. As discussed in Section 2.11.4, the energy-dependent cross section that photons experience while traversing a material is given to an excellent approximation by the Doppler-broadened Lorentzian profile (DBLP) described in equation 2.99. The relative probability that a photon at or near resonant-energy traverses the assay target and then subsequently undergoes NRF in the TD is considered. In Section 3.2.3 the expected NRF probabilities are compared to alternate predictions that would result if approximate models of the energy-dependent cross section were used.

First, we assert that within a few eV of a resonance, it is valid to approximate all non-resonant cross sections as constants. Given that resonances of interest have centroid energies between 1.5 and 5 MeV, we consider for this energy range the attenuation coefficients given in the XCOM database(29). In this energy range, the fastest-varying partial photon cross section for all elements is that for pair production. Pair production cross sections increase smoothly by a factor of approximately 10 for high-Z and up to 33 for low-Z over the energy range of 1.5 to 5 MeV. Approximating the increase as a linear function, we observe that the average fractional increase over the range of 10 eV is less than 10^{-4}, which is negligibly small. While the true non-linear shape of the pair production cross section may result in up to a factor of about five larger fractional increase over the energy range of 1 eV, it remains valid to approximate the effects of all non-resonant photon scattering processes as energy-independent over the width of a typical resonance. Likewise, across the width of a resonance, the intensity of a bremsstrahlung spectrum changes by

$$\frac{\Phi(E_C) - \Phi(E_C + 4\Gamma_D)}{\Phi(E_C)} \approx 3 \times 10^{-6} \tag{3.31}$$

This too may be considered as energy independent for an energy range encompassing a resonance.

From these arguments, the energy-differentiated photon flux, $\Phi_i(E)$, incident upon the assay target is assumed constant and effects due to non-resonant photon attenuation are separated. Neglecting down-scattering, the effective photon flux leaving a target is approximately

$$\Phi_o(E) \approx \Phi_i \exp[-N\sigma_{\mathrm{NRF}}(E)x] \exp\left[-\mu_{\mathrm{atom}}x\right] \tag{3.32}$$

where N is the atom density of the IOI (in units of atoms/cm^3) in the target, x is the target thickness, $\sigma_{\mathrm{NRF}}(E)$ is the cross section due to NRF, and μ_{atom} is the attenuation coefficient for photons in the assay target due to non-resonant processes (assumed to be constant over the energy range of interest).

The rate at which NRF γ-rays emitted into backward angles relative to the direction of the NRF-inducing incident beam are counted in a geometry consisting of a slab target was considered in Section 3.1.1. The only difference here is that the photon flux incident upon the slab is now $\Phi_o(E)$.

$$\frac{dR_{\mathrm{NRF}}}{dE} \approx \frac{1 - \exp[-(\alpha + \mu_{\mathrm{NRF}}(E))t_{\mathrm{TD}}]}{\alpha + \mu_{\mathrm{NRF}}(E)} N_{\mathrm{TD}} \Phi_o(E) \sigma_{\mathrm{NRF}}(E) W_e(\theta) \frac{A\epsilon}{4\pi r_d^2} \tag{3.33}$$

where t_{TD} refers to the TD thickness and α is defined in equation 3.6.

Equation 3.33 may be re-written as follows:

$$\frac{dR_{\mathrm{NRF}}}{dE} = \lambda(E)\Big[\exp[-N\sigma_{\mathrm{NRF}}(E)x]\sigma_{\mathrm{NRF}}(E)\Big] \left[N_{\mathrm{TD}}\Phi_i \exp(-\mu x)W_e(\theta)\frac{A\epsilon}{4\pi r_d^2}\right] \quad (3.34)$$

The first term,

$$\lambda(E, t_{\mathrm{TD}}) = \frac{1 - \exp[-(\alpha + \mu_{\mathrm{NRF}}(E))t_{\mathrm{TD}}]}{\alpha + \mu_{\mathrm{NRF}}(E)} \quad (3.35)$$

is an effective thickness that a photon experiences as it traverses the slab. If the quantity $\alpha + \mu_{\mathrm{NRF}}(E)$ is small, the exponent may be re-written as a linear function:

$$\lambda(E, t_{\mathrm{TD}}) \approx \frac{1 - [1 - (\alpha + \mu_{\mathrm{NRF}}(E))t_{\mathrm{TD}}]}{\alpha + \mu_{\mathrm{NRF}}(E)} = t_{\mathrm{TD}} \quad (3.36)$$

Indicating that the rate of NRF γ-ray detection would be directly proportional to the TD thickness. However, for geometries containing a thick TD or if larger photon interaction probabilities are present, the rate at which NRF is induced in the slab is less than $N_{\mathrm{TD}}\sigma_{\mathrm{NRF}}t_{\mathrm{TD}}$ because $\lambda(E) \leq t_{\mathrm{TD}}$.

We define the first two terms of equation 3.34 as $\Lambda(E, t_{\mathrm{TD}}, Nx)$,

$$\Lambda(E, t_{\mathrm{TD}}, Nx) \equiv \lambda(E)\Big(\exp[-N\sigma_{\mathrm{NRF}}(E)x]\sigma_{\mathrm{NRF}}(E)\Big) \quad (3.37)$$

This function contains all the parameters that can significantly vary over an energy range comparable to the Doppler-broadened width of an NRF resonance. The energy resolutions of all commonly used γ-ray detectors are much wider than the width of an NRF resonance. Therefore energy-dependent variations in Λ will not be directly observed in the detected photon energy spectrum and the quantity $\int \Lambda(E)dE$ provides a quantity that is proportional to the rate at which NRF counts will be measured.

The measured quantity that provides information on the areal density of the IOI in the sensitive volume of the assay target is the reduced rate of NRF γ-ray counts, relative to those expected for a comparable assay target with no IOI present. This quantity is called the *effective attenuation* and is given by:

$$\mathbb{A}(t_{\mathrm{TD}}, Nx) \equiv \frac{\int \Lambda(E, t_{\mathrm{TD}}, Nx)dE}{\int \Lambda(E, t_{\mathrm{TD}}, 0)dE} \quad (3.38)$$

The effective attenuation is dependent upon the parameters of the resonance it describes. Effective attenuation functions are shown for different ^{238}U resonances when $t_{\mathrm{TD}} = 8$ g/cm^2 in Figure 3.18. The parameters of the known ^{238}U NRF resonances between 2 and 3 MeV are shown in Table 4.5. Figure 3.18 indicates that for a target of constant total areal density, but increasing IOI areal density, NRF γ-ray count rates decrease. The rate at which they decrease is proportional to the width of the resonance.
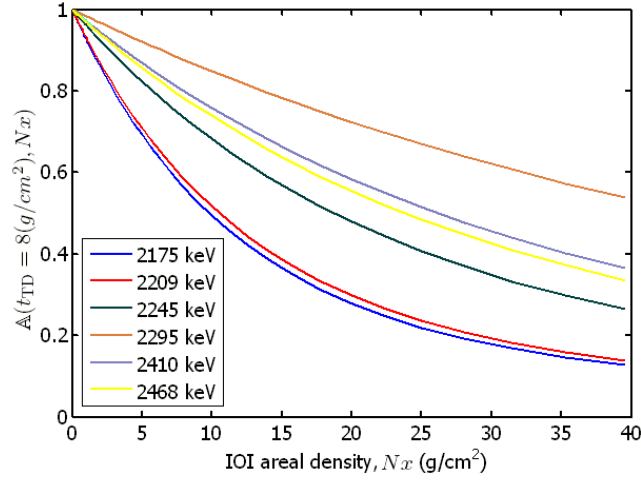
Figure 3.18 The effective attenuation of photons given by equation 3.38 due to selected ^{238}U NRF resonances with $t_{TD} = 8$ g/cm^2. The resonances are indicated by their centroid energies shown in the legend.

We examine how $\Lambda(E, t_{TD}, Nx)$ varies for the 2176-keV ^{238}U resonance. Figure 3.19 shows $\Lambda(E, t_{TD}, Nx)$ for different TD thicknesses with $Nx = 2$ g/cm^2. Here, it is seen that increasing t_{TD} produces an increase in the NRF detection rate, as expected. However, the rate of increase is relatively small for t_{TD} larger than about 1 cm.

The shape of the function, $\Lambda(E, t_{TD}, Nx)$ also varies somewhat with the magnitude of t_{TD}. This is demonstrated in Figures 3.20 and 3.21, where for $Nx = 2$ and 40 g/cm^2, respectively, functions of $\Lambda(E, t_{TD}, Nx)$ are divided by their maximum value and plotted for $t_{TD} = 10^2$ and 10^{-3} cm. Thicker TDs result in slightly increased contributions to the total NRF count rate from photons with energies further from the resonance centroid.

In Figure 3.21, both distributions demonstrate a pronounced decrease at the centroid energy. This decrease is due to the fact that the ^{238}U in the assay target has absorbed the majority of photons near the centroid energy. Photons with energies further from the centroid energy experience smaller resonance absorption cross sections and are less strongly absorbed. Targets with larger resonances or higher IOI areal densities will demonstrate a further shift of the detected intensity toward the tails of the resonance.

The change in the shape of $\Lambda(E)$ for varying t_{TD} also has a significant effect on the effective attenuation, $\mathbb{A}(Nx)$. Figure 3.22 demonstrates this effect as it relates to detection of NRF γ-rays emitted from the 2176-keV ^{238}U for $Nx = 8$ g/cm^2. $\mathbb{A}(Nx)$, increases approximately exponentially with increasing t_{TD} while t_{TD} is small, but it approaches a constant in the limit of large t_{TD}. At sufficiently large t_{TD} all incident resonant-energy photons will have undergone NRF, or been attenuated by non-resonant processes.
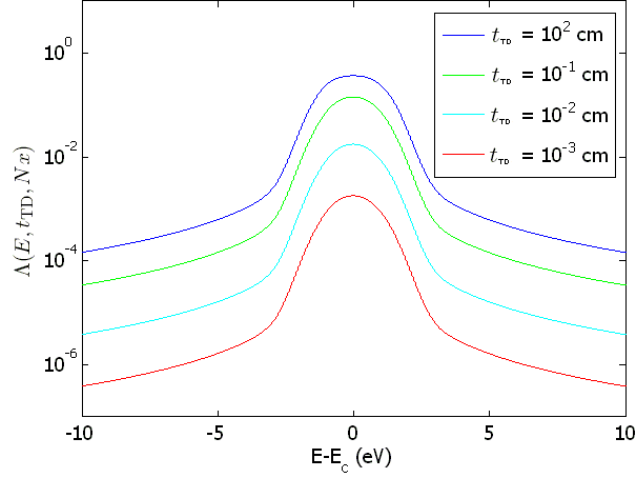
Figure 3.19 Values of $\Lambda(E, t_{\mathrm{TD}}, Nx)$ for the 2176-keV ^{238}U resonance and different TD thicknesses. The abscissa is the difference between the incident photon energy, E, and the centroid energy of the resonance, E_C. The areal density of the IOI in the assay target was $Nx = 2$ g/cm^2.
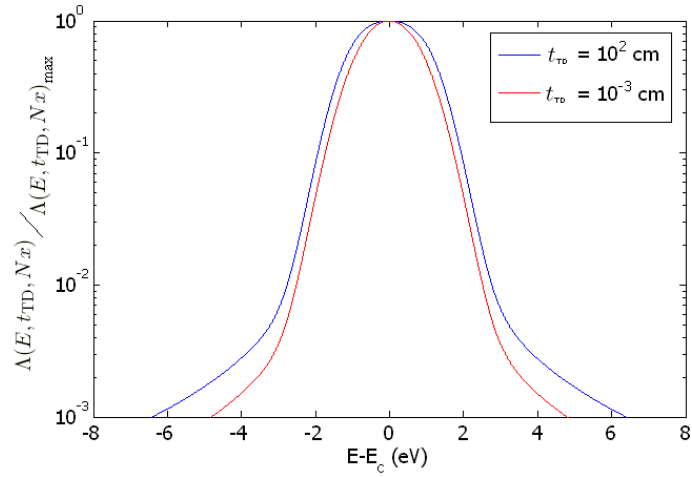
Figure 3.20 $\Lambda(E, t_{\mathrm{TD}}, Nx)/\Lambda(E, t_{\mathrm{TD}}, Nx)_{\max}$ for the 2176-keV ^{238}U resonance. The abscissa is the difference between the incident photon energy, E, and the centroid energy of the resonance, E_C. The areal density of the IOI in the assay target was $Nx = 2$ g/cm^2.
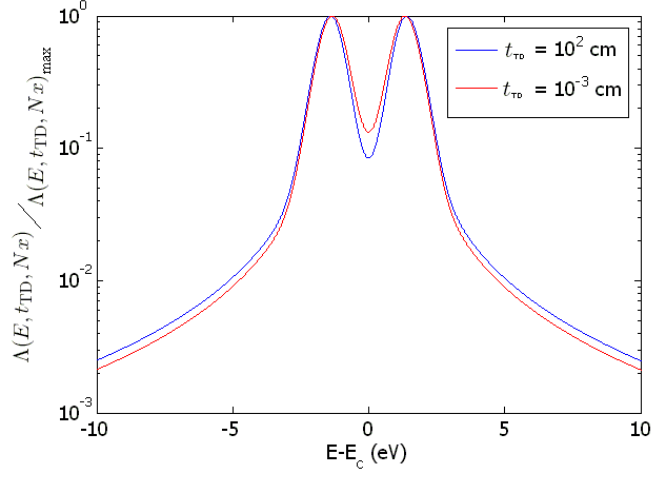
Figure 3.21 Same as Figure 3.20, but for $Nx = 40$ g/cm^2.
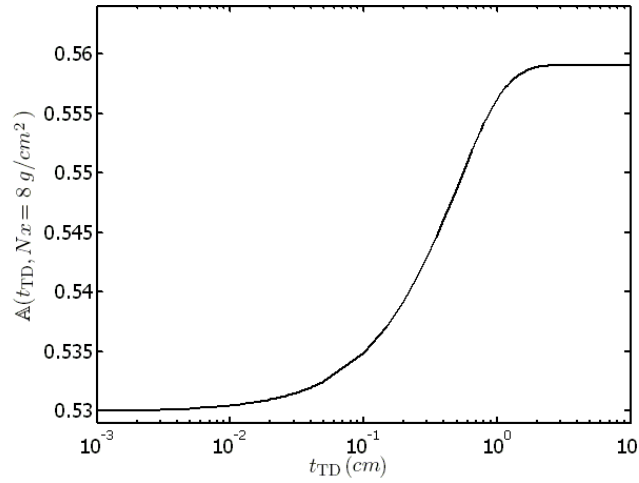
Figure 3.22 The effective attenuation, $\mathbb{A}(t_{\mathrm{TD}}, Nx)$, measured by NRF in the TD of the 2176-keV ^{238}U resonance transition for a target with $Nx = 8$ g/cm^2 plotted as a function t_{TD}.
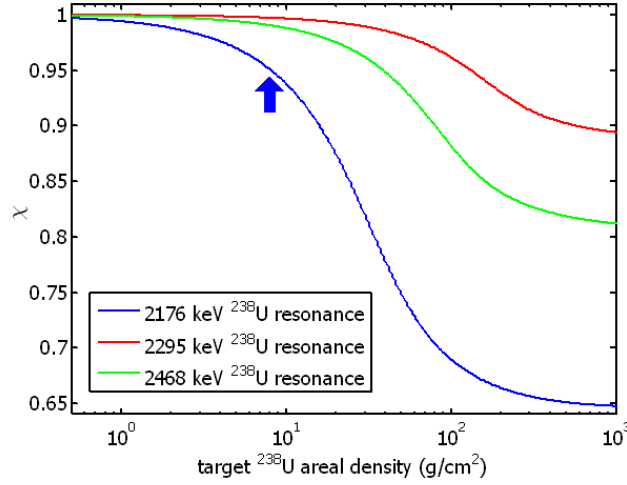
Figure 3.23 Ratios of effective attenuations for the limits of a thin TD to that of a thick TD, $\chi(\rho x)$ for three ^{238}U resonance as a function of ^{238}U areal density in the assay target. The data point from the $\mathbb{A}(Nx)$ curve shown in Figure 3.22 is indicated by the arrow.

The attenuation of resonant-energy photons measured by a thin TD is expected to be smaller than that measured by a thick TD and the difference between these increases for higher areal densities of the IOI in the assay target. It is also more significant for larger resonances than for smaller resonances. A thicker TD is more sensitive to photon energies corresponding to the tails of a resonance. Hence, photons with these energies are less attenuated while penetrating through the assay target, resulting in larger effective attenuation values.

The effects of the TD thickness, related to the observed value of $\mathbb{A}(Nx)$, is examined by comparing between very thin and thick TDs in somewhat more detail. We define the ratio of $\mathbb{A}(t_{\mathrm{TD}}, Nx)$ for a thin TD to that for a thick TD as:

$$\chi(Nx) = \frac{\lim_{t_{\mathrm{TD}}\to 0} \mathbb{A}(t_{\mathrm{TD}}, Nx)}{\lim_{t_{\mathrm{TD}}\to\infty} \mathbb{A}(t_{\mathrm{TD}}, Nx)} \tag{3.39}$$

$\chi(Nx)$ is plotted for three resonances as a function of assay target ^{238}U areal densities in Figure 3.23. Also in this figure is an arrow indicating the data point from the $\mathbb{A}(Nx)$ curve shown in Figure 3.22.

Figure 3.23 provides insight into the validity of the thin-TD approximation represented in equation 3.36. The quantity, χ, is the amount by which the thin-TD approximation would underestimate, $\mathbb{A}(Nx)$ for a given resonance. Chapter 4 describes a transmission assay experiment in which the TD and assay target were ^{238}U. The areal density of the TD was $\sim$8 g/cm^3, and the ^{238}U content in the target was varied up to $\sim$8 g/cm^3. For the analysis of this experiment, use of the thin-TD approximation would have resulted in predictions of $\mathbb{A}(Nx)$ that are inaccurate by up to 5%.

The discussion above indicates the importance of accurately modeling or calibrating an assay system that uses transmitted resonant-energy photons. This is especially true for assay targets with large IOI areal densities or when very strong resonances must be dealt with. It should also be clear that the shape of the resonance must be modeled with rather high quality in order that the transmitted NRF signal be predicted reasonably well. This point is examined in further detail in the Section 3.2.3 for common approximate cross section profiles.

3.2.3   Approximate NRF Cross Section Models

Measurement of the effective attenuation of transmitted resonant-energy photons in the previous section tacitly assumed that all resonances take the Doppler-Broadened Lorentzian Profile (DBLP) given in equation 2.99. However, approximate forms of the DBLP are often assumed. This may be due to format limitations, as described in Section B.1.5. Also, approximating a resonance as a constant may appear to be an attractive simplification, but in this section, it shall be demonstrated that this approximation is too broad for practical use in modeling NRF transmission measurements and experiments.

The forms considered for resonance shapes are:

- a Maxwell-Boltzmann profile of equation 2.95 with width, Δ, given by equation 2.96;

- a point-wise evaluation of the preceding form with linear interpolation between points. The energies at which the Maxwell-Boltzmann distribution was evaluated are the centroid energy, E_C and $E_C \pm 2$ eV and $E_C \pm 4$ eV; and

- a step increase and decrease as defined in equation 3.8.

The cross section from each model is normalized such that the integrated cross section is the same as that of the natural cross section. These functional forms with shape parameters due to the 2209-keV resonance of $^{238}\text{U}(87)$ are shown in Figure 3.24.

The flux transmitted from the target impinges upon a transmission detector made of the IOI. The rate at which a detector viewing the TD registers NRF counts will be given by equation 3.34. As discussed in Section 3.2.2, when determining the effective attenuation of resonant-energy photons in the assay target, the non-resonant portions of equation 3.34 will cancel when comparing NRF rates with those due to a reference assay target. The quantity, $\mathbb{A}$ is the expected effective attenuation for photons with energies close to that of a specific NRF resonance during the transmission measurement. It is given by

$$\mathbb{A}(Nx) = \frac{\int \Lambda(E, t_{\text{TD}}, Nx) dE}{\int \Lambda(E, t_{\text{TD}}, Nx = 0) dE} \tag{3.40}$$
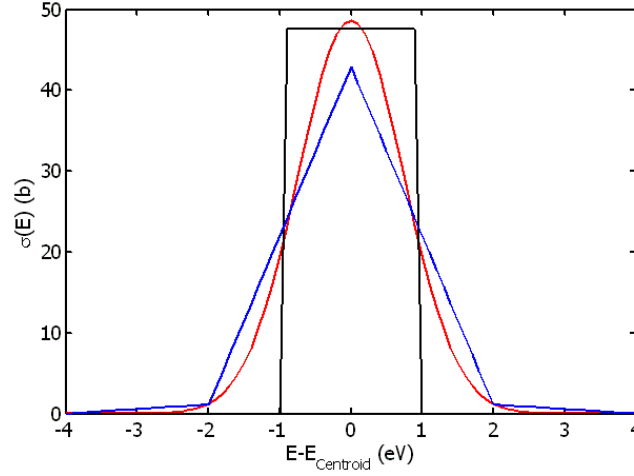
Figure 3.24 Model forms of the resonance cross section profile. Width and total cross section values are from the 2209 keV resonance of ^{238}U. Red = Maxwell-Boltzmann, Blue = point-wise, and Black = step function.

The results from this expression, for the different model approximations of the cross section profile for the 2176-keV resonance of ^{238}U are shown in Figure 3.25. The ratio calculated using the step function distribution quickly becomes very inaccurate, whereas that calculated using the Maxwell-Boltzmann profile and the point-wise evaluation of the Gaussian follow that of the DBLP more closely. The errors associated with these models, relative to the profile given by a DBLP, are shown in Figure 3.26. Use of the Maxwell-Boltzmann profile tends to underestimate the effective NRF response of the TD, relative to the most precise model, whereas the point-wise evaluation of the Maxwell-Boltzmann profile with linear interpolation between the points results in an over-estimation.

Clearly, the assumed shape of the resonance cross section profile has a significant effect on the calculated effective attenuation of resonant-energy photons. The shape becomes more important as the areal density of the IOI increases in the target. We conclude that in the context of transmission-based assay of material, a cross section profile model should be used cautiously and that a step function model is intrinsically inaccurate. It is relevant to note here that the NRF datafiles discussed in Appendix B are based on the point-wise evaluation model.

3.2.4   Expected Precision for Measurement of Actinides in Spent Fuel

In this section, we examine the precision at which the actinide content may be measured in spent by way of a transmission NRF measurement. First, the range at which Pu concentrations are expected in spent fuel will be discussed, followed by a statistical argument to relate counting statistics to the areal density of the IOI in the
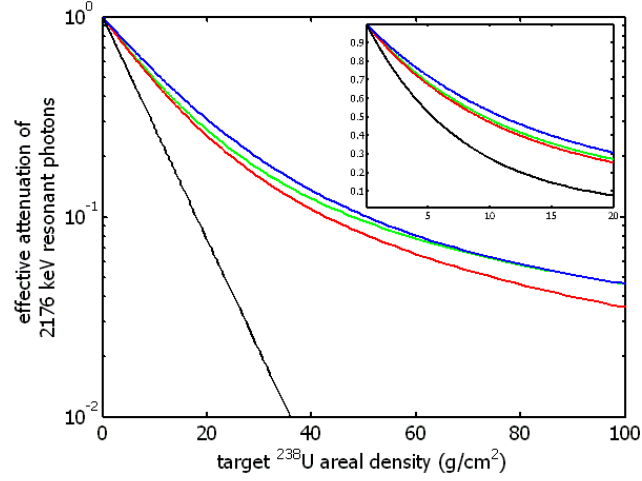
Figure 3.25 The effective attenuation, $\mathbb{A}$ of NRF photons due four models of the 2176-keV ^{238}U NRF resonance profile. The curves correspond to the following cross section profile models: green = DBLP, red = Gaussian, blue = point-wise evaluation of Gaussian with linear interpolation, and black = step-function.
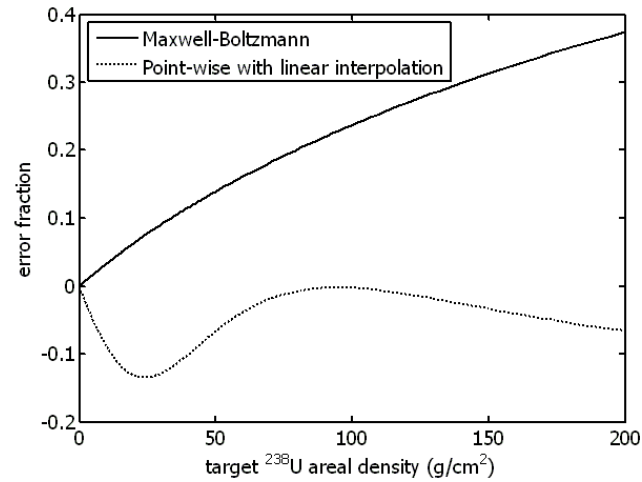
Figure 3.26 Errors resulting from simplified model calculations of the effective NRF attenuation of photons near the 2176-keV ^{238}U NRF resonance relative to that of the DBLP given by equation 2.99.

sensitive volume. Following this, the relationship between statistical uncertainties in the effective attenuation of resonant photons and the uncertainty of the areal density will be derived with an example to estimating the expected precision with which ^{239}Pu content may be measured using a bremsstrahlung spectrum. Next, although the NRF response of ^{240}Pu has not been measured, known NRF resonances of ^{238}U are used to estimate the precision with which a transmission measurement might quantify ^{240}Pu content in spent fuel assemblies. Finally, a generalization between the strength of a resonance and the relative statistical uncertainty a measurement of this resonance would provide is made for low-attenuating assay targets.

Pu Content in Spent Fuel

In reference(4), Phillips presents calculations of the concentrations of Pu isotopes in spent fuel as a function of fuel burn-up. These values were calculated using the computer code CINDER(128) and are shown in Figure 3.27. Phillips indicates that Pu concentrations are expected to be accurate to ± 10% when the reactor spectrum is well-known, and up to ± 25%, if only the type of reactor is known. Because the Pu concentrations are a function of the reactor type, the plutonium concentration values are used to estimate a region of relevant target areal densities. For a typical 15 x 15 fuel assembly, the average areal densities of ^{239}Pu and ^{240}Pu traversed by photons normally incident upon the side of an assembly are $Nx \approx 0.25$ g/cm^2 and ≈ 0.15 g/cm^2, respectively.
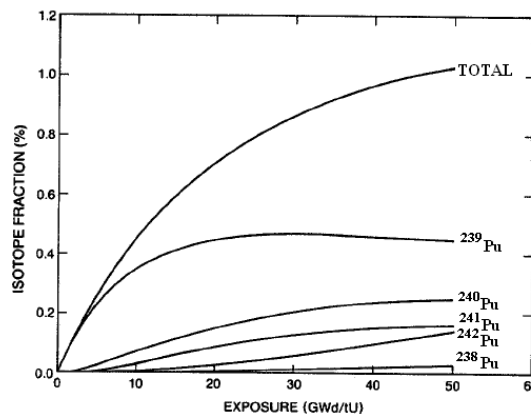
Figure 3.27 Example of computed Pu concentrations in spent fuel as a function of LWR reactor burn-up(4). The figure is reproduced this reference. The ordinate is percentage of Pu atoms to the initial uranium atoms present in the fuel.

Expected Precisions of Areal Density Measurement

Assume there exists a function for each NRF resonance, $f(Nx) \equiv C$ that relates the number of full-energy NRF γ-ray counts, C to the areal density of the IOI in the

target, Nx. Nx is then given by,

$$Nx = f^{-1}(C) \tag{3.41}$$

Likewise, uncertainty in Nx can be written as

$$\sigma_{Nx} = \left| \frac{df^{-1}}{dC} \right| \sigma_C \tag{3.42}$$

Neglecting down-scatter of photons while they penetrate the assay target and the TD, the expected number of γ-ray counts, C, due to NRF in the TD may be expressed as

$$C \equiv f(Nx) = c_t \Phi_0 \exp(-\mu_{\text{atom}} x) \mathbb{A}(Nx) N_{\text{TD}} \sigma_{NRF} \frac{P_f \epsilon \Delta \Omega}{r_{det}^2} \tag{3.43}$$

where c_t is the duration of the measurement, and all remaining terms have been defined previously. Only $\mathbb{A}(Nx)$ in equation 3.43 is dependent upon N, the density of the IOI in the assay target. We re-express $f(Nx)$ as,

$$f(Nx) = \chi \mathbb{A}(Nx) \tag{3.44}$$

where

$$\chi \equiv c_t \Phi_0 \exp(-\mu_{\text{atom}} x) N_{\text{TD}} \sigma_{NRF} \frac{P_f \epsilon \Delta \Omega}{r_{det}^2} \tag{3.45}$$

This is the number of NRF γ-ray counts that are expected to be measured from the TD in the absence of IOI atoms in the assay target.

The function, $f(Nx)$ is therefore directly proportional to $\mathbb{A}(Nx)$, the effective attenuation. Unfortunately, the functional form of $\mathbb{A}(Nx)$ is somewhat complex, and it cannot be analytically differentiated.

$\mathbb{A}(Nx)$ has been shown for many ^{238}U resonances in Figure 3.18 in the case that the TD is 8 g/cm^2 of ^{238}U. Figure 3.28 shows $\mathbb{A}(Nx)$ for ^{239}Pu resonances and a TD thickness of 8 g/cm^2 of ^{239}Pu. The stronger resonances of ^{238}U result in functions of $\mathbb{A}(Nx)$ that more rapidly approach zero at lower areal densities and then flatten for higher values of Nx.

To obtain an analytically differentiable function that approximates $f^{-1}(C)$, We consider a fit to $\mathbb{A}(Nx)$ of the form

$$\mathbb{A}(Nx)_{\text{fit}} = \exp(-\alpha_f Nx) \tag{3.46}$$

for the range $Nx \leq 0.5$ g/cm^2, which is approximately the range of areal densities of interest for spent fuel assemblies[6]. Comparisons between fits of this form and $\mathbb{A}(Nx)$ are shown for ^{239}Pu resonances in Figure 3.29. The fit is quite good over the fitted range, but becomes quite poor for higher Nx. Best-fit values of α_f for each ^{239}Pu resonance are shown in Table 3.7 along with measured resonance parameters from reference(123).
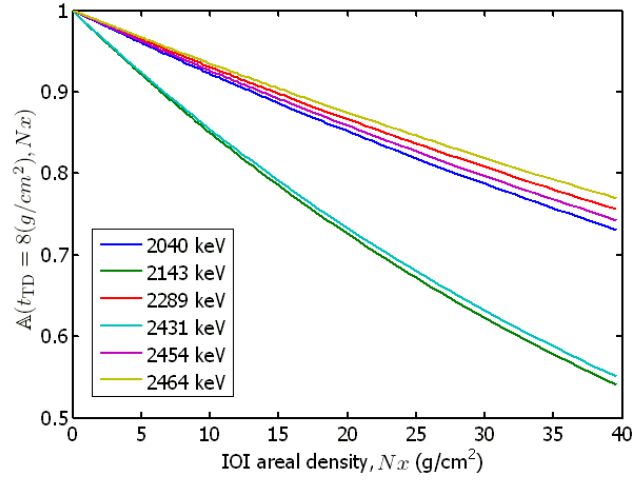
Figure 3.28 The effective attenuation of photons given by equation 3.38 due to ^{239}Pu NRF resonances with $t_{TD} = 8$ g/cm^2. Data for the resonances are shown in Table 3.7 and are from reference (123). Each resonances is indicated by its centroid energy in the legend.
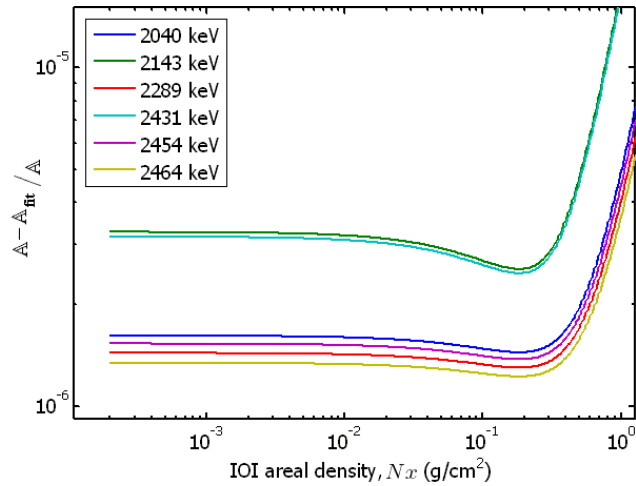
Figure 3.29 Fraction deviation between calculated values of $\mathbb{A}(Nx)$ and those resulting from the best-fit of the form shown in equation 3.46.

E_{level} (MeV)	$g\Gamma$ (meV)		$g\Gamma_0$ (meV)		$\int \sigma_{\text{NRF}} dE$ (eV·b)		α_f (mg/cm^2)	
2.040	4.3	$\pm$ 1.1	4.3	$\pm$ 1.1	8	$\pm$ 2	8.1	$\pm$ 2.1
2.144	13.4	$\pm$ 2.2	10.2	$\pm$ 1.7	17	$\pm$ 3	16.4	$\pm$ 2.7
2.289	5.4	$\pm$ 1.4	5.4	$\pm$ 1.4	8	$\pm$ 2	7.2	$\pm$ 1.9
2.432	30.8	$\pm$ 5.8	14.6	$\pm$ 2.8	19	$\pm$ 4	16.0	$\pm$ 3.0
2.454	7.1	$\pm$ 2.4	7.1	$\pm$ 2.4	9	$\pm$ 3	7.7	$\pm$ 2.6
2.464	6.3	$\pm$ 3.2	6.3	$\pm$ 3.2	8	$\pm$ 4	6.8	$\pm$ 3.4

Table 3.7 ^{239}Pu NRF data. The values of $\int \sigma_{\text{NRF}} dE$ were taken from Reference (123). Where $g\Gamma_0 \neq g\Gamma$, two NRF γ-rays were measured at energies that differ by the excitation energy of the first excited state of ^{239}Pu. It has been assumed that these γ-rays correspond to de-excitation of a single NRF state. Values of $g\Gamma_0$ were calculated from from equation 2.89. The meaning of α_f is explained in the text.

Considering only the cases where $Nx \leq 0.5$ g/cm^2 and using

$$f(C) \approx \chi \exp(-\alpha Nx) \tag{3.47}$$

we can write

$$f^{-1}(C) \approx \frac{\ln \chi - \ln C}{\alpha} \tag{3.48}$$

and

$$\frac{df^{-1}}{dC} = \frac{-1}{C\alpha} \tag{3.49}$$

Using equation 2.107, which relates the statistical precision of a γ-ray counting measurement to the ratio of signal and background intensities, ξ, and substituting equation 3.49 into equation 3.42, we have

$$\sigma_{Nx} = \frac{\sqrt{1 + 2/\xi}}{\alpha\sqrt{C}} \tag{3.50}$$

This relates the precision with which Nx is measured to both counting statistics and the quantity α, which is the magnitude of the slope of the effective attenuation curve at the corresponding areal density.

From equation 3.50, we can infer that large resonances will provide the smallest statistical errors when the IOI areal density in the target is small, but when measuring larger values of Nx, weaker resonances may exhibit more rapidly changing effective attenuation functions, which correspond to larger values of α and resultingly smaller measurement uncertainties.

---

[6]A fit of the form $\mathbb{A}(Nx)_{\text{fit}} = a_1 \exp(a_2 Nx) + a_3 \exp(a_4 Nx)$ provides quite good agreement over a much larger range of areal densities ($\leq 2 \times 10^{-6}$ error fraction for $Nx \leq 30$ g/cm^2), but it also does not provide an analytical form for $df^{-1}(C)/dC$.

E_{level} (MeV)	$\mathbb{A}$	C	ξ	σ_{Nx} (%)
2.040	0.998	7.6×10^6	0.87	32.5
2.144*	0.996	3.4×10^6	0.59	18.9
2.144	0.996	1.1×10^7	1.91	15.4
2.289	0.998	5.5×10^6	1.91	34.0
2.432*	0.996	5.0×10^6	2.44	15.1
2.432	0.996	4.5×10^6	2.72	15.6
2.454	0.998	4.2×10^6	2.60	33.9
2.464	0.998	3.6×10^6	2.34	42.3
total		4.5×10^7		7.3

Table 3.8 Expected effective attenuation values, $\mathbb{A}$, numbers of counted NRF γ-rays due to ^{239}Pu resonances, C, signal-background ratios of the NRF γ-rays, ξ, and statistical relative uncertainties, σ_ρ for the simulated assay described in the text. The assay assumes a 24-hour measurement of a fuel assembly using 170-mA of 2.6-MeV electrons to induce the interrogating bremsstrahlung spectrum and 400 HPGe detectors 100 cm away from the TD. An * indicates that the corresponding NRF γ-ray is due to de-excitation of the NRF state to the first-excited state of ^{239}Pu.

Estimates of Transmission Measurement Precision for Spent Fuel

In the assay of ^{239}Pu in a typical spent fuel assembly), the rate at which a particular resonance undergoes NRF in the TD is proportional to the product of the integrated cross section of that resonance, $\mathbb{A}(Nx)$, and the photon intensity incident upon the TD at the resonance centroid energy. Using Table 3.7 and the photon spectrum given in Figure 3.17, we estimate relative count rates for each of the ^{239}Pu resonances, and use equation 3.50 to estimate the expected experimental uncertainty in a ^{239}Pu areal density measurement. As an example, the uncertainties expected from a 24-hour measurement of a spent fuel assembly using a 170-mA beam of 2.6-MeV electrons are shown in Table 3.8. The estimates assume that 400 100% relative efficiency HPGe detectors are located behind an 8 cm-thick lead filter and 100 cm from a 4 mm-thick TD. In this geometry, 1/3 of the total available backward solid angle is subtendended by the detectors.

To estimate the total uncertainty of the areal density of ^{239}Pu, we assume that the areal density value is determined from a weighted mean of the measured areal densities from each resonance. The weighted mean is given by

$$m_w = \frac{\sum_{i=1}^{n} w_i x_i}{\sum_{i=1}^{n} w_i} \tag{3.51}$$

where n is the number of NRF γ-rays considered (eight for Table 3.8) and the weights

are

$$w_i = 1/\sigma_i^2 \tag{3.52}$$

The standard deviation for the weighted mean is given by

$$\sigma_{m_w} = \sqrt{\sum_{i=1}^{n} \left(\sigma_i \frac{dm_w}{dx_i} \right)^2} \tag{3.53}$$

where

$$\frac{dm_w}{dx_i} = \frac{1}{\sigma_i^2} \frac{1}{\sum_{i=1}^{n} w_i} \tag{3.54}$$

This estimate, based solely on counting statistics is given in the last row of Table 3.8.

The NRF responses of ^{240}Pu and ^{238}Pu have not been been reported in the open literature. However, nuclides with even numbers of neutrons and protons generally have stronger NRF resonances than those with at least one un-paired nucleon (such as ^{239}Pu)[7]. With this in mind, we estimate the accuracy to which a measurement of the ^{240}Pu content in a spent fuel assembly might be obtained. For an expected areal density of 0.15 g/cm^2, and assuming the ^{238}U NRF state characteristics shown in Table 4.5, we estimate a total statistical uncertainty of the areal density of ^{240}Pu of $\sim 1\%$. This demonstrates the importance of the natural widths of measured NRF states.

Resonance Strength and Relative Precisions

To illustrate the importance of the resonance strength for providing precise measurements of target areal densities, we consider a case where Nx is still assumed to be small (i.e. where equation 3.46 remains valid), and compare two hypothetical resonances, a and b. Assume these resonances have widths, Γ_a and Γ_b, respectively, and that $\Gamma_a > \Gamma_b$. The relative uncertainties in areal density that transmission measurements made using resonance a will be reduced by at least

$$\frac{\sigma_a}{\sigma_b} \approx \left(\frac{\Gamma_b}{\Gamma_a} \right)^{1.5-2} \tag{3.55}$$

relative to an identical measurement using resonance b. This is the combination of three factors. First, stronger resonances result in proportionally higher NRF count rates, which, reduces the uncertainty by a factor of $\left(\frac{\Gamma_b}{\Gamma_a} \right)^{1/2}$. Also, stronger resonances increase the slope of the effective attenuation function, α, which result in a relative decrease in uncertainty of approximately $\left(\frac{\Gamma_b}{\Gamma_a} \right)$. Finally, for NRF signals not significantly stronger than background intensity, the term $\sqrt{1 + 2/\xi}$ in equation 3.50 can contribute an additional factor of up to $\left(\frac{\Gamma_b}{\Gamma_a} \right)^{1/2}$.

---

[7]See for example, references(69),(115), and(127)

3.2.5 *Notch Refilling* and Transmission Assay Complications

In transmission measurements, the attenuation of resonant-energy photons in the target provides the signal that relates to areal density of the IOI in the target. The attenuation results in a decrease in the flux intensity at energies in the immediate vicinity of the resonance centroid. The transmitted spectrum will then display a reduction in intensity whose shape is directly related to the excess attenuation produced by the resonance. This is often referred to as a *notch*. *Notch refilling* is the process by which interrogating photons are down-scattered into the notch during transport through the assay target and TD. The down-scattering of photons results in more resonant-energy photons leaving the assay target than would be predicted by the model described in Section 3.2.2. In this section, the relative intensity of the notch-refilling effect is considered.

The extent of notch filling will be dependent on the details of the experimental geometry. The smaller the solid angle subtended by the TD, the more restricted is the geometry for notch refilling. Likewise, increasing the number of photons that have more energy than the excitation energy of a resonance increases the likelihood that some of these photons will down-scatter into the notch created by resonant absorption.

The processes that result in notch refilling are incoherent scattering and bremsstrahlung emitted from photo-electrons. As demonstrated in Chapter 2, both processes predominantly produce down-scattered photons predominantly in forwards angles. Those photons that are down-scattered into a resonant energy and toward the TD effectively refill the notch.

To examine this effect, we first consider a Monte Carlo simulation of 2.3-MeV photons incident upon an assay target. The target consisted of 7 cm-thick slab of Pb behind a 4.4 mm-thick slab of uranium, which is comparable to the average areal density of a fuel assembly[8]. The energy spectrum of photons leaving the assay target within 4.4º of the initial direction were calculated. The results of this simulation are shown in Figure 3.30. Full-energy photons and those that have undergone a single incoherent scattering are the most probable sources of emitted photons. The photons that undergo a single incoherent scattering produce a continuum of energies. Pair production and subsequent positron annihilation, multiple-scattering events, and secondary electron bremsstrahlung produce the events indicated below the Compton continuum.

A 2.3 MeV initial energy photon undergoing incoherent scattering with $\theta \leq$ 4.4º results in a scattered photon with energy $E' \geq 2.27$ MeV. This energy is the lower energy of the Compton continuum. The probability per 2.3-MeV incident photon for an emitted photon to be down-scattered into the Compton continuum is approximately 2×10^{-8} per eV. Doppler-broadened NRF resonances tend to have

---

[8]It is also very similar to the geometry of the experiments described in Chapter 4
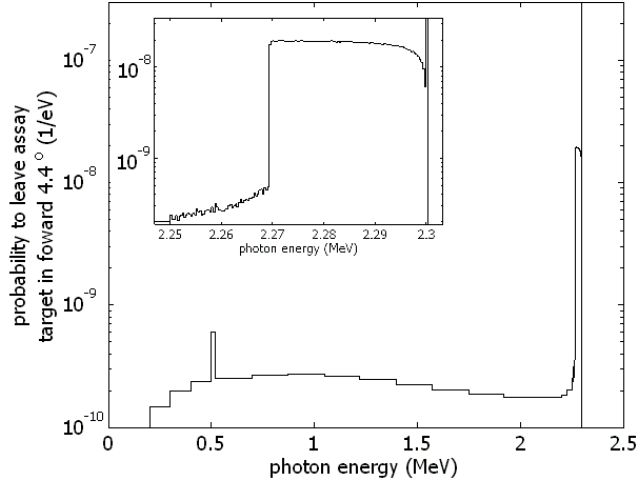
Figure 3.30 Calculated spectrum of photons leaving a target of areal density similar to a homogenized fuel assembly within 4.4º of the initial photon direction. The incident photon energy was 2.3-MeV. The inset shows a larger view of the energy range of 2.25 - 2.3 MeV. The probability that an incident photon leaves the target un-attenuated is 2.1%.

$\Gamma \approx 1.5$ eV, thus we can assume 3×10^{-8} per eV is a reasonable probability for down-scattering of 2.3-MeV photons into its Compton continuum for assay targets of similar areal densities as fuel assemblies.

To consider the potential for refill of a given resonant notch, only photons incident upon the assay target whose Compton continuum includes the resonance energy are of importance. If the TD only subtends a polar angle of 4.4º only photons with $E - E_{res} \lesssim 35$ keV need be considered. From Figure 3.16, we expect $\sim 2 \times 10^8$ photons/eV/Coulomb to impinge upon the assay target in the energy range of 2 - 2.4 MeV. Combining this source photon rate with the notch-refill probability ($\sim 2 \times 10^{-8}$ per eV) and the range of energies of interest, we expect $\sim 1.4 \times 10^5$ notch refill events per Coulomb of electrons incident upon the Bremsstrahlung converter. From Figure 3.17, we also expect in the absence of resonant attenuation, $\sim 4.5 \times 10^6$ photons/eV/C to be incident upon the TD between 2 and 2.4 MeV. Thus, photons that arrive at the TD, after down-scattering, represent 2-5% of the total flux in this energy range.

From these estimates, we expect that notch refilling will result in a slight decrease in the slopes of the effective attenuation curves, $\mathbb{A}(\rho x)$ compared to those predicted by neglecting notch refill. This, in turn, would slightly increase the statistical uncertainties estimated in Table 3.8 and the surrounding discussion. Nevertheless, notch refilling would change the statistical uncertainty estimates for a measurement of a Pu isotope in spent fuel significantly less than the contributions from uncertainties in the measured NRF cross sections. We therefore conclude that while notch refilling is likely to be an important factor in achieving an absolute areal density

measurement with precision near 1%, the NRF cross sections must be known to far better precision before this level of uncertainty can be reached.

3.2.6   Transmission Assay using Quasi-monoenergetic Photon Sources

We consider using a quasimonoenergetic photon source to interrogate the 2431-keV resonance in ^{239}Pu in an identical transmission assay geometry as previously discussed in this chapter. For simplicity, we assume the intensity of source photons is uniform over an energy range of 25 keV. Thus for every $\Delta E_{beam}/\Gamma_D \approx 2 \times 10^4$ photons produced by this quasi-monoenergetic source a single resonant-energy photon is produced. For the sake of argument, we assume that the intensity of a monoenergetic photon source is unlimited[9].

Probabilities that source photons penetrate the assay target (assumed to be a 15x15 homogenized fuel assembly), impinge upon the TD, and are detected in a shielded detector, located 100 cm from the TD, were calculated for photons that undergo NRF (p_{NRF}), and for photons that undergo non-resonant backscattering in the TD (p_{bkg}). These probabilities were calculated for selected thicknesses of the filter, x_f. Because non-resonantly backscattered photons are predominantly lower-energy, p_{bkg} decreases more rapidly with x_f than p_{NRF}, and until x_f becomes quite large, thicker filters result in a larger fraction of detected photons being due to resonant interactions in the TD.

The precision with which the areal density of an IOI in the target is measured is given by equation 3.50, which may be inverted to define the number of NRF counts, C, necessary to conduct a measurement at a given statistical precision. For an interrogation to be accomplished with this precision, the number of resonant-energy photons that must irradiate the assay target in the direction of the TD is then $N_{res} = C/p_{\mathrm{NRF}}$, and likewise the total number of photons that must be produced to make N_{res} resonant photons is

$$N_{tot} \approx \frac{C}{p_{\mathrm{NRF}}} \frac{\Delta E_{beam}}{\Gamma_D} \tag{3.56}$$

If we limit the total count rate at which a detector operates to 2×10^4 c s^{-1}, we can estimate how long a measurement would take to obtain a given statistical uncertainty from a single detector. A summary of estimates of the times and the beam intensities required to provide a statistical uncertainty of 5% on a fuel assembly with a ^{239}Pu content of 0.25 g/cm^2 are shown in Figure 3.31. In this regime, counting statistics scale with $\sqrt{C}$, and therefore a measurement that provides a statistical uncertainty of 1% would take 25 times as long or need 25 times as many detectors.

---

[9]This assumption is not currently practical. HIγS(100) claims to be able to generate $10^7 \gamma$/s, and other quasimonoenergetic photon sources are under development, see(101) and (105).
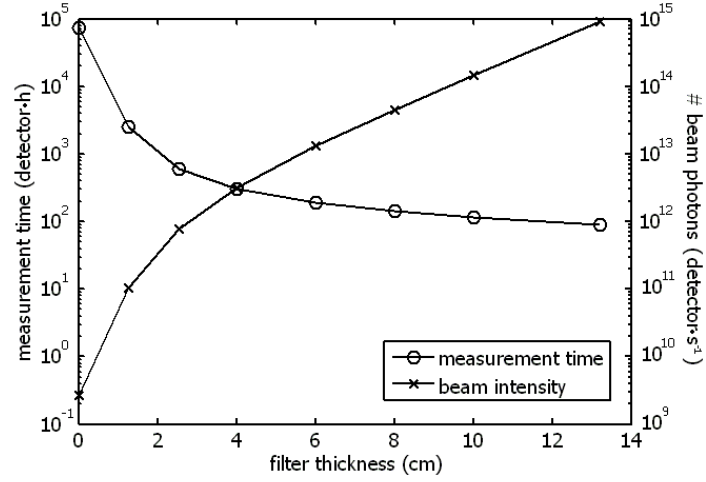
Figure 3.31 Estimated measurement times and necessary photon fluences incident upon assay target to make a 5% relative statistical uncertainty measurement of ^{239}Pu content in a spent fuel assembly assuming its areal density is 0.25 g/cm^2 using a single 100% relative efficiency HPGe detector. Both quantities are inversely proportional to the number of detectors used.

Finally, if we restrict the duration of a measurement, we can determine the number of detectors that would be necessary to obtain a given statistical uncertainty. This value is a function of beam intensity and filter thickness. In Table 3.9, we assume a filter thickness, x_f, and assume the beam is sufficiently strong to induce 2×10^4 c s^{-1} in the shielded 100% relative efficiency HPGe detectors. We then determine the number of such detectors that would be needed to obtain 5% and 1% statistical uncertainties in a 24 h measurement. These values are tabulated for varying filter thicknesses and assume that the 2431-keV resonance of ^{239}Pu was excited to measure 0.25 g/cm^2 of ^{239}Pu in a fuel assembly or that a hypothetical 90-eV·b ^{240}Pu resonance near 2.3 MeV was excited to measure 0.15 g/cm^2 of ^{240}Pu. The hemisphere corresponding to backward scattering angle has a surface area of $\sim 6 \times 10^4$ cm^2, which implies that the assumed geometry which could not physically accommodate more than 1×10^3 100% relative efficiency HPGe detectors.

We conclude by noting that the photon source intensity necessary to induce 2×10^4 c s^{-1} from the TD in a detector with no filter is $\sim$6 times as intense as that of HIγS, and increases to $\sim$2 $\times 10^3$, 10^5, and 2×10^6 times as large for $x_f = 2.54$, 8, and 13.2 cm, respectively. Source intensities several orders of magnitude stronger than HIγS could make high-precision measurements of plutonium content in a spent fuel assembly using a nuclear resonance fluorescence technique practical.

x_f (cm)	Number of HPGe for 5% measurement		Number of HPGe for 1% measurement	
	^{239}Pu 0.25 g/cm^2	^{240}Pu 0.15 g/cm^2	^{239}Pu 0.25 g/cm^2	^{240}Pu 0.15 g/cm^2
0	**3102**	93.7	**77555**	**2342**
1.27	105	3.2	2627	79.4
2.54	25.3	0.76	631	19.1
4	12.7	0.38	318	9.6
6	7.9	0.24	198	6.0
8	5.9	0.18	148	4.5

Table 3.9 Estimated numbers of 100% relative efficiency HPGe detectors necessary to make indicated measurement in 24 h versus filter thickness, x_f. Numbers in **bold** indicate that the solid angle subtended by this number of detectors is larger than 2π and therefore the measurement cannot be made in this geometry in 24 hours. Values smaller than unity indicate that the measurement could be accomplished with a smaller detector or a shorter measurement time. The detectors are assumed to operate at 2×10^4 c s^{-1} in all cases.

Chapter 4

Experimental Measurement of Resonant-Energy Transmission Assay for Nuclear Fuel Assemblies

In order to test the validity of the transmission assay modeling performed in Section 3.2.2, an experiment was conducted in collaboration with Passport Systems Ltd. at the High Voltage Research Laboratory at Massachusetts Institute of Technology. The experiment involved a series of irradiations in which 2.6 MeV electrons were impinged upon a bremsstrahlung converter. The bremsstrahlung emitted from the converter was collimated toward an *assay target* – composed of varying amounts of Pb and depleted uranium (DU). These targets acted as surrogates for real spent fuel assemblies, which are more difficult to obtain and handle. Behind the target, a stack of DU plates functioned as the transmission detector (TD) material. Four HPGe detectors, heavily shielded from direct bremsstrahlung and photons scattered from the target, were placed facing the TD material behind 0.5 inches of Pb, at an angle of 118° from the centroid direction of the bremsstrahlung collimator opening. A schematic drawing of the experimental setup is shown as Figure 4.1.

The assay target material attenuates the interrogating bremsstrahlung beam. When ^{238}U is present, the beam is additionally attenuated at energies corresponding to ^{238}U resonances, producing *spectral notches*. The transmission detector material is composed of DU and the ^{238}U it contains will undergo NRF at a rate proportional to the quantity of resonant-energy photons incident upon the TD. The HPGe detectors are positioned to measure the backscattered radiation from the TD, and therefore the rate at which constituent ^{238}U atoms undergo NRF. The reduction in the measured NRF rate, relative to that when there is no DU in the assay target, is proportional to the areal density of ^{238}U that photons encounter while they traverse the target.
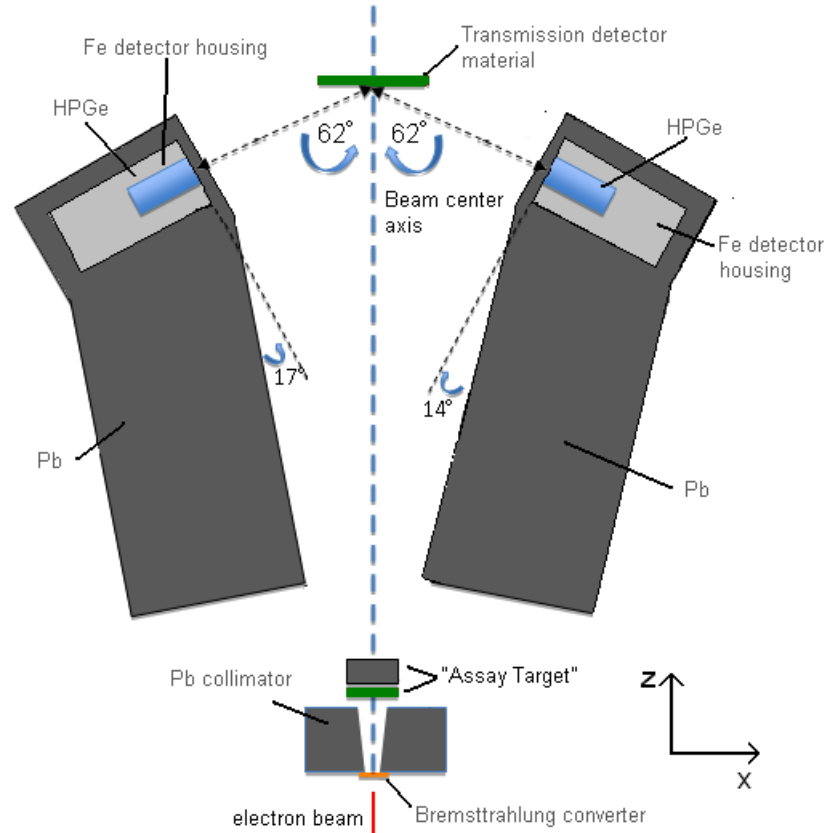
Figure 4.1 Schematic drawing of experimental setup. See text in Section 4.2 for detailed description.

4.1   Experimental Motivation

The experimental goals included the following:

1. test whether notches produced by resonant absorption would remain after beam penetration through a material of comparable attenuation characteristics as that of a spent fuel assembly;

2. demonstrate the applicability of the transmission foil measurement method to measure a percent-level isotopic abundance using a bremsstrahlung photon source; and

3. test beam-current normalization schemes.

The first goal is of utmost importance for the purpose of assaying spent fuel assemblies with NRF. If, while the interrogating beam is transmitted through the assembly, the spectral notches are refilled through photon down-scattering, they will be smaller or non-existent when the beam reaches the TD material. This would limit

the thickness of material for which resonant-energy transmission assay would be useful. Measurements using nearly monoenergetic photon sources have indicated that notch refilling is not measurable for thick targets (129), however this measurement is the first such experiment testing whether notch refilling is problematic for thick target resonant-energy transmission assay using a bremsstrahlung photon source.

Typical fuel assemblies contain fuel pin arrays ranging from 10x10 to 17x17(130). As examples, relevant assembly dimensions are given for the decommissioned Rancho Seco reactor, formerly located in Clay Station, CA and the operable Diablo Canyon 2 reactor located in Avila Beach, CA in Table 4.1. Zr-4 indicates Zircalloy-4, a zirconium alloy of density, $\rho_{Zr-4} = 6.55 \text{g/cm}^3$, containing 1.2-1.7 weight percent (wt.%) Sn, 0.18-0.24 wt.% Fe, and 0.07-0.13 wt.% Cr(131). Using $\rho_{UO_2} = 10.97 \text{g/cm}^3$, we calculate the average areal density experienced by a particle normally incident upon the side of a typical fuel assembly to be approximately 85 g/cm^2.

The second goal is tested by varying the composition of the assay target during the experiment. Table 4.2 summarizes target geometries assayed during the experiment, with the x used to indicate thicknesses and ρx, the areal density. The ^{238}U atom fraction assayed varied from 8.5% to 1.7% in targets of approximately 85 g/cm^2. The total attenuation (μx, the quantity μ/ρ is given by XCOM(29)) of the mock-up assemblies differed from a homogenized Rancho Seco assembly by no more than 1.2% for photon energies between 2 and 2.5 MeV. Likewise, between 2 and 2.5 MeV, the fraction of the attenuation coefficient due to incoherent scattering was no more than 2% smaller than that for the Rancho Seco homogenized assembly. Thus, we conclude that the assembly mock-up targets have very similar photon transport characteristics to those of homogenized fuel assemblies. The question of whether a homogenized assembly would behave similarly to a real assembly in resonant-energy transmission assay is of interest, and is the topic of ongoing research.

Because we compare the attenuation of resonant-energy photons through an assay target to the attenuation of photons through a target blank (Run# 1), we must also be able to compare the intensity of resonant-energy photons that reached the targets between runs. This proved more complicated than one might think. The beam-current monitoring system was nominally accurate to 5%, which is insufficient for this experiment. Materials (^{11}B and ^{55}Mn) were placed behind the TD to undergo NRF and function as beam monitors, but the rate at which their NRF photons were measured was too low to provide statistically valuable information. However, photons reaching the TD at near-resonant energies (in this case 2 - 2.4 MeV) frequently undergo pair-production. The subsequent annihilation of positrons results in 511-keV γ-rays, which are the most prominent feature in the HPGe detector spectra. Therefore, the statistical uncertainty with which spectral normalization occurs via the intensity of annihilation photons is extremely small. The possibility of systematic errors associated with this normalization method is discussed in Section 4.5.6.

	Rancho Seco	Diablo Canyon #2
pellet diameter (mm)	9.36	7.844
fuel material	UO_2	UO_2
clad thickness (mm)	0.67	0.57
cladding material	Zr-4	Zr-4
pin outside diameter (mm)	10.9	9.1
fuel rod pitch (cm)	1.44	1.26
geometry	15x15	17x17
fuel rods per assembly	208	264
homogenized areal density (g/cm^2)	86.28	77.67

Table 4.1 Relevant fuel assembly geometric information for the Rancho Seco and Diablo Canyon 2 nuclear reactors. Data were taken from International Nuclear Safety Center (INSC) website(130). Homogenized areal density values were calculated from preceding data.

Run #	nominal x_{DU} (mm)	measured m_{DU} (g)	nominal x_{Pb} (in)	measured x_{Pb} (cm)	total ρx (g/cm^2)	^{238}U atom%	^{238}U wt.%
1	0	0	3	7.607	86.260	0	0
2	4	3310.0	2 $^{3}/_{4}$	7.001	87.862	8.48	9.62
3	0.8	659.2	2 $^{15}/_{16}$	7.505	86.796	1.69	1.94
4	1.6	1306.9	2 $^{7}/_{8}$	7.336	86.537	3.37	3.86

Table 4.2 Assay target compositions used in resonant-energy transmission assay experimental test. Pb density assumed to be 11.34 g/cm^3, DU plates were measured to be square with 19.752 cm length, and assumed to be 99.799% ^{238}U by mass. Uncertainties in DU target masses are approximately 1%.

4.2   Experimental Arrangement

A schematic drawing of the experiment viewed from above is shown in Figure 4.1. Measured distances used to construct this drawing follow:

- Pb collimator to transmission detector material: 56" (z-direction);

- HPGe detectors all faced the intersecting line of the beam center vertical axis and the horizontal center of TD material. Their distances from this line are:

    - top-right HPGe $10^3/_4$";
    - bottom-right HPGe $10^1/_2$";
    - top-left HPGe $10^3/_4$";
    - bottom-left $10^7/_8$";

- each HPGe detector was facing the center of TD at an angle of 118º relative to the beam centroid direction;

- bottom-right corner of left Pb shielding block:

    - 19" (z-direction) from collimator;
    - $3^1/_8$" (x-direction) from beam center axis;

- bottom-left corner of right Pb shielding block: $18^1/_2$" (z-direction) from collimator;

- Fe detector housings outer measurement: 5" square;

- detector housing Fe thickness: $^1/_4$";

- Fe detector housing depth: 8"

- maximum distance between left and right Fe detector housings: $19^7/_8$" (x-direction);

- minimum distance between left Fe detector housing and beam center axis: $5^7/_8$" (x-direction);

- down-beam diameter of collimator hole: 1";

- up-beam diameter of collimator hole: 1 cm;

- Pb collimator: 8"-thick (z-direction);

- collimator Pb block width: 20" (x-direction);

- collimator Pb block height: 18" (y-direction);
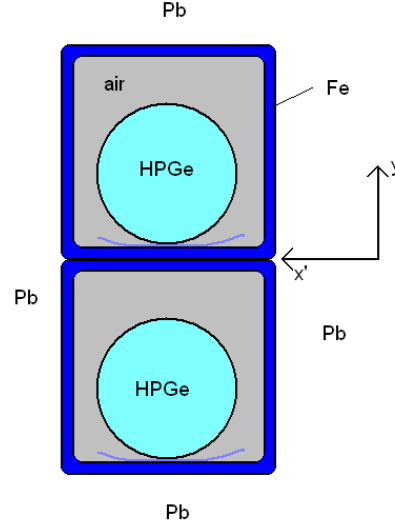
Figure 4.2 Schematic drawing of detector housing arrangement.

- heights (y-direction) of left and right Pb shielding blocks increase in height from 12" to 20" in regular intervals as the Pb block neared the detector housing;

- base plane on which Pb was stacked: 7" below horizontal beam center.

A drawing of the HPGe detector housing is shown as Figure 4.2. The dimension x' is rotated $\pm 62°$ around the y axis, relative to x indicated in Figure 4.1 ($+62°$ for the left-hand detector housings and $-62°$ for the right-hand housings). The housings were entirely enclosed in Pb, 4"-thick in the down-stream direction ($\pm$ x'), 7"-thick in the (+y)-direction, 3"-thick in the (-y)-direction and abutting the large Pb blocks in the up-stream direction. One 6" x 12" x $\frac{1}{2}$" sheet of Pb was placed in front of each detector housing to function as a low-energy γ-ray *filter*. Behind the detector housing, irregularly shaped Pb blocks were positioned to allow through the detector readout, bias wiring, and the mechanical cooling connector, while maintaining approximately 2" of Pb, where possible. Each detector was connected to a mechanical cooling system by a 2" diameter hose. 8" x 4" x 2" lead blocks with 2" diameter semicircular cutouts were placed around the cooling hose. This shielding configuration constrained where the detector faces could be located in the housing and resulted in differing distances between the TD and the front faces of the HPGe detectors.

The bremsstrahlung converter was reported to be 102 μm of Au deposited on a 1 cm-thick Cu backing. It was water cooled and $\sim$3 mm of flowing water passed downstream of the Cu backing.

The electron beam was brought into the experiment hall via a 4" diameter steel beam-pipe entering from the room above. The floor separating the rooms was approximately 18" of concrete and was located $\sim$44" above the horizontal beam center.

The electron beam (and beam-pipe) bent 90° 18" upstream of the bremsstrahlung converter. The beam-pipe was held at 1×10^{-5} torr, except during Run #2 where a turbo pump was malfunctioning and the beam-pipe was held at 8×10^{-6} torr. The concrete floor was located 44" below the horizontal beam center. The Pb shielding and detector blocks were located on 80/20® aluminum tables. The left tabletop was 3" below the beam center and the right tabletop was $6\frac{1}{2}$" below beam center. The extra space was filled with Pb directly below the detectors and a combination of cement blocks and plywood sheets beneath the large Pb shielding block.

The electron source was a 3 MV Van de Graaff accelerator. The accelerator was operated at a voltage of 2.60 ± 0.03 MV and a current of 65 ± 7 μA. The dimension of the electron beam spot could not be directly measured, but was smaller than the 1 cm dimensions of the bremsstrahlung converter when beam operation was stable. After approximately four hours of running, the accelerator would become unstable and require re-conditioning for approximately one hour. A small ionization chamber was located directly outside of the collimator hole to monitor the beam. Also an x-ray imager was located $\sim$2' downstream of TD assembly. The current deposited within the bremsstrahlung converter was also measured. Unfortunately, beam focusing and alignment were not stable, thus the current deposited within the bremsstrahlung converter was not closely correlated with the dose rate measured by the ionization chamber beyond the collimator. When beam irregularities occurred, they resulted in visible distortions on the x-ray imager. The accelerator operator would then adjust beam focusing. Most irregularities lasted for less than 5 s.

The TD consisted of five 8" x 8" DU plates that were nominally 0.8 mm-thick. Each plate was contained in two plastic bags. The 8" side dimensions of the plates were confirmed by measurement. The total mass of the five plates plus the containment bags was measured to be 3341.7 ± 3.3 g. Two of the outer bags were measured to weigh 10.1 ± 0.1 and 9.9 ± 0.1 g respectively. The inner bags were slightly heavier and have been assumed to weigh 15 ± 5 g. Thus the DU mass is expected to be 3226.7 ± 28 g. A 222 ± 1 g Mn disc was taped to the back of the DU plates in the center of the bremsstrahlung beam to function as a NRF beam-flux monitor. The rate of Mn NRF counts was found to be insufficient and a petri dish containing 82.3 ± 0.5 g of 99.52% enriched ^{11}B was also added directly behind the Mn during Run #1. Before Run #3, an additional 102.8 ± 0.5 g of enriched ^{11}B was placed behind the Mn disc, at which point the discs were arranged as indicated in Figure 4.3.

The DU in the assay target was also comprised of 8" x 8", nominally 0.8 mm-thick plates packaged in two plastic bags. The masses of these plates were only measured while they were within two plastic bags. These masses, the runs in which the plate was used, and the estimated DU masses after subtraction of the masses of the bags are shown in Table 4.3

Data were collected over the course of four days during 8 - 12 hour daily shifts. Each run consisted of approximately 6.5 hours beam live time. Three overnight radioactive background counts were conducted during the nights between shifts. The

Run #	mass in bags (g)		mass (g)	
2,3,4	684.2	± 0.7	659.2	± 6
2,4	672.7	± 0.7	647.7	± 6
2	726.1	± 0.7	701.1	± 6
2	679.7	± 0.7	654.7	± 6
2	673.3	± 0.7	648.3	± 6

Table 4.3 Masses of DU plates used in assay targets of Runs #2-4. Plates were measured to be square with 19.75 cm length.
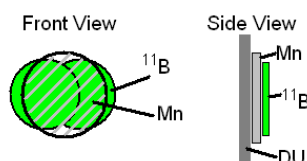
Figure 4.3 Front- and side-view schematic drawings of the disc arrangement behind DU transmission detector.

geometry of overnight background counting was identical to that of the runs with the only difference being that the electron beam was absent. An additional overnight background count was conducted before the experiment. In this measurement, the filter thickness was 1", rather than $^1/_2$". Comparisons between overnight background spectra allow for an estimate of the contribution to the background due to the lead shielding.

The detectors and electronics were manufactured by Ortec and provided by Passport Systems Inc. The detectors were all reported to be approximately 8 cm (diameter) by 8 cm (thickness) cylindrical high-purity germanium (HPGe) crystals. Passport Systems Inc. was able to provide the specification sheet for the detector named G2. The specifications are 'private' information to Ortec, however the geometry of G2 is very similar to that shown in Figure C.2 with dimensions indicated in Table C.1. Each detector was connected to an Ortec DSPEC Pro^{TM} digital γ-ray spectrometer and biasing source. The analogue-to-digital converter (ADC) of the DSPEC Pros had 16384 channels. The parameters at which each detector was operated are included in Table 4.4. Looking down the beam axis, the detector arrangement in clock-wise order, starting at top-right was G5, G2, G3, and G4.

4.3   NRF Levels of Experiment Materials

For the purposes of this experiment, the most important NRF properties are those of the TD material, and those materials behind it. The NRF response of Pb and Al are also of interest because of the quantity of these materials present.

Uranium: No history was available for the DU used in this experiment, however

Detector Name	G2	G3	G4	G5
bias (V)	4880	1940	4040	3040
rise time (μs)	4	4	4	4
flat top (μs)	1.2	1.2	1.2	1.2
pole zero	2585	2697	2845	2805
ADC gain (keV/channel)	0.432	0.458	0.427	0.465
calibration energy resolution (keV)	2.43	2.43	3.58	2.00
beam-on ADC dead time (%)	11.7	16.7	12.6	10.8
beam-on energy resolution (keV)	2.97	2.40	3.40	2.19

Table 4.4 Operating parameters for each DSPEC Pro-HPGe detector combination. Calibration energy resolution is taken from a calibration run and is for the 1332.5 keV peak of ^{60}Co when the accelerator was not running. 'beam-on' dead time and energy resolution are taken from Run #3. 'beam-on' energy resolution is calculated at 1332.5 keV from a best-fit resolution curve of the form $E_{res} = a\sqrt{E} + b$. Quoted energy resolutions are FWHM.
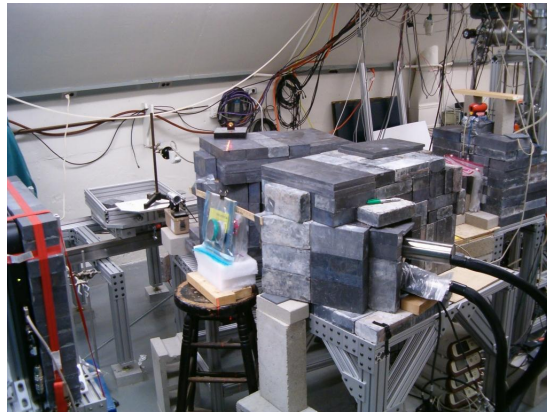
Figure 4.4 A photograph of the experimental setup.

Figure 4.5 Looking up the experimental setup from the TD location toward the beam collimator exit.

E_{level} (MeV)	Γ_0^2/Γ (meV)		Γ_1/Γ_0		Γ_0 (meV)		$\int \sigma dE$ (eV·b)
2.176	23.7	± 1.4	0.52	± 0.02	36.0	± 2.2	87.7
2.209	22.6	± 1.4	0.55	± 0.03	35.0	± 2.3	82.7
2.245	13.4	± 0.9	0.47	± 0.03	19.7	± 1.4	45.0
2.295	5.3	± 0.5	0.59	± 0.10	8.4	± 1.0	14.4
2.410	11.0	± 0.7	0.54	± 0.05	16.9	± 1.2	33.6
2.468	13.4	± 1.0	0.50	± 0.05	20.1	± 1.6	38.0

Table 4.5 Relevant ^{238}U NRF data. Values of Γ_0^2/Γ and Γ_1/Γ_0 were taken from reference(87) where γ-ray emission to the first excited state of ^{238}U ($J^\pi = 2^+$) at 44.92 keV were also measured. Here, it is assumed that this probability is $1 - \Gamma_0/\Gamma$. The final column is calculated from equation 2.89, it has a fractional uncertainty equal to that of Γ_0.

it is probable that the material is predominantly ^{238}U, with less than 0.3% ^{235}U and less ^{234}U than occurs naturally. The NRF response of ^{238}U has been measured several times, including two measurements of resonances between 1.5 and 2.5 MeV(87),(132). The data from reference(87) are shown in Table 4.5[1]. The three levels identified in reference(132) are between 1.7 and 1.85 MeV and were not observed because they were obscured by stronger γ-rays due to radioactive material in the experimental area.

Boron: The B powder that was used in the experiment was enriched to 99.52% ^{11}B. The ^{11}B ground state has spin and parity of $J^\pi = \frac{3}{2}^-$. The first excited ^{11}B state is assigned as $J^\pi = \frac{1}{2}^-$ state at 2124.7 keV. This state has a half-life of 3.8 fs,

---

[1]The authors of reference(87) assumed that the intensity of non-measured decays to states other than the ground and first-excited were 5%± 5% of the intensity of decay to the ground state. This assumption has not been used with the data shown.

E_{level} (keV)	Γ_0/Γ	$W(\theta)g\Gamma_{\gamma0}^2/\Gamma$ (meV)		$g\Gamma_{\gamma0}$ (meV)		$\int \sigma dE$ (eV·b)
1527	0.9	5.2	$\pm$ 1.3	5.3	$\pm$ 2.1	17.5
1884	0.82	41	$\pm$ 10	55	$\pm$ 6	119
2197	0.8	17	$\pm$ 4	17	$\pm$ 3	27.1
2252	0.9	17	$\pm$ 4	13	$\pm$ 3	25.8
2265						
2365	1	3.5	$\pm$ 1.3			
2564		50	$\pm$ 13	61	$\pm$ 12	71.5

Table 4.6 ^{55}Mn NRF data taken from ENDSF(133) and reference(135). γ-ray emission to the first excited state of ^{55}Mn ($J^\pi = \frac{7}{2}^-$) at 125.95 keV were also measured with probabilities of $1 - \Gamma_0/\Gamma$. The final column is calculated from equation 2.89 with a corresponding fractional uncertainty equal to that for $g\Gamma_{\gamma0}$. Blank entries indicate value was not reported.

corresponding to $\Gamma = \Gamma_0 = 0.12 \pm .009$eV and $\int \sigma_{\text{NRF}}(E)\, dE = 51.1$ eV·b(72),(133). ^{10}B has two excited states within the energy range of this experiment, at 1740.1 keV and 2154.3 keV. However neither state has been observed to undergo NRF, and neither have been measured to decay directly to the ground state, instead de-exciting via the $J^\pi = 1^+$ state at 718.4 keV (134).

Manganese: Mn has only one naturally occurring isotope, ^{55}Mn. The NRF properties of this isotope have been measured in reference(135) and are summarized in Table 4.6. The 2197-keV and 2249-keV full-energy resonance γ-rays both appear in spectra as parts of multiplets. Neither the 2071-keV nor 2123-keV γ-rays, which are due to de-excitation of NRF states to the first excited state of ^{55}Mn, were resolved in this experiment. Presence of the 2365-keV resonance cannot be confirmed because of a 2363-keV peak, which is due to the de-excitation of the 2410-keV ^{238}U state to the first excited state. The energy of the 2561-keV resonance was very near the bremsstrahlung endpoint energy and no evidence of a peak could be found.

Lead: Pb has four natural isotopes, ^{204}Pb, ^{206}Pb, ^{207}Pb, and ^{208}Pb with isotopic abundances of 1.4%, 24.1%, 22.1% and 52.4%, respectively. The lowest known excited state of ^{208}Pb is at 2614.5 keV, and therefore ^{208}Pb nuclei is not expected to be excited by the bremsstrahlung beam. ^{207}Pb has two known levels between 1.5 and 2.6 MeV, but both of them differ in spin from the ground state ($\frac{1}{2}$) by three or more units of angular momentum, and have never been observed to undergo NRF. ^{206}Pb has four known levels of spin 1^+ or 2^+ between 1.5 and 2.6 MeV. None of the γ-rays corresponding to these levels were observed in this experiment. ^{204}Pb has 39 known levels between 1.5 and 2.6 MeV, 13 of which have spins of 1 or 2. One state in this energy range, the 2311.6-keV level. It has been observed to undergo NRF, but is not included in the ENDF database. Its mean lifetime was measured to be 28 ± 6 fs, which corresponds to $\Gamma_0 = 23^{+6}_{-4}$ meV, and an integrated cross section of

E_{level} (MeV)	Run #2 / Run #1		Run #3 / Run #1		Run #4 / Run #1	
2.176	0.545	$\pm$ .018	0.880	$\pm$ .006	0.779	$\pm$ .011
2.209	0.567	$\pm$ .019	0.888	$\pm$ .006	0.792	$\pm$ .011
2.245	0.722	$\pm$ .016	0.936	$\pm$ .004	0.877	$\pm$ .008
2.295	0.870	$\pm$ .014	0.972	$\pm$ .003	0.946	$\pm$ .006
2.410	0.790	$\pm$ .013	0.953	$\pm$ .003	0.911	$\pm$ .006
2.468	0.772	$\pm$ .016	0.949	$\pm$ .004	0.902	$\pm$ .007

Table 4.7 Expected intensities of ^{238}U NRF γ-rays for different runs ratioed to the corresponding NRF γ-ray intensity of Run #1.

50^{+14}_{-8} eV·b (80). If this line is present in the data, it is very weak.

Aluminum: The aluminum table on which shielding and detectors were located introduced several kg of Al into the periphery of the experiment. Most of the tables were heavily shielded from the bremsstrahlung beam, however the corners of the left table were not well-shielded from view of the right-side detectors. ^{27}Al has one known level whose excitation energy is within the energy range of interest, and it is well-known to undergo NRF. The level is at 2212.0 keV and has a half-life of 26.3$\pm$ 0.7 fs, which corresponds to an integrated cross section of 18.0 $\pm$ 0.3 eV·b(137). A small peak at 2212 keV was observed as part of a multiplet in the right-hand side detectors. It did not appear to be present in the spectra measured by the bottom-left (G3) or top-left (G4) detectors. However, the poorer energy resolution of G4 makes it difficult to conclude whether or not 2212-keV γ-rays contributed to the observed multiplet.

4.4   Predicted TD Response

Photon attenuation is the key to resonant-energy transmission assay. Resonant-energy photons will be more attenuated than photons of similar, but non-resonant energies. The relative rate at which NRF is induced in the TD reflect the rate of resonant-energy photon attenuation by the target material, which is correlated to the amount of DU in the target. Table 4.7 presents the effective attenuation due to NRF in the target, based on the properties of ^{238}U resonances, shown in Table 4.5. The energy-dependent cross section functions are all based on the Doppler-broadened Lorentzian profile (DBLP) given by equation 2.99. Each value is the expected ratio, $\mathbb{A}(Nx)$, computed by equation 3.38 for the areal density of ^{238}U in the target of each run.

4.5   Data Analysis

Data analysis was performed in the following steps:

1. energy calibration for each detector;

2. re-bin pulse-height spectra onto common energy grid;

3. sum re-binned spectra;

4. fit energy resolution of the summed spectrum;

5. identify and fit peaks in NRF energy regions;

6. normalize each peak to corresponding integral of the 511-keV peak;

7. ratio normalized NRF peak integrals of Runs #2-4 to Run #1;

8. extract expected ^{238}U areal density from each peak ratio; and

9. take weighted average of each peaks' expected areal density to obtain final areal density.

Steps 8 and 9 were also re-done using a correction to the model relating areal densities to peak ratios based on MCNPX simulations of the process of notch refilling.

4.5.1   Energy Calibration

The gain initially set on the ADC was done rather crudely due to a shortage of calibration sources available. After collection of overnight background data, peaks with energies up to 2.615 MeV were easily identified using data from the Table of Radioactive Isotopes(138). The peaks shown in Table 4.8 were identified in overnight background runs and used to calibrate each detector's ADC gain.

^{234m}Pa and ^{214}Bi are isotopes present in the ^{238}U decay series, ^{208}Tl is in the thorium decay series, and ^{40}K is a common radioisotope that is often present in concrete. Comparing between the overnight background runs with $^{1}/_{2}$" and 1"-thick filters indicates that the detected γ-rays are produced outside of the detector shielding. This is because the additional lead reduces the background count rates for each γ-ray by amounts proportional to $\exp[-\mu(E) \cdot ^{1}/_{2}'']$, where $\mu(E)$ is the corresponding attenuation coefficient in lead at each γ-ray energy.

Each night's background run was analyzed and the energy calibration was fit to a polynomial of the form, $E_{\text{fit}} = aE^2 + bE + c$, using a linear least-squares fitting routine. Between each night's runs, there was no significant variation between detectors' best-fit energy calibrations, and thus it is assumed that ADC gains remained stable during the experiment.

E_{line} (keV)	Isotope
766.36	$^{234\text{m}}$Pa
1001.03	$^{234\text{m}}$Pa
1193.77	$^{234\text{m}}$Pa
1460.83	^{40}K
1737.73	$^{234\text{m}}$Pa
1911.17	$^{234\text{m}}$Pa
2204.21	^{214}Bi
2614.49	^{208}Tl

Table 4.8 γ-ray lines identified in overnight background spectra used to calibrate ADC gains(138).
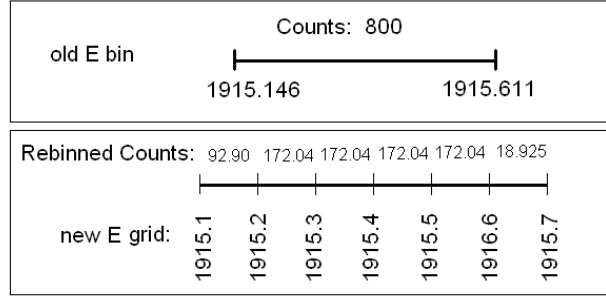
Figure 4.6 Schematic example of re-binning a single bin onto a 100 eV-wide bin grid.

4.5.2 Re-binning and Summing of Pulse-Height Spectra

Because the energy gains of the four detectors varied, they were re-binned to an identical energy grid and then summed. The grid was selected to be 100 eV wide for convenience. Counts within an initial energy bin were separated according to the fraction of bin overlap between the initial energy bin and bins in the new 100 eV-wide grid. Figure 4.6 provides a schematic example of the rebinning process. If a bin initially had a lower boundary of 1915.146 keV, an upper boundary of 1915.611 keV, and contained 800 counts, these counts would be separated into 100 eV-wide bins, with upper energies 1915.2, 1915.3, 1915.4, 1915.5, 1915.6 and 1915.7 keV. The width of the initial bin was 465 eV, thus $800 \cdot 100/465 = 172.043$ counts would be assigned to each of the four bins that were entirely overlapped by the original bin. The lower and upper 100 eV-wide bins receive a fraction of counts corresponding to their respective overlap with the initial bin, which in this case, are 92.903 and 18.925 counts, respectively.

After each detector's pulse-height spectra are re-binned to the common energy grid, they are summed. Example pulse-height spectra are shown before and after summing in Figure 4.7. Before analysis, the summed spectra were convolved by
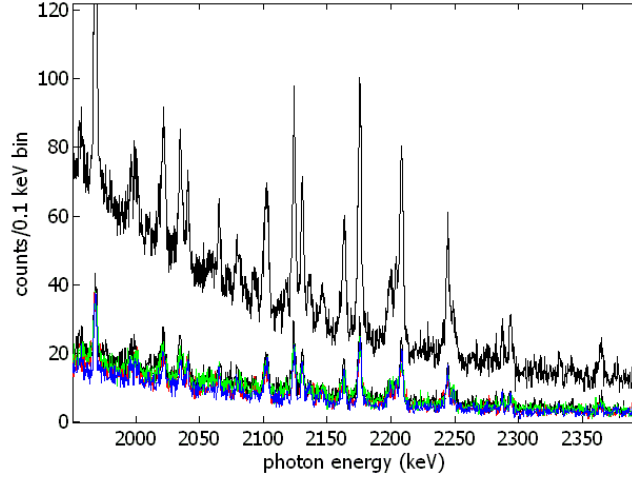
Figure 4.7 Spectra from all four detectors taken during Run #1, before (lower) and after (upper) summing.

400 eV-wide step-wise functions, resulting in a 400 eV running average of the pulse-height spectrum. This was done to reduce statistical fluctuations without degrading the intrinsic energy resolution, which is limited by initial ADC bin widths. By analyzing these smoothed, summed spectra it is easier to identify peaks above statistical fluctuations.

4.5.3 Energy Resolution Calibration

After detector spectra summing, large isolated peaks in the spectrum were identified for use in detector resolution calibration. The peaks selected are a sub-set of the peaks used for energy calibration listed in Table 4.8. The energies of the selected peaks are 1001.03 keV, 1193.77 keV, 1737.73 keV, 1911.17 keV and 2614.49 keV. These peaks were found to be large enough and sufficiently isolated in the summed spectra of Runs #1-4 to be fit to a single Gaussian distribution function atop a linearly varying background with relatively little fitting uncertainty. For a given run's summed spectrum, each of the five peaks were fit, and the standard deviation, σ_i, and fitting error, ϵ_i, of the fitted Gaussian distributions were used as input to a weighted least-squares fitting routine where the weight of each point was defined as $w_i = 1/\boldsymbol{\epsilon_i}$. The functional form to which the peak standard deviations were fit to is given by

$$\sigma(E) = aE^b + C \tag{4.1}$$

The best-fit functions of peak-widths versus peak energy are shown in Figure 4.8. The fit values of b for all of the runs are within one standard deviation uncertainty bounds of the value expected value of $1/2$. This value is expected due to the statistical nature of the population of charge carriers in a HPGe detector (96). Also,
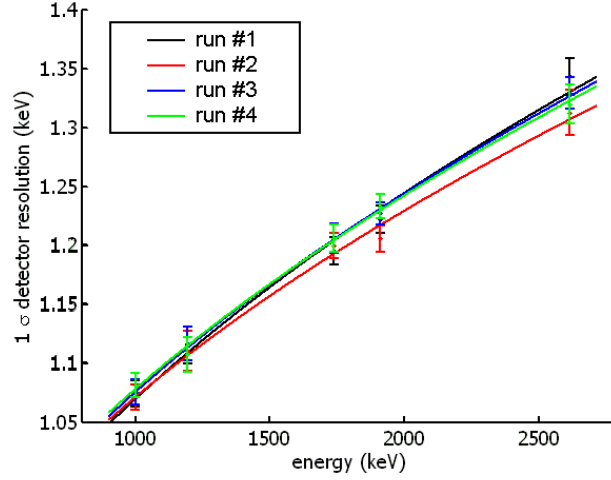
Figure 4.8 Summed HPGe detectors best-fit peak widths, σ and weighted best-fit function of the form $\sigma(E) = aE^b + C$. Points correspond to measured values of σ and the error bars to one standard deviation fitting errors.

between the four runs, the peak-width versus energy fits did not vary beyond the one standard deviation uncertainty of a fit.

4.5.4   Peak Identification and Fitting

To identify which peaks in the obtained spectra were due to the bremsstrahlung beam irradiating the experimental setup, overnight background spectra were normalized to each detector's live-time and subtracted from corresponding detector's live-time normalized spectrum collected during Runs #1-4. Two regions of a spectrum undergoing background subtraction are shown in Figures 4.9 and 4.10. The data are directly from detector G2. The 'beam-on' data were collected during Run #2 and the background data were collected the preceding night.

In Figure 4.9 several peaks clearly visible in the 'beam-on' spectrum are not in the overnight background spectrum. The energy resolutions of the HPGe detectors were found to increase (worsen) when spectra were collected with the bremsstrahlung beam on. With beam on, ADC dead times increased from $\sim 3\%$ to $\sim 15\%$. The worsening of digital spectrometer system resolutions with increasing count rates has been previously observed(139). Worsened resolution causes artifacts in the background-subtracted spectrum, as are visible in Figure 4.10. Because of this, as well as statistical considerations, overnight background spectra were only subtracted from 'beam-on' data for peak identification. Overnight background spectra were not subtracted from 'beam-on' spectra for the purpose of peak fitting, integration, and analysis.

When spectra are summed, statistics on candidate NRF peaks improve. All peaks above 2 MeV that appear above the counting continuum have been identified as
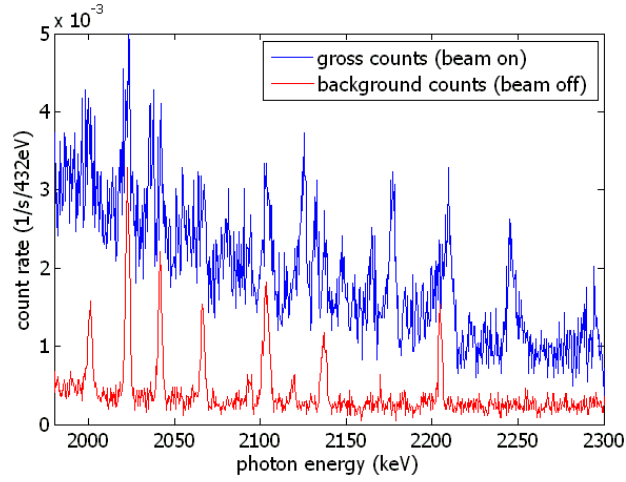
Figure 4.9 The NRF energy region of the live-time normalized gross and background counts in the G2 detector. Gross count spectrum is taken with beam on during Run #2. The background spectrum was collected the preceding night.
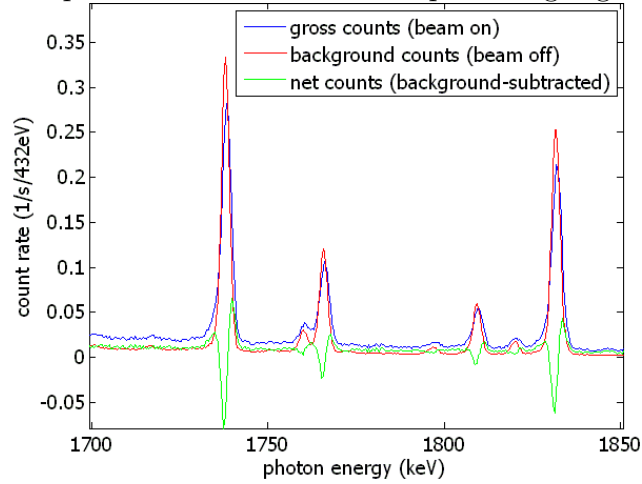
Figure 4.10 Background subtraction of spectra from the G2 detector for energies between 1.7 and 1.85 MeV. Gross count spectrum is taken with beam on during Run #2. The background spectrum was collected the preceding night. The net counts spectrum appears to have dips at peak centroid energies because the energy resolution of the detector systems increased when operating at high count rates.

either candidate NRF γ-rays or are present in overnight background spectra. Peaks identified as candidate NRF γ-rays, as well as nearby peaks forming multiplets, have been fit and integrated. These peaks, their integrated areas, the associated statistical error of the integration, and the identified source of each peak are listed in Tables 4.9 and 4.10.

Peaks whose source is identified as 'bkg' were detected in the overnight background. The peak near 511 keV, labeled 'e$^+$e$^-$' is due to annihilation of positrons primarily in the TD. Use of this phenomenon will be discussed in Section 4.5.5. Peaks whose source is identified as 'U' are due to NRF γ-rays emitted after excitation of known states identified in Table 4.5. The γ-ray energies are either indistinguishable from, or are 45 keV less than the excitation energy of the known state. Those γ-rays of 45 keV less energy are due to de-excitation of the state to the first excited state in ^{238}U, which lies 44.916 keV above the ground state and has a spin and parity of 2^+.

Four candidate NRF lines have been identified as probable ^{238}U NRF γ-rays and are denoted by 'U?'. The pair at 2080.0 and 2035.0 keV corresponds to γ-rays separated in energy by 45 keV, which implies that each pair is due to de-excitation of a 2080-keV state to both the ground and first excited state. The second pair at 2287.4 and 2241.1 keV is separated in energy by 46.3 keV. This difference from the expected 44.9 keV may be attributed to the difficulty fitting the 2241 keV peak due to its minor presence in the 2245-keV multiplet.

The sources of three additional peaks identified in the 'beam-on' spectrum have been labeled as '?'. The peaks at 1996.6 and 2146.0 keV differ in energy by 149.4 keV. This may indicate that the 1996.4-keV peak is due to de-excitation of an 2146-keV state to the 4^+ second-excited state of ^{238}U, which lies 148.4 keV above the ground state. Were this the case, a 2041-keV γ-ray would also be expected, however observation of this peak is obstructed by the presence of a background peak at the same energy. The background-subtracted spectra indicate a bremsstrahlung-induced peak may be present. If the two peaks in question are not due to the same NRF level, but are due to ^{238}U NRF, one would expect to observe additional peaks at either 45 keV above or below the identified peak's energy. As previously mentioned, for the 1996.4-keV peak, a background peak obstructs observation of a 2041-keV NRF γ-ray and there is no evidence of a peak at 1951 keV. For the 2146-keV level, background peaks at 2103 and 2104.5 keV obstruct observation of a potential NRF γ-ray. Also, no peak appears at 2191 keV. The last un-attributed peak, at 2471 keV is very weak, and may be due only to statistical fluctuations of the spectral continuum. Finally, the two entries in Table 4.9 with only 'x' correspond to a doublet region corresponding to a ^{11}B NRF peak and a background peak. Since the area behind the TD contained no ^{11}B in Run #1, this peak was not present and therefore this region was not analyzed.

Run #1			Run #2			
E_C (keV)	Area		E_C (keV)	Area		Source
510.4	1.1×10^8	$\pm 1.8 \times 10^5$	510.4	9.0×10^7	$\pm 1.5 \times 10^5$	e^+e^-
1996.5	497.3	$\pm$ 61.4	1996.6	259.3	$\pm$ 56.9	?
2000.3	548.7	$\pm$ 61.4	2000	436.9	$\pm$ 56.9	bkg
2035	1159.8	$\pm$ 61.1	2034.9	800.1	$\pm$ 53.8	U?
2041	808.4	$\pm$ 58.1	2041	668.2	$\pm$ 52.6	bkg
2080	510.7	$\pm$ 51.2	2080	403.3	$\pm$ 46.1	U?
2102.4	1019.6	$\pm$ 54.4	2102.6	946.7	$\pm$ 50.2	bkg
x	x		2118.9	218.4	$\pm$ 39.8	bkg
x	x		2124.1	1609	$\pm$ 54.4	^{11}B
2130.6	1491.6	$\pm$ 56.0	2130.8	707.2	$\pm$ 45.3	U
2136.2	509.5	$\pm$ 46.4	2136.3	489.7	$\pm$ 42.9	bkg
2146.1	406.5	$\pm$ 45.3	2146	375.1	$\pm$ 41.5	?
2163.3	1234.1	$\pm$ 51.9	2163.3	609.8	$\pm$ 42.5	U
2175.6	2702.6	$\pm$ 64.5	2175.6	1310.4	$\pm$ 50.1	U
2196.6	261	$\pm$ 40.5	2197.2	175.5	$\pm$ 40.2	Mn
2199.7	825.7	$\pm$ 45.1	2199.7	440.8	$\pm$ 39.9	U
2204.1	842.8	$\pm$ 45.3	2204	732.1	$\pm$ 42.1	bkg
2208.2	2209.3	$\pm$ 58.4	2208.2	1177.3	$\pm$ 47.1	U
2210.9	246	$\pm$ 43.0	2211.8	153.6	$\pm$ 35.3	Al
2242.3	197	$\pm$ 38.2	2240.2	97.9	$\pm$ 31.5	U?
2244.9	1397.8	$\pm$ 49.6	2244.8	883.4	$\pm$ 41.4	U
2249.1	479.5	$\pm$ 39.3	2249.2	378.4	$\pm$ 34.8	U
2252.3	72.9	$\pm$ 37.0	2252.7	138.8	$\pm$ 31.5	Mn
2287.1	398	$\pm$ 35.5	2287.5	233.2	$\pm$ 31.6	U?
2293.6	491.7	$\pm$ 36.8	2294	377.5	$\pm$ 33.9	U
2364.7	344	$\pm$ 32.1	2365.2	199.5	$\pm$ 28.8	U
2409.8	550.8	$\pm$ 33.0	2409.9	428.5	$\pm$ 29.8	U
2422.5	263.8	$\pm$ 28.3	2422.2	114.1	$\pm$ 24.1	U
2467.4	289.5	$\pm$ 25.9	2467.5	186.9	$\pm$ 22.3	U
2470.6	56.1	$\pm$ 22.0	2470.3	49.5	$\pm$ 21.1	?

Table 4.9 Analyzed γ-ray lines in NRF energy region for Runs #1 and 2.

Run #3			Run #4			
E_C (keV)	Area		E_C (keV)	Area		Source
510.4	9.9×10^7	$\pm1.5\times10^5$	510.4	9.2×10^7	$\pm1.6\times10^5$	e^+e^-
1996.4	498.5	$\pm$ 59.0	1996.7	506.6	$\pm$ 56.8	?
2000.2	650.6	$\pm$ 59.1	2000.5	563.7	$\pm$ 56.8	bkg
2035.1	1115.8	$\pm$ 59.1	2034.9	899.4	$\pm$ 56.1	U?
2040.8	699.3	$\pm$ 55.4	2041	638.8	$\pm$ 53.7	bkg
2080.1	391.1	$\pm$ 49.3	2079.9	368.1	$\pm$ 46.4	U?
2102.4	1188.1	$\pm$ 54.2	2102.6	929.1	$\pm$ 50.2	bkg
2118.2	285	$\pm$ 43.0	2119.4	258.4	$\pm$ 41.5	bkg
2124.1	1801.9	$\pm$ 57.7	2124.2	1693.3	$\pm$ 55.6	^{11}B
2130.5	1200.7	$\pm$ 52.2	2130.7	1077.5	$\pm$ 49.8	U
2136.3	389.1	$\pm$ 43.7	2136	474	$\pm$ 43.3	bkg
2146.3	323	$\pm$ 43.0	2145.8	300.5	$\pm$ 41.5	?
2163.3	1049.7	$\pm$ 48.4	2163.2	753.3	$\pm$ 44.7	U
2175.6	2300.8	$\pm$ 59.9	2175.6	1809.7	$\pm$ 55.3	U
2197.4	327.3	$\pm$ 41.7	2197	183.4	$\pm$ 38.2	Mn
2200	576.6	$\pm$ 41.3	2200	525.3	$\pm$ 40.0	U
2204.1	747	$\pm$ 43.3	2204.2	718.7	$\pm$ 42.4	bkg
2208.2	1874.1	$\pm$ 54.8	2208.3	1574.2	$\pm$ 51.5	U
2211.9	102.6	$\pm$ 37.0	2211.8	62.2	$\pm$ 37.0	Al
2240.5	131.7	$\pm$ 34.6	2240.5	59	$\pm$ 33.8	U?
2244.5	1117.1	$\pm$ 45.7	2244.8	1145.2	$\pm$ 45.4	U
2248.4	411.8	$\pm$ 38.4	2249.4	310.1	$\pm$ 35.5	U
2251.1	179.7	$\pm$ 39.1	2252.3	16.1	$\pm$ 35.6	Mn
2287.6	273.9	$\pm$ 33.2	2287.5	236.9	$\pm$ 32.1	U?
2293.9	465.9	$\pm$ 36.0	2293.6	381.3	$\pm$ 34.3	U
2364.5	338.8	$\pm$ 31.6	2364.8	285.7	$\pm$ 30.0	U
2409.6	475.3	$\pm$ 31.1	2409.7	468.2	$\pm$ 30.7	U
2422.2	225.2	$\pm$ 26.7	2421.9	179.3	$\pm$ 25.5	U
2467.3	289.8	$\pm$ 25.2	2467.5	307.1	$\pm$ 25.2	U
2471.5	80	$\pm$ 20.6	2471.7	55.2	$\pm$ 20.0	?

Table 4.10 Analyzed γ-ray lines in NRF energy region for Runs #3 and 4.

Peak Fitting and Integration

In this section the process of peak fitting, continuum subtraction, peak integration, and calculation of the estimated error is discussed. Candidate NRF peaks are identified. If a peak is part of a multiplet, all peaks within the multiplet are analyzed. This process populated the peak list in Tables 4.9 and 4.10. Each multiplet (or singlet) is individually analyzed. The analysis proceeds by the following steps:

- as summarized in Section 4.5.2, spectra are re-binned to 100 eV-wide bins, summed, and then smoothed with a 400-eV running average;

- a linear fit is applied to the non-peak continuum;

- the continuum is subtracted from the peak regions;

- peak(s) are fit to Maxwell-Boltzmann distribution whose width is defined by equation 4.1; and

- fit peaks are integrated.

The summed spectra were binned to a 100 eV wide grid. A 400-eV running average is accomplished by convolving these spectra with an array composed of four values of 0.25, resulting in smoothed spectra. This process has very little effect on the energy resolution of the spectra because initial ADC bin widths were between 427 and 465 eV and were re-binned to finer energy resolution to accommodate spectra summing. The non-peak regions above and below the peak (or multiplet) are fit to linear functions. Nearby peaks may be excluded from the continuum fitting routine. The energy-dependent intensity of the continuum beneath the peak/multiplet is estimated by imposing a linear function between the two linear fits to the continuums adjacent the peak/multiplet. Counts due to the estimated linearly varying continuum are subtracted from each bin in the peak/multiplet region. Identified peaks are fit to Gaussian distributions using least-squares fitting routine. The widths of the distributions are defined by the best-fit energy-resolution function, equation 4.1. Centroid energies are allowed to vary, but only over a range of 1 eV beyond the standard deviation of the best-fit resonance width. The only other constraint on the fitting is that each peak area must be non-negative. A graphical representation of the fitting process is shown in Figure 4.11.

The errors associated with each reported peak area are obtained using the following observations. The Gaussian least-squares fitting routine provides a 68% confidence interval on the area, A, of each continuum-subtracted peak, from which a fitting standard deviation, σ_F, can be obtained, assuming that the fitting routine produces a Gaussian error distribution. Poisson statistics dictate that the standard deviation of the number of counts in a peak, $\sigma_P = \sqrt{A}$. The standard deviation of the continuum-subtracted peak is assigned as $\sigma_T = \max(\sigma_F, \sigma_P)$. One ^{238}U NRF peak in each of Runs #2-4 had a $\sigma_F > \sigma_P$, as did several smaller peaks. For the
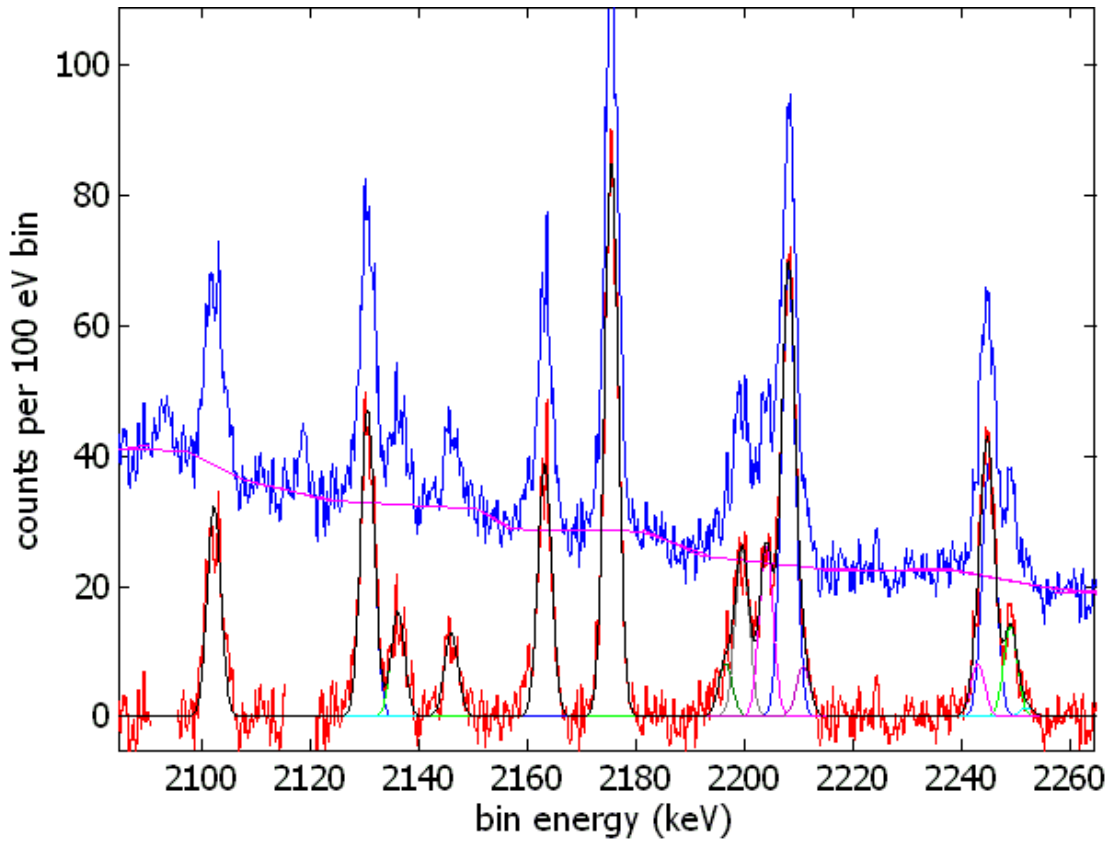
Figure 4.11 Portion of Run #1 summed spectrum with peak fitting graphically demonstrated. The upper spectrum (blue) is summed re-binned data from all four detectors. The piece-wise linear function following this spectrum's baseline (magenta) is the linear fit of the continuum in each peak/multiplet region. The lower spectrum (red) is the 400-eV running averaged, continuum-subtracted data. The black curve is the result of least-squares multiple-Gaussian fitting routine, which for multiplets is the sum of the other colored Gaussian curves.

2200-keV ^{238}U NRF peak in Run#2, $\boldsymbol{\sigma}_F = 23.5$ eV whereas $\boldsymbol{\sigma}_P = 21$ eV. The 2248-keV ^{238}U NRF peak had $\boldsymbol{\sigma}_F > \boldsymbol{\sigma}_P$ by 10% and 5% for Runs #3 and 4, respectively.

The standard deviation, $\boldsymbol{\sigma}_{\mathrm{Cnt}}$ of the subtracted continuum is defined by the following expression

$$\boldsymbol{\sigma}_{\mathrm{Cnt}} = \sqrt{\int_{E_C - 2\sigma_{\mathrm{pk}}}^{E_C z + 2\sigma_{\mathrm{pk}}} N_{\mathrm{Cnt}}(E)dE} \qquad (4.2)$$

σ_{pk} denotes the best-fit standard deviation of the peak shape, and N_{Cnt} is the estimated number of continuum counts as a function of energy. Finally, the net standard deviation of a given peak's area is given by

$$\boldsymbol{\sigma} = \sqrt{\boldsymbol{\sigma}_T^2 + \boldsymbol{\sigma}_{\mathrm{Cnt}}^2} \qquad (4.3)$$

Fitting of the 511-keV peak also yielded a fitting error, $\boldsymbol{\sigma}_F$ that was larger than the error due to Poisson statistics, $\boldsymbol{\sigma}_P$, despite the fact that the Gaussian width, σ, was allowed to vary freely. However, the total error associated with the 511-keV peak fitting process was only 0.1% of the peak area, which is negligibly small compared to other error sources. Thus, no effort was made to improve the fitting of the annihilation peak.

4.5.5 Spectra Normalization to Annihilation Peak

In order to compare rates at which NRF is induced in the TD, the rate at which photons near resonant energies impinge upon the TD must be known. Direct measurement of this rate is difficult and was not attempted in this experiment. However, the relative rate at which pair production occurs in the TD between runs is proportional to the relative intensities of near-resonant-energy photons to a high precision.

To demonstrate this fact, we use MCNPX(23) to calculate the photon spectrum (normalized to electron beam current) impinging upon the TD for each of the four target geometries. These spectra are shown in Figure 4.12. The general shapes of the spectra appear similar, but the overall intensities vary by approximately 10% between runs. These spectra indicated that even if the integrated electron current incident upon the bremsstrahlung converter were precisely known and well-focused for the duration of each run, it would be necessary to normalize counting data from each run to take into account differing photon attenuations between targets, before data could be compared between runs.

To perform this normalization, we define a value, R_{PP}^i that is proportional to the rate at which pair production occurs in the TD for each run, i.

$$R_{\mathrm{PP}}^i = \int \Phi^i(E)\sigma_{\mathrm{PP}}(E)dE \qquad (4.4)$$

In this definition we have omitted photon attenuation within the TD. This is an approximation, most valid when the TD is thin compared to the mean photon path
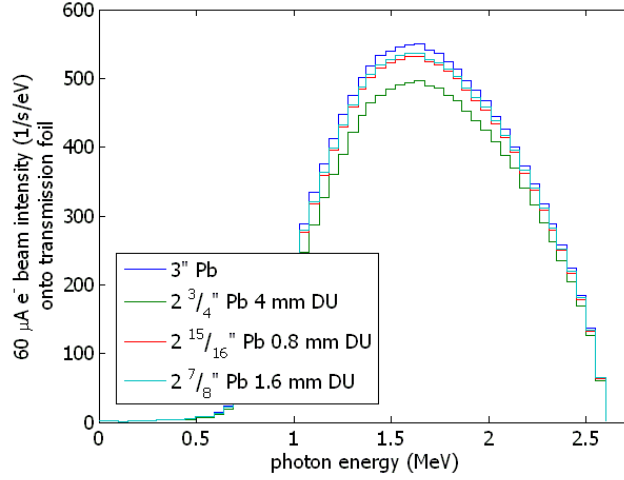
Figure 4.12 Photon spectra (normalized to electron beam current) impinging upon the transmission detector for each of the four target geometries. These spectra were calculated using MCNPX. For clarity, statistical error bars are not shown, but errors were calculated to be less than 1% for energy bins above 0.5 MeV.

length before pair production, which is 6 - 11 mm for 1.5 - 2.6 MeV photons in uranium. However, since the TD geometry did not change during the experiment, the systematic inaccuracies due to this approximation will be very similar between runs and therefore will generally cancel each other later, when different values of R_{PP}^i are ratioed to obtain peak normalization.

The pair production cross section for photons incident upon uranium is shown in Figure 4.13. The cross section is zero below the energy 1.022 MeV, and begins to slowly turn upwards before becoming approximately linear at $\sim$ 1.3 MeV. This implies that normalization of photon intensity to the rate of pair production will be most sensitive to the highest energy portion of photon spectra.

Figure 4.14 presents the spectra in Figure 4.12, re-normalized by dividing by R_{PP}^i. The spectra appear very similar. To further examine the similarity of these spectra, each normalized spectrum has been divided by that of Run #1. The resulting ratios are shown in Figure 4.15. The values plotted on the ordinate are those given by equation 4.5 for $i = 2, 3$ and 4. For $i = 1$, the $Y^1(E)$ would be unity at all energies.

$$Y^i(E) = \frac{\Phi^i(E)}{R_{\mathrm{PP}}^i} \frac{R_{\mathrm{PP}}^1}{\Phi^1(E)} \tag{4.5}$$

In Figure 4.15, we can see three regimes of behavior. Below 0.5 MeV, the ratios have large errors and satisfactory conclusions as to how the spectra relate can not be made. Between 0.5 and 1.6 MeV the normalization has resulted in spectral intensities that are lower than for Run #1, especially in the case of Run #2. However, we are not measuring resonant attenuation of any photons at these energies, and therefore,
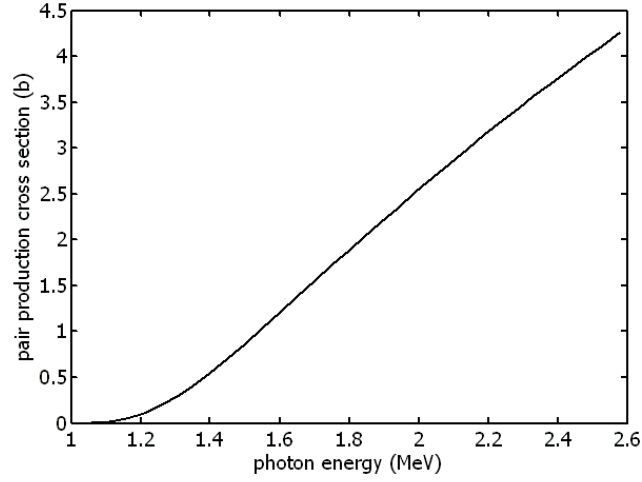
Figure 4.13 Pair production cross section for photons incident upon uranium.
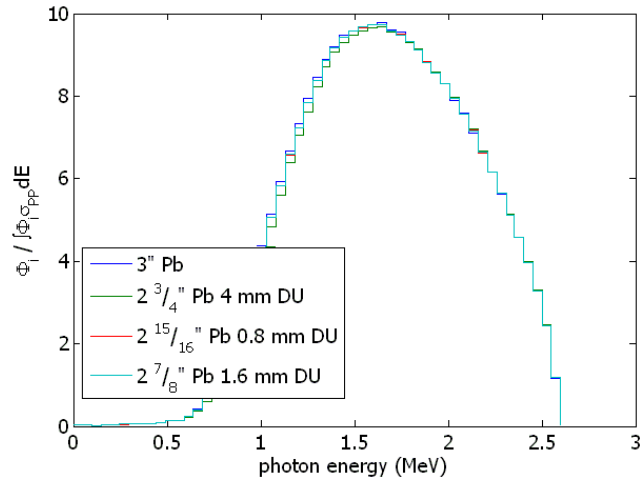
Figure 4.14 Calculated photon spectrum shown in Figure 4.12, re-normalized by dividing by R_{PP}^i, resulting in spectra normalized to a value approximately proportional to the rate at which pair production occurs in the transmission detector. For clarity, statistical error bars are not shown, but errors were calculated to be less than 1% for energy bins above 0.5 MeV
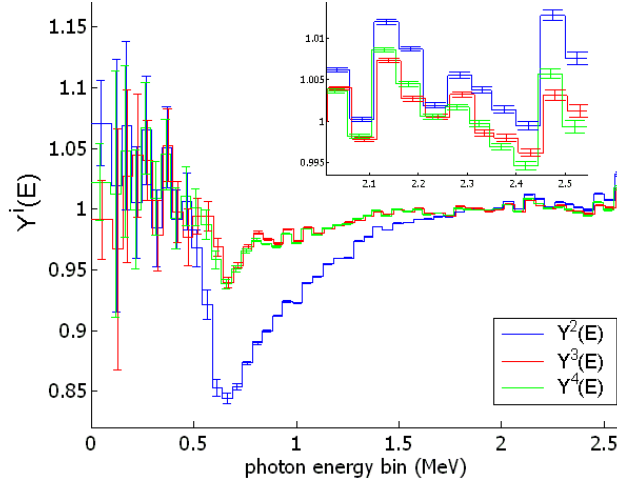
Figure 4.15 Spectra shown in Figure 4.14 ratioed to the 3" Pb spectrum. The values for the three functions plotted on the ordinate are $Y^i(E)$ from equation 4.5 for $i = 2, 3$ and 4. The inset box is a larger view of the energy region between 2 and 2.6 MeV.

the spectral differences after normalization have no effect on conclusions based on the NRF induced by higher-energy photons.

Above 1.6 MeV, the normalized spectra all appear to be within 1.5% of each other. Furthermore, the sawtooth shape of the calculated ratios shown in the inset appear to vary about an average of 1 for $Y^3(E)$ and $Y^4(E)$, whereas the mean value for $Y^2(E)$ is about 1.005. Sawtooth shapes are very rare in nuclear data, and this shape is probably more indicative of failings of the linear interpolation method used to calculate incoherent scattering functions of Pb and U in MCNPX, than of anything physical. We therefore, tentatively accept for 2.0 to 2.5 MeV photons, the mean value of the oscillation as representative of the photon spectral intensities incident upon the TD, relative to those intensities in Run #1, after pair production normalization.

The experimental goal was to measure the rate of attenuation of resonant-energy photons. By normalizing to each spectra's 511-keV peak, we effectively equate intensities incident upon the TD of non-resonant photons in the energy range of 2.0 - 2.5 MeV. This in turn, gives a baseline, relative to which resonant-energy photon absorption may be compared with systematic errors of less than approximately 1.5%. Due to the large counting errors present in the Poisson statistics, we neglect this error in subsequent error analyses.

4.5.6   Normalized NRF Peak Ratios

Peaks identified in Runs #2-4 as due to either a known or possible ^{238}U resonance were fit, integrated and compared to corresponding peak intensities from Run

#1. Mathematically, the compared peak intensities are expressed as

$$\mathbb{A}^i_{E_{pk}} = \frac{A^i_{E_{pk}}}{A^1_{E_{pk}}} \frac{A^1_{511}}{A^i_{511}} \tag{4.6}$$

where $\mathbb{A}^i_{E_{pk}}$ is the relative intensity (also referred to as the *measured effective attenuation*) of the peak at $E = E_{pk}$ for Run i, relative to Run #1. $A^i_{E_{pk}}$ corresponds to the fit area of that peak, and the subscript, '$_{511}$' indicates the annihilation peak.

The statistical error associated with $\mathbb{A}^i_{E_{pk}}$ is derived to be

$$\sigma_{\mathbb{A}^i_{E_{pk}}} = \sqrt{\left(\frac{\sigma^1_{511}}{A^1_{511}}\right)^2 + \left(\frac{\sigma^i_{511}}{A^i_{511}}\right)^2 + \left(\frac{\sigma^1_{E_{pk}}}{A^1_{E_{pk}}}\right)^2 + \left(\frac{\sigma^i_{E_{pk}}}{A^i_{E_{pk}}}\right)^2} \tag{4.7}$$

where values of A^i_{pk} are given in Tables 4.9 and 4.10, and each $\sigma^i_{E_{pk}}$ is given by Equation 4.3. The resulting measured effective attenuation values are shown in Table 4.11 for each of the three runs containing ^{238}U in the assay target. The peaks have been arranged such that two peaks separated by 45 keV, which presumably correspond to de-excitation of the same NRF level, are shown in a single box. We note that the statistical quality of data corresponding to potential NRF peaks that have not been previously reported NRF states is generally very low. Furthermore, listed peaks without a corresponding peak due to de-excitation to the first excited state do not appear to obey the systematic trends that would be expected theoretically and have been observed in known NRF states.

NRF γ-rays due to de-excitation of the NRF level to the first excited state contain the same type of information as those that decay to ground state – the rate of attenuation of photons that would excite the NRF level. Therefore attenuation rates of the coupled levels are combined to improve statistics. The net result of the effective attenuations for the six previously reported NRF levels, as well as the levels at 2080 and 2288 keV are shown in Table 4.12.

These values are compared with the values expected from the theoretical model of photon attenuation (shown in Table 4.7) in Figures 4.16 and 4.17. Figure 4.17 only shows the comparison for the largest three resonances, which when analyzed result in better statistics. Both figures contain data points and error bars in three colors. Each color corresponds to data from a specific Run and each point represents a single NRF level. The vertical error bars are associated with the statistical (and possibly fitting) uncertainty of the peak pairs in each Run and the horizontal error bars are due to the effects of the uncertainty in the measured NRF cross sections as reported in reference (87). All data would fall on the line $y = x$, within statistical uncertainties, if the theoretical model described in Section 3.2.2 perfectly represented photon transport within the experimental geometry. The solid magenta lines shown in the figures represent weighted linear best-fits. In Figure 4.16, the best-fit line was constrained to pass through the point (1,1), whereas in Figure 4.17, the line was

E_{pk} (keV)	Run #2		Run #3		Run #4	
1996.6	0.627	$\pm$ 0.252	1.100	$\pm$ 0.171	1.206	$\pm$ 0.167
2035.0	0.829	$\pm$ 0.085	1.056	$\pm$ 0.075	0.918	$\pm$ 0.082
2080.0	0.949	$\pm$ 0.152	0.840	$\pm$ 0.161	0.854	$\pm$ 0.161
2146.0	1.108	$\pm$ 0.157	0.872	$\pm$ 0.174	0.875	$\pm$ 0.177
2130.7	0.570	$\pm$ 0.074	0.884	$\pm$ 0.057	0.855	$\pm$ 0.060
2175.6	0.583	$\pm$ 0.045	0.934	$\pm$ 0.035	0.793	$\pm$ 0.039
2163.3	0.594	$\pm$ 0.081	0.934	$\pm$ 0.062	0.723	$\pm$ 0.073
2208.2	0.640	$\pm$ 0.048	0.931	$\pm$ 0.040	0.844	$\pm$ 0.042
2199.9	0.641	$\pm$ 0.106	0.766	$\pm$ 0.090	0.753	$\pm$ 0.094
2244.7	0.759	$\pm$ 0.059	0.877	$\pm$ 0.054	0.970	$\pm$ 0.053
2241.1	0.597	$\pm$ 0.376	0.734	$\pm$ 0.326	0.355	$\pm$ 0.604
2287.4	0.704	$\pm$ 0.162	0.755	$\pm$ 0.151	0.705	$\pm$ 0.162
2249.0	0.948	$\pm$ 0.123	0.942	$\pm$ 0.124	0.766	$\pm$ 0.141
2293.8	0.923	$\pm$ 0.117	1.040	$\pm$ 0.108	0.918	$\pm$ 0.117
2364.8	0.697	$\pm$ 0.172	1.081	$\pm$ 0.132	0.983	$\pm$ 0.140
2409.7	0.935	$\pm$ 0.092	0.947	$\pm$ 0.089	1.007	$\pm$ 0.089
2422.2	0.520	$\pm$ 0.237	0.937	$\pm$ 0.160	0.805	$\pm$ 0.178
2467.4	0.776	$\pm$ 0.149	1.099	$\pm$ 0.125	1.256	$\pm$ 0.121
2471.0	1.060	$\pm$ 0.580	1.566	$\pm$ 0.470	1.166	$\pm$ 0.534

Table 4.11 Measured values of $\mathbb{A}^i_{E_{pk}}$ with statistical errors. Peaks grouped within the same box correspond to de-excitation of the same NRF level.

E_{level} (keV)	Run #2		Run #3		Run #4	
2175.6	0.578	$\pm$ 0.050	0.916	$\pm$ 0.062	0.815	$\pm$ 0.058
2208.2	0.624	$\pm$ 0.059	0.932	$\pm$ 0.069	0.800	$\pm$ 0.067
2244.7	0.715	$\pm$ 0.087	0.836	$\pm$ 0.088	0.890	$\pm$ 0.096
2293.8	0.935	$\pm$ 0.159	0.992	$\pm$ 0.163	0.843	$\pm$ 0.154
2409.7	0.843	$\pm$ 0.164	0.998	$\pm$ 0.159	0.998	$\pm$ 0.166
2467.4	0.654	$\pm$ 0.183	1.021	$\pm$ 0.207	1.041	$\pm$ 0.224
2080.0	0.865	$\pm$ 0.151	0.990	$\pm$ 0.176	0.899	$\pm$ 0.162
2287.4	0.669	$\pm$ 0.274	0.748	$\pm$ 0.269	0.589	$\pm$ 0.369

Table 4.12 Measured values of $\mathbb{A}^i_{level}$ with statistical errors.
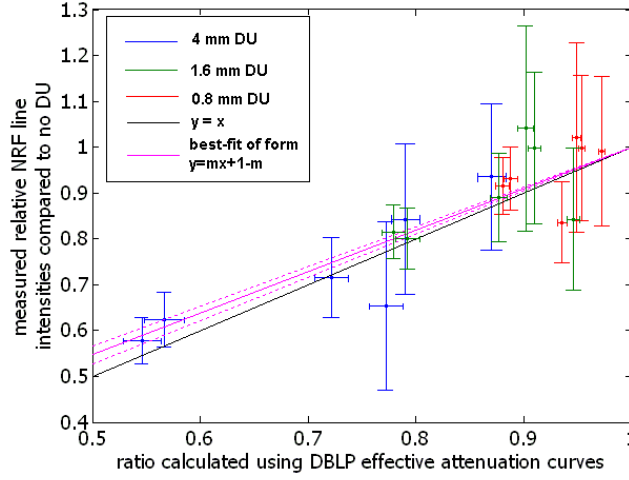
Figure 4.16 Comparing measured NRF line intensities with predicted values based on the DBLP model described in Section 3.2.2. Each data point color represents data from a single Run, the black line indicates $y = x$, the solid magenta line is a best-fit line constrained to intersect the point (1,1), with the dotted lines corresponding to 68% error intervals.

unconstrained. This line passes very close to the point (1,1) and therefore we will assume that the constrained fit is a valid representation of the data.

For the most attenuated NRF lines (the left-most data points), there appears to be disagreement between the model and the measured data. To investigate whether this disagreement was due to other scattering processes neglected in the analytical model, the experimental setup was simulated in MCNPX using the code changes described in Appendices A and B. The NRF lines that have been entered into the MCNPX data files are evaluations of the Maxwell-Boltzmann distribution at five energies. These lines, with the cross section profiles used in MCNPX were also attenuated using the model described in Sections 3.2.2 and 3.2.3. This model produced effective attenuation values that were smaller (more attenuation) than those predicted by MCNPX (see Table 4.13). From this we can infer that detailed particle transport, as is simulated by MCNPX, results in larger effective attenuation values than were predicted by the analytical model using the same resonance cross section functions.

Constrained linear weighted best-fits of form $y-1 = m(x-1)$ are applied to two sets of 9 ordered pairs. In each set, y represents the measured attenuation ratios for three resonances and three runs, and x represents the corresponding calculated expected attenuation ratios from Table 4.13. In both fittings, each point was weighted by $1/(\sigma^i_{E_{level}})^2$, where $\sigma^i_{E_{level}}$ represents statistical errors given in Table 4.12. When the MCNPX data was used as abscissa values, a best-fit value of $m_X = 1.040 \pm 0.055$, whereas when the analytical evaluation of point-wise Maxwell-Boltzmann distribution was used as abscissa values, the best-fit value of $m_{MB} = 0.977 \pm 0.045$. Thus,
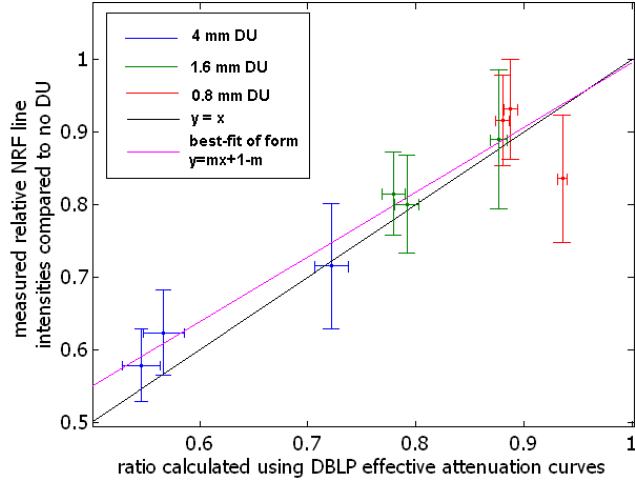
Figure 4.17 Same as Figure 4.16 except only data corresponding to three largest NRF lines are considered, and the best-fit line shown is unconstrained.

E_{level}	Run #2		Run #3		Run #4	
(keV)	MCNPX	Analytical	MCNPX	Analytical	MCNPX	Analytical
2176	0.595	0.581	0.909	0.893	0.810	0.801
2209	0.623	0.591	0.911	0.897	0.833	0.807
2245	0.766	0.742	0.964	0.941	0.918	0.887
2295	0.897	0.885	0.979	0.976	0.967	0.953
2410	0.838	0.811	0.963	0.958	0.970	0.920
2468	0.820	0.791	0.979	0.944	0.939	0.910

Table 4.13 Effective attenuation of resonant-energy photons for largest three ^{238}U resonances examined. Values labeled MCNPX result from Monte Carlo simulations of the experimental geometry. Values labeled Analytical result from the analytical energy-dependent attenuation of resonant photons assuming the cross section profile is given by a point-wise evaluation of a Maxwell-Boltzmann distribution, as described Section 3.2.3.
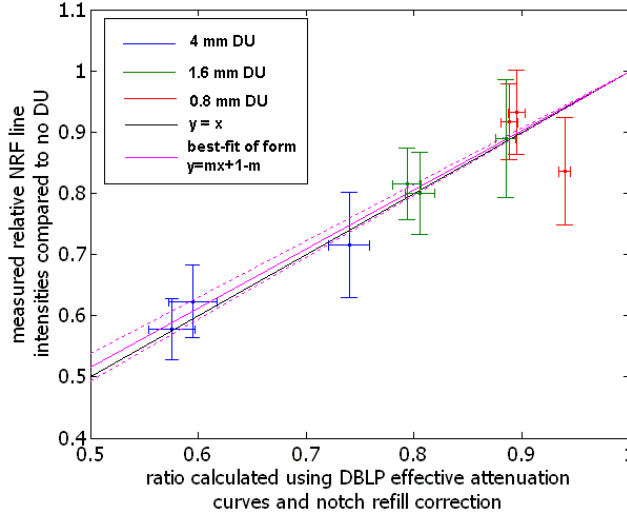
Figure 4.18 Same as Figure 4.17 except that the values of the calculated ratio on the abscissa include the notch-refilling correction as outlined in the text.

we attribute to the MCNPX transport of particles an addition to the best-fit slope of $\Delta m = 0.063$.[2] We will name this correction the *MCNPX-based notch-refill correction*. This correction, when applied to a best-fit line constrained to (1,1) of the data shown in Figure 4.17, changed the best-fit slope from $m_{DBLP} = 0.906 \pm 0.041$ to $m_{DBLP}^{corr} = 0.969 \pm 0.045$. This new best-fit line is shown as a magenta line with dotted $\pm 1\ \sigma$ errors in Figure 4.18, along with the data after application of the MCNPX-based notch-refill correction to the predicted effective attenuation values.

It is of interest to note that the intensity of the MCNPX-based notch-refill correction is comparable to the predicted intensity of the notch-refilling discussed in Section 3.2.5. There, the intensity was predicted by consideration of the photon spectrum leaving a side of an assay target after monoenergetic photons irradiated the opposite side.

4.6 Results

4.6.1 Measured ^{238}U Areal Densities

We now have a measured effective attenuation for each resonance and each run. Using the theoretical model for effective attenuation, we may relate the measured values to expected ^{238}U areal densities. Figure 4.19 presents calculated functions for the effective attenuation of the largest three ^{238}U resonances versus areal density. Given a measured effective attenuation value, one inverts these curves to obtain an

---

[2]The quoted errors are correlated to each other as well as to the DBLP curve and therefore we do not propagate them in this formulation
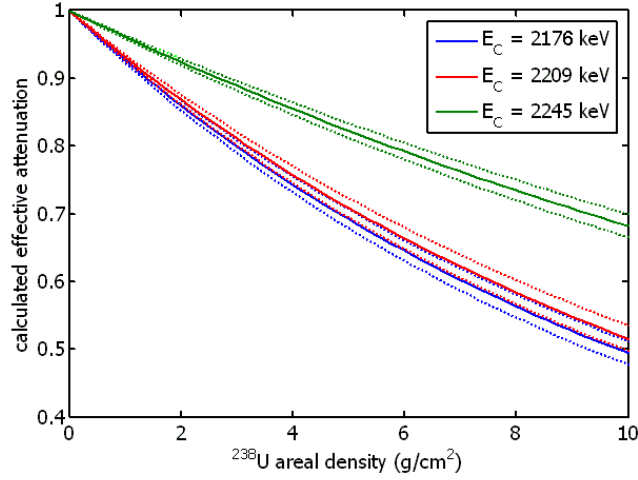
Figure 4.19 Model-calculated effective attenuation versus ^{238}U areal densities for largest three ^{238}U NRF resonances in experimental energy range. The model was the attenuation and TD response model using the DBLP cross sections as described in Section 3.2.2. Dotted lines indicate errors due to reported uncertainties in experimental measurement of Γ_0. $E_C = 2176$ keV curve is identical to that shown in Figure 3.25.

expected areal density based on the DBLP response model described in Section 3.2.2. By combining the expected areal densities of the three resonances, we obtain an estimate of the areal density of ^{238}U in the target for each of Runs #2, 3 and 4. The measured individual areal density values are shown as points with error bars in Figure 4.20, with data from each run in a single color. The solid lines indicate expected areal densities based on the values shown in Table 4.2. Dashed lines indicate the weighted average areal density based on the measured NRF peaks.

Taking the results of the discussion in the previous section, we expect to underestimate ^{238}U areal densities because the MCNPX results have indicated that the analytical model underestimates the effective attenuation value (corresponding to too much attenuation). To correct for this, we shift each predicted effective attenuation values by the difference between the corrected best-fit line (shown in Figure 4.18) to the uncorrected best-fit line (shown in Figure 4.16). This shift is given by

$$x_{DBLP}^{corr} = \frac{m_{DBLP}x_{DBLP} + \Delta m}{m_{DBLP} + \Delta m} \tag{4.8}$$

The fractional increase in the predicted effective attenuation value due to correction is shown as a function of x_{DBLP} in Figure 4.21. By multiplying a predicted attenuation ratio by the value of the function in equation 4.8 at that value, we obtain an MCNPX-based notch-refill-corrected expected attenuation value. Likewise, we may produce functions analogous to those shown in Figure 4.19 using the corrected expected attenuation values. By inverting the resulting functions for each
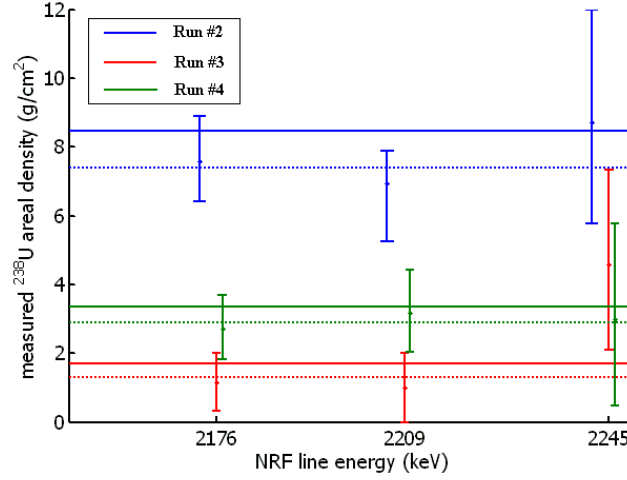
Figure 4.20 NRF-assay measured areal densities for the three Runs based on inverting effective attenuation curves shown in Figure 4.19. Dashed lines correspond to weighted averages of the values and solid lines correspond to the measured areal densities obtained from values shown in Table 4.2.

measured effective attenuation, we obtain values of the measured areal density that includes the MCNPX-based notch-refilling correction for each observed NRF resonance. These values are shown in Figure 4.22 along with weighted mean values for each Run (dotted lines), the $\pm 1\,\sigma$ errors of the weighted mean (dashed lines), and the directly measured areal densities (solid lines). Each color corresponds to values for a single run. The smaller black error bars indicate $\pm 1\,\sigma$ systematic errors due to reported uncertainties in measured values of $\Gamma_0(87)$.

After applying the MCNPX-based notch refill correction to the data, the resulting weighted mean (as described by equations 3.51- 3.54) areal density measurements are shown in Table 4.14. All values are within $\pm 1\,\sigma$ of the values obtained by weighing the plates and measuring their dimensions. However, the fact that the areal density is under-predicted in all three Runs may indicate a remaining systematic disagreement between experiment and prediction. The oxygen content in the target DU plates was not measured, and the presence of oxygen would decrease ^{238}U areal densities relative to those stated as the actual measured values. For the data to closely match predicted values, however, there would need to be approximately equal numbers of uranium and oxygen atoms in the DU plates. Improved statistics would help determine whether the impurities such as oxygen or other elements have effected the experimental results.

It is also probable that the some disagreement between experiment and prediction is due to inaccuracies of ^{238}U NRF cross sections reported by reference (87). The black error bars on each point in Figure 4.22 indicate the magnitude that the reported $\pm 1\,\sigma$ uncertainties on reported values of Γ_0 have on the expected results. These error bars are correlated for data from all three Runs; if the true value of Γ_0
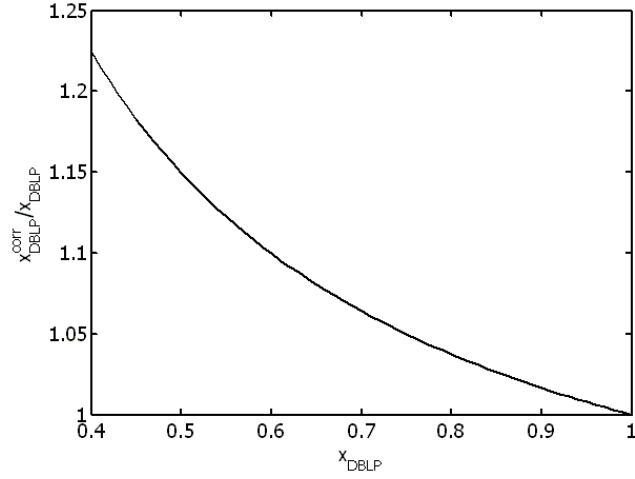
Figure 4.21 Ratio of the corrected best-fit line to uncorrected best-fit lines both constrained to the point (1,1) as a function of the attenuation ratio.
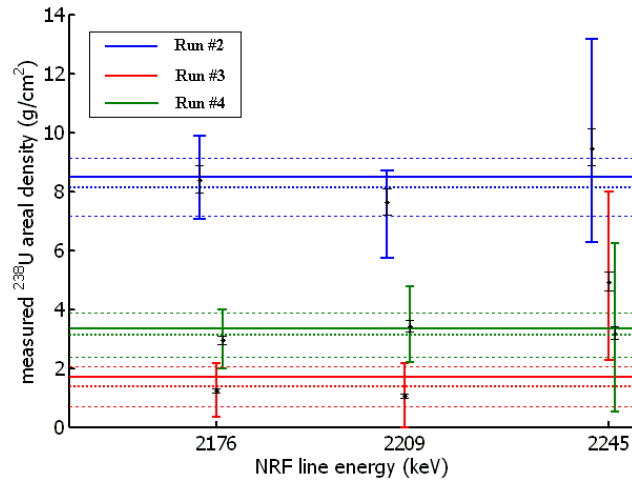
Figure 4.22 NRF-assay measured areal densities for three Runs based after application of the MCNPX-based notch-refill correction. Dotted lines correspond to weighted best fits, with $\pm 1\ \sigma$ error bounds given by the dashed lines. Solid lines correspond to the measured areal density as obtained by weighing and measuring the surface area of the DU plates used in the targets. Black error bars indicate systematic errors due to reported cross section uncertainties(87).

Run #	NRF-measured ρx (g/cm^2)			direct ρx (g/cm^2)	deviation (%)
2	8.14	$\pm^{0.98}_{0.99}$	$\pm\, 0.49$	8.47	3.9
3	1.37	± 0.68	$\pm\, 0.08$	1.69	19
4	3.12	$\pm^{0.73}_{0.76}$	$\pm\, 0.15$	3.34	10

Table 4.14 Values of the measured areal density of ^{238}U obtained by analysis of NRF peaks, and by direct measurement of the mass and area of the ^{238}U plates used in the assay target. The first errors listed for the NRF measurement are 1σ errors due to counting statistics in this experiment. The second stated errors are due to the reported uncertainties in NRF parameters indicated by reference (87). Values in the column labeled 'deviation' indicate the fractional deviation between the NRF-measured areal densities and those determined through direct measurement.

for the 2209-keV resonance is smaller than reported, the value of measured areal density due to attenuation of the 2209-keV peak would increase for each of the three Runs. In the following section, values of the NRF cross sections that best agree with the data obtained in this experiment are presented, along with other measured NRF parameters.

4.6.2   Measured NRF State Parameters

Using the MCNPX-based notch-refill correction described in equation 4.8, and knowing the true areal density of ^{238}U in the targets, we can calculate integrated cross section values (which are proportional to Γ_0) that best agree with the experimental data. These values for each NRF state and the weighted averages between runs are shown in Table 4.15. The weighted average values have also been used to re-calculate the expected effective attenuation of each NRF line for each target geometry. These data are plotted on the abscissa, and MCNPX-based notch-refilling-corrected measured effective attenuation values are plotted as the ordinate in Figure 4.23. As one would expect, these data obey the $y = x$ trend-line. The horizontal error bars are also significantly larger than in Figures 4.16 - 4.18 due to the larger uncertainties that resulted from back-calculating Γ_0. Also, comparing the data with the expected values of $y = x$, we find no trend in the deviations of the data except that the higher-energy resonances tend to deviate more than lower energy resonances. This can be explained by the fact that the areas of these peaks had significantly larger fractional uncertainties.

The ratio of measured NRF γ-rays counts that were due to de-excitation to the first-excited state in ^{238}U versus those due to de-excitation to the ^{238}U ground state, $R_{1,0}$, can be expressed by assuming equal detection probabilities for the two γ-rays
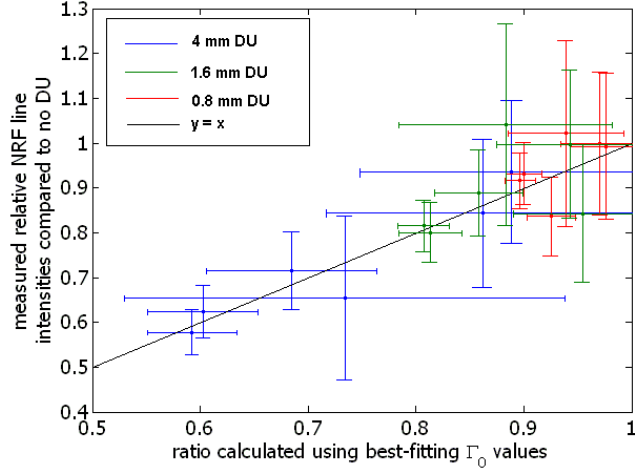
Figure 4.23 Comparing measured NRF line intensities after MCNPX-based notch-refill correction with predicted values based on the DBLP model using best-estimate values of Γ_0 from each NRF resonance based on this work. Each data point color represents data from a single Run and the black line indicates $y = x$.

E_{level}	Run#2		Run#3		Run#4		Weighted Average	
(keV)	Γ_0 (meV)		Γ_0 (meV)		Γ_0 (meV)		Γ_0 (meV)	
2176	31.28	$\pm$ 5.15	24.75	$\pm$19.64	29.39	$\pm$10.56	30.59	$\pm$4.50
2209	30.38	$\pm$6.46	22.13	$\pm$24.40	35.96	$\pm$14.17	30.83	$\pm$5.71
2245	22.13	$\pm$8.37	60.95	$\pm$38.44	19.30	$\pm$18.54	23.14	$\pm$7.48
2295	4.51	$\pm$11.87	2.76	$\pm$59.54	29.86	$\pm$33.75	7.14	$\pm$11.00
2410	13.25	$\pm$15.74	0.62	$\pm$65.86	0.46	$\pm$34.32	10.56	$\pm$13.98
2468	36.52	$\pm$26.57	-8.77	$\pm$91.64	-8.51	$\pm$43.67	24.25	$\pm$22.67
2080	7.95	$\pm$8.4	2.51	$\pm$48.45	13.79	$\pm$24.35	7.95	$\pm$8.40
2288	27.81	$\pm$32.58	106.48	$\pm$126.64	99.39	$\pm$111.95	37.60	$\pm$30.37

Table 4.15 Values of Γ_0 that best represent the measured attenuation of a NRF peak from each run, as well as the weighted average of Γ_0 for each peak. The statistical factor, g, has been assumed to be 1.5 for all resonances. For the 2468-keV resonance, the measured NRF γ-ray intensities for Runs #3 and 4 were larger than Run #1 and the resulting effective attenuation is negative. These values were assigned $\Gamma_0 = 0$ and the error for the weighted average values was assumed to be entirely that from Run #2.

E_{level} (keV)	$R_{1,0}$		Γ_1/Γ_0 (Heil)	
2080	2.39	$\pm$ 0.63	x	x
2176	0.55	$\pm$ 0.06	0.52	$\pm$ 0.02
2209	0.53	$\pm$ 0.07	0.55	$\pm$ 0.03
2245	0.52	$\pm$ 0.09	0.47	$\pm$ 0.03
2288	0.41	$\pm$ 0.32	x	x
2294	0.92	$\pm$ 0.23	0.59	$\pm$ 0.1
2410	0.60	$\pm$ 0.16	0.54	$\pm$ 0.05
2467	0.72	$\pm$ 0.26	0.5	$\pm$ 0.05

Table 4.16 Observed ratios of de-excitation of ^{238}U NRF states to first excited state versus ground state, with comparison to values of Γ_1/Γ_0 reported by Heil(87).

as

$$R_{1,0} \equiv \frac{\Gamma_1 W_1(\theta)}{\Gamma_0 W_0(\theta)} \tag{4.9}$$

where Γ_0 and Γ_1 are the partial widths for decay of the NRF state to the ground and first-excited state, respectively, and $W_i(\theta)$ is the angular correlation function discussed in Section 2.11.1. The measured values are shown in Table 4.16.

For this experiment, the average angle of scattering is $\theta = 118^\circ$. However, the proximity of the HPGe detectors to the TD, their relatively large diameters, and the divergence of the beam allow the HPGe detectors to detect photons that have scattered between $\theta = 105^\circ$ and $\theta = 150^\circ$.

Comparing the angular correlation functions for spin-1 excited states, shown in Figures 2.40 and 2.42, we note that the angular correlation functions all cross from less-than to greater-than unity at $\theta = 128^\circ$, and therefore, we expect the ratio of these angular correlation functions to be near unity as well. The angular correlation functions for spin-2 excited states exhibit different behavior. They are shown Figures 2.40 and 2.43, we observe that $W(\theta = 118^\circ) = 0.68$ for the sequence $0 \to 2 \to 0$ and $W(\theta = 118^\circ) \approx 0.95$ for the sequence $0 \to 2 \to 2$, regardless whether the emitted NRF γ-ray has angular momentum of 1 or 2. Thus, we expect the ratio of angular correlation functions to be near 1.5 for cases where the spin of the NRF state is 2, and de-excitation rates to the ground and first excited state are being compared. All NRF lines reported by Heil were found to be magnetic dipole lines, and therefore neglect of the factor $W_1(\theta)/W_0(\theta)$ is valid. The Heil experiment also used higher-energy electrons to produce bremsstrahlung, which explains why the statistical uncertainty quoted for their values increases more slowly with increasing NRF line energy compared to the uncertainty shown for these data.

Two additional pairs of peaks appear to be due to the de-excitation of previously un-reported NRF states to the ^{238}U ground and first-excited state. These γ-rays correspond to levels at 2080 keV and 2288 keV. The $R_{1,0}$ value of the 2288-keV resonance is similar to those of other NRF peaks, indicating it is probably another

$J = 1$ state. The $R_{1,0}$ value of the 2080-keV resonance is 2.39 ± 0.63, which can lead to two interpretations. One is that the state is a $J = 2^+$ state, and the other is that $J = 1$, but the total spin projection onto the nuclear symmetry axis, $K = 0$, in which case theory predicts that $R_{1,0} = 2$. The assumption of the spin of the NRF state influences the expected values of g and $W(\theta)$ for the NRF transition. These values influence estimates of the width, Γ of the state when compared to other states.

By only comparing effective attenuation ratios, integrated cross sections for the 2080-keV and 2288-keV states were found to be 22.1 ± 23.3 and 82.9 ± 66.9 eV·b, respectively. Uncertainties resulting from deriving cross sections by this technique are very large. However, by comparing measured NRF γ-ray intensities to those of the largest NRF peaks, we may provide better estimates of $g\Gamma_0 W(\theta)$ for the resonances. For each peak, the ratio of peak intensities can be expressed as

$$R = \frac{A_{pk}}{A_{pk}^r} = \frac{\epsilon(E)\Phi(E)g\Gamma_0 W(\theta \approx 118^\circ)/\mathbb{A}_{pk}(\rho x)}{\epsilon(E^r)\Phi(E^r)g^r\Gamma_0^r W^r(\theta \approx 118^\circ)/\mathbb{A}_{pk}^r(\rho x)} \tag{4.10}$$

where the superscript, ^{r} refers to the reference state, which was taken as the 2176-keV resonance, $\epsilon(E)$ corresponds the combined processes of full-energy detection of a photon incident upon the detector and penetration of the photon through the Pb filter, $\Phi(E)$ indicates the intensity of photons that are expected incident upon the TD neglecting resonant absorption (Figure 4.12), and $\mathbb{A}_{pk}$ is the expected excess attenuation of resonant photons. $\mathbb{A}_{pk}$ is a function of Γ_0, therefore equation 4.10 was iteratively evaluated to determine values of Γ_0 and $(A)_{pk}$ that reproduce R.

Although full details of the geometries of three of the four HPGe detectors used in the experiment are unavailable, they are all approximately 8 cm-diameter, by 8 cm-depth cylindrical crystals. A MCNPX simulation of the detector response when shielded in this geometry has been described in Section C.4. With $x_f = 1.27$ cm, we find that for 2.0-MeV photons incident upon the shielded detector, approximately 12.2% will deposit their full energy in the HPGe detector, and 11.0% of 2.4-MeV photons. Values calculated in this way were used for $\epsilon(E)$ in equation 4.10

It was further assumed that $W^{2288}(\theta) = W^r(\theta)$ and $g^{2288} = g^r$. For the 2080-keV state, both hypothesized spin states are considered. If $J^{2080} = 2$, $g^{2080} = 5g^r/3$, and otherwise, $g^{2080} = g^r$. These substitutions resulted in $\Gamma_0^{2288} = 5.1 \pm 2.6$ meV, $\Gamma_0^{2080} = 12.9 \pm 1.0$ meV if $J^{2080} = 1$, and $\frac{\Gamma_0^{2080}W^{2080}(\theta \approx 118^\circ)}{W^r(\theta \approx 118^\circ)} = 7.7 \pm 0.6$ meV if $J^{2080} = 2$. $W^{0 \to 2 \to 0}(\theta = 118^\circ) = 0.67$ and $W^{0 \to 1 \to 0}(\theta = 118^\circ) = 0.92$, thus we can estimate that if $J^{2080} = 2$, $\Gamma_0^{2080} \approx 10.6 \pm 0.8$ meV without performing numerical integrations of $W(\theta)$ for specific detector geometries.

The value of Γ_0^{2080} falls within one standard deviation uncertainty of that determined via the effective attenuation method, and the value of Γ_0^{2288} determined by comparison with known resonances is about 1.1 standard deviations from the value determined via the effective attenuation method. These results indicate the weaknesses of using the resonant attenuation method to determine NRF parameters for peaks with limited total counts which results in poor statistical confidence.

4.7   Experimental Conclusions

This experiment demonstrated the applicability of a beam-normalization scheme using 511-keV γ-rays, instead of a known NRF γ-ray peak and that the trends of resonant-energy attenuation generally follow that predicted in Section 3.2. However, each large resonance has exhibited a higher NRF rate than was predicted by the analytical model, and when the data are treated collectively, the deviation from the analytical predictions is approximately twice the error, indicating that the deviations are likely to be statistically significant. The deviation between the model and data can be explained by the process of notch refilling. MCNPX was used to estimate the intensity of the notch refilling effect, and indicated that notch refill is a larger effect for larger values of effective attenuation, as described in Figure 4.21. A correction based on the notch refill modifies the analytical predictions such that the relative rates of NRF γ-ray measurement shift from $2.09\,\sigma$ above the prediction to $\sim 0.69\,\sigma$ above the prediction. These results appear to be the first experimental observation of notch refilling in a transmission measurement of resonant-energy photons.

The experiment has also indicated that the intensity of the two largest ^{238}U resonances (2176 and 2209-keV) are slightly smaller than reported by Heil et. al.(87). The disagreement adds credence to the assertion, made herein, that these resonances do not have additional strength that had not been observed due to weaker de-excitation modes. The disagreement between the intensities of the states measured in this experiment and those reported by Heil (excluding the additional intensity that was inferred) is approximately one standard deviation.

Two additional states that undergo NRF were also observed with excitation energies of 2080 and 2288 keV. Both states are quite weak, and the 2288-keV state appears to be more likely to de-excite via the first-excited state, rather than directly to the ground state.

Better statistics could improve all of these conclusions. The experiment lasted for four 10-hour days, but with a stronger and more reliable accelerator (i.e. $\sim$10 mA and stable operation), it is possible that better statistics could be attained by significantly shorter experiments.

Chapter 5

Summary and Conclusions

5.1 Backscatter and Transmission Measurements

The prospect of using nuclear resonance fluorescence to non-destructively and quantitatively assay radioactive targets with bremsstrahlung radiation has been investigated by explicit consideration of two example applications; spent nuclear fuel and large radiological sources. Although measurement parameters have not been optimized for either application, the strengths and weaknesses of nuclear resonance fluorescence for these applications are evident. Direct measurement of backscattered NRF γ-rays may be subject to large backgrounds due to the radioactivity of the assay target. This measurement method is more sensitive to the composition of the exterior of the assay target than the interior and measurement of low-intensity NRF γ-rays due to small resonances or low concentrations of the resonating isotope may be difficult.

Direct measurement of the reduction in resonant-energy photons transmitted through a target would be very difficult. This is due to the large intensity of transmitted photons and is mitigated by use of a TD, which is composed of the isotope whose resonance absorption is being measured. Radiation detectors that view the TD can be effectively shielded from photons emitted from the assay target. The quantity of the TD isotope in the assay target is determined by measuring the decrease in the NRF γ-ray rate relative to the rate in the absence of the isotope of interest in the assay target. The precision to which this quantity can be measured was discussed in Section 3.2.4. Measuring an isotope with large NRF resonances at small concentrations in a target is the most attractive regime for transmission assay.

5.1.1 Assay Parameter Selection

Many of the parameters that are adjustable in the examples that have been presented were not optimized. These parameters include geometric considerations such as target-detector separations and shielding thicknesses, bremsstrahlung converter

dimensions and electron energies. However, the parameters chosen for study represent reasonable choices. Increasing beam energy increases NRF γ-ray rates at the expense of further increasing both the background count rates and the rates in the vicinity of the full-energy peak of interest. Increasing spacing between converters, targets, TDs, and detectors generally reduces signal and background count rates, but allows for more shielding to reduce the detection of photons that have not followed the desired trajectory for assay. In the case of a transmission measurement, larger dimensions also allow more shielding between the detectors and the assay target, reducing the impact of its radioactivity.

Locating an assay target closer to the bremsstrahlung converter would allow it to subtend a larger fraction of the incident bremsstrahlung photons. If the TD were made to subtend the same fraction of the bremsstrahlung beam, the efficiency of the system would increase. However, if the TD consists of a fissile actinide, the possibility of a large TD poses other drawbacks due to material security concerns. Generally, using more efficient detectors that can operate at higher rates than assumed here (10^4 c s^{-1}) can proportionally improve expected NRF count rates. If the NRF assay system is set up such that detector count rates are the limiting factor, increasing target-to-detector distances and increasing the number of detectors can, in principle, reduce or eliminate the need for a filter, which would dramatically reduce measurement times. The development of γ-ray detector arrays has been an ongoing field of research(136), however the array size necessary to sufficiently reduce count rates is significantly larger than those under development. Beyond detector and source improvements, parameters such as bremsstrahlung beam energy, target orientation can potentially reduce measurement times by perhaps a factor or two, but significant changes to the conclusions drawn here would only come from technological improvements.

5.1.2   Non-resonantly Scattered Backgrounds

The utility of NRF for assay systems is strongly dependent on the ratio of the intensities of NRF γ-rays and non-resonant background photons. Chapter 2 described photon transport processes at energies that are relevant for NRF interrogation. This discussion indicated that photonuclear elastic scattering has generally been ignored in Monte Carlo radiation transport codes and other inadequacies are found in treating photo-atomic elastic scattering. As part of this work, a modification of MCNPX was developed that enables this code to simulate the process of Rayleigh scattering as described by the photo-atomic cross section data files. This modification, described in Appendix A, has been shown to simulate the scattering of incident interrogating bremsstrahlung interrogating photons in good agreement with experimental data up to approximately 2 MeV. Above this energy, photonuclear elastic processes significantly contribute to the total coherent scattering cross section. This causes MCNPX and other popular Monte Carlo radiation transport codes

to underestimate the intensities of backscattered photons. These shortcomings have been addressed in this work by explicitly modifying MCNPX-calculated background photon fluences to include additional photons expected from elastic scattering processes. The photonuclear elastic scattering contributions become more important with higher-energy photon spectra.

It is desirable to implement more complicated photon transport physics in the radiation transport codes. However, at present, there is no complete compilation of Delbrück scattering amplitudes. Any existing elastic photonuclear cross section database will be subject to modification as the physics describing Delbrück scattering is better refined. However, for relevant energies and most scattering angles and targets, Rayleigh and nuclear Thomson scattering contribute the majority of the elastic cross section and therefore the accuracy of the Delbrück scattering amplitudes is of secondary importance. Modification of the radiation transport codes and datafiles to explicitly treat photon scattering in terms of cross sections, rather than form factor multipliers of differential Thomson scattering cross sections, would significantly improve performance at the expense of increased data file sizes. Photo-atomic cross section data libraries would probably be comparable in size to neutron or photonuclear data libraries, which pose no onerous storage requirements for modern computer systems.

While Monte Carlo radiation transport codes tend to be inaccurate in simulating backscattering of photons, they have been shown to be quite accurate in simulating spectra and intensities of photons transmitted through materials. The process of down-scattering of photons into the immediate energy range of nuclear resonances, called *notch refilling*, is dependent on geometry, materials, and beam characteristics in a non-trivial way. For these reasons, Monte Carlo simulation of radiation transport will continue to play an important role in modeling of transmission NRF measurements. This observation provides even further motivation to improve the physics describing large-angle photon scattering in Monte Carlo codes.

5.2 Large Radiological Sources

The backscatter assay method appears capable of age-dating large radiological sources in reasonable time-periods without the need to develop any new photon sources or radiation detector systems. This conclusion relies on the fact that daughter isotopes of radiological sources such as ^{137}Ba have states that exhibit large NRF signatures at energies significantly larger than the energy of γ-rays emitted after ^{137}Cs β^--decay. This enables shielding to suppress detector sensitivity to the ^{137}Cs radioactivity, while still allowing sufficient intensity of ^{137}Ba NRF γ-rays to be detected.

NRF responses of parent isotopes such as ^{137}Cs and ^{90}Sr have not yet been measured. It is probable that both isotopes will have NRF responses similar to those of their daughters. If this is the case, the relative populations of both parent and
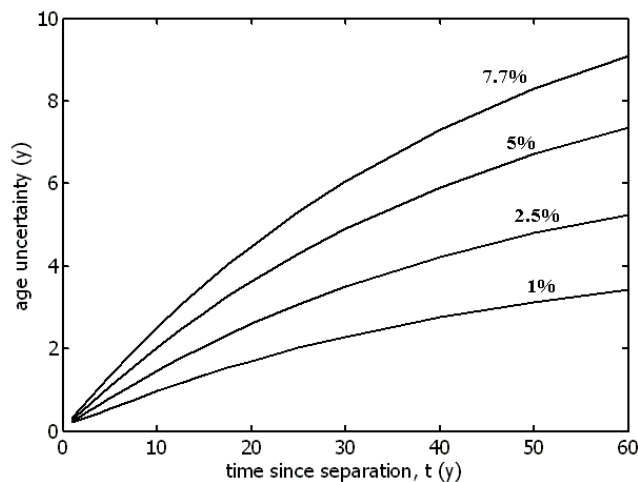
Figure 5.1 Calculated uncertainties in the time since chemical separation of a 1 kCi initial activity ^{137}Cs radiological source if the statistical precision to which the 3761 keV resonance is known is 7.7, 5, 2.5 or 1%. The corresponding curve where the uncertainty of the intensity of the 3761-keV resonance is neglected has been shown in Figure 3.11.

daughter (grand-daughter in the case of ^{90}Sr) may be directly measured in a single irradiation, resulting in age-dating by direct comparison of NRF γ-ray intensities, which in turn, reduces systematic uncertainties.

In Section 3.1.3, the fundamental limit to the precision that the time since chemical separation of a radiological source may be quantified by a backscatter NRF measurement was considered. This limit is based on the expected number of NRF γ-ray full-energy deposition events observed during a measurement and the resulting counting statistics. An estimate of the statistical precision of the age-dating process for a ^{137}Cs source subject to an 8-hour irradiation by bremsstrahlung produced by a 20 mA electron beam and viewed by a single detector were shown in Figure 3.11 for varying amounts of ^{137}Ba relative to ^{137}Cs (as defined by the time since chemical separation). However, the potential for systematic errors was not considered. The largest source of systematic errors is the uncertainty in the strength of the NRF resonance. In the case of the 3761-keV ^{137}Ba resonance, the cross section has a reported uncertainty of 7.7% (1σ) (115). This uncertainty tends to dominate the total uncertainty. Figure 5.1 presents the uncertainty in the time since separation of a 1-kCi ^{137}Cs source in the limit that both the counting statistics and the uncertainty of the total cross section of the 3761 keV ^{137}Ba resonance are considered. The figure also gives uncertainty estimates if the uncertainty in the cross section were reduced to 1, 2.5, and 5%.

From this discussion, it seems clear that the precision to which NRF cross sections are known limit the precision to which an assay method based on NRF can measure a nuclide within the assay target. Significant improvement in NRF cross

sections is therefore desirable for the successful application of NRF assay technologies.

5.3   Penetration Model Accuracy

A significant portion of Section 3.2 was devoted to describing the *effective attenuation* of resonant-energy photons as they traverse an assay target and subsequently interact in a transmission detector. Chapter 4 describes an experiment that tested many of the conclusions from Chapter 3. The experiment observed slightly more resonant-energy photons than were predicted by the analytical model. The magnitude of these differences were approximately two standard deviations of the statistical experimental error. However, modeling suggests that a significant portion of this difference is due to the process of notch refilling, which was not included in the initial analytical model.

The magnitude of notch refilling was examined both by simulating down-scattering of monoenergetic photons through an assay target (described in Section 3.2.5), and by simulating the entire experiment (Section 4.5.6). Both examinations suggested that the notch refilling process can induce up to approximately a 5% effect for the geometry experimentally studied. By adding a notch refilling correction based on the Monte Carlo simulations, the experimental data were found to differ from the modified predictions by less than one standard deviation. In order to make further conclusions to the accuracy of the models derived in this dissertation, more experimental precision would be needed.

The primary source of uncertainty in the data is statistical, associated both with counting of the NRF γ-ray peaks, and knowledge of the intensities of the resonances. Transmission measurement counting statistics could be improved by implementation of one or more of the following:

- increase photon beam intensity at resonant energies;

- decrease photon beam intensity at non-resonant energies;

- increase measurement duration;

- increase the number of detectors used in the measurement;

- improve detector resolution;

- increase radiation detector count rates;

- use less-radioactive shielding and TD; and

- improve detector shielding from un-scattered beam photons.

Some steps are directly advantageous, increasing measurement time and number of detectors used do not have any physical drawbacks. Likewise, less-radioactive materials would reduce background count rates. Increasing the input rates of detectors generally worsens their energy resolution. Using a narrow-band photon beam would significantly reduce the beam intensity at non-resonant energies, however the technology to make them sufficiently intense at resonant-energies does not yet exist. With a bremsstrahlung source, increasing the photon beam intensity proportionally increases count rates (which were already near 2×10^4 c s^{-1}) and thus thicker filters must be used. This would reduce NRF γ-ray detection probabilities, but this reduction is less than the total count rate reduction induced by thicker filters, which indicates that the combination of increasing filter thickness and bremsstrahlung beam intensity reduces the time needed to make a measurement.

The hypothesis that notch-refilling has been observed in the experiment could be easily tested in a subsequent experiment by modifying the target geometry. In the previous experiment, the depleted uranium in the target was placed upstream of the lead. If the depleted uranium were placed downstream of the lead, the notch-refilling should, in principle, be dramatically reduced.

The functional form describing the cross section of a resonance influences the model predictions of the effective attenuation. The functional form becomes more important with increasing areal density of the IOI in the target. For the 2176-keV ^{238}U resonance described in Section 3.2.3, use of the least-accurate cross section form considered, the step-function, would result in a 1% error relative to the Doppler-Broadened Lorentzian Profile (DBLP) form for 0.2 g/cm^2 ^{238}U in the assay target. The sensitivity of the effective attenuation to the cross section form increases quickly with larger areal densities of the isotope being measured in the assay target. For the same resonance, a Maxwell-Botzmann cross section form results in a 5% difference from the DBLP for an IOI areal density of 15 g/cm^2. When using the transmission assay technique for large areal density targets, or with larger resonances than those described in this work, it may be important to consider the phonon spectrum in the material to define a more-accurate profile than that of the DBLP.

5.4 Spent Fuel Assay Outlook

Spent nuclear fuel provides difficult challenges for non-destructive assay techniques. It is strongly radioactive and the material of most interest to nuclear safeguards, the plutonium, comprises a small fraction of both the target mass and activity. The weakness of NRF signals, relative to both non-resonantly scattered beam photons and the radioactivity of the spent fuel indicates that direct detection of bremsstrahlung-induced NRF γ-rays emitted by ^{235}U, plutonium, and other actinides appears to be difficult and very time-consuming.

The transmission NRF assay technique, which uses indirect detection of resonant-photon absorption appears, in principle, capable of isotopically, and non-destructively

quantifying actinide content of spent nuclear fuel. However, the method appears to suffer from weak signals, which may limit its applicability.

Resonance Strength Uncertainties

The experiments performed to measure widths of actinide NRF states have all been backscatter measurements similar to those described in Section 3.1. These experiments have two limitations. First, the statistical uncertainties that have been reported are generally so large that subsequent transmission assay measurements would be subject to systematic inaccuracies. The backscatter method also only directly measures the value $g\Gamma_i\Gamma_0/\Gamma$, where Γ_i is the partial width for emission of the observed NRF γ-ray. The intensity of resonant-photon absorption is proportional to $g\Gamma_0$, so unless NRF γ-rays that may be emitted during de-excitation of the resonant state are measured, Γ, and therefore Γ_0, will be under-estimated. This implies that the ^{239}Pu resonances that have been observed may have larger values of Γ_0 than indicated by the backscatter measurements, although it is unlikely that the un-observed portion of the de-excitation spectrum would be significantly stronger than the observed portion.

Because the systemic uncertainties arising from imprecise cross section measurements can, in principle, be reduced, the limiting factor is the statistical precision in a given measurement. The examples in Section 3.2.4 indicate that even with very intense bremsstrahlung beams, approximately 200 detector·days of measurement would be required to obtain 10% uncertainty in the amount of ^{239}Pu in an assembly (assuming the resonances are no stronger than observed). However, if ^{240}Pu has similarly-intense resonances as those known for ^{238}U, only approximately 16 detector·days could provide a 5% uncertainty ^{240}Pu measurement. This indicates that transmission nuclear resonance fluorescence measurements of isotopes with strong resonances such as those observed in even mass number actinide isotopes may provide very useful information for safeguarding spent fuel.

5.5   Future Work

This dissertation has described many aspects relating to the detection of nuclear resonance fluorescence γ-rays to perform non-destructive measurements of radioactive materials of interest to nuclear security. To either make these measurements practical or possible, further improvements to the technology should be made. Some improvements are as simple as improving the knowledge of the states and the strengths of their nuclear resonance fluorescence transitions. Further improvements can also be made to the databases that are used to model NRF and the competing photon-scattering processes. Finally, photon source and detector improvements could greatly increase the potential and applicability of this technology.

5.5.1   NRF Data

The strengths of resonances used to perform an assay measurement must be known to better precision than the desired uncertainty in the assay measurement. The majority of NRF transitions that have been discussed in this dissertation are known to precisions between 5% and 15%. A measurement of ^{27}Al excited-state natural widths is described in Reference(137). These widths were measured by transmission measurement of an Al target and agreed with values obtained by other techniques(65). The authors report uncertainties of 3% for the widths of the larger resonances, but do not specify how non-statistical uncertainties contributed to their estimates.

As indicated in Section 5.2, knowledge of the 3761-keV ^{137}Ba resonance to ∼2.5% would reduce the uncertainty with which large ^{137}Cs source could be measured by a factor of approximately two. Improvement of the precision of the ^{235}U and ^{239}Pu resonance widths could also be accomplished with larger samples than those that were used in the measurenents by Bertozzi et.al.(123).

Measurement of NRF γ-rays emitted from the daughter isotopes of radiological sources such as ^{137}Cs or ^{90}Sr can, with knowledge of the radiological source activity, provide the time since chemical separation of the radiological source. If the NRF responses of the parent isotopes were also known, a single NRF measurement could be used to date the source, with only a relative measurement. This makes the measurement of the NRF responses of ^{137}Cs, ^{90}Sr, and other radiological source isotopes that are produced by chemical separation from fission products an attractive extension of this work.

5.5.2   Model Improvements

The models discussed in Chapter 3 have, to a reasonable degree of detail, examined the back-scatter and transmission assay techniques. Appendices A and B describe modifications to the computer code MCNPX that enables the simulation of NRF, and the simulation of Rayleigh scattering to be conducted more accurately. However, both computational and analytical modeling can continue to be improved.

The analytical model describing the excess attenuation of resonant-energy photons appears to need to be corrected to take into account the down-scattering of higher-energy photons that results in resonant-energy photons. These corrections had been estimated by Monte Carlo simulations and were applied to the analysis of the experiment described in Chapter 4, but a more explicit model treating the notch-refilling process would be desirable.

The investigation of the transmission assay technique to spent fuel assemblies has explicitly assumed that assemblies can be approximated as homogeneous rectangular parallelepipeds, rather than discrete fuel pins. If the orientation of a fuel assembly is such that streaming paths through the assembly exist, this appears to be a poor approximation. However, if photons impinge upon the assembly at an

angle where no such streaming paths exist, the applicability of the homogenized approximation appears more valid. This is the subject of ongoing study.

The approximation that a resonance is Doppler-broadened due to thermal atomic motion defined by a Maxwellian energy distribution neglects the properties of the crystalline structure, which induces more complex energy distributions for the constituent atoms. Descriptions of more complex recoil spectra were described in Section 2.11.4, but the models described in Section 3.2 have only assumed cross section distributions that are broadened by a Maxwellian energy distribution for the atoms. If they become available, more detailed descriptions should be used. However, each distribution is specific to the crystalline structure it describes. Further, the uncertainty associated with approximating the atomic thermal motion increases with target areal density, but appears to be insignificant for the purpose of using a transmission measurement to quantify any isotope except ^{238}U in spent nuclear fuel. For other targets of nuclear security interest, such kilogram-quantities of plutonium, more accurate energy distributions of crystalline atoms may be need to be considered.

The insertion of NRF physics responses to photonuclear ENDF and ACE datafiles required additional approximations due to constraints in the ENDF data format. To more accurately represent the data in ENDF, this data format would need to be altered. Alternatively, ACE datafiles used in the MCNP codes could be directly generated without using the ENDF format. In this case, MCNPX is capable of accommodating the NRF data to a high degree of precision. Conversely, the implementation of more accurate elastic scattering physics would require MCNPX source code modifications. Likewise, the ENDF format would require changes, and the computational process of accurately calculating Delbrück scattering amplitudes should be completed.

5.5.3   Technological Improvements

Measurement of relatively weak signals in a very strong background is a perennial challenge in radiation detection applications. From the perspective of nuclear resonance fluorescence assay techniques, the options are to increase the NRF signal strength, relative to the background, or to make the γ-ray detectors more effective at measuring the signal.

The NRF signal can be made stronger by increasing beam intensity and filter thickness. Testing the applicability of the models with very thick filters is necessary to ensure that no complications arise from thicker filters. One potential complication is that the beam normalization technique described in Section 4.5.5 that was used to analyze the experimental data will be less effective with thicker filters. Measured 511-keV annihilation γ-rays becomes less likely to be due to beam photons inducing pair production in the TD and more likely due to scattered photons inducing pair production in the filter.

The signal may also be significantly increased by altering the interrogation photon spectrum. Throughout Section 3.2, the ramifications of using a quasi-monoenergetic photon source has been discussed, and the development of such sources is being attempted. However, even quasi-monoenergetic photon sources would require high count-rate detection systems to make NRF assays of spent fuel practical. Whether this is accomplished by a combination of HPGe detectors and shielding, or different detector types remains to be seen.

In general, fast, high-resolution, γ-ray detectors that are able to subtend a large fraction of the backwards solid angle are needed for NRF measurements. Any technological developments that make these devices more available are favorable for this type of assay system.

5.5.4   Study of More Applications

This dissertation has considered two particular non-destructive analysis applications; forensics measurements of very large radiological sources produced through chemical separation of fission products, and the measurement of ^{239}Pu and ^{235}U content in spent nuclear fuel. These may be thought of as two extreme cases; both involving very radioactive targets.

Many other applications of nuclear resonance fluorescence should and are being considered. Scanning cargo for nuclear weapons is one of the primary technical drivers pushing NRF photon source technology and prompted the measurement of the NRF response of ^{235}U and ^{239}Pu. The potential to use the technology to measure relative concentrations of ^{235}U ^{238}U in UF$_6$ at enrichment facilities, as well as confirmation measurements for shipments of new and used fuel should also be examined.

The examination of measuring spent fuel could also be continued. With an exhaustive study of fission product resonance strengths, multiple attractive isotopes may be identified to measure. The possibility of using multiple isotopes in a TD has not been discussed in this dissertation, but in principle the TD need not consist only of one isotope.

Appendix A

Rayleigh Scattering in MCNP

A.1 Introduction

Documentation of the MCNP series of codes has claimed for years to accurately represent the data present in evaluated nuclear data files (18),(23),(25),(38). The photo-atomic data in the ENDF/B-VI format are based on the evaluated photon data library (EPDL97)(19). However, the work supporting this thesis observed that the sections of code describing the form factor evaluation of coherent and incoherent scattering had not been updated since their precursor code, MCP, was written in 1973(26). This legacy code results in significant inaccuracies in photon spectra computed by MCNPX when simulating geometries that are typical of NRF experiments(43).

MCNP treats all coherent scattering as Rayleigh scattering and follows the form factor approximation outlined in Section 2.3.1. Data libraries used in MCNP are created by the code NJOY, which reads ENDF tabulations of atomic form factors and converts them into the ACE format used in MCNP(44). Atomic form factor values are tabulated for a given Z and momentum transfer between the scattered photon and the atomic electron, q. The units of q should be units of momentum, however q has traditionally been tabulated in *reduced wave number*, which has units of inverse length[1]. The derivation and use of momentum transfer values in MCNP has been poorly documented. MCP and MCNP user manuals describes q in units of cm^{-1},(38),(26) however the data tabulated in MCNPX are in units of $\AA^{-1}$(15).

---

[1]The conversion between momentum transfer, $\hbar k \sin(\theta/2)$, and reduced wave number is accomplished by dividing by Plank's constant, h, inserting $\frac{c}{c} \frac{m_e c^2}{m_e c^2}$, equating, $E = \hbar c k$ and, $\sin(\theta/2) = \sqrt{\frac{1-\cos\theta}{2}}$. Evaluating the constants:

$$q = \frac{c}{hc} \frac{m_e c^2}{m_e c^2} 2\hbar k \sin(\theta/2) = \frac{E}{m_e c^2} \frac{2 m_e c^2}{\sqrt{2}hc} \sqrt{1 - \cos\theta} = 29.1445[\AA^{-1}] \frac{E}{m_e c^2} \sqrt{1 - \cos\theta}$$

E (keV)	Angle
74.4	180º
105	90º
194	45º
853	10º
1733	4.9º
2423	3.5º

Table A.1 Maximum coherent scattering angles allowed in the MCNP codes.

The shortcoming comes from the fact that MCNP has historically had a fixed array of q-values for which coherent scattering form factors, $C(Z, q)$ are defined. Despite the fact that the EPDL97 (and ENDF) now tabulates form factors for q up to $10^{11} \mathring{A}^{-1}$, q in MCNP was restricted to $q \leq 6\ \mathring{A}^{-1}$ and coherent scattering form factors for $q > 6$ were assumed to be 0. Table A.1 demonstrates the maximum coherent scattering angles, θ_{max}, that were allowed by this restriction. Figure A.1 helps to explain why this short-coming had gone un-noticed by many MCNP users[2]. In it, the fraction of the Rayleigh scattering cross section that is due to scattering above θ_{max} is plotted versus photon energy for various elements, i.e.

$$f = \frac{\int_{q=6[\mathring{A}^{-1}]}^{q_{max}} \sigma_{Ray}(\theta)d\mathbf{\Omega}}{\int_{q=0}^{q_{max}} \sigma_{Ray}(\theta)d\mathbf{\Omega}} \tag{A.1}$$

where $q_{max} = 29.1445[\mathring{A}^{-1}]\frac{E}{m_e c^2}\sqrt{2}$. The omission is most significant in high-Z materials, and is most important when photon energies exceed approximately 100 keV. As will be described, this omission is only important when coherently-scattered photons can be distinguished from incoherently-scattered and annihilation photons. The distinction is most obvious when backscattering of multi-MeV photons from high-Z materials is considered, and this is precisely what is done in experiments designed to measure NRF.

Modification of the MCNPX source code and the NJOY data processing code are described in Section A.4. These modifications enable MCNPX to simulate Rayleigh scattering for all problems.

To test that modifications of the MCNPX code and datafiles were successful, two pairs of simulations were conducted comparing elastic scattering rates before and after implementation of the modifications. For each pair a pencil beam of monoenergetic 1.7-MeV photons was normally impinged upon a 1 cm-radius by 100 mm-depth cylindrical target of either uranium or iron. Photons emitted from the target were tallied as they crossed a spherical surface of 10 cm-radius, centered at the center of the target cylinder. The direction of the emitted photons relative to

---

[2]This short-coming was independently observed by Lodwick and Spitz when they compared in vivo x-ray fluorescence measurements of lead in bone to MCNP calculations(140)
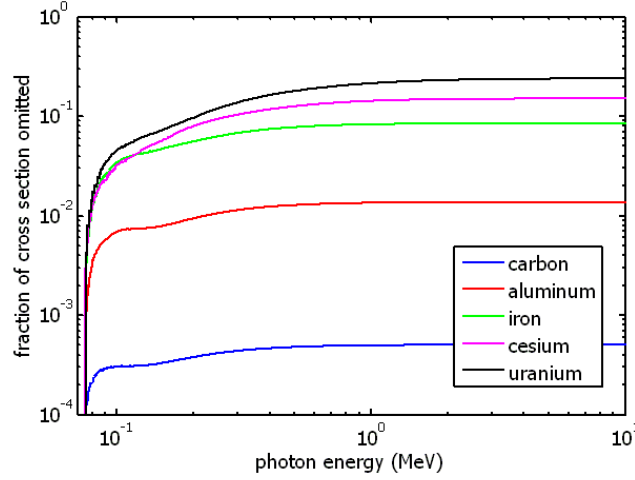
Figure A.1 Fraction of Rayleigh scattering cross section that corresponds to a reduced momentum transfer value, $q \geq 6 \ \mathring{A}^{-1}$.

the direction of the incident beam were tallied in 1° angular bins up to 10°, and then in 5° bins. The energy of the emitted photons were also tallied, with photons within 860 eV of the initial energy being considered elastically scattered. This bin width was selected to ensure that incoherently scattered photons are not tallied into the elastic bin for scattering angles greater than 1°. The effective elastic scattering cross section was then calculated by the relation

$$\frac{d\sigma_{\mathrm{ES}}}{d\mathbf{\Omega}} \approx \frac{N_{\mathrm{F1}}}{\Delta\Omega}\frac{M}{N_A\rho x} \tag{A.2}$$

where N_{F1} is the number of photons in the elastic tally bin, $\Delta\Omega$ is the solid angle subtended by the angular bin, M is the molar mass of the target material, N_A is Avagadro's number, and ρx is the areal density of the target.

Figures A.2 and A.3 present the simulated angle-differentiated cross sections for elastic scattering of 1.7-MeV photons before (red) and after (black) the implementation of the extended Rayleigh scattering cross section library. The EPDL97 cross section for elastic scattering is also shown in green in both figures. The cross sections resulting from simulations that include the new form factor arrays closely follow the EPDL97 values. For the red histogram, non-zero values calculated for scattering into angles above the critical angle of 5.2° are due to the relatively improbable combination of photoelectric absorption followed by bremsstrahlung emission. This process yields photons in the elastic bin, and would yield an even smaller (nominally) elastic scattering probability were the highest energy bin made narrower. Regardless, the five (uranium) and seven (iron) decade decreases in effective elastic scattering cross section between the $3^{\circ} - 4^{\circ}$ and $6^{\circ} - 7^{\circ}$ bins indicate effects of the non-physical cutoff that had been implemented in MCNP. That the effective cross section was calculated to be 30% (uranium) and 8.5% (iron) lower after implementation of the
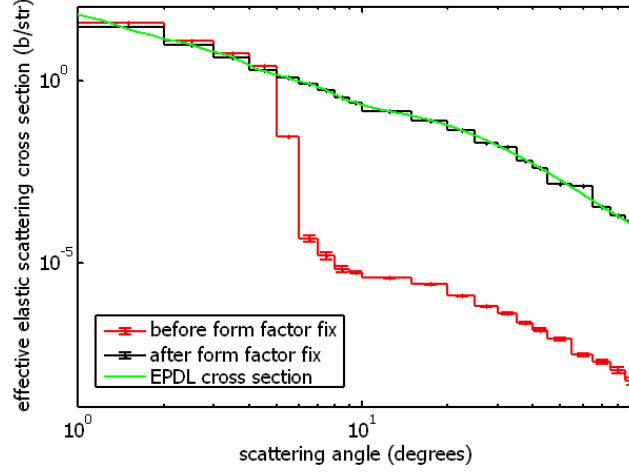
Figure A.2 MCNPX-simulated differential cross section for scattering of 1.7-MeV photons within 860 eV of initial energy from 100 μm-thick uranium with EPDL Rayleigh scattering cross section overlaid.

extended library for the range $1^{\mathrm{o}}-5^{\mathrm{o}}$ is explained by the fact that photons probabilistically sampled to undergo coherent scattering had been constrained to the forward 5.2^{o}, whereas now all angles are physically allowed. The amount by which MCNPX had overpredicted the Rayleigh scattering cross section is exactly the inverse of the fractions shown in Figure A.1 for 1.7-MeV photons. Thus, as another result of the truncated form factor arrays, MCNP had previously been overestimating elastic scattering of photons in forwards directions, and this effect was most severe for high photon energies and high-Z materials.

A.2   Form Factor Sampling Methodology

This section describes the method used in MCNPX to sample the coherent scatter cross section. This method defines the integrated form factors, which must also be included in the ACE files that provide the photo-atomic data for MCNP.

Suppose we want to sample a probability density function (PDF), $P(y)$, defined in the interval $a \leq y \leq b$, and related to another known PDF, $Q(y)$ by the following

$$P(y) = C_0 F(y) Q(y) \tag{A.3}$$

where C_0 is a constant, $C_0 > 1$ and $F(y)$ is a function with range $0 \leq F(y) \leq 1$.
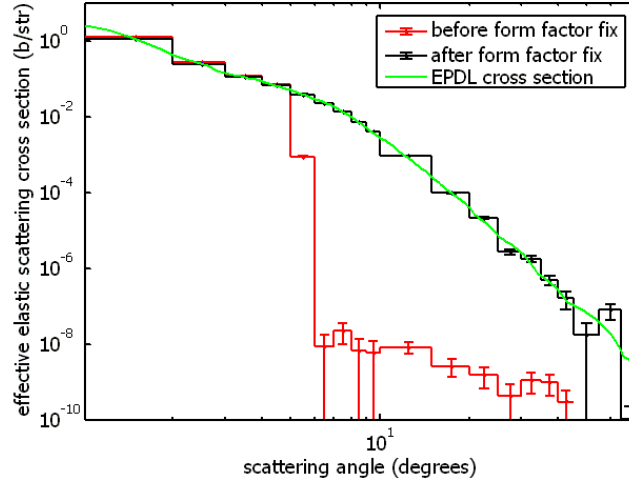
Figure A.3 MCNPX-simulated differential cross section for scattering of 1.7-MeV photons within 860 eV of initial energy from 100 : μm-thick iron with EPDL Rayleigh scattering cross section overlaid The large statistical uncertainty at high angles is due to the rarity of the events.

A.2.1   Sampling a Simple PDF

First we must define what is meant by 'sampling a PDF'. Assume the PDF, $Q(y)$, is a normalized and integratable function in some interval,

$$\int_a^b Q(y) = 1 \tag{A.4}$$

Sampling of $Q(y)$ is accomplished by using a random number, $0 \le r \le 1$, to select a value, y_{sample}, between a and b with a probability proportional to the value of the PDF.

The cumulative (or integrated) distribution function (CDF) for $Q(y)$ is defined as,

$$\mathbf{Q}(y') = \int_a^{y'} Q(y) dy \tag{A.5}$$

Therefore $\mathbf{Q}(a) = 0$ and $\mathbf{Q}(b) = 1$. By inverting the function $\mathbf{Q}(y')$, we have a function with a domain of [0,1]. Using the random number, r_1, we obtain

$$y_{\text{sample}} = \mathbf{Q}^{-1}(r_1) \tag{A.6}$$

which is a value of y, sampled from the PDF $Q(y)$. Clearly, this only works for PDFs than can be integrated, and whose integral can be inverted.

A.2.2   Rejection-Sampling Method

Sampling of equation A.3 is accomplished by use of the *rejection-sampling method*. First, $Q(y)$ is sampled. The value of y is accepted, with a probability

of $F(y)$, by using a second random number, r_2 to check that

$$r_2 < F(y) \tag{A.7}$$

The probability of not accepting a sampled value for y is given by

$$P_{\text{reject}} = 1 - \int_a^b F(y)Q(y)dy \tag{A.8}$$

When y is rejected, we sample another value of $Q(y)$ and again check with a new random number against equation A.7, potentially allowing an infinite number of samplings.

To prove that this will give an appropriate sampling of $P(y)$, first note that

$$1 = \int_a^b P(y)dy = \int_a^b C_0 F(y)Q(y)dy \tag{A.9}$$

so

$$\int_a^b F(y)Q(y)dy = C_0^{-1} \tag{A.10}$$

The probability of k rejections is then

$$P_k = (1 - C_0^{-1})^k \tag{A.11}$$

and the probability of accepting the $k + 1$-th iteration is

$$(1 - 1/C_0)^k F(y) \tag{A.12}$$

Using

$$\sum_{k=0}^{\infty} (1 - 1/C_0)^k = C_0 \tag{A.13}$$

we see that if an infinite number of iterations is allowed, the PDF for sampling y is given by

$$C_0 F(y)Q(y) = P(y) \tag{A.14}$$

A.3   Sampling Rayleigh Scattering Cross Sections

The angle of Rayleigh scattering is sampled in MCNPX by the rejection - sampling method. In this formulation, the independent variable, y, is given by, q^2, the square of the momentum transfer of the scattering event, which for a given photon energy is

$$q = K\alpha\sqrt{1 - \mu} \tag{A.15}$$

where $K = 29.1445 \ \mathring{A}^{-1}$, $\alpha = E/m_e c^2$, and $\mu = \cos(\theta)$.

The Rayleigh scattering cross section is given by

$$\sigma_{Ray}(\theta) = \sigma_{Th}(\theta)\,[F(q,Z)]^2 \tag{A.16}$$

where the Thomson scattering cross section is given by

$$\sigma_{Th}(\theta) = \frac{r_e^2}{2}(1+\cos^2\theta) = \frac{r_e^2}{2}(1+\mu^2) \tag{A.17}$$

The PDF for scattering into the angle, μ, is given by

$$p(\mu) = \frac{\sigma_{\mathrm{Ray}}(Z,\alpha,\mu)}{\int \sigma_{\mathrm{Ray}}(Z,\alpha,\mu)d\mu} \tag{A.18}$$

The PDF for a given squared-momentum transfer is given by

$$P(q^2)d(q^2) = p(\mu)\left|\frac{d\mu}{d(q^2)}\right|d(q^2) \tag{A.19}$$

Solving equation A.15 for μ and differentiating, we have

$$\frac{d\mu}{d(q^2)} = \frac{-1}{K\alpha^2} \tag{A.20}$$

Substituting, equations A.16, A.17, A.20, and A.18 into equation A.19, we obtain the expression for the angular scattering PDF

$$P(q^2) = \frac{r_e^2}{(K\alpha)^2}\frac{1+\mu^2}{2}\frac{[F(q,Z)]^2}{\int \sigma_{\mathrm{Ray}}(Z,\alpha,\mu)d\mu} \tag{A.21}$$

In MCNPX, equation A.21 is re-expressed by multiplying numerator and denominator by pairs of Z^2 and $\int_0^{q_{max}^2}[F(Z,q^2)]^2 d(q^2)$ to obtain

$$P(q^2) = \left[\frac{r_e^2 Z^2 \int_0^{q_{max}^2} Z^{-2}[F(Z,q^2)]^2 d(q^2)}{(K\alpha)^2 \int \sigma_{\mathrm{Ray}}(Z,\alpha,\mu)d\mu}\right]\left[\frac{1+\mu^2}{2}\right]\left[\frac{[F(q,Z)]^2 Z^{-2}}{\int_0^{q_{max}^2}[F(Z,q^2)]^2 Z^{-2}d(q^2)}\right] \tag{A.22}$$

This cumbersome expression is actually written in the form of equation A.3, where the expression in the first brackets

$$C_0 = \frac{r_e^2 Z^2 \int_0^{q_{max}^2} Z^{-2}[F(Z,q^2)]^2 d(q^2)}{(K\alpha)^2 \int \sigma_{Ray}(Z,\alpha,\mu)d\mu} \tag{A.23}$$

is, in fact, a constant. The integral, $\int \sigma_{\mathrm{Ray}}(Z,\mu)d\mu$, is the total Rayleigh scattering cross section and the other integral is obtained through interpolation between tabulated *integrated form factor* values. The expression in the second brackets of equation A.22 is

$$F(y) = \frac{1+\mu^2}{2} \tag{A.24}$$

which is a function with range, [0,1]. The third brackets contain,

$$Q(y) = \frac{[F(q,Z)]^2 Z^{-2}}{\int_0^{q_{max}^2}[F(Z,q^2)]^2 Z^{-2}d(q^2)} \tag{A.25}$$

which is the PDF for selecting a squared momentum transfer, where again, the tabulated integrated form factor is used.

A.3.1   Integrated Form Factors

The quantity,

$$\int_0^{q_{max}^2} Z^{-2}[F(Z,q^2)]^2 d(q^2) \tag{A.26}$$

is the integrated form factor. It is numerically integrated in NJOY and values are tabulated for corresponding values of q^2. The ENDF form factor tabulation specifies that $\ln[F(Z,q^2)]$ shall be linearly interpolated with $\ln[q^2]$. Thus the integrated form is tabulated as

$$\int_0^q {}^2 Z^{-2}[F(Z,q^2)]^2 d(q^2) \approx \exp\left(\sum_i \ln[Z^{-2}[F_i(Z,q_i^2)]^2]\Delta[\ln(q_i^2)]\right) \tag{A.27}$$

The interpolation scheme is slightly more complicated in that $\ln(0)$ is undefined, and the first momentum transfer entry, $q_1 = 0$. Such problems are fixed in NJOY by the use of linear integration as necessary. Likewise, the ENDF creators were aware of this, and correspondingly recommend linear interpolation in such cases.

A.4   Description of MCNPX Patch 'Rayleigh Fix'

The modification described here successfully allowed MCNPX to simulate Rayleigh scattering properly, but it has been superseded by the modifications described in reference(45), which use the same logic, but also dynamically allocate variables such that the data used in MCNPX is identical to that in the EPDL97 libraries.

A description of the sampling method used to determine the scatter angle of a photon that underwent Rayleigh scattering is described in Section A.2. MCNP uses tabulated values of $C(Z,q^2)$ for each element, Z, and for fixed array of a momentum transfer values, q. The length of these tabulations was defined by the variable, MCOH= 55 words. Two arrays whose contents are defined during MCNPX initialization, VCO and WCO contained the corresponding values of q and q^2, respectively. The maximum value in VCO was $q = 6 \, \mathring{A}^{-1}$. The EPDL97 contains values of $F(Z,q)$ for $q \le 10^{11} \, \mathring{A}^{-1}$. To enable MCNPX to simulate Rayleigh scattering at all possible angles for energies of interest, new arrays of length MCOHE = 77 words were also defined in MCNPX initialization. They contained the original 55 values of q and q^2,

as well as 22 additional values, increasing quickly to $q = 10^4 \, \mathring{A}^{-1}$. These arrays were named VCOE and WCOE. The only additional changes necessary to the MCNPX code was a logical check of the length of the form factor arrays (part of the JXS array). If the new form factor array had a length of MCOHE, the code would perform the exact same logic for sampling the coherent scatter PDF as is done in the un-modified code, except that the form factor array and integrated form factor arrays would be defined according to q and q^2 values of VCOE and WCOE, respectively.

The PERL scripting of the MCNPX patch follows:

```
*/ ----------------------------------------------------- GLOBAL1_zc.F
*ident 05p ( File: src/mcnpx/mcnpf/GLOBAL1_zc.F )
*i,mgp5e.24
      integer(kindi), parameter :: mcohe = 77
*/ ----------------------------------------------------- GLOBAL2_vv.F
*ident 05p ( File: src/mcnpx/mcnpf/GLOBAL2_vv.F )
*i,mgt.330
      real(kindr) :: vcoe(mcohe) = (/
     & 0.,.01,.02,.03,.04,.05,.06,.08,.1,.12,.15,.18,.2,.25,
     & .3,.35,.4,.45,.5,.55,.6,.7,.8,.9,1.,1.1,1.2,1.3,1.4,1.5,1.6,
     & 1.7,1.8,1.9,2.,2.2,2.4,2.6,2.8,3.,3.2,3.4,3.6,3.8,4.,4.2,4.4,
     & 4.6,4.8,5.,5.2,5.4,5.6,5.8,6.,6.5,7.,7.5,8.,9.,10.,11.,12.,
     & 14.,16.,18.,20.,25.,30.,40.,50.,75.,100.,500.,1000.,5000.,
     & 10000. /)
*i,mgt.339
      real(kindr) :: wcoe(mcohe) = (/
     & 0.,.0001,.0004,.0009,.0016,.0025,.0036,.0064,.01,
     & .0144,.0225,.0324,.04,.0625,.09,.1225,.16,.2025,.25,.3025,.36,
     & .49,.64,.81,1.,1.21,1.44,1.69,1.96,2.25,2.56,2.89,3.24,3.61,
     & 4.,4.84,5.76,6.76,7.84,9.,10.24,11.56,12.96,14.44,16.,17.64,
     & 19.36,21.16,23.04,25.,27.04,29.16,31.36,33.64,36.,42.25,49.,
     & 56.25,64.,81.,100.,121.,144.,196.,256.,324.,400.,625.,900.,
     & 1600.,2500.,5625.,10000.,250000.,1000000.,
     & 25000000.,100000000. /)
*/ ----------------------------------------------------- colidp.F
*ident 05p ( File: src/mcnpx/mcnpf/colidp.F )
*i,cp.137
      if ((jxs(4,iex)-jxs(3,iex))/2.eq.mcoh) then
*i,cp.153
      else
      if(t5.lt.wcoe(mcohe))go to 191
      t7=xss(jxs(3,iex)+mcohe-1)
      go to 221
  191 do 201 i=2,mcohe
```

```
 201 if(t5.lt.wcoe(i))go to 211
 211 t3=(t5-wcoe(i))/(wcoe(i-1)-wcoe(i))
     ib=jxs(3,iex)+i-1
     t7=xss(ib)+t3*(xss(ib-1)-xss(ib))
 221 t3=t7*rang()
     ib=jxs(3,iex)-1
     do 231 i=2,mcohe
 231 if(t3.lt.xss(ib+i))go to 241
 241 t3=(t3-xss(ib+i))/(xss(ib+i-1)-xss(ib+i))
     cs=1.-2.*(wcoe(i)+t3*(wcoe(i-1)-wcoe(i)))/t5
     t3=1.+cs**2
     if(t3.le.2.*rang())go to 221
     end if
*/ ------------------------------------------------- calcps.F
*ident 05p ( File: src/mcnpx/mcnpf/calcps.F )
*i,ct.96
      if ((jxs(4,iex)-jxs(3,iex))/2.eq.mcoh) then
*i,ct4b.10
     else
     if(t3.ge.vcoe(mcohe))go to 600
     do 131 i=2,mcohe
 131 if(t3.lt.vcoe(i))go to 141
 141 ib=jxs(3,iex)+mcohe+i-1
     psc=(.2494351/(tpd(2)-tpd(1)))*(1.+cs**2)*(xss(ib)+(xss(ib-1)-
    & xss(ib))*(t3-vcoe(i))/(vcoe(i-1)-vcoe(i)))**2
     end if
```

The data processing code, NJOY, must also be modified in order to create data files that contain form factor and integrated form factor arrays that reflect the MCNPX changes. This process was quite simple. The array VCO in MCNPX corresponds to an array VC in the ACER routine of NJOY. This array is modified, and subsequent assumptions of the length of VC by the following NJOY patch, created to modify NJOY259:

```
*ident upBQ05p
*d acer.14675
      dimension vi(21),vc(77)
*d acer.14687
    & 5.0d0,5.2d0,5.4d0,5.6d0,5.8d0,6.0d0,6.5d0,7.0d0,7.5d0,8.0d0,
    & 9.d0,10.d0,11.d0,12.d0,14.d0,16.d0,18.d0,20.d0,25.d0,30.d0,
    & 40.d0,50.d0,75.d0,100.d0,500.d0,1000.d0,5000.d0,10000.d0/
*d acer.14785
      jflo=jcoh+154
```

```
*d acer.14801
      do i=1,77
*d acer.14804
        xss(jcoh+76+i)=s
*d acer.14814
      do i=1,77
*d acer.15084
      write(nsyso,'(1x,1p,6e14.4)') (xss(jcoh-1+i),i=1,77)
*d acer.15088
      write(nsyso,'(1x,1p,6e14.4)') (xss(jcoh+76+i),i=1,77)
*d acer.15142
        n=21+2*77
```

Unfortunately, NJOY259 appears to have a bug that causes the program to crash in a latter section in which formatted x-ray fluorescence data tables are produced. These tables are supposed to follow the form factor array portion of the ACE file. To bypass this problem, each new ACE file, containing additional form factor data, that was produced by the modified NJOY259 code was combined with properly formatted x-ray data tables in the previously distributed ACE files. This resulted in properly functioning data files that appropriately represent the Rayleigh scattering evaluated data present in the EPDL97.

Appendix B

Addition of NRF Data to Photonuclear Datafiles

This appendix describes the inclusion of NRF data into the photonuclear ENDF and ACE datafiles used by MCNPX. Because of constraints regarding both the ENDF data format and the NJOY code, several approximations were made, modifying the theoretical shape of the NRF resonances and eliminating correlated γ-ray emission cascades. After describing the process by which ENDF and ACE datafiles were created, the ramifications of these approximations are discussed.

B.1   Description of Datafile Creation Method

The capability of simulating photonuclear interactions has been in place within MCNPX since version 2.3(24). These interactions include photo-fission, other photonuclear interactions such as (γ,n) reactions, and in principle, (γ,γ') reactions. In the most recent release of MCNPX (version 2.6.0)(23), descriptions of (γ,γ') interactions were absent from the photonuclear data files. Below, is summarized the work that has been performed to add NRF data - which is a subset of the (γ,γ') reactions - to photon transport in MCNPX.

The process of adding NRF data to the ENDF-B/VII(18) and the MCNPX data file format, which are called ACE files, consists of the following steps:

1. NRF Data literature search. The Discrete Level Scheme Library (DLSL) of the Reference Input Parameter Library 2 (RIPL-2)(141) was used as the primary database of NRF levels. For each isotope, the corresponding Evaluated Nuclear Structure Data File (ENSDF) and documents referred to therein were also reviewed to search for more NRF lines.

2. A computer code, RIPL2FIX.EXE was written and used to improve the resolution with which energies of emitted γ-rays are described in the RIPL-2 DLSL.

The program also modifies the DLSL database to take into account the fraction of the decay energy that is taken as recoil kinetic energy by the nucleus during γ-ray emission.

3. NRFXSSI step 1: information gathering

4. NRFXSSI step 2: NRF level identification and analysis.

5. NRFXSSI step 3: DLSL Level Trimming

6. NRFXSSI step 4: γ-ray cascade analysis

7. NRFXSSI step 5: data formatting

8. NRFXSSI step 6: data insertion into photonuclear ENDF file

9. ACE file creation using NJOY(44)

10. NJOY bug repair.

More detailed descriptions of the above process follow. Step 1 is done by hand. Step 2 is accomplished by invoking the program RIPL2FIX.EXE, which was written for this project. Steps 3-8 are accomplished in the program NRFXSSI.EXE, (NRF cross(X) SectionS Inserter) also written for this project. Step 9 involves operating the nuclear data processing code NJOY, and step 10 is post-processing of the NJOY output because the code was found to have a minor bug when creating photonuclear ACE files from ENDF files where photon creation processes are present more than once within the data file.

B.1.1   NRF Data Search

For each isotope, the ENSDF(133) and documents describing (γ,γ') reaction studies cited therein were examined. If levels not contained in the DLSL were identified and were within energy ranges deemed important for NRF-based assay, the state, its half-life, and its decay scheme were added to a modified DLSL file. Scientific literature post-dating the ENSDF cutoff date are also reviewed by searching the INSPEC(142) database with the key words 'nuclear resonance fluorescence' and the isotope being updated. The values of E_0, and $g\Gamma_0$ are required to calculate the total NRF cross section of a resonance. The product, $g\Gamma_0$ is often provided in the ENSDF, but the spin of the NRF state and therefore, g, cannot be individually measured. In this case the spin is assumed to be a single unit greater than the ground state spin, and the value of Γ_0 that preserves the measured $g\Gamma_0$ is entered into the modified DLSL.

B.1.2 NRF γ-ray Energy Description and ripl2fix.exe

The DLSL describes the excitation energies of nuclear states to a precision of 1 eV, although these values are often not known to this precision. The energies of γ-rays corresponding to the de-excitation of an excited nuclear level are only described to a precision of 1 keV. This could result in emission of NRF γ-rays at the resonance energy, which would dramatically alter the transport of NRF γ-rays. To correct for this, a program named RIPL2FIX.EXE was written.

RIPL2FIX.EXE modifies DLSL files by calculating de-excitation γ-ray centroid energies to 10 meV precision. After calculating these energies, RIPL2FIX re-writes modified DLSL files with higher γ-ray energy precision. RIPL2FIX.EXE accomplishes this through the following steps:

RIPL2FIX.EXE reads through each DLSL file located in the /LEVELS/ directory. It first reads the nominal level energies and mass number for each isotope. Then the energy of the γ-ray emitted during the de-excitation of the parent state to a daughter state (which may, or may not be the ground state) is computed by the following equation:

$$E_\gamma = E_{\text{parent}} - E_{\text{daughter}} - \frac{(E_{\text{parent}} - E_{\text{daughter}})^2}{2Mc^2} \qquad \text{(B.1)}$$

Where Mc^2 is the rest mass-energy of the γ-emitting nucleus. The energy lost to the recoiling nucleus is 9 eV for a 2 MeV transition from a nucleus with mass number, $A = 238$. This mass is approximated as the product of A and the mass of a neutron. This effectively neglects nuclear binding energies, however these differences would result in less than a 0.5% correction. Likewise, our expression for the energy of the γ-ray is not exact: it is obtained from a second order binomial expansion of the quadratic equation that is solved when conservation of momentum and energy are imposed upon the two particle problem of photon emission from an isotope. The next term in the binomial expansion is $\frac{(E_{\text{parent}} - E_{\text{daughter}})^3}{4M^2c^4}$, which for the previous example is 40 μeV. The output modified DLSL files are created in the directory /OUT/. Compilation has been performed using CYGWIN C++(143)[1].

B.1.3 NRFXSSI Step 1: Information Gathering

The NRFXSSI program is run by the routine NRFXSSI.CPP. This routine only calls subroutines that perform the steps described. In the first subroutine called, GATHER.CPP, the user is asked to identify the name of the isotope to be analyzed. After the specified isotope is located in the DLSL, the width, spin, de-excitation modes, and corresponding daughter levels are loaded into memory for each excited level. The Debye temperature of the elemental material and the ground state spin of

---

[1]The version of C++ used to compile this was produced by Cygnus Solutions Inc. Cygwin is now owned by Redhat, and the version used to produce the programs described herein appears to be no longer distributed.

Row type	Column #				
	[0]	[1]	[2]	[3]	[4]
1st Row	N_{Levels}	IB	θ	A	0
Level Row	$N\gamma D$	E_{Level}	LN	τ	J
Subsequent $N\gamma D$ Rows	-1	E_γ	daughter LN	P_γ	0

Table B.1 CASCADE and DATASET array formats. Descriptions of the variables are described in the text.

the isotope are also are loaded into memory. GATHER.CPP returns thee arrays to the main program: ATOMINF is a 3 element array containing the elemental symbol, Z, and A of the isotope; the other two arrays are DATASET and CASCADE. The layout of these arrays is depicted in Table B.1 and the content is described below.

The first row of CASCADE and DATASET is a header that contains information specific to the isotope being processed. N_{Levels} is an integer describing the number of nuclear levels described in the DLSL for the isotope. IB is a Boolean, which is 1 if the isotope has an even number of both protons and neutrons, and zero, otherwise (at this point, this information is un-used by NRFXSSI). θ is the Debye temperature of the material in Kelvin, and A is the isotope's mass number. After the header row, a Level Row follows. Each Level Row describes a specific nuclear level defined in the DLSL. $N\gamma D$ is the number of different γ-ray emissions this level may undergo. LN is an integer describing the level, τ is the mean lifetime of the level, in seconds, and J is the spin of the level. After each Level Row, $N\gamma D$ rows follow, describing each γ-ray emitted from the level. The first entry in the γ-ray row is always a -1. The energy of the emitted γ-ray is given as E_γ. The daughter's level is LN, and the probability for emission of the γ-ray is given by P_γ. After the $N\gamma D$ γ-ray emission rows, another Level Row follows, until all N_{Levels} have been listed.

At this point in the code, DATASET and CASCADE only differ by the ordering of the Level Rows. CASCADE is ordered from highest to lower energy, whereas in DATASET, they are ordered as read from the DLSL. This facilitates subsequent program flow.

B.1.4   NRFXSSI Step 2: DLSL Data Trimming

After the data are collected into the arrays, DATASET and CASCADE, both arrays are trimmed of unnecessary levels. Each level in DATASET is subjected to six checks:

1. If the daughter of the highest-energy γ-ray emitted from a level is not the ground state, the level is removed from the data array.

2. If no γ-ray data is known, the level is removed from the data array.

3. If the lifetime of the level is unknown, it is removed from the data array. The lifetime of the state must be known because it is related to the NRF cross

section, which must be known.

4. If the spin of the level is unknown, it is removed from the data array. Often, the quantity, $g\Gamma_0$, is experimentally measured, instead of the spin and lifetime. It is important to note that values of J and τ must be assigned or the code will purge the state.

5. If the spin of the level is greater than 10 it is removed from the data array. This removal triggers a printed warning in the code execution window.

6. If the probability that a state emits a γ-ray resulting in direct de-excitation to the ground state state is less than an adjustable tolerance level (set to 0.001 in the code), the level is removed from the data array. This removal triggers a printed warning in the code execution window.

For each level that is removed from DATASET, the subsequent $N\gamma D$ rows corresponding to γ-ray emission information for the level are also removed.

CASCADE also undergoes series of checks to purge unnecessary data, however, since a state may be relevant for an NRF cascade, yet not directly excited by NRF absorption, different checks are necessary:

1. Identical to #2 for DATASET.

2. If a level is higher energy than the highest-energy level in the trimmed DATASET array, the entire level is removed from the data array.

3. Lines corresponding to individual γ-rays are also purged from cascade if the intensity associated with the γ-ray emission is less than the tolerance of 0.001.

B.1.5   NRFXSSI Step 3: NRF Cross Section Analysis

The cross section for NRF to occur for each resonance is calculated in the subroutine NRFCALC.CPP. This routine determines a cross section function for each excited state in the trimmed DATASET array. First the subroutine asks the user to define a temperature at which the cross section will be calculated. The code assumes that the cross section is either calculated from a Maxwell-Boltzmann distribution, equation 2.95, whose width is defined by the Doppler width of the resonance, equation 2.96, or the natural width of the NRF line, Γ, whichever is wider. The actual profile is given by equation 2.99, and the code should be modified to reflect this, but for the uses of the code to date, values Γ describing the NRF lines have been trivially small, and therefore can be somewhat accurately neglected. The ambient temperature, T_a, at which Doppler-broadened cross section has been calculated is 300 K in all the produced ENDF files. The temperature used in equation 2.96 has modified by

$$T = T_a \cdot [.906 \exp(.1555/(T_a/\theta))] \tag{B.2}$$

to take into account the effects of crystal lattices. Equation B.2 is only valid for $T_a \gg \theta$, and the code should be modified to instead include a numerical integration of equation 2.100.

Because of constraints in both NJOY and the ENDF format, data points can be defined on an energy grid no finer than 2 eV. If the width of the cross section distribution is greater than 6 eV, an energy grid spacing of $\Gamma/2$ is used. This coarse energy resolution causes Gaussian distributions, whose full width at half maximum (FWHM) is normally 1 - 2 eV, to be highly prone to discretization errors that will alter the total integrated cross section during the discretization process. To correct this, the resonant integral is analytically computed in the code, and the point-wise integrated cross section values are multiplied by the ratio of the analytic integral to that of the discretized function. This ensures that the integrated cross section is correct. A schematic description of the discretization and renormalization process is shown in Figure B.1.
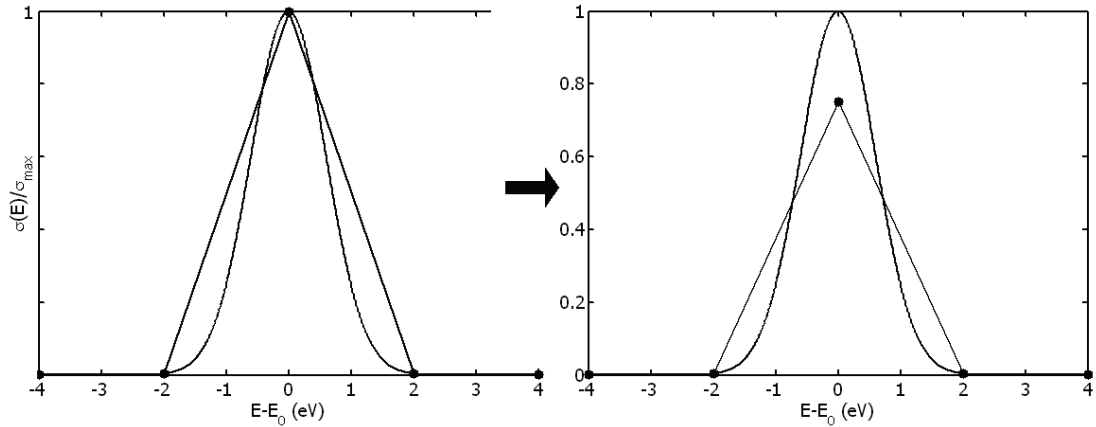
Figure B.1 Point-wise discretization of Maxwell-Boltzmann cross section, renormalized to preserve integrated cross section.

The resulting array, TOTXS, is two columns wide, with each row containing an energy in the first column and the corresponding computed NRF cross section in the second. Each level in the DATASET array results in five rows in the TOTXS array. In the above formulations, it is assumed that the resonances can be well-represented as isolated from one another.

B.1.6   NRFXSSI Step 4: γ-ray Cascade Analysis

The subroutine CASCADECALC.CPP processes the γ-ray cascades emitted from each NRF level. It does this by identifying the levels in CASCADE that correspond to NRF levels identified in DATASET. With the level identified, CASCADECALC.CPP calls a subroutine CASCADEGRAB that loops over each γ-ray emitted from level, finds the probability of emission for each γ-ray, and, if necessary, calls itself to analyze the

daughter levels populated by γ-ray emissions from the level. The net result is a new array named GAMARRAYPRELIM. The entries of the columns of GAMARRAYPRELIM are the following:

0. Energy of the NRF level. (All energies are expressed in eV.)

1. Energy of the level that emitted the γ-ray.

2. Energy of the γ-ray.

3. Number of emissions of the γ-ray per excitation of the level.

4. Level number (LN) of the γ-ray emitting level. This is subsequently changed to the total number of discrete γ-ray energies that can be emitted the corresponding NRF level.

5. Spin of the γ-ray-emitting state.

6. LN of the daughter γ-ray level. This subsequently becomes the spin of ground state or -1.

After CASCADEGRAB is complete, GAMARRAYPRELIM is sorted. γ-rays emitted from a given NRF level are placed in ascending order and redundant γ-ray lines are combined, with their respective probabilities summed.

After this sorting process, LN in Column 4 of GAMARRAYPRELIM is replaced with the number of γ-rays emitted from a given NRF level and the daughter LN in Column 6 is replaced by the spin of the daughter level, or -1 to denote that the state populated by the γ-ray emission is the ground state.

With GAMARRAYPRELIM complete, CASCADECALC.CPP computes the γ-ray multiplicity of each NRF level. The multiplicity of a level is defined as the mean number of emitted γ-rays per excitation of the NRF level, which is the sum of the values in Column 3 of the GAMARRAYPRELIM array corresponding to a single NRF level. The multiplicities are stored in the Column 1 of the array GMULTS, and the corresponding energy of each level is stored in Column 0. GMULTS also has a header row which contains the total number of resonances in both entries in the row.

Finally, CASCADECALC.CPP produces the array, GAMARRAY. The values of the rows of GAMARRAY are nearly identical to those of GAMARRAYPRELIM. The primary difference is that GAMARRAY is formatted to be entered into the ENDF format as a point-wise evaluation of the multiplicity versus energy function. It is assumed that outside of the resonance energies, the multiplicity for γ-ray emission is zero. Because of this, each line in GAMARRAYPRELIM becomes 3 lines in GAMARRAY. The first of the three lines corresponds to the lower energy bound of possible γ-ray energies emitted during a specific de-excitation of the state. The entry in Column 2 (the energy of this data point) is 10 eV less than the energy of the γ-ray. The corresponding yield, Column 3, is set to 0. The second row is identical to the

corresponding GAMARRAYPRELIM row, except that the yield must be re-normalized such that the integral over the multiplicity function results in the yield computed for GAMARRAYPRELIM (Column 3), and the γ-ray multiplicity in GMULTS is factored out. This value is $Y_i/10/M_i$, where Y_i is the corresponding value in Column 3 of GAMMARAYPRELIM, and M_i is the corresponding value in Column 1 of GMULTS. The number, 10, is one-half the width of the multiplicity function which is integrated in radiation transport codes to determine yield. The third row for a single γ-ray in GAMARRAY is identical to the first row, except that the energy is now 10 eV above the nominal energy of the γ-ray - the upper bound for the yield distribution function. GAMARRAY is passed to INSERT.CPP, which formats the data and inserts it into the MT6 MF5[2] section of the resulting ENDF file.

B.1.7   NRFXSSI Step 5: Data Formatting and Integration

NEW355.CPP is called to combine NRF cross section data (produced in NRF-CALC.CPP) with cross section data that may be present in the photonuclear ENDF datafile that already exists for the isotope. The data in MT3 in an ENDF file is the cross section data. MF3 corresponds to the total cross section and MF5 corresponds to cross section data for 'other types of reactions', which NRF is considered. The subroutine reads the cross section data in the old ENDF file, and inserts the NRF cross sections from the TOTXS array into the appropriate location. In the event that the pre-existing cross section is non-zero at an energy where TOTXS is defined, values of the pre-existing cross section are linearly interpolated to the energies where the NRF cross sections are defined and the resulting total cross section is determined by adding these values to the NRF cross section. The resulting arrays, A33 and A35 are then formatted to be inserted into the ENDF photonuclear file.

B.1.8   NRFXSSI Step 6: Data Insertion into Photonuclear ENDF File

The final step of NRFXSSI is to insert the NRF data into the a photonuclear ENDF file. The subroutine INSERT.CPP accomplishes this. INSERT opens the photonuclear ENDF file, updates the file's descriptor block, and inserts NRF cross section and secondary γ-ray emission data along with the proper header information.

The first step is to read the data already present in the ENDF file and to modify the file descriptor section (MT1 MF451). All information is read from the input file and either copied or modified as it is written to a temporary output file, TEMP.ENDF. The changes to the descriptor section include incrementing by 1 NMOD, an integer describing how many modifications this ENDF file has undergone, adding a text boilerplate that describes the changes to the ENDF file, checking that there are MT3 MF3, MT3 MF5, and MT6 MF5 section directories in the description section,

---

[2]See reference(144) for descriptions of the data formats used in ENDF files.

and either deleting the entries for the lengths of these sections, which will later be updated, or making directory place-holders for these sections to be updated later.

After the descriptor section is modified, INSERT skips forward to the section MT3 MF3, deletes all old data and inserts the array, A33, along with the proper header information. The subroutine NRFIMP.CPP is called to perform the insertion. After MT3 MF3, the MT3 MF5 section is modified using identical logic as the MT3 MF3 section except that the array A35 is used as the data source. The MT6 MF5 insertion involves slightly different formatting, and is accomplished by inserting the GMULTS multiplicity data, and GAMARRAY secondary photon data. Similar logic to the NRFIMP.CPP subroutine is present in this section of INSERT.

Finally, INSERT rewinds TEMP.ENDF and opens the final output file, whose name is identical to the original input file, but is located in the folder /OUT/. TEMP.ENDF is copied verbatim to the output file, but the lengths (in number of rows) of the newly inserted or modified sections are added to the file directory in the file descriptor section.

B.1.9   ACE file Creation using NJOY

With ENDF files created, the data processing code NJOY was used to convert the ENDF files to ACE files. NJOY was called by the following command: NJOY259<IN.DAT. An example of IN.DAT for processing the ^{238}U ENDF file is shown below:

```
reconr
 20 -22
 'NRF U238 from endf/b-vii' /
 9237 1 /
 .1 0 .05 1e-5 /
 'U238 from modified endf/b-vii U238.endf' /
 0/
 acer
 20 -22 0 26 27/
 5 /
 'U238@300deg, photo-nuclear'
 9237 /
 Stop
```

NJOY assumes all input and output files are 'tapes'. To use the above example, the ^{238}U ENDF file output from NRFXSSI must first be copied to /NJOY/TAPE20. Likewise, the outputs of NJOY are the files TAPE26 and TAPE27. TAPE26 is an ACE file and TAPE27 is the XSDIR line corresponding to the ACE file. The number 9237 identifies ^{238}U, and the '5' in the second line of the ACER call tells NJOY that the ENDF data is photonuclear.
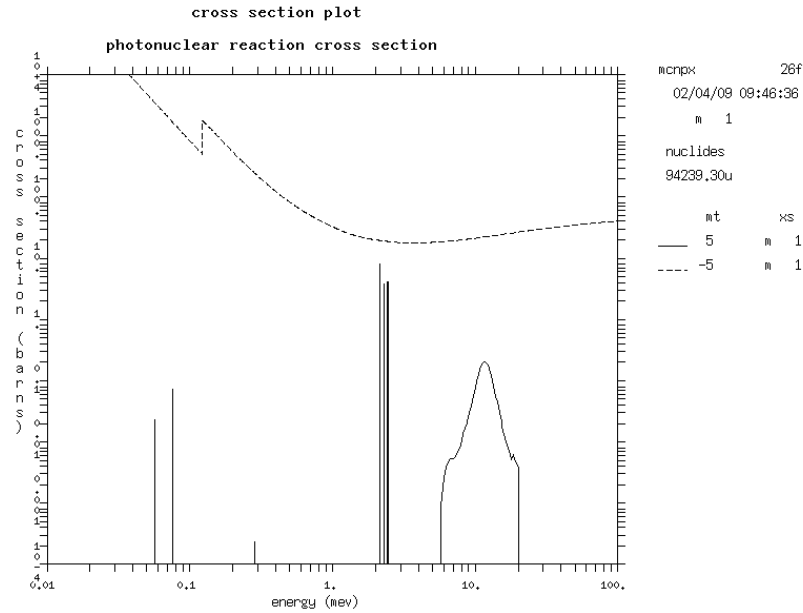
Figure B.2 The ^{239}Pu cross photon sections as read by MCNPX. The dashed line indicates the photo-atomic cross section, and the solid line indicates the photonuclear cross section. Before this modification, the photonuclear cross section file only contained of the feature in the 6 to 20 MeV range.

B.1.10   NJOY Bug Repair

NJOY was found to have a simple systematic bug when processing the photonuclear ENDF files produced by NRFXSSI. Upon completing an NJOY run, the angular distribution locators for secondary particles (the LANDP array) in the output ACE file are incorrectly defined. The error was found to be systematic. The first entry of LANDP should always be 1, but instead, the correct value for the second entry is inserted. Similar problems continue for the remaining entries. The code TAPE26FIX.EXE was written to fix the LANDP array. The output of TAPE26FIX is a properly formatted photonuclear ACE file that may be used in MCNPX.

B.1.11   NRF data insertion results

Figure B.2 provides an example of a NRF cross section read by MCNPX, and displayed using the cross section plotting functionality in the code.

Figures B.3 and B.4 demonstrate a spectrum that was calculated using the new photonuclear datafiles and the modification of the MCNPX code described in Appendix A. In this simulation, a pencil beam of photons, uniformly intense between 2.430 and 2.432 MeV, irradiated a cylinder of ^{239}Pu with 0.5 cm-diameter and 1 cm-length. The photon flux at a distance 60 cm from the cylinder center was calculated at an angle of 135° relative to the pencil beam direction using the
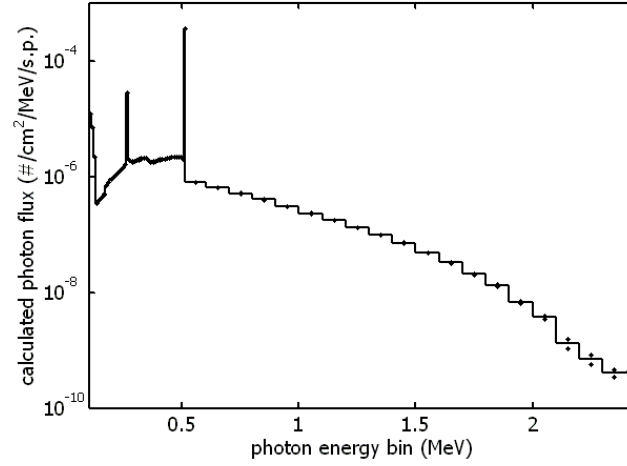
Figure B.3 MCNPX-calculated backscattered photon spectrum per simulated photon due to 2431 ± 1 keV photons incident upon ^{239}Pu. Statistical uncertainties are shown as dots above and below the center of each energy bin.

next-event-estimator tally (see Section C.3). The spectrum demonstrates several features. A energies below 2.4 MeV, the spectrum is dominated by the inelastic scattering processes that are described in the first half of Chapter 2. These processes result in an annihilation peak at 511 keV, a Compton-scatter photo-peak at 266 keV, and a continuum due to photo-electron bremsstrahlung production. At the initial beam energy, elastic scatter of photons produces a profile that is similar to the beam profile. This feature is only present because of the modifications to the code described in Appendix A. Finally, two additional peaks are visible at 2431.7 and 2423.8 keV. These are due to resonance fluorescence of the 2431-keV state in ^{239}Pu, which de-excites to the ground and first-excited states by γ-ray emission, resulting two NRF γ-rays separated in energy by 7.9 keV.
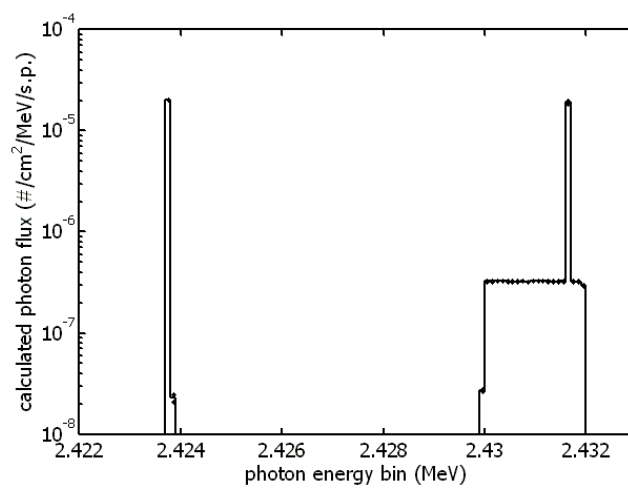
Figure B.4 Same as Figure B.3, except the energy range between 2422 and 2433 keV is expanded.

Appendix C

Supporting Documentation of MCNPX Simulations

Throughout this dissertation, results of MCNPX simulations have been presented. This appendix describes the logic behind some more complicated simulations and presents example input files. The primary cause of complications is the use of variance reduction techniques. Variance reduction is defined as using methods to reduce the statistical uncertainty (or variance) of a simulation result in the same amount of time. There are three primary types of variance reduction. The first is to truncate a problem in either geometry or energy space such that irrelevant portions of the simulation-space are not simulated. This is essentially done in all simulations since no model may contain all details of the physical world.

In MCNPX, variance reduction may also take the form of non-physically adjusting the number of particles simulated and correspondingly modifying the *weights* of these particles. For example, the simulation described in Section C.3 calculates the photon flux backscattered from a target. Photons that are incident upon the target volume are forced to undergo an interaction, which would normally provide non-physical results. To keep the results physical, MCNPX does the following. First, the probability, p_{int}, for the incident photon to interact along its path through the TD is computed. The location of the forced interaction along the photon's path is then randomly sampled, and a new particle is created at that location with weight, p_{int} relative to the weight, w of the incident photon. This photon is forced to undergo some collision, whereas the fate of the initial photon continues is then simulated without any modification, except that its weight is reduced to $w(1-p_{int})$. The effect of this weight-adjusting variance reduction technique is to promote the simulation of particles that have interacted in the target volume, which for this simulation, results in reducing the statistical uncertainty of the calculated flux.

Weight-varying methods may also be implemented during definition of the probability of generating particles during the simulation (see Section C.1), by increasing the probability that a simulated particle is transmitted through a material, or by

inducing extra particles to be simulated in portions of the geometry that are deemed important (see Section C.2).

A third type of variance reduction methods involves *next-event estimators*. Next-event estimators essentially add deterministic treatment to otherwise stochastic modeling. A point or region of interest is defined and each time a particle interacts within the simulation, the expected contribution of the flux at this point is deterministically calculated. This method works quite well when the majority of interactions occur sufficiently far from the point of interest and the angular distribution of particles emitted due to the interaction event are known. Next-event estimators are used in the backscattered photon flux calculations described in Section C.3 Finally, details concerning the treatment of electrons and the production of bremsstrahlung by MCNPX are provided in Sections C.6 and C.5

C.1   Bremsstrahlung Source Simulations

Bremsstrahlung was assumed to be the photon source for most of the simulated NRF experiments described in this dissertation. These spectra were calculated using MCNPX with input files similar to the one provided below. The simulated geometry is monoenergetic electrons normally incident upon a 102 μm-thick gold converter (Z=79) that is supported by 1 cm-thick copper (Z=26) slab. There is no shielding simulated. In the simulation, the energy and relative angle of photons that cross the surface of a 50 cm-radius sphere whose center is the intersection of the electron beam and the gold foil (surface 10) are counted. The lines phys:e 2.9 8j 1 and bbrem 1. 1. 46l 2.0 1 are of primary interest. The first line indicates that the electron data library need only extend up to 2.9 MeV, that all electron physics processes are default except that bremsstrahlung photon production is biased such that one reduced-weight photon is produced at each electron substep rather than probabilistic sampling of full-weight photon production. The second line indicates that bremsstrahlung photon production in material 1 (gold) is to be biased such that higher energy photons are more likely to be produced at correspondingly reduced weight.

```
2.6 MeV
c -- cells
1   1 -19.3  1 -3 2 -4 5 -6           imp:p=1 $Ag
11  2 -8.96  1 -3 2 -4 6 -7           imp:p=1 $Cu
12  0          -10 #1 #11              imp:p=1
13  0          10                      imp:p=0

c -- surfaces
1 px -1
2 py -1
```

```
3 px 1
4 py 1
5 pz 0
6 pz .0102     $Ag
7 pz 1.0102    $Cu
10 so 50

c -- materials
m1 79000.03e 1
m2 28000.03e 1
mode p e
nps 2e9
phys:e 2.9 8j 1
bbrem 1. 1. 46I 2.0 1
sdef pos=0 0 0 par=3 erg=2.6 dir=1 vec = 0 0 1 $2.6 MeV es inc on Au
cut:e j 0.09 3j        $electrons below 90 keV are not simulated
cut:p j 0.09 3j        $photons below 90 keV are not simulated
F1:P 10
E1 .1 25I 2.6000001
ft1 FRV 0 0 1
c1 -.9961947 -.98480775 -.9396926 -.8660254 -.766044443119
    -.642787609 -.5 -.34202014 -.173648 0 .173648 .34202014
    .5 .642787609 .766044443119 .8660254 .9396926 .98480775
    .9961947 1
```

C.2   Photon Penetration Through Thick Shielding

Shielding calculations tend to be difficult to simulate with Monte Carlo radiation transport codes. For example, the probabilities that a 0.5, 1, and 2-MeV photon penetrates 25 cm of Pb without interacting are 3.4×10^{-19}, 4.2×10^{-9}, and 2.1×10^{-6}, respectively. To calculate shielding requirements for a bremsstrahlung spectrum, or to shield a large ^{137}Cs source, variance reduction techniques must be used to avoid using unnecessary computation time simulating particles that will never reach the opposite side of the shield.

The variance reduction technique uses the following routine.

- The simulation is conducted with no variance reduction, but with reduced shielding density. Weight-windows are generated.

- The density of the shielding is increased and the simulation is re-run with variance reduction. New weight-windows are regenerated.

- This process continues until the full shielding density is simulated.

Use of weight windows is a to particle-weight-modifying variance reduction technique. Weight windows divide the geometry of a simulation into segments, and each segment is assigned weight cutoffs. If a simulated particle enters a segment with a weight greater than the segment's upper weight cutoff, the particle is divided into multiple particles of reduced weight, which are then separately simulated. If a simulated particle enters a segment with a weight below the segment's lower weight cutoff the particle is subjected to termination (also called *Russian Rouletting*), with probability, p_{RR}. If the particle is not terminated, the weight of the particle is increased by $1/p_{RR}$. Likewise, weight-window segments can be generated for different energy ranges.

To generate weight windows, the WWG and WWGE (for energy segmentation) cards are used in the MCNPX input files. These cards cause the code to determine from which segments, and at which energies, came particles that contribute to the flux (or an energy range of the entire flux) that is specified to be important. If a segment is found to be important, the weight cutoffs are lowered, causing more particles with reduced weight be generated in the segment. After the weight window-generating simulation, the weight-windows are written to a file, which may be read for subsequent simulation. The method of iteratively increasing the shielding material density and creating a series of weight-window files allows simulated particles to contribute to the flux with higher probability (and reduced weights), which subsequently allows the code to more efficiently determine how to weight the segments.

A second variance reduction method was also employed to increase the probability that simulated photons would penetrate the shielding. This involved the *exponential transform* function, invoked by the EXT card. The exponential transform modifies probability distribution function (PDF) that describes the distance to collision, x_c. Normally, this PDF is given by $P(x) = N\sigma \exp(-N\sigma x)$ where N is the number density of atoms in the material and σ is the total reaction cross section. This PDF may be sampled using a random number[1], r, to obtain $x_c = \frac{-\ln(r)}{N\sigma}$ The exponential transform creates a new non-physical cross section, σ^*, samples x_c using this value, and if the particle interacts within the transform cell, it increases the weight of the particle by

$$w = \frac{\sigma \exp(-N\sigma x_c)}{\sigma^* \exp(-N\sigma^* x_c)} \tag{C.1}$$

If the particle does not react, its weight is reduced by

$$w = \frac{\exp(-N\sigma x_c)}{\exp(-N\sigma^* x_c)} \tag{C.2}$$

This conserves the probability for particle transport by correctly increasing interacting particle weights and reducing weights for transmitted particles.

---

[1]See Section A.2 for a description of PDF sampling.

   The draw-back of the exponential transform is that it may under-sample scattering events. Because of this, the statistical analyses of the Monte Carlo simulation are carefully considered and the value of σ^*/σ is taken to be as close to unity as is practical.

   An example of an input file for a MCNPX shielding simulation is shown below. The simulation is one of the series of simulations described in Section 3.1.2. This particular file is the last of four iterations simulating the penetration of the 40-50º angular range of a 2.5 MeV endpoint-energy bremsstrahlung beam through 40 cm of tungsten.

```
40cm W shield, 2.5 MeV endpoint-E photons  rho should be 19.3g/cm3
c -- cells
1   1 -19.3   1 -2 -3            imp:p=1 $p is lower in earlier iterat
2   0          91 -1             imp:p=1
3   0          1 -2 3            imp:p=0
4   0          2                 imp:p=0
5   0          -91               imp:p=0


c -- surfaces
1 px 0
2 px 40
3 cx 30
91 px -1


c -- materials
m1 74000 1
mode p
nps 2e7
ext:p .8X 0 0 0 0
wwg 1 0 0 4j 0
wwge:p 1 1.5 2.50001
wwp:p 2 2j 0 -1 0 2j 3e-7 $this line is commented out in 1st iterat
mesh  geom=cyl ref=0 0 0 axs = 1 0 0 origin=-.1 0 0 vec=0 1 0
      jmesh   40.1
      jints   40
      imesh   30
      iints   3
      kmesh   1
      kints   1
sdef pos=-0.1 0 0 par=2 dir=1 vec 1 0 0 erg=d1
si1 0 .1 23i 2.5
sp1 0 1.25 1.23 2.69 3.7 3.33 2.74 2.16 1.74 1.39 1.14 .927 .764
      .629 .521 .434 .359 .297 .242 .201 .16 .124 .0929 .0631 .0357
```

```
    .00886
sb1 0 .2 8r .3 .4 .5 .6 .7 .8 .9 1 1.1 1.2 1.5 2 2.5 3 5 10
phys:p 3
TF11 6j 3 j $tally between 1.75 and 2 MeV most important
E1 0  24i 2.50001
f1:p 2
E11 0 1.75 2.5
f11:p 2
```

C.2.1   Comparison to Published Build-up Factors

The effect of down-scattering has been approached by modifying simple attenuation by use of a *build-up factor*, $B(Z, E, \mu x)$, that is a function of energy, material composition, and geometry. This results in an effective attenuation expression that is written as

$$I = I_o B(Z, E, \mu x) \exp(-\mu(Z, E)x) \qquad (C.3)$$

There are several different formulations of build-up factors. The factors most commonly encountered apply to dose-rates rather than fluxes.

One build-up formulation is the polynomial form:

$$B(Z, E, \mu x) = 1 + a(Z, E) \times (\mu x) + b(Z, E) \times (\mu x)^2 + c(Z, E) \times (\mu x)^3 \qquad (C.4)$$

Values of a, b, and c for energy transmission through shielding from an isotropic point photon source were taken from reference (111), and used to find an expected build-up factor. $B(Z, E, \mu x) = 23.42$ for 4-MeV photons, emitted from the center of a 30-cm radius tungsten shield. Using equation C.3 and an attenuation coefficient, $\mu = 0.779 \text{ cm}^{-1}(19)$, we expect each photon to transmit, on average the following energy:

$$
\begin{aligned}
E &= E_\gamma B \exp(-\mu x) \\
&= 23.42 \times 4[\text{MeV}] \times \exp(-30[\text{cm}] \times 0.779[\text{cm}^{-1}]) = 6.60 \times 10^{-9}[\text{MeV}] \quad (C.5)
\end{aligned}
$$

The energy build-up formalism is useful for estimating the energy or dose due to a photon fluence penetrating shielding, but it does not provide an estimate of the number of individual photons that escape the shielding. This renders these build-up factors useless for predicting detector responses, to shielded photon fluxes when detectors are operated in pulse mode[2]. To make these predictions, we turn to Monte Carlo calculations using MCNPX and built-in variance reduction functionality, while using the published build-up parameters as a check on our use of the code.

---

[2]The converse is true, if detectors are operated in an integrating mode, where the charge deposited in a detector is continuously integrated by a capacitive circuit.
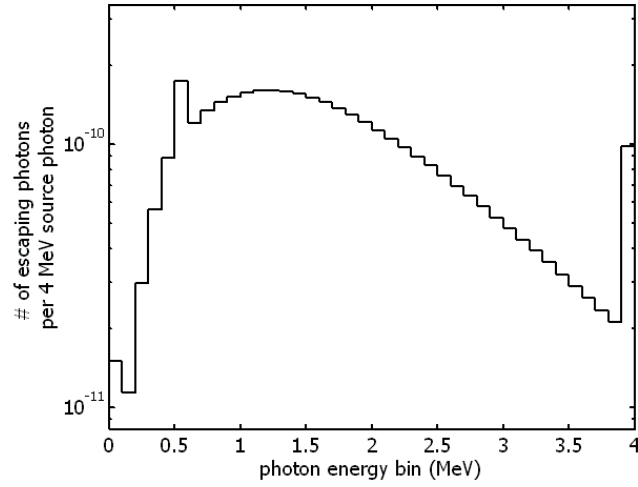
Figure C.1 MCNPX-calculated photon spectrum leaving tungsten shielding for a 4 MeV point isotropic source located at the center of a tungsten sphere of 30 cm radius. Statistical errors are negligible.

To check the validity of the MCNPX results, we first simulate a geometry identical to that whose build-up constants are tabulated; a point isotropic 4-MeV photon source located in the center of a 30 cm-radius W sphere. The calculated energy spectrum of photons emitted from the tungsten shield is shown in Figure C.1. To convert this spectrum into emitted energy, and subsequently, a build-up value, probability of photon emission is multiplied by the corresponding energy, and summed for the entire spectrum. This calculation results in the computed average energy leaving the tungsten sphere per 4-MeV photon emitted from the sphere's center, which was 6.14×10^{-9} MeV per 4-MeV source photon for the MCNPX computation. The corresponding energy build-up factor is $B_{\mathrm{MCNPX}} = 21.8$. The agreement between this value and that from equation C.5 is impressive, given that differing photon cross section data were used for the two computations. We thus conclude that using variance reduction techniques enables MCNPX to provide reasonable estimates of build-up factors, suggesting that the MCNPX calculations are likely to be accurate for studies of photon fluences penetrating through shielding.

C.3   Backscattered Photon Flux Calculations

Calculations of backscattered photon spectra and intensities is an important part of predicting the relative strengths of the NRF γ-rays and background photons. The simulations cannot be accurately performed without variance reduction because the fraction of photon scattering events that result in large-angle scatter without significant energy loss is very small. For example, if a 2.4-MeV photon is incident upon a 1 cm-thick slab of uranium, it will interact with a probability of approximately 0.6.

Of the fraction of photons leaving 1 cm of uranium due to scattering, approximately one-fifth are in the backwards direction, and the majority of these are low-energy. Of the entire backscattered intensity, approximately 10^{-3} are elastically scattered, and approximately 2×10^{-4} are inelastically down-scattered to an energy between 2.1 and 2.2 MeV. Because of these low probabilities, direct simulation of backscattered photon intensities near the endpoint energy of a bremsstrahlung spectrum requires approximately 10^4 particles to simulate a single energetic photon scattered into the backwards direction, which is very inefficient.

To improve upon these efficiencies, a next-event estimator technique is used for the backscatter simulations. These simulations model the backscattered photon spectrum resulting from some defined photon spectrum incident upon a target (or TD). To determine the expected photon spectrum that would be incident upon a radiation detector, the flux at the center of the detector, at point $\mathbf{r_d}$, is determined by the next-event estimator routine. In the simulation, each time a particle (presumably photon or photo-electron) interactions in the target, the probability-weighted flux contribution at point $\mathbf{r_d}$ is calculated. This contribution is given by

$$\Delta\Phi(\mathbf{r_d}) = w \frac{p(\mathbf{\Omega})}{R^2} \exp\left[-\int_0^R N(s)\sigma(s)ds\right] \tag{C.6}$$

where w is the weight of the interacting particle, which may be non-zero if other variance reduction techniques are employed, $p(\mathbf{\Omega})$ is the differential probability that the interaction will result in production of a photon directed toward $\mathbf{r_d}$, R is the distance between the interaction point and $\mathbf{r_d}$, therefore the $1/R^2$ term takes into account the reduction of emanating photon intensity with distance from the interaction point. Finally, the term $\exp[-\int_0^R N(s)\sigma(s)ds]$ reduces the contribution to the fluence by the amount proportional to the attenuation of the photon before reaching $\mathbf{r_d}$. s is the parameterized distance along the line between the interaction point and $\mathbf{r_d}$, and $N(s)$ and $\sigma(s)$ correspond to the atom density, and interaction cross section for photons in the material present at the distance s along the path, respectively.

Although not explicitly contained in equation C.6, the energy of the contribution to the next-event estimation is at least partially determined by the interaction type and angle. The following examples further explain this. If the interaction that causes the next-event flux estimation is a coherent scatter, the energy at which the next-event flux estimate at $\mathbf{r_d}$ contributes is equal to that of the scattered photon. If the interaction is an incoherent scatter, the angle, $\mathbf{\Omega}$ defines the contribution energy by equation 2.23. Other interaction types do not constrain the energy when the scattering angle is fixed, such as a bremsstrahlung emission from a slowing electron. In this case the energy of the bremsstrahlung photon is first sampled, then the PDF relating the energy of a bremsstrahlung photon to the angle of emission is sampled to determine $p(\mathbf{\Omega})$ at that bremsstrahlung photon energy.

Next-event estimators can result in multiple contributions to the calculation of an expected photon spectrum per particle history. For example all three events

described in the preceding paragraph could occur when a single photon impinges upon a target. Next-event estimators result in simulations that give statistically convergent and significant results in reasonable calculation times. The following two examples of MCNPX input files indicate the use of next-event estimator tallies (called F5 tallies in MCNPX) for simulating the backscattered photon flux. The first example produced the calculated spectrum shown in Section B.1.11. This input file reflects modifications to the MCNPX code and its data files described in Appendices A and B. Particularly, the line, (plib=.05)calls for the .05P photo-atomic data files, which contain the full set of form factors for Rayleigh scattering, and the .30U photonuclear data files contain NRF resonances and secondary particle information pertaining to NRF γ-rays.

```
2 keV-wide uniform intense pencil beam of 2431 keV photons on Pu239
100     1   -19.6 -10 -20 21 imp:p=1  $Pu cyl
200     0         10 -11 -20 21 #202 #203 imp:p=0 $shielding
202     0         10 -20 -15 16 #203      imp:p=1 $viewing hole
203     0         10 -11 -22 23           imp:p=1 $collimator
997     0         20         imp:p=0
998     0        -21         imp:p=0
999     0         11 -20 21 imp:p=0


10       cy 0.5
11       cy 80
15    1  cx 0.5
16    1  px 0
20       py 60
21       py -60
22       cx 0.5  $collimator
23       px 0

*tr1 0 0 0 45 315 90 135 45 90 90 90 0
mode   p e
m1   94239.30u          1
        plib=.05
xs1 94239.30u    236.998600 PU239Ace 0 1   1  71391  0 0 0.000E+00
sdef pos=60 0 0 par=2 erg=d2 dir=1 vec = -1 0 0 ara=1
si2 H 0 2.430 2.432
sp2 0 0 1
cut:p j 0.09 3j
cut:e j 0.09 3j
prdmp j -60 j 2 0
phys:p 3.0 j j 1 j
ctme 2000
```

```
f15:p 42.426 42.426 0  0  $60 cm from center,
e15 0.1 39i .5 .509 .513 .6 14i 2.1 31i 2.42 119i 2.43201
```

A second example explicitly excluded the .05p and .30u data libraries so that the elastic scattering contribution to the backscattered photon spectrum could be calculated using elastic cross section values that also included nuclear Thomson and Delbrück scattering. This calculation was combined with a similar calculation in which the minimum simulated energy was 3 MeV to estimate the inelastic scattering contribution to the background for measurement of ^{137}Ba content in aged ^{137}Cs sources. The cutoff of 3 MeV was used in the following simulation to provide lower uncertainties in the upper energy bins.

```
Cs/BaCl 4 MeV endpoint energy S-T 60cm, T-D 60cm 45 degs
100 1  -2  -10           imp:p=1  $Cs/BaCl sphere 20% theor
101 2  -7.7   10 -11        imp:p=1  $Steel sph cont
200 3  -19.3  21 11 -20 12 13 #300 #301 imp:p=1  $most of shield
201 0          11 -20 -12 13           imp:p=0  $bottom no imp
202 0          11 -20 -13             imp:p=0  $back no imp
203 0        -21 11 -20 12 13 #301    imp:p=1  $most of shield
300 0          11 -20 -15 21 #301        imp:p=1  $irrad hole
301 0          11 -20  -16 22         imp:p=1  $viewing hole
999 0          20                 imp:p=0  $rest of world


10     so 1.742
11     so 2.042
12     pz -15
13     py -15
15     cx 1.742
16   1 cx 1.742
20     so 65
21     px 0
22   1 px 0

*tr1 0 0 0 45 315 90 135 45 90 90 90 0
mode p
fcl:p -1 0 6r
m1 17000 0.5 55000 .25 56000 .25  $Cs1Ba1Cl2
m2 26000 0.72 24000 .18 28000 .10
m3 74000 1
dd0 0 0
print
sdef pos=60 0 0 par=2 erg=d2 dir=d1 vec = -1 0 0
si1 H -1 .996194 1  $0-5 degrees
```

```
sp1  0 0 1
si2  0 .1 40I 4
sp2  0 3.6636e-8 9.1549e-7 8.3803e-6 5.1766e-5 0.00010238
 0.00013271 0.0001291 0.00012422 0.00011573  0.0001064
 9.7301e-5  8.9228e-5 8.0441e-5  7.3751e-5 6.6967e-5
 6.1339e-5  5.5978e-5 5.1208e-5 4.6852e-5  4.3017e-5
 3.94e-5 3.6243e-5  3.3137e-5  3.0822e-5 2.8333e-5
 2.5915e-5  2.4092e-5  2.2167e-5 2.0309e-5  1.8582e-5
     1.7074e-5 1.562e-5  1.4258e-5  1.2778e-5  1.1468e-5
     9.9432e-6 8.6647e-6  7.2497e-6  5.9731e-6  4.6801e-6
     3.3235e-6  1.6381e-6
sb2 0 1 40I 100
c prdmp 0 50000000 0 2 5000000
nps 2e9
f5:p 42.426 42.426 0  0  $60 cm from center
fm5 .0018294  $convert to per electron from per photon
e5 0 39i 4.0
fc15 TALLY PER SOURCE ELECTRON
```

C.4   Detector Response Modeling

Semiconducting radiation detectors *count* interactions by measuring a short impulse of electrical current, resulting from the movement of electron-ion pairs in an electric potential. The electron-ion pair is created by interacting particles. The amount of charge liberated is predicted by the energy deposited by the radiation and the well-studied average energy required to create an ion-pair(96). The purpose of the MCNPX simulations described in this work is to determine the rate of depositions, and amount of energy deposited, within the detector materials for a given NRF assay geometry. The detector response modeling is accomplished in a very simple manner in MCNPX. The sum energy of simulated particles leaving the detector volume is subtracted from the sum energy of particles entering volume for each simulated history.

For the detector response calculations used in this dissertation, incident photon spectra were calculated by separate MCNPX simulations, such as those described in Sections C.2 and C.3. These simulations provide calculated spectra at a point or passing through a plane in the modeled space. The detector response model simulations assume that these calculated photon spectra may be represented as though they were uniformly-intense and normally incident upon a plane representing an outer surface of a shielded detector geometry. To further simplify the calculations, monoenergetic photons were simulated as incident upon the shielded geometry and results were superposed to determine the expected detector response to more complicated spectra.
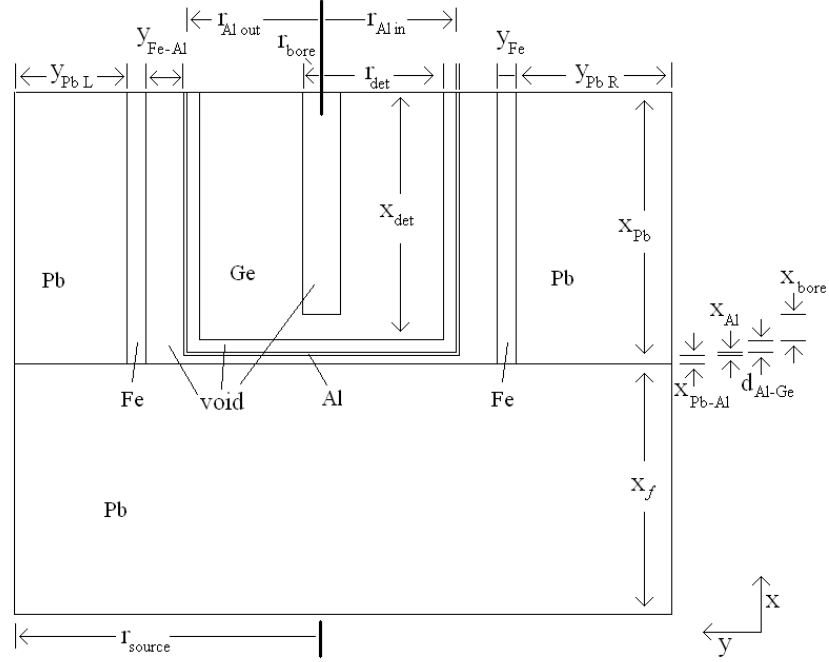
Figure C.2 Horizontal cut-through of the geometry used in MCNPX simulations to estimate photon energy depositions within a shielded HPGe detector. Photons enter the geometry from the bottom, uniformly distributed on the (y,z) plane within a radius, r_{source}, from the germanium crystal center. Dimensions are given in Table C.1. Dimensions given as r indicate radii, and that the object is circular in the perpendicular plane. The HPGe detector is assumed to be set inside an Fe enclosure. The Fe is modeled as a hollow, open-sided rectangular parallelepiped. Below the Fe is additional Pb shielding.

C.4.1   Model Geometry

Monoenergetic photons were emitted uniformly over a 12 cm-radius disc in the (y,z) plane and irradiated the shielded geometry shown in Figure C.2. The photons are incident from the bottom of the figure. The shielded detector geometry consists of lead of variable thickness, x_f, in front of a coaxial germanium crystal in an aluminum housing, contained in a square iron enclosure that is open on its front and back. Lead shielding of at least 5 cm-thickness is also present on the sides surrounding the iron enclosure. The geometry of the simulated shielded coaxial HPGe detector is shown in Figure C.2 with dimensions indicated in Table C.1

The input file for the simulation of the detector response to 3.761-MeV photons for $x_f = 13.2$ cm is shown below.

```
3761 keV photons penetrating 13.2cm pb shielding to 100% r.e. HPGe
```

dimension	value	
y_{PbL}	5	cm
$y_{\text{Fe}-\text{Al}}$	≥ 1.21	cm
r_{bore}	6.2	mm
r_{det}	3.975	mm
r_{Alin}	4.375	mm
r_{Alout}	4.505	mm
y_{Fe}	1.27	cm
y_{PbR}	8	cm
x_{det}	8.05	cm
x_{Pb}	8.85	cm
$x_{\text{Pb}-\text{Al}}$	3	mm
x_{Al}	1	mm
$d_{\text{Al}-\text{Ge}}$	4	mm
x_{bore}	8.2	mm
x_f	variable	
r_{source}	12	cm
$z_{\text{Fe}-\text{Al}}$	≥ 2.42	cm
z_{PbBottom}	7.5	cm

Table C.1 Dimensions of shielded HPGe detector geometry shown in Figure C.2. The final two dimensions listed are not indicated in the figure. $z_{\text{Fe}-\text{Al}}$ is the distance between the top of the Al case and the top, inner, surface of the Fe enclosure. The dimension, z_{PbBottom} indicates thickness of Pb beneath the Fe.

```
1     1  -11.34 1 -2 40 -33 41 -42      imp:p=1 $front pb filter
2     2   -5.323 5 -6 -11 #3            imp:p=1 $Ge det
3     0          7 -6 -13              imp:p=1 $bore hole
4     3   -2.702 -15 3 -4              imp:p=1 $cap
5     0          -11 4 -5              imp:p=1 $bt cap and Ge
6     0          -15 2 -3              imp:p=1 $bt Pb and cap
7     0        11 -14 4 -6            imp:p=1 $air b/t side Al and Ge
8     3  -2.702  14 -15 4 -6           imp:p=1  $Al side wall
9     0        15 30 -32 34 -36  2 -6 imp:p=1 $air bt side al and Fe
10    4  -7.8   31 -33 35 -34 2 -6     imp:p=1 $Left Fe Wall
11    4  -7.8   31 -33 36 -37 2 -6     imp:p=1 $Right Fe Wall
12    4  -7.8   32 -33 34 -36 2 -6     imp:p=1 $Top Fe Wall
13    4  -7.8   31 -30 34 -36 2 -6     imp:p=1 $Bottom Fe Wall
20    1  -11.34 40 -31 41 -42 2 -6     imp:p=1 $Pb bottom
21    1  -11.34 31 -33 41 -35 2 -6     imp:p=1 $Pb left
22    1  -11.34 31 -33 37 -42 2 -6     imp:p=1 $Pb right
102   0          -99 -1               imp:p=1 $front air
103   0          -99 6                imp:p=1 $back air
104   0          -99 1 -6 33           imp:p=1 $center air top
105   0          -99 1 -6 -40          imp:p=1 $center air bottom
106   0          -99 1 -6 40 -33 -41   imp:p=1  $center air left
107   0          -99 1 -6 40 -33 42    imp:p=1 $center air right
999   0          99                   imp:p=0  $

1 px 10
2 px 23.2 $13.2 cm shield
3 px 23.5 $3mm bt Pb and detector front
4 px 23.6 $1mm end cap thickness
5 px 24.0 $4mm endcap to xtal gap FRONT PLANE
6 px 32.05 $8.05cm xtal BACK PLANE
7 px 24.82 $bore depth=0.82cm from surf 5
11 cx 3.975  $Ge det radius
13 cx .62     $bore hole radius
14 cx 4.375  $4mm gap b/t Ge and Al
15 cx 4.505  $1.5mm wall
30 pz -4.505 $fe inner bottom
31 pz -5.14  $fe outter bottom
32 pz 6.925  $fe inner top
33 pz 8.195   $fe outter top (2 boxes)
34 py -5.715  $fe left inner
35 py -6.35   $fe left outter
36 py 5.715   $fe right inner
```

```
37 py 6.35     $fe right outter
40 pz -12.64   $pb bottom
41 py -11.43   $pb left
42 py 15       $pb right (keeps going)
80 px 0
99 so 105


mode  p e
nps 5e8
m1     82000   1  $U
m2     32000   1  $HPGe
m3     13000   1  $Al
m4     26000   1  $Fe
c cut:e j .01
cut:p j .01
ext:p .2X 0 21r
sdef par=2 pos=0 0 0 sur=80 erg=3.761 dir=1 axs=1 0 0 &
     rad=d3 vec =1 0 0
si3 0 12
sp3 -21 1
f8:p 2
e8 0 .1 34i 2.501 300i 4.001
```

C.5   Electron Stopping Treatment in MCNP

The process of bremsstrahlung production described in Section 2.6.2 is compli-
cated by the details of energetic electron transport in materials. Because electrons
are charged, they are subjected to the Coulomb force, which has an infinite range.
Thus, rather than describing single discrete interactions (as is considered in neutral-
particle transport), electrons are treated statistically in the electron transport code,
ETRAN(35). MCNP's electron transport mimics this approach(38). The energy
loss per unit length along the trajectory of an electron is described as a distribu-
tion function(36) whose mean is the nominal stopping power of the material(37).
Likewise, the angular deflection of the electron (i.e. θ_{12}), and the production of
bremsstrahlung are also treated as probability distribution functions(39).

To reduce computational requirements, the electron transport probability dis-
tributions are calculated for an energy group whose energy boundaries are given
iteratively by

$$E_{n+1} = \frac{E_n}{2^{1/8}} \tag{C.7}$$

where E_1 is the maximum electron energy expected in the problem, which is set

by default to 100 MeV, but is recommended to be changed by the user. The mean distance that an electron travels during energy loss from E_n to E_{n+1} is called a *step*. Each *step* is further divided into m *substeps*. There is an empirically predefined default m for each element in MCNPX, increasing with Z from 2 to 15, and the value can be increased above the default through user input. At each *substep*, the emission of bremsstrahlung, non-radiative energy loss, and angular deflection of the electron are randomly sampled, and the energy and direction of the electron are updated. When the electron energy decreases outside the *step*, distributions corresponding to the next *step* are calculated and the process is repeated. This results – on average – in approximately the correct treatment of electron stopping and bremsstrahlung production, however correlations between sampled distributions are ignored. Also, if materials are thinner than a *step*, inaccuracies may result because the actual electron transport is too coarsely discretized during the sampling of only a few *substeps*.

There is an additional way in which MCNP can determine the energy group for an electron. This is referred to as the nearest-boundary method, where the *step* parameters are recalculated when the electron energy becomes closer to E_{n+1} than E_n. The differences between the two methods become more significant when predicting bremsstrahlung from lower-energy electrons than are of interest here.

C.6   Thick-Target Bremsstrahlung Model

An additional *feature* in MCNPX is the thick-target bremsstrahlung model. The code allows the user to select which types of particles are transported during the simulation. When photon transport is turned on (as must be the case in all simulations of interest for NRF), electron transport is not turned on by default. This is primarily due to the hundredfold increase in computation time required to include electron transport. With the exception of the following example, all computational results in this work include electron transport.

When electron transport is not included, a model for bremsstrahlung production is applied whenever an electron would be created during photon transport. The model, called the *thick-target bremsstrahlung* (TTB) model, immediately produces photons sampled from a bremsstrahlung spectrum at the point of electron creation. The number and direction of the photons are sampled from a tabulated probability distribution that assumes the electron loses all its energy while stopping in a thick target. This assumption is generally quite good. However, when photo-electrons are produced within the electron's range of a material surface, the TTB model can over-predict bremsstrahlung production. Furthermore, the model appears to under sample the emission of bremsstrahlung at large angles relative to the trajectory of the electron-producing photon. The spectra of monoenergetic 1.7-MeV photons normally incident upon the circular surface of a uranium cylinder of 1 cm-radius and 1 cm-thick, as calculated by MCNPX, are shown in Figure C.3. The effective photon scattering cross sections are shown for the angular ranges $4^\circ - 5^\circ$ and

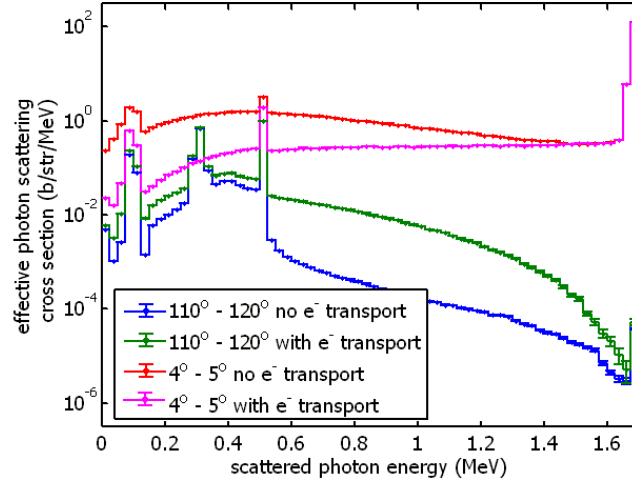Figure C.3 MCNPX-simulated differential cross section for scattering of 1.7-MeV photons from 1 cm uranium with and without full electron transport enabled.

$100^{\rm o} - 110^{\rm o}$, with and without electron transport. The TTB model appears to over-estimate low-energy bremsstrahlung emission in forwards directions and significantly underestimate bremsstrahlung production in backwards directions.

Bibliography

[1] "Remarks by President Barack Obama" Hradcany Square, Prague, Czech Republic, 5 April, 2010. Available online at http://www.whitehouse.gov/the_press_office/ Remarks-By-President-Barack-Obama-In-Prague-As-Delivered/ Retrieved 18 May, 2010.

[2] "Annual Energy Review," Energy Information Administration. available online at http://tonto.eia.doe.gov/cfapps/ipdbproject/IEDIndex3.cfm accessed 18 May, 2010.

[3] "International Energy Outlook, 2009," Energy Information Administration. Report #:DOE/EIA-0484(2009). 27 May, 2009.

[4] J.R. Phillips, "Irradiated Fuel Measurements," in *Passive Nondestructive Assay of Nuclear Materials*, D.T. Reilly, editor. Office of Nuclear Regulatory Research, NUREG/CR-5550. LA-UR-90-732 (1990) pp. 556.

[5] A.B. Lovins, "Nuclear weapons and power-reactor plutonium," Nature Vol. 283 (1980) pp. 817.

[6] "Global Fissile Material Report 2006", First report of the International Panel on Fissile Materials (2006). Available online at http://www.fissilematerials.org Accessed 18 May 2010.

[7] T. Katsuta and T. Suzuki, "Japan's Spent Fuel and Plutonium Managament Challenges," Research report No. 2 Internation Panel on Fissile Materials (2006). Available online at http://www.fissilematerials.org Accessed 18 May 2010.

[8] D. Bannick, J. Boer, T. Geurtsen, H. Linnebank, P. de Rijk, and S. von Vangerow, "Reprocessing: State of the art 1999," WISE News Communique 506, February 5, 1999. Available online at http://www10.antenna.nl/wise/506/index.html

[9] S.J. Tobin, W.S. Charlton, M.H. Ehinger, M.L. Fensin, A.S. Hoover, H.O. Menlove, B.J. Quiter, A. Rajasingam, N.P. Sandoval, S.F. Saavedra, D. Strohmeyer, M.T. Swinhoe, and S.J. Thompson, "Determining Plutonium in

Spent Fuel with Nondestructive Assay Techniques," Proceedings of 31st Annual Meeting of ESARDA, Vilnius, Lithuania (2009)

[10] O. Beck, T. Ruf, Y. Finkelstein, M. Cardona, T.R. Anthony, D. Belic, T. Eckert, D. J ager, U. Kneissl, H. Maser, R. Moreh, A. Nord, H.H. Pitz, and A. Wolpert, "Nondestructive determination of the ^{13}C content in isotopic diamond by nuclear resonance fluorescence," J. App. Phys. 83 (1998) pp. 5484.

[11] O. Klein and Y. Nishina, "Über die Streuung von Strahlung durch freie Elektronen nach der neuen relativistischen Quantendynamik von Dirac," Z. f. Phys. 52 (1929) pp. 853-868.

[12] J.A. Bearden and A.F. Burr, "Reevaluation of X-Ray Atomic Energy Levels," Rev. Mod. Phys. 39, (1967) 125.

[13] J.M. Blatt and V.F. Weisskopf, *Theoretical Nuclear Physics.* (John Wiley & *Sons, NewYork*, 1952).

[14] S.G. Prussin, *Nuclear Physics for Applications* (Wiley-VCH, Weinheim Germany, 2007).

[15] Lynn Kissel, "RTAB: the Rayleigh scattering database," Radiation Physics and Chemistry Vol. 59, (2000) 185-200.

[16] P.P. Kane, L. Kissel, R.H. Pratt, and S.C. Roy, "Elastic scattering of γ-rays and X-rays by atoms," Physics Reports Vol. 140, No.2 (1986) 75-159.

[17] L. Kissel, R.H. Pratt, and S.C. Roy, "Rayleigh scattering by neutron atoms, 100 eV to 10 MeV," Phys.Rev. A Vol 22, No. 5 (1980).

[18] M.B. Chadwick, P. Obloinsk, M. Herman, N.M. Greene, R.D. McKnight, D.L. Smith, P.G. Young, R.E. MacFarlane, G.M. Hale, S.C. Frankle, A.C. Kahler, T. Kawano, R.C. Little, D.G. Madland, P. Moller, R.D. Mosteller, P.R. Page, P. Talou, H. Trellue, M.C. White, et al. "ENDF/B-VII.0: Next Generation Evaluated Nuclear Data Library for Nuclear Science and Technology," Nuclear Data Sheets Volume 107, Issue 12, (December 2006) Pages 2931-3118.

[19] D.E. Cullen, J.H. Hubbell, and L. Kissel, "EPDL97: the evaluated photon data library, '97 version," UCRL-50400, Vol. 6, Rev. 5 (1997).

[20] L. Kissel, B. Zhou, S.C. Roy, S.K. Sen Gupta, R.H. and Pratt "The Validity of Form-Factor, Modified-Form-Factor and Anomalous-Scattering-Factor Approximations in Elastic Scattering Calculations," Acta Cryst. A51, (1995) 271-288.

[21] S. Agostinelli, et al. "GEANT4 – a simulation toolkit," NIM A 506, No. 3 (2003) pp. 250-303.

[22] R. Buck and E. Lent, "COG: A New, High-Resolution Code for Modeling Radiation Transport," UCRL-52000-93-6, (1993).

[23] J.F. Pelowitz (ed.), "MCNPX™ USERS MANUAL Version 2.6.0," LA-CP-07-1473 (2008).

[24] L.S. Waters (ed.), "MCNX™ USER'S MANUAL Version 2.3.0," LA-UR-02-2607 (2002).

[25] J.E. Sweezy, et. al, "MCNP A General Monte Carlo N-Particle Transport Code, Version 5," LA-UR-03-1987, (2003, revised 2005).

[26] E.D. Cashwell et. al. "Monte Carlo Photon Codes: MCG and MCP" LA-5157-MS, (March 1973).

[27] J.H. Hubbell, W.J. Weigele, E.A. Briggs, R.T. Brown, D.T. Cromer, and R.J. Howerton, "Atomic Form Factors, Incoherent Scattering Functions, and Photon Scattering Cross Sections," J. Phys. Chem. Ref. Data Vol 4, No. 3 (1975).

[28] R. Littlejohn *UC Berkeley Physics 221A/B Lecture Notes* available online at http://bohr.physics.berkeley.edu/classes/221/0708/221.html (2008) retrieved 14 December, 2009.

[29] M.J. Berger, J.H. Hubbell, S.M. Seltzer, J. Chang, J.S. Coursey, R. Sukumar, and D.S. Zucker, "XCOM: Photon Cross Sections Database, NIST Standard Reference Database 8 (XGAM)" available online at http://physics.nist.gov/PhysRefData/Xcom/Text/XCOM.html (1998).

[30] H. Bethe and W. Heitler, "On the Stopping of Fast Particles and on the Creation of Positive Electrons," Proc. R. Soc. Lond. A 146 (1934) pp. 83-112.

[31] F. Salvat, J.M. Fernández-Varea, E. Acosta, and J. Sempau, "PENELOPE A Code System for Monte Carlo Simulation of Electron and Photon Transport," OECD Nuclear Energy Agency, ISBN 92-64-18475-9, (2001).

[32] S.M. Seltzer and M.J. Berger, "Bremsstrahlung spectra from electron interactions with screened atomic nuclei and orbital electonrs," NIM B 12, (1985) pp. 95-134.

[33] A. Sommerfeld, Ann. Phys. (Leipzig) 11, (1931) pp. 257

[34] R.H. Pratt and H.K. Tseng, "Tip region of the bremsstrahlung specturm from incident electrons of kinetic energy 50 keV - 1.84 MeV," Phys. Rev. A 11, No. 6 (1975).

[35] ETRAN, S.M. Seltzer, "An Overview of ETRAN Monte Carlo Methods," Ch. 7 of *Monte Carlo Transport of Electrons and Photons*, edited by T.M Jenkins, W.R Nelson, and A. Rindi, Plenum Press (1988).

[36] L. Landau, "On the Energy Loss of Fast Particles by Ionization, J. Phys. USSR 8 (1944).

[37] M. J. Berger, "Monte Carlo Calculation of the Penetration and Diffusion of Fast Charged Particles, in *Methods in Computational Physics, Vol. 1*, edited by B. Alder, S. Fernbach, and M. Rotenberg, Academic Press, New York, (1963) 135.

[38] J.F. Briesmeister (ed.), "MCNP^{TM} A General Monte Carlo NParticle Transport Code Version 4C," LA13709M, (2000).

[39] S. Goudsmit and J. L. Saunderson, "Multiple Scattering of Electrons, Phys. Rev. 57 (1940) pp. 24.

[40] J. A. Halbleib, R. P. Kensek, T. A. Mehlhorn, G. D. Valdez, S. M. Seltzer, and M. J. Berger, "ITS Version 3.0: Integrated TIGER Series of Coupled Electron/Photon Monte Carlo Transport Codes, SAND91-1634 (1992).

[41] J.J. Demarco, T.D Solber, R.E. Wallace, and J.B. Smathers, "A verification of the Monte Carlo code MCNP for thick target bremsstrahlung calculations," Med. Phys. 22, (1995) pp. 11-16.

[42] J.H. Hubbell, H.A. Gimm, and I. Øverbø, "Pair, Triplet, and Total Atomic Cross Sections (and Mass Attenuation Coefficients) for 1 MeV - 100 GeV Photons in Elements Z = 1 to 100," J. Phys. Chem. Ref. Data 9, No. 4 (1980) pp. 1023-1147.

[43] B.J. Quiter, B.A. Ludewigt, V.V. Mozin, and S.J. Tobin, "Nondestructive Spent Fuel Assay Using Nuclear Resonance Fluorescence," INMM, July 12-16, 2009, Tucson, AZ.

[44] R. E. MacFarlane, "NJOY 99 Nuclear Data Processing System", code available at http://t2.lanl.gov/codes/njoy99/.

[45] J.S. Hendricks and B.J. Quiter, "MCNP/X Form Factor Upgrade for Improved Photon Transport," (LA-UR-10-01096) Submitted to Journal of Nuclear Technology.

[46] C.J. Hagmann and J. Pruet,"Photon production through multi-step processes important in nuclear resonance fluorescence experiments," NIM B 259, (2007) pp. 895-909.

[47] A.I. Milstein and M. Schumacher, "Present status of Delbrück scattering," Physics Reports 243, (1994) pp. 183214.

[48] H.C. Cheng, E.-C. Tsai, and X. Zhu, "Delbrück scattering," Phys. Rev. D 26, no. 4, (1982) pp. 908.

[49] A. Scherdin, A. Schäfer, W. Greiner, G. Soff, and P.J. Mohr, "Coulomb corrections to Delbrück scattering," Z. Phys. A 353, (1995) pp. 273-277.

[50] B. Kasten, D. Schaupp, P. Rullhausen, F. Smend, M. Schumacher, and L. Kissel, "Coulomb correction effect in Delbrück scattering and atomic Rayleigh scattering of 1-4 MeV photons," Phys. Rev. C 33, No. 5 (1986) pp. 1606.

[51] R. Solberg, K. Mork, and I. Øverbø, "Coulomb and screaning corrections to Delbrück forward scattering," Phys. Rev. A 51, No. 1 (1995) pp. 359.

[52] P. Rullhausen, F. Smend, and M. Schumacher, "Delbrück scattering of 2754 keV photons by Nd, Ce, I, Sn, Mo, and Zn," Phys. Letters 84B, No. 2 (1979) pp. 166.

[53] H. Falkenberg, A. Hünger, P. Rullhausen, and M. Schumacher, "Amplitudes for Delbrück scattering," Atomic Data and Nuclear Data Tables 50, (1992) pp. 1-27.

[54] T. Bar-Noy and S. Kahane, "Numerical calculations of Delbrück scattering amplitudes," Nuc. Phys. A 288, (1977) pp. 132-140.

[55] U. Berg and U. Kneissl, "Recent progress on nuclear magnetic dipole excitations," Ann. Rev. Nucl. Part. Sci 37, (1987) 33-69.

[56] H. Arenhövel, "Photon scattering by nuclei: theory and experiment," *Procedings of the Internation Conference on Photonuclear Reactions and Applications*, edited by B.L. Berman, Lawrence Livermore Laboratory (1973) pp. 449.

[57] W.D. Myers, W.J. Swiatecki, T. Kodama, L.J.El-Jaick, and E.R. Hilf, "Droplet model of the giant dipole resonance," Phys. Rev. C 15, No. 6 (1977) pp. 2032.

[58] L. Jianfeng, S. Zongdi, and Z. Yixin, "Giant dipole resonance parameters," Reference Input Parameter Library. Available online at http://www-nds.iaea.org/RIPL-2/ (2001).

[59] T.E.O. Ericson and J. Hüfner, "Low-frequency photon scattering by nuclei," Nuc. Phys. B 57, (1973) pp. 604-616.

[60] P. Rullhusen, W. Mückenheim, F. Smend, M. Schumacher, G.P.A Berg, and L. Kissel, "Test of vacuum polarization by precise investigation of Delbrück scattering," Phys. Rev. C 23, No. 4 (1981) pp. 1375.

[61] B.L. Berman, "Atlas of photoneutron cross sections obtained with monoenergetic photons," Atomic Data and Nuclear Data Tables 15, (1975) pp. 319-390.

[62] J.L. Frian, "Low-Energy Theorems for Nuclear Compton and Raman Scattering and $0^+ \rightarrow 0^+$ Two-Photon Decays in Nuclei," Annals of Physics 95, (1975) pp. 170-201.

[63] P. Rullhusen, F. Smend, and M. Schumacher, "Elastic Scattering of 2.754 MeV Photons by Ta and Interference between Rayleigh, Thomson and Delbrück Scattering," Z. Physik A 288, (1978) 119-123.

[64] P. Rullhusen, F. Smend and M. Schumacher, "Delbrück scattering of 2754 keV photons by Nd, Ce, I, Sn, Mo and Zn," Physics Letters 84B, No. 2 (1979) pp. 166.

[65] P.M. Endt and C. Van der Leun, "Energy levels of A=21-44 nuclei (VI)," Nuc. Phys. A 310, (1978) pp. 1-751.

[66] J.M. Blatt and V.F. Weisskopf, "Theoretical Nuclear Physics," Chapter 12, John Wily Sons, Inc. New York (1952).

[67] U. Kneissl, H.H. Pitz, and A. Zilges, "Investigation of Nuclear Structure by Resonance Fluoresence Scattering," Prog. Part. Nucl. Phys. 37, (1996) pp. 349-433.

[68] D.R. Hamilton, "On Direction Correlation of Successive Quanta," Phys. Rev. 58, (1950) pp. 122.

[69] W. Geiger, Zs. Németh, I. Bauske, P. von Brantano, R.D. Heil, R.-D. Herzberg, U. Kneissl, J. Margraf, H. Maser, N. Pietralla, H.H. Pitz, C. Wesselborg, A. Zilges, "Low-lying dipole excitations in the isotopes ^{113,114}Cd," Nuc. Phys. A 580, (1994) 263-276.

[70] U. Kneissl, H.H. Pitz, and A. Zilges, "Investigation of Nuclear Structure by Resonance Fluoresence Scattering," Prog. Part. Nucl. Phys. 37, (1996) pp. 352 and references therein.

[71] B. Özel, J. Enders, P. von Neumann-Cosel, I. Poltoratska, A. Richter, D. Savran, S. Voltz, and A. Zilges, "Systematics of the pygmy dipole resonance in stable tin isotopes from resonant photon scattering," Nuc. Phys. A 788, (2007) pp. 385c-388c.

[72] F. Ajzenberg-Selove, "Energy levels of light nuclei A=11-12," Nuc. Phys. A 506 (1990) pp. 1-158.

[73] S.M. Wong, "Introductory Nuclear Physics, 2nd Edition," Ch. 5, WILEY-VCH Verlag GmbH Co. KGaA (2004).

[74] W. Donner and W. Greiner, "Octupole Vibrations of Deformed Nuclei," Z. fur Phys. 197, (1966) pp. 440-472.

[75] J. Bryssinck, L. Govor, V.Y. Ponomarev, F. Bauwens, O. Beck, D. Belic, P. von Brentano, D. De Frenne, T. Eckert, C. Fransen, K. Govaert, R.-D. Herzberg, E. Jacobs, U. Kneissl, H. Maser, A. Nord, N. Pietralla, H.H. Pitz, and V. Werner, "Systematic study of electric quadrupole excitations in the stable even mass Sn nuclei", Phys. Rev. C. 61 (2000) 024309-1.

[76] J. Bryssinck, L. Govor, D. Belic, F. Bauwens, O. Beck, P. von Brentano, D. De Frenne, T. Eckert, C. Fransen, K. Govaert, R.-D. Herzberg, E. Jacobs, U. Kneissl, H. Maser, A. Nord, N. Pietralla, H.H. Pitz, V.Y. Ponomarev, and V. Werner, "Uniform

properties of $J^{\pi} = 1^-$ two-phonon states in the semimagic even-even tin isotopes ^{116,118,120,122,124}Sn," Phys. Rev. C 59, No. 4 (1999) pp. 1930.

[77] B.A. Brown, P.M.S. Lesser, and D.B. Fossan, "Properties of high-spin states in ^{91}Nb and ^{91}Zr via ^{6}Li-induced reactions," Phys. Rev. C 13, No. 5 (1976) pp. 1900.

[78] D.R. Tilley, J.H. Kelley, J.L. Godwin, D.J. Millener, J.E. Purcell, C.G. Sheu, and H.R. Weller, "Energy levels of light nuclei A=8,9,10," Nuc. Phys. A 745, (2004) 155-362.

[79] M.B. Chadwick, P. Oblozinsky, A.I. Blokhin, T. Fukahori, Y. Han, Y.-O. Lee, M.N. Martins, S.F. Mughabghab, V.V. Varlamov, B. Yu, and J.Zhang, "IAEA Photonuclear Data Library," available online at http://www-nds.iaea.org/photonuclear/ (2000).

[80] J. Enders, P. von Brentano, J. Eberth, A. Fitzler, C. Fransen, R.-D. Herzberg, H. Kaiser, L.Käubler, P. von Neumann-Cosel, N. Pietralla, V.Yu. Ponomarev, A. Richter, R. Schwenger, and I. Wiedenhöver, "Nuclear resonance fluorescence experiments on ^{204,206,207,208}Pb up to 6.75 MeV," Nuc. Phys. A 724, (2003) 243-273.

[81] E. Hammarén, P. Heikkinen, K.W. Schmid, and A. Faessler, "Microscopic and phenomenological analysis of the Alaga rule for dipole states," Nuc. Phys. A 541 (1992) pp. 226-240.

[82] A. Zilges, P. von Brentano, A. Richter, U. Kneissl, H.H. Pitz, anc C. Wesselborg, "Uncommon mixing ratios of spin-one states in the rare-earths region and evidence for K mixing," Phys. Rev. C 42 (1990) pp. 1945.

[83] F.R. Metzger, "Resonance Fluorescence in Nuclei," Prog. in Nuc. Phys. 7, (1959) pp. 54.

[84] R.L. Mössbauer, "Kernresonanzfluoreszenz von Gammastrahlung in Ir^{191}," Z. fur Phys. 151, (1958) pp. 124-143.

[85] "Properties of Isotopes Relevant to Mössbauer Spectroscopy" from the *Mössbauer Effect Data Center* available online at http://orgs.unca.edu/medc/Resources.html (2009).

[86] W.E. Lamb, Jr., "Capture of Neutrons by Atoms in a Crystal," Phys. Rev. 55, (1939) pp.190

[87] R.D. Heil, H.H. Pitz, U.E.P Berg, U. Kneissl, K.D. Hummel, G. Kilgus, D. Bohle, A. Richter, C. Wesselborg, and P. Von Brentano, "Observation of orbital magnetic dipole strength in the actinide nuclei ^{232}Th and ^{238}U." Nuc. Phys. A476 (1988) pp. 39-47

[88] C. Kittel, "Introduction to Solid State Physics," 7th edition. John Wiley Sons, Inc. New York (1996) Chap. 5 pp. 126 and refences therein.

[89] R.-D. Herzberg, I. Bauske, P. von Brentano, Th. Eckert, R. Fischer, W. Geiger, U. Kneissl, J. Margraf, H. Maser, N. Pietralla, H. H. Pitz, and A. Zilges, "Lifetimes of two-phonon 1^- states in even N = 82 nuclei," Nucl. Phys. A 592, No. 2 (1995) pp. 211-220.

[90] G. Kehlenbeck, L. Ziegeler, F. Smend, and M. Schumacher, "The Slowing-Down of Low-Energy Recoil Atoms in Solids and Liquids Investigated by Nuclear Resonance Fluorescence," Z. Phys. B 66, (1987) pp. 147-151.

[91] F. Wolf, J. Ahlert, L. Ziegeler, F. Smend, and M. Schumacher, "Dependence of the Nuclear Recoil Motion on the Phonon Spectrum of Solids Investigated by Nuclear Resonance Fluorescence," Z. Phys. B 55, (1984) pp. 287-291.

[92] K. Treml and H. Langhoff, "The Slowing Down of Atoms with Energies of E10eV in Crystals," Z. Physik B 25, (1976) pp. 123-129.

[93] H. Langhoff, "On the Slowing Down of Atoms with E 15 eV in Solids" Z. Physik 241, (1971) pp. 236-243.

[94] A. Sadiq, "Gaussian Approximation for Phonon Frequency Distribution Function for PuO_2 and UO_2," J. of Nucl. Sci. and Tech. 12, (1975) pp. 275-279.

[95] G. Dolling, R.A. Cowley, and A.D.B. Woods, "The crystal dynamics of uranium dioxide," Can. J. of Phys. 43, No. 8 (1965) pp. 1397.

[96] G.F. Knoll, "Radiation detection and measurement," John Wiley Sons Inc. New York, (2000)

[97] M.F. Cunningham, J.N. Ullom, T. Miyazaki, S.E. Labov, J. Clarke, T.M. Lanting, A.T. Lee, P.L. Richards, J. Yoond, and H. Spieler, "High-resolution operation of frequency-multiplexed transition-edge photon sensors," Appl. Phys. Letters 81, No. 1 (2002) pp. 159.

[98] J.N. Ullom, J.A. Beall, W.B. Doriese, W.D. Duncan, L. Ferreira, G.C. Hilton, K.D. Irwin, C.D. Reintsema, and L. R. Vale, "Optimized transition-edge x-ray microcalorimeter with 2.4 eV energy resolution at 5.9 keV," Appl. Phys. Letters 87, (2005) 194103.

[99] H. Yang, "Active interrogation methods for detection of special nuclear material," Ph. D. Dissertation, University of Michigan Nuclear Engineering (2009).

[100] HIGS flux performance table, DFELL/TUNL, Feb. 5, 2010 (Version 1.0). Accessed online 2, April 2010. http://www.tunl.duke.edu/pdfs/HIGSPerformance.pdf

[101] F.V. Hartemann, S.G. Anderson, C.P.J Barty, D.J. Gibson, C.A. Hagmann, M.S. Johnson, I. Jovanovic, D.P. MaNabb, M.J. Messerly, J.A. Pruet, M.Y. Shverdin, C.W. SIders, and A.M. Tremaine, "Gamma-ray compton light source development at LLNL," Proceedings of PAC07, Albuquerque, New Mexico, (2007) pp. 1245

[102] B.J. Micklich, D.L. Smith, T.N. Massey, C.L. Fink, and D. Ingram, "FIGARO: detecting nuclear materials using high-energy gamma-rays," Nuclear Instruments and Methods in Physics Research A 505, (2003) pp. 406-469.

[103] H. Ohgaki, T. Noguchi, S. Sugiyama, T. Yamazaki, T. Mikado, M. Chiwaki, K. Yamada, R. Suzuki, and N. Sei, "Linearly polarized photons from Compton backscattering of laser light for nuclear resonance fluorescence experiments," Nuclear Instruments and Methods in Physics Research A 353, (1994) pp. 384-388.

[104] F. Albert, S.G. Anderson, G.A. Anderson, S.M. Betts, D.J. Gibson, C.A. Hagmann, J. Hall, M.S. Johnson, M.J. Messerly, V.A. Semenov, M.Y. Shverdin, A.M. Tremaine, F.V. Hartemann, C.W. Siders, D.P. McNabb, and C.P.J Barty, "Isotope-specific detection of low-density materials with laser-based monoenergetic gamma-rays," Optics Letters 35, No. 3, (2010) pp. 354.

[105] F.V. Hartemann, F. Albert, G.G. Anderson, S.G. Anderson, A.J. Bayramian, S.M. Betts, T.S. Chu, R.R. Cross, C.A. Ebbers, S.E. Fisher, D.J. Gibson, A.S. Ladran, M.J. Messerly, V.A. Semenov, M.Y. Shverdin, C.W. Siders, D.P. McNabb, C.P.J Barty, A.E. Vlieks, E.N. Jongewaard, and S.G. Tantawi, "Development of a precision tunable gamma-ray source driven by a compact x-band linac," Proceedings of PAC09, Vancouver, British Columbia, (2009) WE5RFP030.

[106] C.G.R Geddes, Cs. Toth, J. van Tilborg, E. Esarey, C.B. Schroeder, D. Bruhwiller, C. Nieter, J. Cary, and W.P Leemans, "High-quality electron beams from a laser wakefield accelerator using plasma-channel guiding," Nature 431, (2004) pp. 538.

[107] AK Steel Corporation, "316/316L Stainless Steel" Product Data Sheet (2007) West Chester, OH. www.aksteel.com/pdf/markets_products/stainless/austenitic/316_316L_Data_Sheet.pdf

[108] L.I. Cover, "Waste Encapsulation and Storage Facility Basis for Interim Operation," Hanford Technical Document HNF-SD-WM-BIO-002 Rev. 1, (2000).

[109] "Locating and Characterizing Disused Sealed Radioactive Sources in Historical Waste," IAEA Nuclear Energy Series No. NW-T-1.17, (2008).

[110] J. Pérez-Calatayud, F. Ballester, J.L. Lluch, M.A. Serrano-Andrés, E. Casal, V. Puchades, and Y. Limami, "Monte Carlo calculation of dose rate distributions around the Walstam CDC.K-type ^{137}Cs sources," Phys. Med. Biol. 46 (2001) 2029-2040.

[111] M.L. Tobias, D.R. Vondy, and M.P. Lietzke, "NIGHTMARE – An IBM 7090 Code for the Calculation of Gamma Heating in Cylindrical Geometry," USAEC Report ORNL-3198, Oak Ridge National Laboratory, Feb. 26, (1972).

[112] DOE RECLAIMS FINAL LEASED CESIUM CAPSULES. Hanford Press Release. Hanford, WA July 1996. Accessed online 17 Mar. 2009. http://www.hanford.gov/press/1996/96-083.htm.

[113] K. Mayer, E. Dahms, J. Horta, K.L utzenkirchen, S. Millet, A. Nicholl, J. Sch onfeld, A. Schubert, H. Thiele, M. Wallenius, and T. Wiss, "Nuclear Forensics: From specialized analytical measurements to a fully developed discipline in science," IAEA-CN-154/035 in Procedings from the International Conference on Illicit Nuclear Trafficking, Edinburgh 19-22 November, 2007.

[114] T.R. England and B.F. Rider, "Status of Fission Yield Evaluations," Los Alamos National Laboratory, LA-UR-94-3106; ENDF-349 (1993).

[115] M. Scheck, H. von Garrel, N. Tsoneva, D. Belic, P. von Brentano, C. Fransen, A. Gade, J. Jolie, U. Kneissl, C. Kohstall, A. Linnemann, A. Nord, N. Pietralla, H.H. Pitz, F. Stedile, C. Stoyanov, and V. Werner, "Dipole strength distributions in the stable Ba isotopes $^{134-138}$Ba: A study in the mass region of a nuclear shape transition." Phys. Rev. C 70 044319 (2004).

[116] E. Casal, F. Ballester, J.L. Lluch, J. Pérez-Calataud, and F. Lliso, "Monte Carlo calulations of dose rate distributions around Amersham CDCS-M-type ^{137}Cs source," Med. Phys. 27 (2000) pp. 132.

[117] R.B. Firestone, S.Y.F. Chu, and C.M. Baglin, "1998 Update to the 8th Edition of the Table of Isotopes," CD-ROM, John Wiley Sons, Inc. (1998).

[118] N. Pietralla, D. Belic, P. von Brentano, C. Fransen, R.-D. Herzberg, U. Kneissl, H. Maser, P. Matschinsky, A. Nord, T. Otsuka, H.H. Pitz, V. Werner, and I. Wiedenh over, "Isovector quadrupole excitations in the valence shell of the vibrator nucleus ^{136}Ba: Evidence from photon scattering experiments" Phys. Rev. C 58 No.2 (1998) pp. 796.

[119] J.-H. Chao, C.-L. Tseng, "Determination of ^{135}Cs by neutron activation analysis," Nuc. Inst. and Meth. A 372 (1996) pp. 275.

[120] J. Pottier, "A new type of RF electron accelerator: the rhodotron," Nucl. Instr. Meth. B40/41 (1989) pp. 943-945.

[121] SCALE-4.3, Modular System for Performing Standardized Computer Analyses for Licencing Evaluation. Oak Ridge National Laboratory, 1997. RSICC Computer Code Collection CCC-0545/12.

[122] A. Tanskanen, "Assessment of the neutron and gamma sources of the spent BWR fuel". Interim report on Task FIN JNT A 1071 of the Finnish Support Programme to IAEA Safeguards. STUK-YTO-TR 170. Helsinki 2000. 17 pp + Appendices 14 pp.

[123] W. Bertozzi, J.A. Caggiano, W.K. Hensley, M.S. Johnson, S.E. Korbly, R.J. Ledoux, D.P. McNabb, E.B. Norman, W.H. Park, and G.A. Warren, "Nuclear resononce fluorescence excitations near 2 MeV in ^{235}U and ^{239}Pu," Phys. Rev. C 041601(R) (2008).

[124] G.A. Warren, J.A. Caggiano, E.A. Miller, W. Bertozzi, A. Klimenko, S.E. Korbly, R.J. Ledoux, and W.H. Park, "Nuclear Resonance Fluorescence of ^{235}U above 3 MeV," 2007 IEEE Nuclear Science Symposium Conference Record. pp. 2047.

[125] J. McFarland, M.S. Thesis. Department of Nuclear Engineering, University of California, Berkeley. (2009).

[126] E. Browne, "Nuclear Data Sheets for A = 235,239," Nuclear Data Sheets 98, (2003) pp. 665-800.

[127] I. Bauske, J.M. Arias, P. von Brentano, A. Frank, H. Friedrichs, R.D. Heil, R.-D. Herzberg, F. Hoyler, P. Van Isacker, U. Kneissl, J. Margraf, H.H. Pitz, C. Wesselborg, and A. Zilges, "First Observation of Scissors Mode States in an Odd-Mass Nuclueus," Physical Review Letters 71 (1993) pp. 975.

[128] W.B. Wilson, T.R. England, M. Herman, R.E. MacFarlane, and D.W. Muir, "CINDER'90 code for transmutation calculations," Nuclear Data for Science and Technology Conference, Trieste, Italy (1997).

[129] C.A. Hagmann, J.M. Hall, M.S. Johnson, D.P.McNabb, J.H. Kelley, C. Huibregtse, E. Kwan, G. Rusev, and A.P. Tonchev, "Transmission-based detection of nuclides with nuclear resonance fluorescence using a quasimonoenergetic photon source," J. App. Phys. 106, 084901 (2009).

[130] International Nuclear Safety Center, Available online at: http://www.insc.anl.gov/

[131] ATI Wah Chang, "Reactor Grade Zirconium Alloys for Nuclear Waste Disposal," ZirAly-019 data sheet, (2003).

[132] A. Zilges, P. von Brentano, R.-D. Herzberg, U. Kneissl, J. Margraf, H. Maser, N. Pietralla, and H.H. Pitz, "Srong dipole excitations around 1.8 MeV in ^{238}U," Phys. Rev. C 52, No. 2 (1995) pp. R468.

[133] Jag Tuli, "Evaluated Nuclear Structure Data File (ENSDF)," Database version of January 20, 2010, Brookhaven National Laboratory. Available online at: http://www.nndc.bnl.gov/ensdf/ (2010).

[134] F. Ajzenberg-Selove, "Energy levels of light nuclei A=5-10," Nuc. Phys. A 490, (1988) pp. 1-225.

[135] W.J. Alston III, H.H. Wilson, and E.C. Booth, "Resonance fluorescence and absorption measurements of transition strenghts in odd-mass nuclei," Nuc. Phys. A 116, (1968) pp. 281-288.

[136] I.Y. Lee, R.M. Clark, M. Cromaz, M.A. Deleplanque, M. Descovich, R.M. Diamond, P. Fallon, A.O. Macchiavelli, F.S. Stephens, and D. Ward, "GRETINA: A gamma ray energy tracking array," Nuc. Phys. A 746 (2004) pp. 255c-259c.

[137] N. Pietralla, I. Bauske, O. Beck, P. von Brentano, W. Geiger, R.-D. Herzberg, J. Margraf, H. Maser, H.H. Pitz, and A. Zilges, "Absolute level widths in ^{27}Al below 4 MeV," Phys. Rev. C 51, No. 2 (1995) pp. 1021.

[138] L.P. Ekström and R.B. Firestone, "WWW Table of Radioactive Isotopes," database version 2/28/99 from URL http://ie.lbl.gov/toi/index.htm

[139] D.T. Vo and P.A. Russo, "Comparisons of the Portable Digital Spectrometer," Los Alamos National Laboratory Report LA-13895-MS (2002).

[140] C.J. Lodwick and H.J. Spitz, "Modification to the Monte Carlo N-Particle Code for Simulating Direct, In Vivo Measurements of Stable Lead in Bone," Health Physics, Vol. 94, No. 6 (2008) pp. 519-526.

[141] T. Belgya, "Discrete level library files," Reference Input Parameter Library. Available online at http://www-nds.iaea.org/RIPL-2/ (2002).

[142] Thomson Reuters, "INSPEC," Available online at http://thomsonreuters.com/products_services/science/ science_products/a-z/inspec (2009).

[143] Redhat, "Cygwin," Datasheet available online at http://www.redhat.com/services/custom/cygwin (2008).

[144] "ENDF-6 Formats Manual," ed. M. Herman. Document ENDF-102, BNL-NCS-44945-05-Rev (2001).